

N72-12953  
NASA CR 115242  
REPORT NO. GDCA-DDB71-005  
CONTRACT NAS 9-10956

**CASE FILE  
COPY**

**COMPUTATIONAL TECHNIQUES FOR DESIGN  
OPTIMIZATION OF THERMAL PROTECTION SYSTEMS  
FOR THE SPACE SHUTTLE VEHICLE**

VOLUME I ♦ FINAL REPORT

**GENERAL DYNAMICS**  
*Convair Aerospace Division*

REPORT NO. GDCA-DDB71-005

**COMPUTATIONAL TECHNIQUES FOR DESIGN  
OPTIMIZATION OF THERMAL PROTECTION SYSTEMS  
FOR THE SPACE SHUTTLE VEHICLE**

VOLUME I ♦ FINAL REPORT

30 September 1971

Prepared Under  
Contract NAS9-10956

Submitted to  
National Aeronautics and Space Administration  
MANNED SPACECRAFT CENTER  
Houston, Texas

Prepared by  
CONVAIR AEROSPACE DIVISION OF GENERAL DYNAMICS  
San Diego, California

## FOREWORD

This investigation was performed for the NASA Manned Spacecraft Center Structures and Mechanics Division. Dr. Donald M. Curry was the technical monitor, and Dr. Kenton D. Whitehead was the project manager. The study was conducted by Dr. Whitehead and a project team consisting of Dr. K. T. Shih - Thermodynamics, Mr. G. L. Getline - Dynamics, Mr. R. S. Wilson - Stress, and Messrs R. H. Trelease and S. T. Hitchcock - Weights/Cost Analysis. All work was done at the San Diego Operation of the Convair Aerospace Division of General Dynamics with the exception of consultation provided by Mr. J. D. Anderson of the Fort Worth Operation on the acoustic fatigue computer program. Results of the study are published in two volumes; the Final Report (Vol I) and User's Manual (Vol II).

## TABLE OF CONTENTS

<u>Section</u>	<u>Page</u>
1 INTRODUCTION	1-1
1.1 TASK 1 — DEVELOPMENT OF THE COMPUTATIONAL PROCEDURE	1-1
1.2 TASK 2 — DESIGN OPTIMIZATION STUDIES	1-2
1.3 TASK 3 — SENSITIVITY STUDIES	1-2
1.4 TASK 4 — PROGRAM DEMONSTRATION AND DOCUMENTATION	1-3
1.5 TASK 5 — RECOMMENDATIONS AND PROGRAM REFINEMENTS	1-3
1.5.1 Computer Program Improvements	1-3
1.5.2 Program Applications and Optimization Techniques	1-4
1.5.3 Optimization and Sensitivity Studies	1-4
1.5.4 Program Demonstration and Documentation	1-4
2 COMPUTER PROGRAM	2-1
2.1 PROGRAM ORGANIZATION	2-1
2.2 AEROTHERMODYNAMIC ENVIRONMENT	2-1
2.2.1 Flow Field Calculations	2-2
2.2.2 Flat Plate, Wedge, and Cone Aerodynamic Heating	2-12
2.2.3 Sphere and Cylinder Aerodynamic Heating	2-18
2.3 STRUCTURAL TEMPERATURE DETERMINATION	2-25
2.4 STRUCTURAL ANALYSIS	2-31
2.4.1 Loads Analysis and Nodal Breakdown of Panel	2-32
2.4.2 Temperature Interpolation	2-37
2.4.3 Computation of Stresses	2-37
2.4.4 Calculation of Design Factors	2-41
2.4.5 Calculation of Creep Strain	2-44
2.5 FATIGUE ANALYSIS	2-45
2.5.1 Prediction of Fatigue Life	2-45
2.5.2 Life Prediction Methods	2-48
2.5.3 Program Organization	2-51
2.6 TPS SECTION REDESIGN	2-72
2.6.1 Stress Redesign of the Panel	2-72
2.6.2 Thermodynamic Redesign of Panel	2-73
2.7 WEIGHTS/COST ANALYSIS	2-74
2.7.1 Parts Listing	2-74
2.7.2 Weights	2-75
2.7.3 Manufacturing Processes	2-75



## TABLE OF CONTENTS, Contd

<u>Section</u>		<u>Page</u>
2.7.4	Standard Hours	2-78
2.7.5	Realization	2-81
2.7.6	Labor and Overhead Rates	2-82
2.7.7	Material	2-83
2.7.8	Program Cost Summary	2-86
2.7.9	K-Tables	2-89
2.8	INPUT, OUTPUT, AND MATERIAL PROPERTIES	2-91
3	OPTIMIZATION STUDIES	3-1
4	SENSITIVITY STUDIES	4-1
5	PROGRAM DEMONSTRATION AND DOCUMENTATION	5-1
6	RECOMMENDATIONS AND PROGRAM REFINEMENTS	6-1
6.1	COMPUTER PROGRAM IMPROVEMENTS	6-1
6.1.1	Mathematical and Numerical Methods	6-1
6.1.2	Additional TPS Designs	6-11
6.2	PROGRAM APPLICATIONS AND OPTIMIZATION TECHNIQUES	6-20
6.2.1	Short-Term Improvements	6-20
6.2.2	Formal Optimization Procedures	6-20
6.3	OPTIMIZATION AND SENSITIVITY STUDIES	6-21

## LIST OF FIGURES

<u>Figure</u>		<u>Page</u>
2-1	Enthalpy Vs. Temperature for Air	2-3
2-2	Wedge Pressure Ratio Vs. $M_\infty \sin \alpha$	2-4
2-3	Wedge Enthalpy Ratio Vs. $M_\infty \sin \alpha$	2-5
2-4	Wedge Velocity Parameter Vs. $M_T \sin \alpha$	2-6
2-5	Cone Pressure Ratio Vs. $M_\infty \sin \alpha$	2-7
2-6	Cone Enthalpy Ratio Vs. $M_\infty \sin \alpha$	2-8
2-7	Cone Velocity Parameter Vs. $M_T \sin \alpha$	2-9
2-8	Limit Turning Angle	2-13
2-9	Speed of Sound Parameter for Air as a Function of Temperature	2-18
2-10	Correlation Between $Re_{tr}$ and Ratio $Re_E/Re_{tr}$	2-19
2-11	Effect of Mach Number on the Transition Zone Reynolds Number	2-19
2-12	Variation of Recovery Temperature Around Circumference of Cylinder at Station 2	2-21
2-13	Geometry of Flat Face Velocity Gradient Correction	2-22
2-14	Viscosity Ratio Vs. Enthalpy	2-23
2-15	Density-Viscosity Product Vs. Enthalpy	2-24
2-16	Surface/Structure Segmentation	2-25
2-17	Structure Heat Transfer Matrix	2-27
2-18	Panel Geometries	2-28
2-19	Configurations for Thermodynamic and Stress Analysis	2-29
2-20	Panel Loads Analysis	2-32
2-21	Geometry of Configuration No. 1	2-33
2-22	Larson-Miller Plot of Creep Data	2-45
2-23	Relationship Between Q and Effective Bandwidth ( $f_n/Q$ )	2-46
2-24	Acoustic Fatigue Failure Showing Crack Propagation Along Rivet Line	2-47
2-25	Mode Shapes of First Five Modes of an Integrally Stiffened Panel	2-47

## LIST OF FIGURES, Contd

<u>Figure</u>		<u>Page</u>
2-26	Acoustic Fatigue Estimation Procedure	2-48
2-27	Linear Damage Rule Diagram	2-49
2-28	Equivalent Fatigue Damage Diagram, Random Loading	2-50
2-29	Rectangular Honeycomb Panel Geometry	2-55
2-30	Integrally-Stiffened Panel Geometry	2-56
2-31	Corrugated Panel Geometry	2-57
2-32	Booster/Noise Source Relationship	2-61
2-33	Schematic of Jet Flow Field	2-62
2-34	Rayleigh Stress Distribution	2-70
2-35	Equivalent Fatigue Damage Diagram for Random Loading	2-72
2-36	Thermodynamic Resizing Procedure	2-74
2-37	Panel Concepts	2-74
2-38	Manufacturing Cost Summary	2-75
2-39	Drilling Time in Titanium	2-79
2-40	Example of a Shop Planning Order for a Brace	2-80
2-41	Typical Realization Factors and Standard Hours	2-82
2-42	Typical Factory Direct Labor Rates and Overhead Ratios	2-83
2-43	Program Cost Summary	2-88
2-44	Thermal Conductivity for Candidate Metals for Heat Shield Application	2-94
2-45	Specific Heat for Candidate Metals for Heat Shield Applications	2-94
2-46	Modulus of Elasticity for Candidate Metals for Heat Shield Applications	2-95
2-47	Coefficient of Thermal Expansion for Candidate Metals for Heat Shield Applications	2-95
2-48	Yield Strength for Candidate Metals for Heat Shield Applications	2-96
2-49	Ultimate Tensile Strength for Candidate Metals for Heat Shield Applications	2-96
2-50	Creep Data for 2219-T6 Aluminum	2-101

# LIST OF FIGURES, Contd

<u>Figure</u>		<u>Page</u>
2-51	Creep Data for (Annealed) Titanium, Ti-5Al-2.5 Sn	2-102
2-52	Creep Data for Titanium, Ti-8Al-1Mo-1V (Mill Annealed)	2-103
2-53	Creep Data for 718 Nickel, Aged	2-104
2-54	Creep Data for 718 Nickel, 20 Percent CW + Aged	2-105
2-55	Creep Data for René 41, ST + Aged	2-106
2-56	Creep Data for L-605 Cobalt, Annealed	2-107
2-57	Creep Data for Hastelloy X, Annealed	2-108
2-58	Creep Data for TD Nickel, As Rolled	2-109
2-59	Creep Data for B-66 Columbium, Recrystallized, Uncoated	2-110
2-60	Creep Data for B-66 Columbium, Chromizing Corp	2-111
2-61	Creep Data For TZM Molybdenum, Stream Relieved, Uncoated	2-112
2-62	Creep Data for TZM Molybdenum, Recrystallized, Uncoated	2-113
2-63	Creep Data for TZM Molybdenum, As Rolled, Uncoated	2-114
2-64	Creep Data for TZM Molybdenum, Si, Cr, B Coated (Pack Cementation Process)	2-115
2-65	Creep Data for TZM Molybdenum, Disilicide Coated	2-116
2-66	Creep Data for T-111 Tantalum, Recrystallized, Uncoated	2-117
2-67	S-N Curves for Smooth René 41 Alloy Two Heat Treatments at Room Temperature, 1200°F, 1400°F, and 1600°F with Zero Steady Loads ( $A = \infty$ )	2-118
2-68	S-N Curves for Smooth René 41 Alloy, Two Heat Treatments at Room Temperature, 1200°F, 1400°F, and 1600°F, with Steady Loads ( $A = 0.67$ )	2-119
2-69	S-N Curves for Smooth René 41 Alloy, One Heat Treatment, at 1400°F and 1600°F with Steady Loads ( $A = 0.25$ )	2-120
2-70	S-N Curves for Smooth and Notched Specimens of Titanium Alloy, RC 55 Type	2-120
2-71	S-N Plot of Fatigue Tests of Titanium Alloys Ti-150A and RC-130B	2-121
2-72	S-N Curves for Titanium Alloy RC-130B	2-122
2-73	S-N Diagram for Ti-75 Titanium Alloy Tested at Different Speeds With and Without Coolant	2-122

# LIST OF FIGURES, Contd

<u>Figure</u>		<u>Page</u>
2-74	S-N Curves for 6Al-4 Titanium Alloy Bar, Heat Treatment to 160 ksi Minimum UTS	2-123
3-1	Booster Panel Location	3-5
3-2	Body TPS Shell Structure	3-6
3-3	Skin Corrugation Geometry	3-7
3-4	Panel Geometry	3-7
3-5	Mathematical Model	3-8
3-6	Thermodynamic Properties of René 41 Alloy	3-8
3-7	Mechanical Properties of René 41	3-9
3-8	Typical Trajectory for Aluminum TPS Study	3-9
3-9	Heating Multiplication Factor Distribution	3-10
3-10	TPS Panel Unit Weight	3-13
3-11	TPS Panel Unit Cost	3-14
3-12	TPS Theoretical First Unit Cost	3-14
3-13	TPS Unit Total Cost	3-15
3-14	Panel Size vs $\bar{t}$ for Corrugated Heat Shields with Hat Sections and Clip Support	3-15
4-1	Turbulent Flat Plate Heating Data	4-3
4-2	Weight Sensitivity to Heating Amplification	4-4
4-3	Cost Sensitivity to Heating Amplification	4-4
4-4	Peak Skin Temperature	4-5
4-5	Peak Tank Temperature	4-6
6-1	TPS Design Computer Program	6-2
6-2	Mach Number Correction Factor Versus Mach Number	6-4
6-3	Plot of $q/f(M)$ Versus Mach Number With Parametric Variation in Altitude	6-5
6-4	Aerodynamic Parameter $2/f(M)$ Versus $l/w$ With Variation in Structural Parameter $(t_B/l)^3$	6-6

## LIST OF FIGURES, Contd

<u>Figure</u>		<u>Page</u>
6-5	Equivalent Panel Segments for Computation of Stress in Higher Panel Modes	6-7
6-6	Example Output of a Program Cost Summary	6-9
6-7	RSI Concepts	6-11
6-8	Space Shuttle High-Crossrange Orbiter	6-12
6-9	Three-Dimensional Reinforced Carbon-Carbon Core Configurations	6-13
6-10	Carbon-Carbon Leading Edge Designs	6-14
6-11	Influence of Operating Temperature Variation Upon Panel Unit Weight	6-15
6-12	LH <sub>2</sub> Tank Wall Temperature Vs. Tank Wall Thickness	6-16
6-13	Coolant Weight Requirements Versus Wall Temperature	6-17
6-14	Laminar Coolant Effectiveness	6-18

## LIST OF TABLES

<u>Table</u>		<u>Page</u>
2-1	Notations for Two Coordinate Systems	2-30
2-2	Input Parameters for Sonic Fatigue Analysis	2-52
2-3	Bandwidth Frequencies	2-62
2-4	Summary of the Available Material Forms and the Corresponding Material Form Index	2-85
2-5	Quantity Buy Price Differentials for Typical Aluminum Extruded Items	2-86
2-6	Typical Manufacturing Usage Variance Factors for a Past Commercial Transport Aircraft Program	2-87
2-7	Summary of the Values Stored in the KCOSWT Table for Titanium	2-87
2-8	Summary of the Values Stored in The KSETUP Table for Titanium	2-90
2-9	Summary of the Values Stored in the KRUN Table for Titanium	2-91
2-10	Summary of the Values Stored in the KCC Table	2-92
2-11	Thermomechanical Properties	2-93
2-12	Candidate Heat Shield Materials	2-93
2-13	Larson-Miller Creep Rupture Data	2-97
2-14	Insulation Properties	2-99
3-1	Fatigue Analysis Input	3-11
3-2	Weight/Cost Dat Input	3-12
4-1	TPS Uncertainty Factors	4-2
5-1	Fortran V Programming Reminders	5-2
6-1	Candidate Heat Sink Materials	6-15

## SUMMARY

A study was performed to assimilate and develop computational techniques for the design optimization of thermal protection systems for the space shuttle vehicle. The resulting computer program was then used to perform initial optimization and sensitivity studies on a typical thermal protection system TPS to demonstrate its application to the space shuttle TPS design. The program was developed in Fortran IV for Convair Aerospace's CDC 6400, but it was subsequently converted to the Fortran V language to be used on the MSC Univac 1108. Documentation for the study is reported in two volumes - the Final Report and the User's Manual. The latter contains input instructions and a sample problem to illustrate use of the program.

The major effort of the investigation consisted of the development of the computational techniques and programming of the subsequent methodology. The program itself was effected in modular fashion to allow continuing improvement and update of the performance prediction techniques. The program logic involves subroutines which handle the following basic functions: (1) a driver which calls for input, output, and communication between program and user and between the subroutines themselves, (2) a thermodynamic analysis which includes prediction of both the aerodynamic heating rates and the resulting heat transfer and temperature response of the TPS, (3) a thermal stress analysis which predicts the internal stresses and creep rates of the TPS by a discrete element analysis which structurally models the TPS subject to both external forces due to aerodynamic pressure and thermal stresses caused by heating, (4) an acoustic fatigue analysis which predicts both the noise excitation due to a number of external sources and the fatigue life of the panel, and (5) a weights/cost analysis which determines the weight and manufacturing cost of the system by identifying and evaluating these parameters for each of the TPS's components parts. In addition, a system total cost is predicted based on system weight and historical cost data of similar systems. Each of the major components of the program described above is complemented by other subroutines which provide specialized calculations for the analyses.

Two basic types of input are provided, both of which are based on trajectory data. In the first, vehicle attitude (altitude, velocity, and angles of attack and sideslip) is input and external heat and pressure loads are calculated. In the second, heating rates and pressure loads are provided to the program as a function of time. Standard program output includes heating rates, temperature, and stresses for the discrete elements of the TPS analyzed as well as dynamic stresses and the number of stress reversals for the panel and its weight and cost. A panel redesign technique is included to increase the panel thickness to transfer mechanical loads and to increase insulation thickness to protect the underlying load-bearing structure. In a subsequent investigation these redesign iterations are being refined.



Optimization and sensitivity studies are performed by the user by varying panel size, material properties, and configuration (six different metallic panel cross-section geometries are provided) in a series of computer runs. The program sizes panel and insulation thicknesses. An optimum design is then identified as the one giving either minimum weight or cost as a function of the parameters being varied for the investigation. Sensitivity studies are performed by noting the change in system weight or cost due to the variation in some independent variable such as trajectory or heating prediction method for an optimum panel configuration.

As the final task of this study, recommendations are made for computer program improvements which include new thermal protection systems (both active and passive) and improved computational and iterative techniques.

## SECTION 1

### INTRODUCTION

The objective of this contract was to develop a computer program for use in optimizing the thermal-structural design of the thermal protection system (TPS) for manned spacecraft in terms of cost, weight, rescue, and performance, both thermal and structural. The study was divided into five subtasks including documentation.

#### 1.1 TASK 1 — DEVELOPMENT OF THE COMPUTATIONAL PROCEDURE

This task was based on an existing capability for performing state-of-the art prediction of the aerothermodynamic environment and the simultaneous structural and temperature response of a simply-supported metallic TPS panel. The input parameters to the program included either (1) a given trajectory for various body locations, or (2) specific pressure and heating conditions.

The computer program is composed of a number of subroutines that are called in turn by the driver program. These subroutines perform the following functions:

- a. Input/output communication with the program user.
- b. Prediction of the aerothermodynamic environment with free stream conditions based on the 1963 Patrick Reference Atmosphere.
- c. Determination of the TPS structural temperature response including resizing of the insulation to satisfy system temperature constraints.
- d. Performance of a thermal stress analysis of the TPS panel cross section and panel resizing to preclude panel failure due to ultimate tension and compression, yielding, crippling, and elastic stability.
- e. Determination of TPS weight and cost per unit area, the latter including manufacturing, engineering, inspection, and refurbishment costs.

The thermal analysis is performed first. For the initial configuration, an explicit finite difference statement of the energy equation predicts heat transfer and temperature response of the panel, the insulation, and the underlying structure. If the temperature constraint of a part of the TPS is exceeded, insulation is resized to satisfy the constraint. Next, a section of the panel is isolated and analyzed as a simply-supported beam by a discrete element thermal-stress prediction procedure for the steady loads which include thermal stresses and aerodynamic pressure; the system is resized should structural failure occur. A sonic fatigue analysis is performed for the panel which has been thus far sized for thermodynamic and aerodynamic loads. The panel is assumed to resonate at its fundamental frequency due to any combination of noise sources such as:

a turbulent boundary layer, the booster engine, and the jet (flyback) engines. The analysis of the jet engines can also include the effect of the jet engine exhaust scrubbing the panel of interest. The resulting applied dynamic stresses are then compared to the allowable stresses of the S-N data using Convair Aerospace's cumulative fatigue damage theory, and the number of stress reversals endured by the structure at the applied level is printed out. This can be related by the program user to the fatigue life of the panel by evaluating the data point in terms of the allowable S-N curve.

The resulting TPS design is next analyzed to determine system weight and cost per unit area. The weights procedure adds up weights of component parts of the TPS such as the cover panel, insulation, substructure, and fasteners. The cost routine, in its current state of development, estimates TPS unit costs by two methods: (1) system manufacturing costs are predicted by identifying manufacturing costs for each of the component parts of the TPS, and (2) theoretical first unit costs and both recurring and non-recurring operational costs are identified as functions of material weight and complexity. Results printed out in the computer program include heating rates, structural temperature, stresses, and material property values, combined dynamic stresses and stress reversals, and weight and costs per unit area of the TPS and its component parts. Program discussion is presented in Section 2.

## 1.2 TASK 2 — DESIGN OPTIMIZATION STUDIES

The computer program developed in Task 1 was used to perform a design study for a typical metallic TPS configuration to demonstrate the validity of the procedure in terms of cost, weight, reuse, performance, and mission requirements. The panel demonstrated was located on the bottom centerline of the booster. The configuration chosen was an open semi-smooth corrugation (a corrugation wavelength of six inches and a depth of 0.5 inch) of Rene' 41. The temperature constraint on the system was a 300°F temperature limitation on the underlying cryogenic tank. The results of the analysis along with descriptions of the thermodynamic and thermal stress models and other pertinent input data and results are shown in Section 3.

## 1.3 TASK 3 — SENSITIVITY STUDIES

Results of the optimization studies of Task 2 were analyzed to demonstrate application and validity of the TPS sizing methodology. The same semi-smooth Rene' 41 panel with open corrugations was investigated to show the effects of heating uncertainties. The nominal case considered the application of conservative heating amplification factors to account for the heating reduction and increase respectively for a separated and reattached boundary layer. Two off-nominal cases were considered next: (1) no heating amplification, i.e., flat plate heating for an attached boundary layer, and (2) amplification upon the nominal case of 25 percent for turbulent heating and 10 percent for laminar heating. A more detailed description of this study and computed results and sensitivities are presented in Section 4.

#### 1.4 TASK 4 — PROGRAM DEMONSTRATION AND DOCUMENTATION

The computer code was developed in Fortran IV for the CDC 6400 at Convair Aerospace in San Diego. Section 5 of this report discusses a few elementary differences noted between the Fortran IV and V programs which run on the GDC and MSC machines. The conversion and demonstration at MSC offered no difficulties. The program documentation is shown in detail in the companion volume, the User's Manual.

#### 1.5 TASK 5 — RECOMMENDATIONS AND PROGRAM REFINEMENTS

The following paragraphs summarize recommendations for an extension to the work of the present contract. Details are presented on Section 6. The objective of a continued program is (1) to refine development of a computer program for use in optimizing the thermal-structural design of the thermal protection system of the space shuttle vehicle, and (2) to employ both the computer program developed under Contract NAS 9-10956 and an improved version to generate parametric weight and cost data for optimum TPS for a variety of materials, panel and support configurations, vehicle locations, and vehicle trajectories. This investigation is divided into four tasks, the first two of which update the computer program to include new TPS concepts and to improve computational speed, the third is the design of optimum TPS at local areas on the shuttle vehicle, and the fourth is documentation.

1.5.1 COMPUTER PROGRAM IMPROVEMENTS. The primary function of the task is to employ refined numerical and mathematical models to decrease computer run time and make application of the computer program for design optimization easier for the program user. The mathematical and numerical methods improvements include refinements in varying degrees of difficulty to all of the major subroutines of the analysis: thermodynamic, stress, fatigue, weight, and cost. In addition, current TPS concepts on the space shuttle will be included in the sizing program. These include reusable surface insulation, carbon-carbon systems, mass transfer cooling, and ablators.

Improved thermodynamic analysis involves incorporation of newly developed aerodynamic heating prediction at high angles of attack including real gas effects, cross-flow, and boundary layer transition. Internally, the adoption of any one of a number of implicit heat transfer equations presently available at Convair Aerospace is recommended after a short evaluation study has been conducted of a few typical configurations and problems. The major changes and additions proposed for the TPS stress analysis include reorganization and refinement of existing analyses of the metallic panels and their support, computation of stress redistributions due to creep and panel deflections, and development of additional models for reusable surface insulation, carbon-carbon systems, mass transfer cooling, and ablators. Fatigue analysis refinements will include an assessment of the effects of damping of the panel due to edge constraints and edge members, supporting structure, and the insulation. Also a low frequency analysis (panel flutter and stability) will be adopted to include the effects of this structural requirement on TPS redesign.

Weights and cost analyses will increase the depth of their considerations to include variations in manufacturing and development techniques and newly developed data on refurbishment costs. Mathematical models will be developed to predict weight and cost of the new TPS's in sufficient depth to allow valid comparisons of these important parameters. Finally, an intensive effort will be made in a search of the literature to obtain better material property data; this will include the effects of material degradation with time. Also, whatever new data (either S-N fatigue data, or weight/cost data) are developed and published will be included in a form for quick and ready access to the computer input.

**1.5.2 PROGRAM APPLICATIONS AND OPTIMIZATION TECHNIQUES.** This task will be divided into two subtasks: short term improvements and formal optimization procedures. In the former, techniques will be evaluated and employed (if practicable) to automate the computational procedures. These might include the stacking of successive cases, the curve fitting of resulting weights and costs, and minimization of the resulting curves to determine the optimum configuration. In the latter task, MSC's previous experience in the application of optimization procedures to the thermal sizing of TPS will be assessed to determine if there is a rational but economically feasible approach to combine the TPS sizing program with a formal optimization procedure. Finally, additional TPS designs, possibly including active cooling systems for localized areas and probably leading edge concepts, will be incorporated into the size procedure.

**1.5.3 OPTIMIZATION AND SENSITIVITY STUDIES.** Detailed optimization and sensitivity studies of configuration and materials already available to the program will be begun at program go-ahead. The parametric studies will consider typical vehicle areas, materials, and trajectories and will in fact be an organized concerted effort to size the shuttle TPS locally. Particular attention will be paid to one vehicle area and TPS concept to gather information on the time and costs of running a detailed sizing study with the techniques developed under this contract. The remaining study time can then be scheduled to develop valid parametric data in a cost effective manner.

**1.5.4 PROGRAM DEMONSTRATION AND DOCUMENTATION.** The TPS Optimization Computer Program will be developed at Convair Aerospace in Fortran IV for the CDC 6400. The resulting program will then be checked out on the Univac 1108 in Fortran V.

Early in the program development, programming instructions will be established to ensure a minimum number of changes both in computer languages and systems. The documentation of the User's Manual will include all mathematical descriptions, methods of solution, program listings, flow charts, list of symbols, diagnostic messages for typical failures, and sample problems. Documentation of the entire study will include, in addition, results of the optimization and sensitivity studies and all conclusions and recommendations.

## SECTION 2

### COMPUTER PROGRAM

This chapter describes the prediction methods and analyses adapted for use in the TPS sizing computer program. The complete listing and operating instructions for the program are presented in a companion volume entitled User's Manual.

#### 2.1 PROGRAM ORGANIZATION

The thermal protection system sizing program consists of a number of modules or subroutines each of which is designed to perform a specific function of design and/or communication with other subroutines as well as the main or driver program. The major modules perform the tasks of program input, program output, thermodynamic, stress, sonic fatigue analyses, thermodynamic and structural redesign, and weight and cost evaluations. A number of smaller subroutines have been developed to perform specific auxiliary tasks for each of the major analyses. For example, these smaller problems include nodal specification of the stress analysis model, determination of applied and allowable dynamic stresses for the acoustic fatigue analysis, and storage of various data blocks in the weight/cost subroutine to name just a few.

The following sections describe each of the major analyses alluded to above with the discussion of input and output (including an extensive description of a number of thermostructural properties required for program operation) presented in Section 2.8.

#### 2.2 AEROTHERMODYNAMIC ENVIRONMENT

The prediction of aerothermodynamic environment is based on Convair Aerodynamic/Structural Heating Program 3020 (References 1 and 2). The local environment is established by the prediction of the flow field about simple geometric shapes such as flat plates, wedges, cones, cylinders, or spheres.

Prediction of aeroheating is classified into two regimes: high and low local angle of attack. For low angle-of-attack applications, the shock waves are assumed attached to the body, and flow field properties are computed from tangent wedge/cone techniques. Using these local properties, the algorithm then computes local heating rates using either the Eckert reference enthalpy method or the Spalding-Chi technique. Transitional heating between the laminar and turbulent boundary layers will then be calculated as a linear interpolation of turbulent and laminar heating values, the degree of turbulence depending on the "turbulent fraction" exhibited by the boundary layer with respect to values of Reynolds number for transition onset and end.

At high angles of attack, the flow field cannot be predicted so conveniently as at low angles of attack. Thus, current state-of-the-art techniques recommend aeroheating

rate calculation by swept cylinder methods, either laminar or turbulent. At the moment, no transition criterion has been established for the switch from laminar to turbulent swept cylinder heating prediction techniques.

Detailed descriptions of the aeroheating and (where applicable) pressure prediction equations are given in the following:

2.2.1.1 FLOW FIELD CALCULATIONS. The effective angle of attack,  $\tau$  is defined as

$$\sin \tau = \text{DNX} \cos \alpha \cos \beta + \text{DNY} \sin \beta + \text{DNZ} \cos \beta \sin \alpha \quad (2-1)$$

where

$\alpha$  = angle of attack

$\beta$  = yaw angle

$\text{DNX}$ ,  $\text{DNY}$ ,  $\text{DNZ}$  = direction cosines of outer normal from surface, and the high angle of attack is defined arbitrarily for  $\tau > 35^\circ$ .

2.2.1.1.1 Low Angle of Attack. The thermodynamic properties of the air ahead of the shock,  $P_\infty$ ,  $T_\infty$ , and  $\rho_\infty$  and the free stream Mach number  $M_\infty$ , are determined from the given flight conditions using the 1963 Patrick AFB atmosphere. Once  $T_\infty$  and the surface temperature  $T_w$  are known, the free stream and wall enthalpies can be determined using Figure 2-1. A set of empirical equations (Reference 3), shown in Figures 2-2 through 2-7, is used in determining the shock layer thermodynamic properties at the boundary layer edge as functions of the hypersonic similarity parameters  $M_\infty \sin \alpha$  and  $M_\infty \alpha$  (Reference 4). For the flat plate configuration,  $\alpha = 0$  degrees, it is assumed that the free stream conditions exist at the boundary layer edge.

2.2.1.1.2 High Angle of Attack. At high angle of attack the pressure is calculated by a method developed by Convair Aerodynamics Group (Reference 5). Other properties are not available for the present program.

The method which was developed is a modified flat plate approach in that the pressure at a point depends only on Mach number and on the local slope of that point. However, the local slope depends not only on the geometry of the point, angle of attack, and yaw but also is corrected for a boundary layer displacement term which accounts for wall temperature, Mach number, unit Reynolds number, and distance from a leading edge.

Thus the pressure model contains three main parts:

- a. Boundary layer displacement correction.
- b. Windward pressure model.
- c. Leeward pressure model.

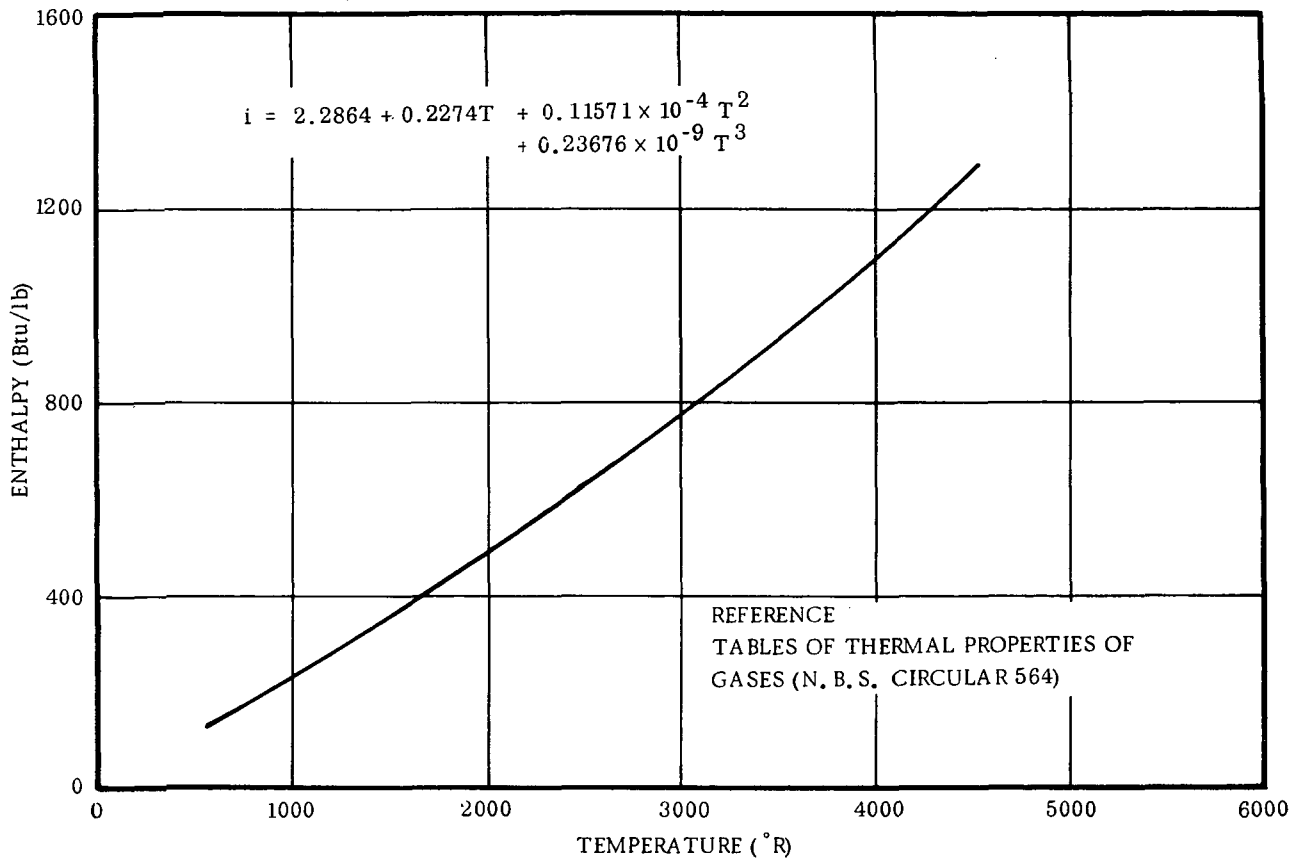


Figure 2-1. Enthalpy Vs. Temperature for Air

Boundary Layer Displacement Correction. Failure to derive correlations of pressure using combinations of impact pressure laws, viscous induced pressure laws, and blast induced pressure laws led to the belief that the pressure data could be correlated by a common pressure law in which the effect of the viscous terms is accounted for in a revised local slope. Thus:

$$C_P = K(M, \tau')$$

where

$$C_P = \text{pressure coefficient}$$

$$M = \text{Mach number}$$

$$K(M, \tau') = \text{unknown pressure law}$$



**EQUATIONS:**

$$M_{\infty} \sin \alpha \leq 1.8 : P_s/P_{\infty} = 1.041 + 0.693 M_{\infty} \sin \alpha + 1.889 (M_{\infty} \sin \alpha)^2 - 0.0661 (M_{\infty} \sin \alpha)^3$$

$$M_{\infty} \sin \alpha > 1.8 : P_s/P_{\infty} = -2.320 + 4.045 M_{\infty} \sin \alpha + 1.036 (M_{\infty} \sin \alpha)^2 + 0.0161 (M_{\infty} \sin \alpha)^3$$

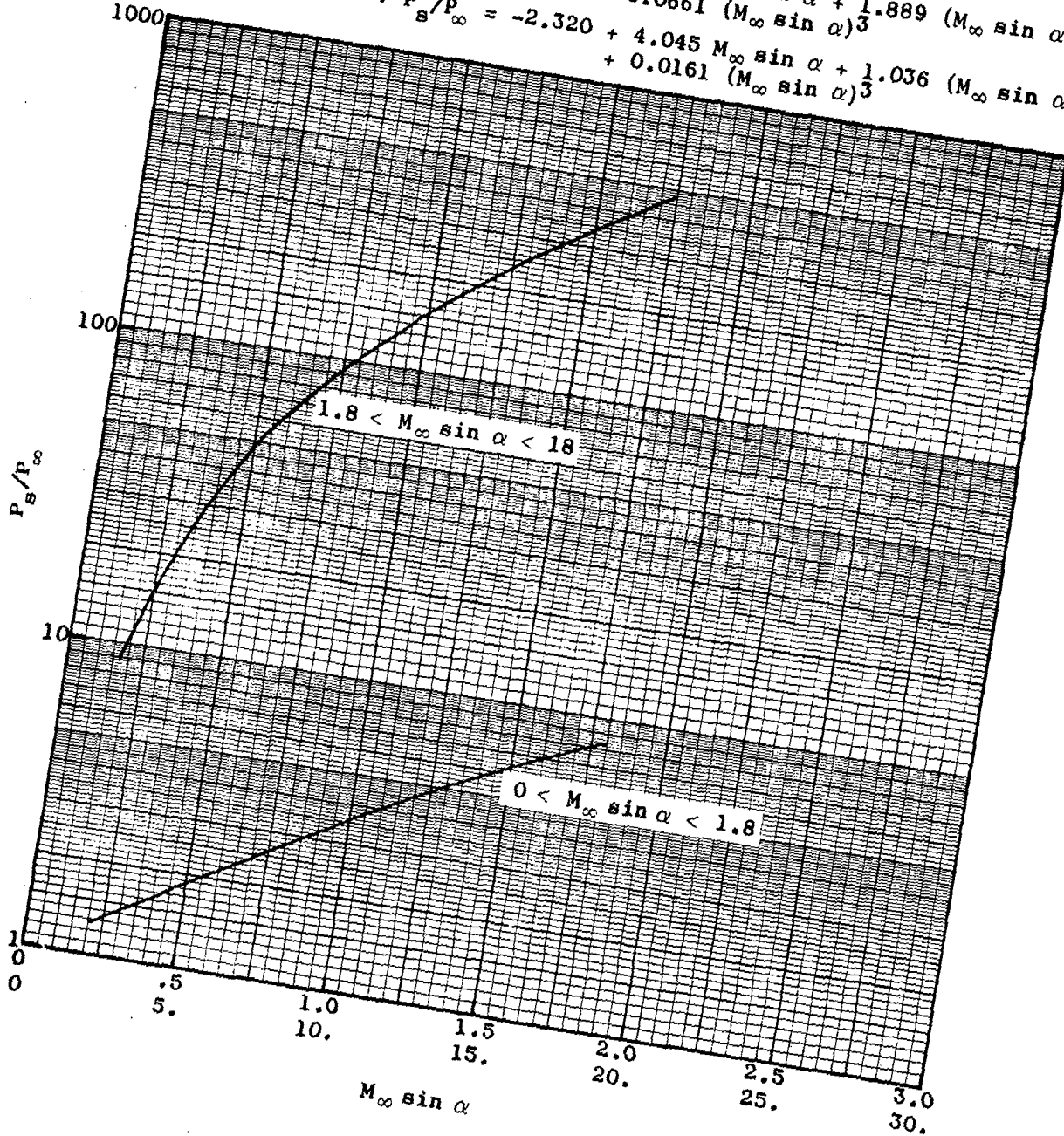


Figure 2-2. Wedge Pressure Ratio Vs.  $M_{\infty} \sin \alpha$

EQUATIONS:

$$M_{\infty} \sin \alpha \leq 8.0 : i_s/i_{\infty} = 0.9167 + 0.3203 M_{\infty} \sin \alpha + 0.236 (M_{\infty} \sin \alpha)^2 - 0.4484 \times (10)^{-3} (M_{\infty} \sin \alpha)^3$$

$$M_{\infty} \sin \alpha > 8.0 : i_s/i_{\infty} = 1.107 - 0.2209 M_{\infty} \sin \alpha + 0.3644 (M_{\infty} \sin \alpha)^2 - 0.008462 (M_{\infty} \sin \alpha)^3$$

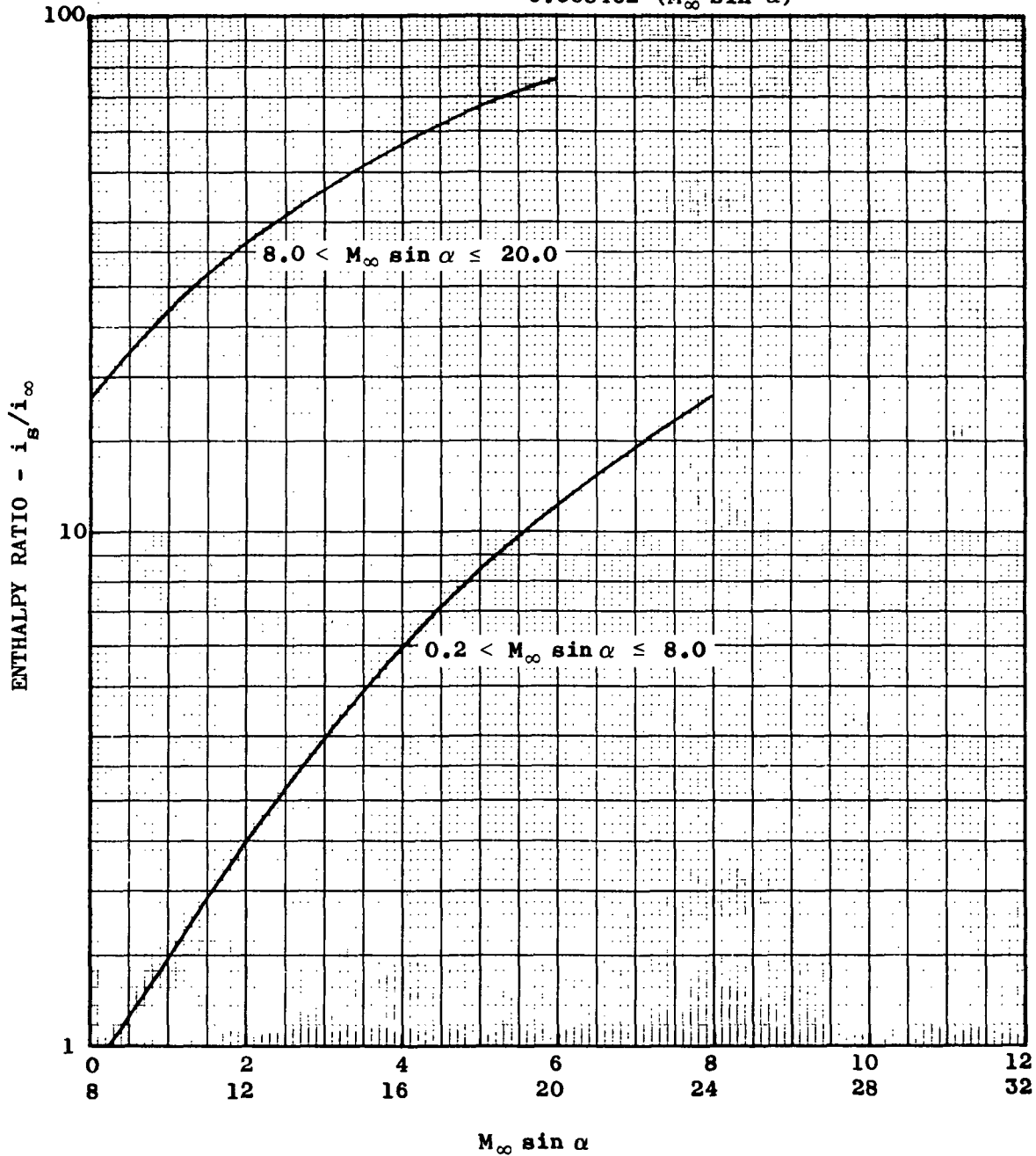


Figure 2-3. Wedge Enthalpy Ratio Vs.  $M_{\infty} \sin \alpha$

$$M_r = M_\infty \times 10^{-3}$$

EQUATIONS:

$$0 \leq M_r \sin \alpha < 0.6 : (V_\infty^2 - V_s^2) \times 10^{-6} = 0.1923 + 1.404 M_r \sin \alpha + 1.147 (M_r \sin \alpha)^2 + 0.3361 (M_r \sin \alpha)^3$$

$$0.6 \leq M_r \sin \alpha < 6 : (V_\infty^2 - V_s^2) \times 10^{-6} = 0.5958 + 0.4494 M_r \sin \alpha + 1.838 (M_r \sin \alpha)^2 - 0.0331 (M_r \sin \alpha)^3$$

$$6 \leq M_r \sin \alpha : (V_\infty^2 - V_s^2) \times 10^{-6} = 78.03 - 19.58 M_r \sin \alpha + 3.13 (M_r \sin \alpha)^2 - 0.05054 (M_r \sin \alpha)^3$$

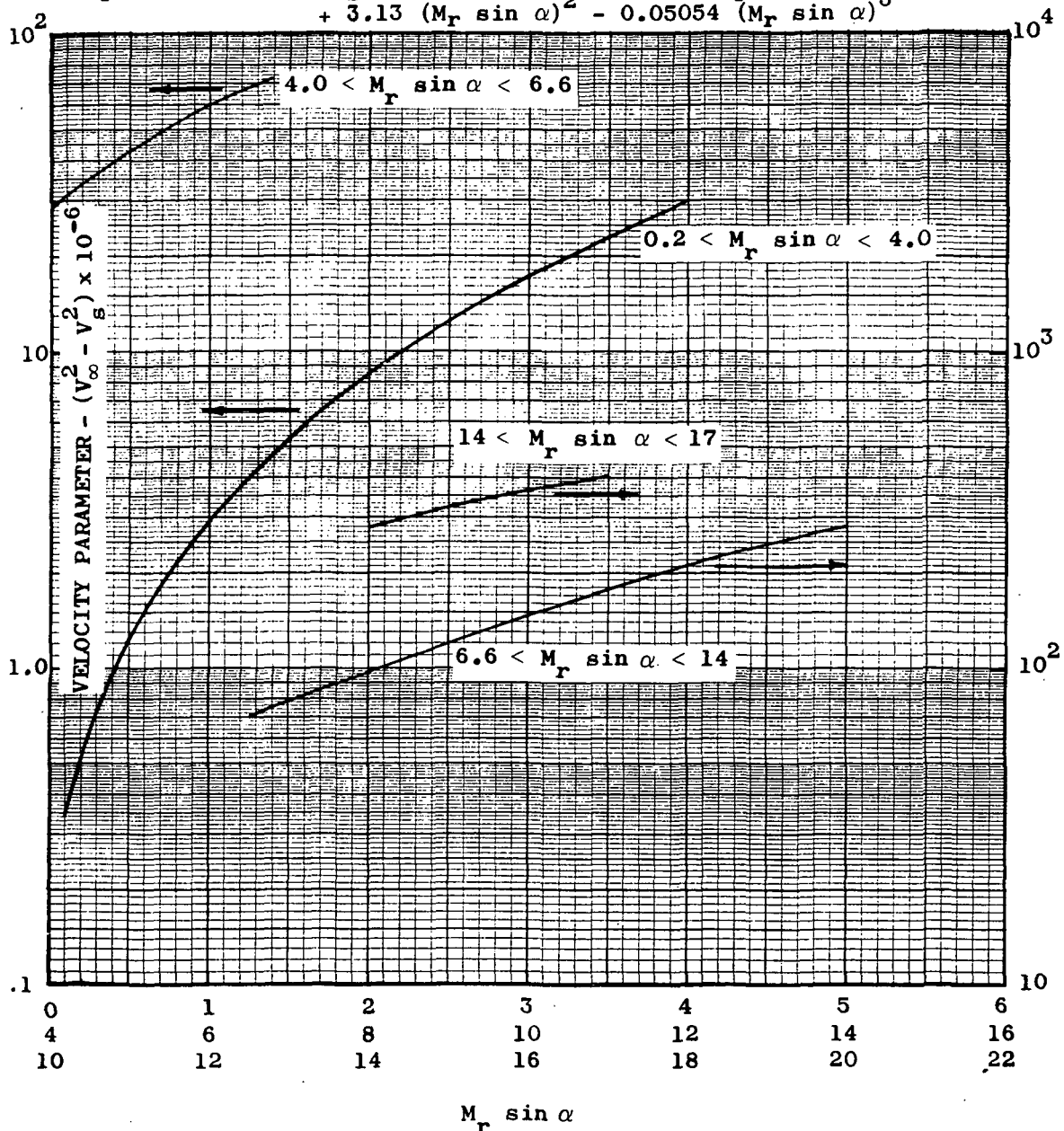


Figure 2-4. Wedge Velocity Parameter Vs.  $M_r \sin \alpha$

**EQUATIONS:**

$$M_{\infty} \sin \alpha < 1.5 : P_s/P_{\infty} = 1.007 + 0.3816 M_{\infty} \sin \alpha + 1.522 (M_{\infty} \sin \alpha)^2 - 0.1593 (M_{\infty} \sin \alpha)^3$$

$$1.5 \leq M_{\infty} \sin \alpha < 5.0 : P_s/P_{\infty} = 0.2397 + 1.161 M_{\infty} \sin \alpha + 1.06 (M_{\infty} \sin \alpha)^2 + 0.0489 (M_{\infty} \sin \alpha)^3$$

$$5.0 \leq M_{\infty} \sin \alpha : P_s/P_{\infty} = -3.182 + 4.177 M_{\infty} \sin \alpha + 0.8373 (M_{\infty} \sin \alpha)^2 + 0.0216 (M_{\infty} \sin \alpha)^3$$

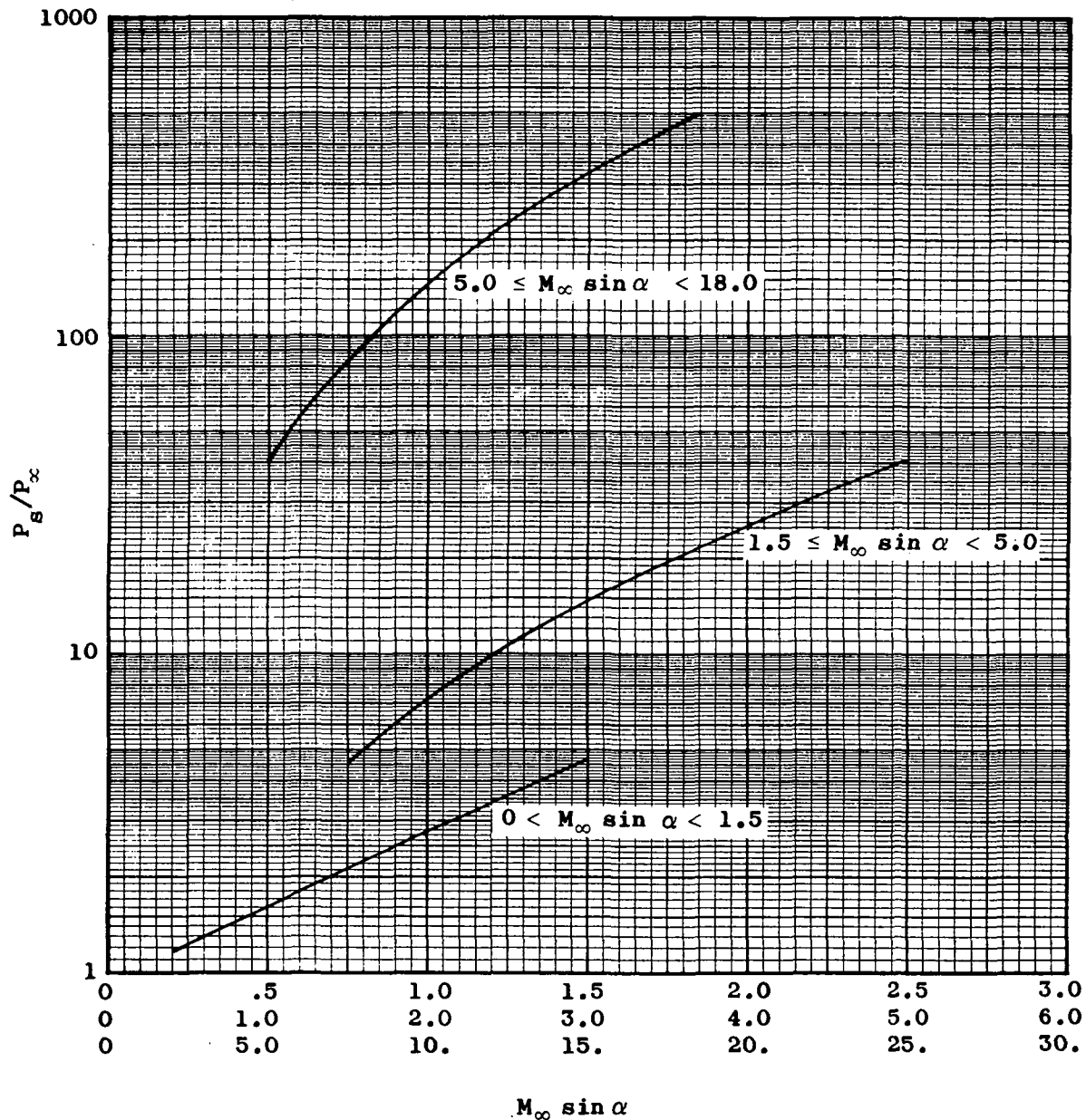


Figure 2-5. Cone Pressure Ratio Vs.  $M_{\infty} \sin \alpha$

EQUATIONS:

$$M_{\infty} \sin \alpha \leq 8.0 : i_s/i_{\infty} = 1.03 + 0.0827 M_{\infty} \sin \alpha + 0.2354 (M_{\infty} \sin \alpha)^2 - 0.6956 \times 10^{-3} (M_{\infty} \sin \alpha)^3$$

$$M_{\infty} \sin \alpha > 8.0 : i_s/i_{\infty} = 1.106 - 0.3685 M_{\infty} \sin \alpha + 0.3466 (M_{\infty} \sin \alpha)^2 - 0.007766 (M_{\infty} \sin \alpha)^3$$

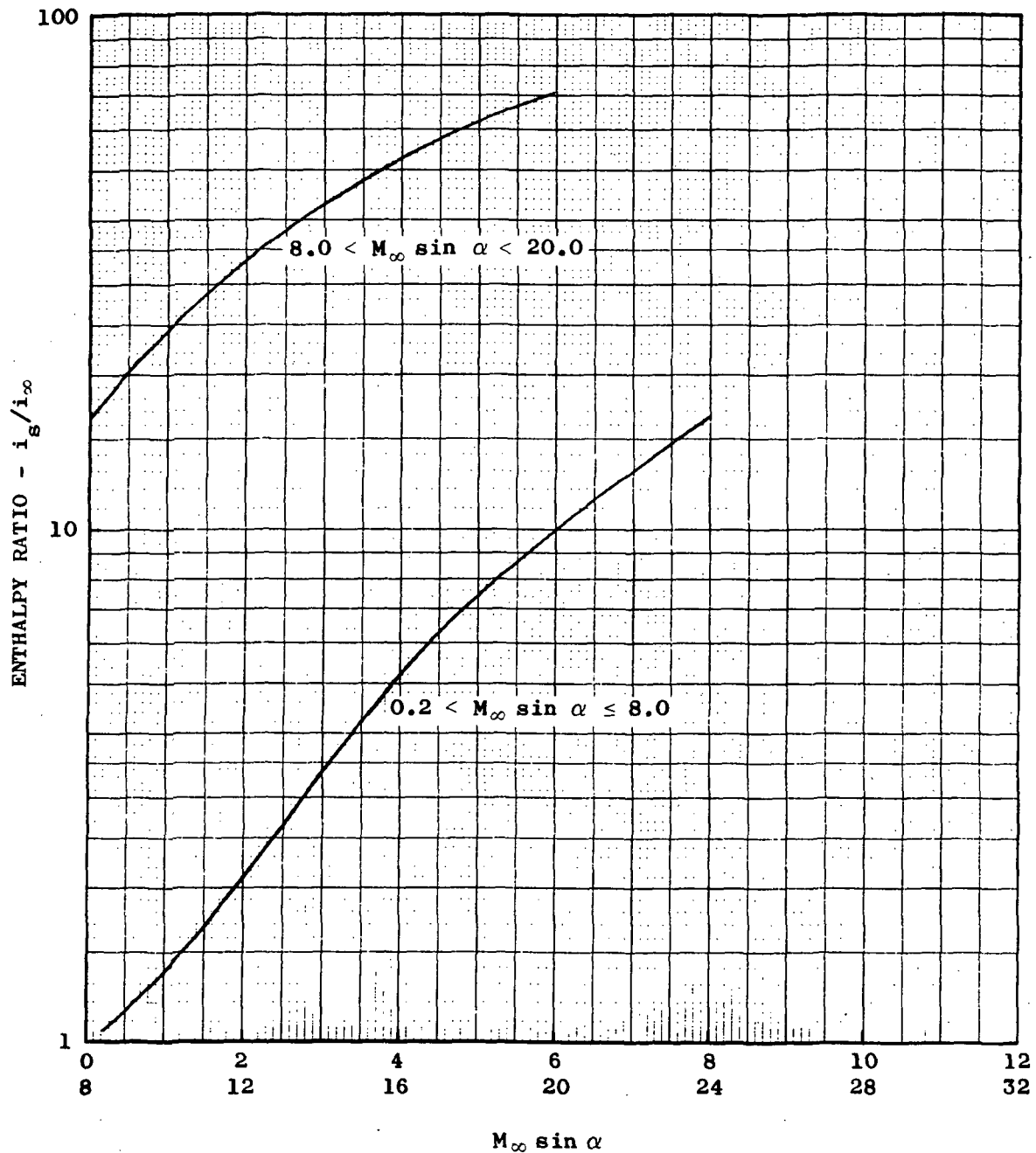


Figure 2-6. Cone Enthalpy Ratio Vs.  $M_{\infty} \sin \alpha$

$$M_r = M_\infty \times 10^{-3}$$

**EQUATIONS:**

$$0 < M_r \sin \alpha < 4.4 : (V_\infty^2 - V_s^2) \times 10^{-6} = 0.157 + 0.75 M_r \sin \alpha + 0.9861 (M_r \sin \alpha)^2 + 0.06944 (M_r \sin \alpha)^3$$

$$4.4 \leq M_r \sin \alpha : (V_\infty^2 - V_s^2) \times 10^{-6} = 6.187 - 1.038 M_r \sin \alpha + 1.414 (M_r \sin \alpha)^2 - 0.0062 (M_r \sin \alpha)^3$$

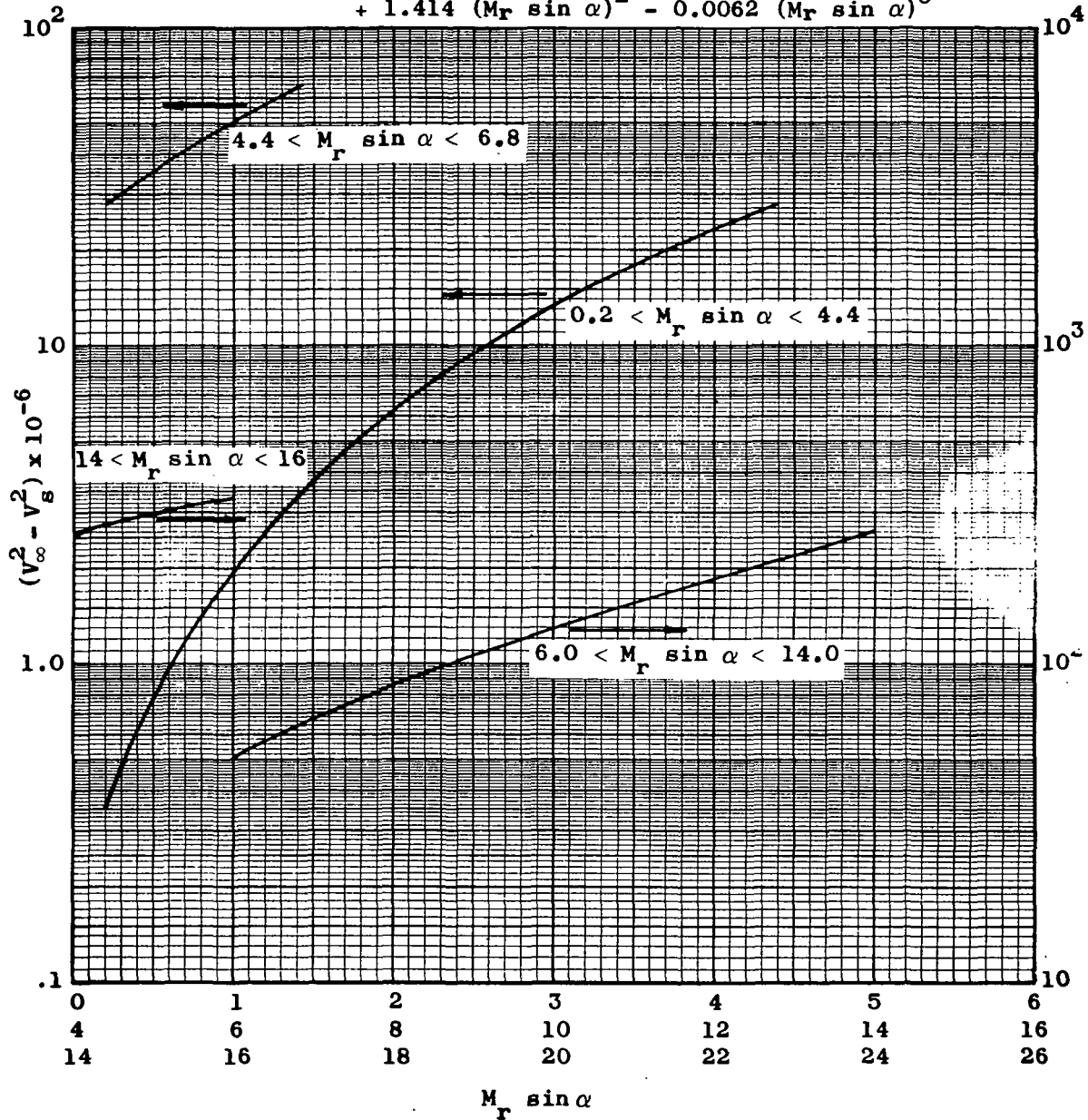


Figure 2-7. Cone Velocity Parameter Vs.  $M_r \sin \alpha$

and

$$\tau' = \tau + \Delta\tau \text{ (approximately)} \quad (2-2)$$

$\Delta\tau$  = viscous effect correction

Equation 2-2 is an approximation because the boundary layer correction should be applied to the direction cosines of the outer normal at the point in question and the correct expression for corrected local slope is

$$CST = \cos (\Delta\tau) \quad (2-3)$$

$$SST = \sin (\Delta\tau) \frac{DNY}{\sqrt{(DNZ^2 + DNY^2)}} \quad (2-4)$$

$$BST = \sin (\Delta\tau) \frac{DNY}{\sqrt{(DNZ^2 + DNY^2)}} \quad (2-5)$$

$$\left. \begin{aligned} DNX' &= DNX \cdot CST + DNZ \cdot SST \\ DNZ' &= DNZ \cdot CST - DNX \cdot SST \\ DNY' &= DNY \cdot CST - DNZ \cdot BST \end{aligned} \right\} \quad (2-6)$$

$$\sin \tau' = \cos \alpha \cos \beta DNX' + \sin \beta DNY' + \cos \beta \sin \alpha DNZ' \quad (2-7)$$

where Equations 2-3 to 2-5 are used to give the proper magnitude and sign to the Y and Z components of the boundary layer corrections.

The correction was derived from the Chapman-Rubesin laminar displacement thickness expression for a flat plate in the following way:

$$\delta^* \sqrt{\frac{Re_I}{CX}} = 1.721 \frac{T}{T_\infty} + 0.322 (\gamma - 1) M_\infty^2 \quad (2-8)$$

and

$$\Delta\tau = \tan^{-1} \left( \frac{d\delta^*}{dx} \right) \quad (2-9)$$

$$\Delta\tau = \tan^{-1} \left[ \frac{1}{2} \sqrt{\frac{C}{Re_I}} \left( 1.721 \frac{T}{T_\infty} + 0.0332 (\gamma - 1) M_\infty^2 \right) X^{-1/2} \right]$$

where

$Re_I$  = unit Reynolds number

$C$  = Chapman-Rubesin constant

$T_w$  = wall temperature

$T_\infty$  = ambient temperature

$M_\infty$  = free stream Mach number

$X$  = distance from leading edge

A turbulent correction has not been developed yet so that the laminar correction is used at all conditions at present.

An arbitrary limit is presently applied to prevent this term from generating very large corrections at the leading edges of the vehicle (where  $X$  goes to zero) so that the largest correction which can be made is 30 degrees. This correction also causes some points to have positive slopes where geometrically they have negative slopes and thus can result in positive pressure on the leeward side of vehicles which agrees with test data.

Windward Pressure Model. An equivalent body shape has been defined and the corrected local slope at the point in question is positive so that it is a windward point. A modified tangent wedge pressure formula was derived (Reference 5).

$$C_p = \sin^2(\tau') \left[ \left( \frac{\gamma+1}{2\gamma} \right)^2 \left( \frac{\beta}{M} \right)^2 + \left( \frac{\gamma+1}{2} \left( \frac{\beta}{M} \right)^2 + \frac{1}{K^2} \right)^{1/2} \right] \quad (2-10)$$

where

$K = M \sin \tau'$

$\beta^2 = M^2 - 1$

$\tau'$  = corrected local slope

$C_p$  = pressure coefficient

$\gamma$  = ratio of specific heats

$M$  = free stream Mach number



This pressure model predicts pressures very close to Van Dykes tangent wedge at small inclinations to the stream and closely follows modified Newtonian at large inclinations to the stream.

Leeward Pressure Model. The leeward pressure model is composed of three parts:

- a. Small disturbance theory law.
- b. Two dimensional base pressures.
- c. Limit turning angle.

The small disturbance theory pressure formula is used to predict pressures on surfaces from zero inclination to the stream to negative inclinations defined by a limit turning angle. The small disturbance theory law is

$$C_P = \sin^2 \tau' \left\{ \frac{2}{\gamma K^2} \left[ \left( 1 - \frac{\gamma-1}{2} |K| \right)^{\frac{2\gamma}{\gamma-1}} - 1 \right] \right\} \quad (2-11)$$

$$K = \beta \sin \tau'$$

The limit turning angle is defined from Love's limit turning angle of Reference 6 and is shown in Figure 2-8. Two-dimensional base pressures are used on surfaces which have larger negative inclinations than the limit turning angle and the pressure is computed using the following empirical fit:

$$C_P = (-0.3008/(M-0.5434)) + 0.01132M - 0.05252 \quad (2-12)$$

for Mach numbers less than 6 and

$$C_P = \frac{-1}{0.7 M^2} \quad (2-13)$$

for Mach numbers greater than 6.

**2.2.2 FLAT PLATE, WEDGE, AND CONE AERODYNAMIC HEATING.** At low angle of attack, the flow field properties are computed by tangent wedge/cone techniques as described in Section 2.2.1; aerodynamic heating rates are computed in two combinations:

- a. Eckert laminar with Eckert turbulent.
- b. Eckert laminar with Spalding-Chi turbulent.

Eckert reference enthalpy method (Reference 7) depends upon the assumption that the incompressible mass, momentum, and energy equations can be used for compressible

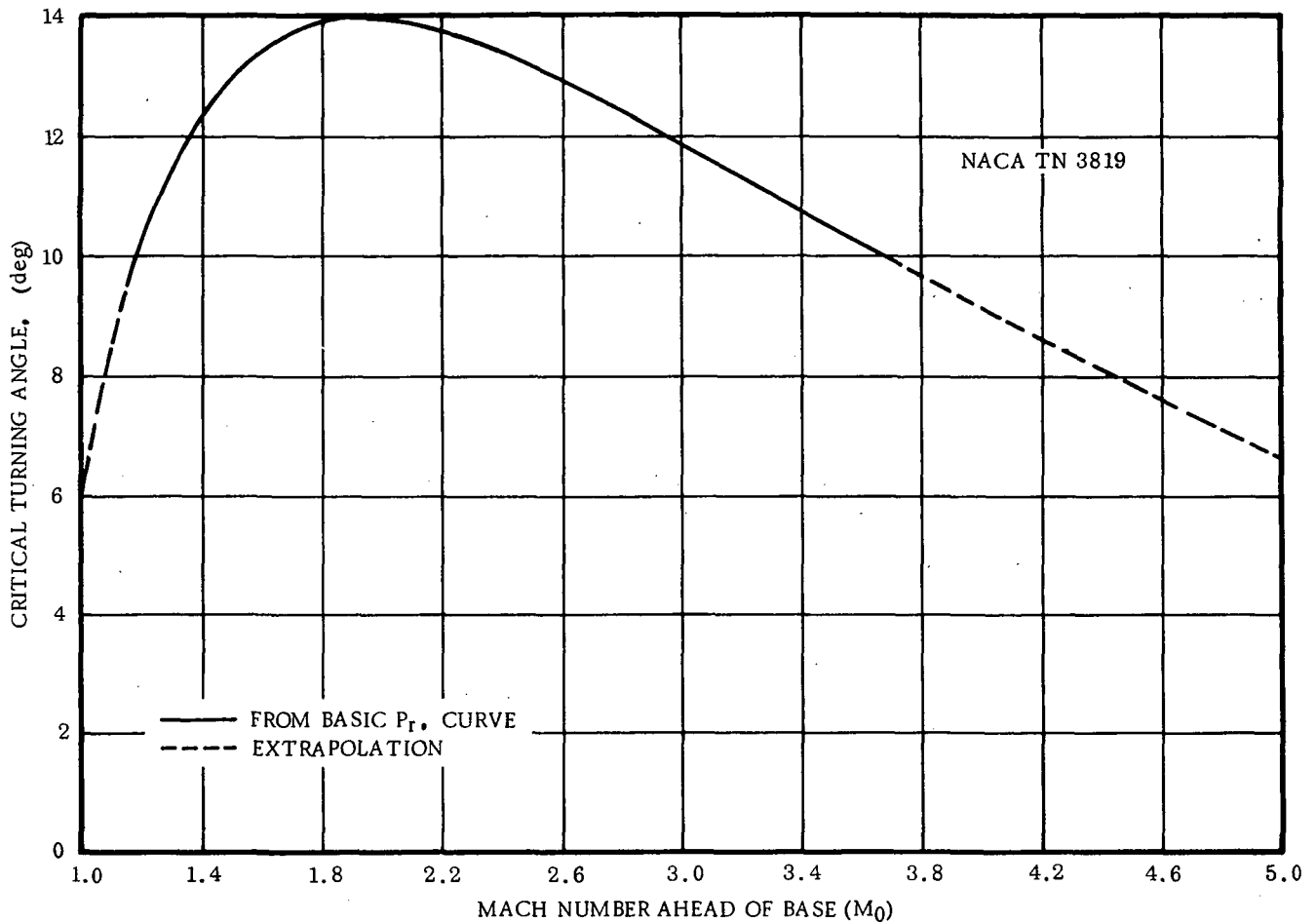


Figure 2-8. Limit Turning Angle

flow solutions provided the thermodynamic and transport properties of the gas are known and are evaluated at an appropriate reference enthalpy. Real gas effects, including dissociation, are taken into account in the determination of the properties of the gas just outside the boundary layer. The Eckert reference enthalpy is

$$i^* = i_s + 0.5 (i_w - i_s) + 0.22 (i_r - i_s) \quad (2-14)$$

where  $i_s$  is the shock layer (just outside the boundary layer) static enthalpy,  $i_w$  is the enthalpy of air at the wall temperature, and  $i_r$  is the boundary layer recovery enthalpy, given by

$$i_r = i_s + r \frac{V_s^2}{2g_c J} \quad (2-15)$$

where the flow recovery factor,  $r$ , is 0.84 for laminar flow and 0.89 for turbulent flow.

2.2.2.1 Laminar Boundary Layer. The Blasius solution for an incompressible laminar boundary layer gives a skin friction coefficient

$$C_f = \frac{0.664}{\sqrt{Re^*}} \quad (2-16)$$

Substitution into the Reynolds analog relation

$$Pr^{*2/3} St = \frac{C_f}{2} \quad (2-17)$$

yields the solution for Stanton number

$$St = \frac{0.332}{\sqrt{Re^*} Pr^{*2/3}} \quad (2-18)$$

where the Stanton number is defined by

$$St = \frac{h_i}{\rho^* V_s g_c} \quad (2-19)$$

and the Prandtl and Reynolds numbers are

$$Pr^* = \frac{\mu^* C_p^*}{k^*} \quad (2-20)$$

$$Re^* = \frac{\rho^* V_s X}{\mu^*} \quad (2-21)$$

A constant value of 0.71 is assumed for  $Pr^*$ , based on the data of Hansen (Reference 8), as a convenient approximation. The heat transfer coefficient is defined by

$$h_i = \frac{q_i}{(i_r - i_w)} \quad (2-22)$$

Using the relationships given above, the heat transfer coefficient can be expressed as

$$h_i = \frac{13.43 \sqrt{\rho^* \mu^* V_s}}{\sqrt{X}} \quad (2-23)$$

The heat transfer coefficient,  $h_i$ , is multiplied by the factor 1.73 for conical flow (Reference 9).

### 2.2.2.2 Turbulent Boundary Layer

Eckert's Reference Enthalpy Method. The Schultz-Grunow solution for the local skin friction coefficient is (Reference 10).

$$C_f = \frac{7.485 \rho^* V_s}{(\log_{10} Re^*)^{2.584}} \quad (2-25)$$

For conical flow (Reference 11), the heat transfer coefficient is multiplied by the factor 1.176.

Spalding-Chi Heating and Drag Technique. The original intent of the Spalding-Chi method was to develop a procedure whereby skin friction for the compressible flow over a flat plate could be computed rapidly by hand (Reference 12). The theoretical development is based upon the postulate that, for incompressible flow, skin friction can be expressed functionally in terms of Reynolds number based on momentum thickness as  $\tilde{c}_f = \Psi_\theta (Re_\theta)$  where the tilde denotes incompressible quantities. The relationship between incompressible and compressible quantities is such that

$$\tilde{c}_f = c_f F_c \text{ and } \tilde{Re}_\theta = F_{r\theta} Re_\theta$$

where the transformation variables  $F_c$  and  $F_{r\theta}$  are functions of temperature ratio (free stream to wall) and Mach number. (The values of these parameters approach unity for incompressible flow, i.e.,  $T_w/T_e = 1$ ,  $Me = 0$ ). Another expression can be derived theoretically to yield  $1/2 c_f F_c = \Psi_x (F_{tx} Re_x)$  with a new coefficient  $F_{rx}$ . The transformation coefficients were evaluated from equations suggested by previously successful correlation techniques. Hence, the expression

$$F_c = \left[ \int_0^1 \left( \frac{\rho}{\rho_e} \right)^{1/2} d \left( \frac{u}{U_e} \right) \right]^{-2} \quad (2-26)$$

is evaluated across the isobaric boundary layer using the Crocco relation and the perfect gas law. Similarly, it was postulated that

$$F_{r\theta} = \left( \frac{T_w}{T_e} \right)^p \left( \frac{T_{aw}}{T_w} \right)^q \quad (2-27)$$

and the exponents were evaluated for a wide variety of experimental data to be  $p = -0.702$  and  $q = 0.722$ . The parameters  $F_c$ ,  $F_{r\theta}$ , and  $F_{rx}$  were tabulated as functions of Mach number and temperature ratio. The computational technique is comprised of evaluating the transformation parameters for certain flight conditions and then, with the proper Reynolds number, computing the compressible skin friction coefficient. Application of a suitable Reynolds analogy factor leads to calculation of the film heating coefficient.

Wallace (Reference 13) suggested that the technique could be improved for high free stream enthalpy by employing enthalpy instead of temperature ratios to evaluate  $F_{r\theta}$ . With a view toward computer application, Komar (Reference 14) avoided the lengthy double interpolations necessary to determine  $F_c$ ,  $F_{rx}$ , and  $F_{r\theta}$  by curve fitting the product  $c_f F_c$  as a function of the products  $F_{rx} Re_x$  and  $F_{r\theta} Re_\theta$ . The incompressible skin friction coefficient  $c_f F_c$  is computed as

$$c_f F_c = \exp \left( \sum_{j=1}^n g_j A^{j-1} \right) \quad (2-28)$$

where

$$A = \log_e (F_{rx} Re_x) \quad (2-29)$$

The equations necessary to compute the parameter  $F_c$  are outlined below (Reference 14). Thus

$$F_c = \left\{ \frac{1}{\sqrt{-c}} \left( \sin^{-1} \left[ \frac{-(2c+b)}{\sqrt{b^2 - 4ac}} \right] - \sin^{-1} \left[ \frac{-b}{\sqrt{b^2 - 4ac}} \right] \right) \right\}^{-2} \quad (2-30)$$

where

$$\left. \begin{aligned} a &= \frac{i_w}{i_e} \\ b &= 1 + \frac{r}{2} (\gamma - 1) M_e^2 - \frac{i_w}{i_e} \\ c &= -\frac{r}{2} (\gamma - 1) M_e^2 \end{aligned} \right\} \quad (2-31)$$

Then

$$F_{r\theta} = \left( \frac{i_w}{i_e} \right)^{-0.702} \left( \frac{i_{aw}}{i_w} \right)^{0.72} \quad (2-32)$$

and

$$F_{rx} = F_{r\theta} / F_c \quad (2-33)$$

$$A = \log_e (F_{rx} Re_x) \quad (2-34)$$

$$c_f F_c = \exp \left( \sum_{j=1}^n g_j A^{j-1} \right) \quad (2-35)$$

The coefficients  $g_j$  are those developed by Komar for the curve fits.

$$\begin{aligned} g_1 &= 9.2809 & g_2 &= -4.7340 & g_3 &= 6.6859 \times 10^{-1} \\ g_4 &= -4.1877 \times 10^{-2} & g_5 &= -5.5055 \times 10^{-4} & g_6 &= 2.8367 \times 10^{-4} \\ g_7 &= -2.1250 \times 10^{-5} & g_8 &= 8.0162 \times 10^{-7} & g_9 &= -1.5901 \times 10^{-8} \\ g_{10} &= 1.3236 \times 10^{-10} \end{aligned}$$

Successive calculation of the parameters of Equations 2-31, 2-30, 2-32, 2-33, 2-29, and 2-28 gives  $c_f$ . Reynolds analogy leads to the heating coefficient. A recommended equation for the Reynolds analogy factor is that of Karman as proposed by Bertram (Reference 15).

$$S = 1 + 5 \sqrt{\frac{F_c c_f}{2}} \left( \text{Pr} - 1 + \log_e \frac{5 \text{Pr} + 1}{6} \right) \quad (2-36)$$

The only parameter still undertermined in this analysis is the shock layer Mach number. For a Prandtl-Meyer expansion; this computation was already made but not printed as output. For oblique shock waves, the local speed of sound is computed from an approximation (Figure 2-9) of the data of Hansen (Reference 8). The sound speed is computed from the relation

$$\left. \begin{aligned} \frac{a^2 \rho_e}{p_e} &= m T + b \\ \text{for } T < 2700^\circ\text{K}, \quad m &= -8.75 (10)^{-4} / ^\circ\text{K}, \quad b = 1.432 \\ \text{for } T > 2700^\circ\text{K}, \quad m &= 0, \quad b = 1.2 \end{aligned} \right\} \quad (2-37)$$

**2.2.2.3 Transitional Boundary Layer.** The transitional boundary layer is represented as a linear transition from laminar into turbulent flow. Transition is assumed to begin at a specified value of the shock layer Reynolds number, denoted  $Re_{tr}$ , and end at a specified value of the shock layer Reynolds number, denoted  $Re_F$ . The heating rate is computed as the linear interpolation between laminar and turbulent values, the virtual origin of both being the leading edge. Interpolation is performed using the

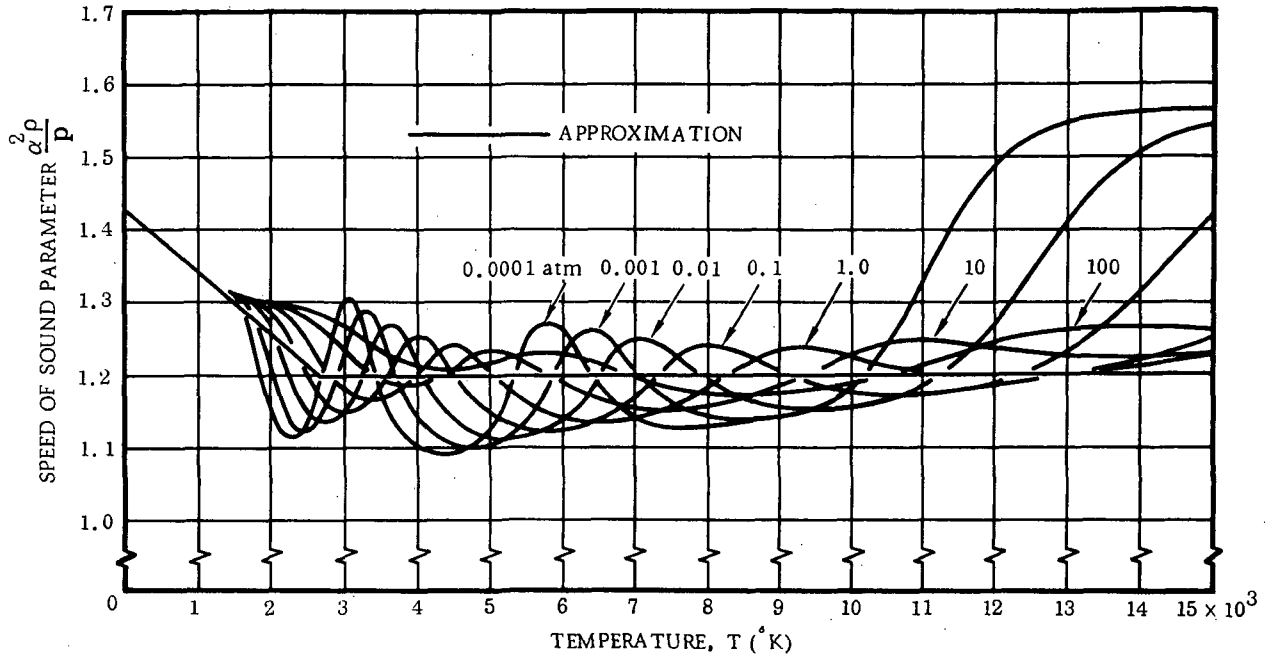


Figure 2-9. Speed of Sound Parameter for Air as a Function of Temperature

value of Reynolds number that occurs between the input values specifying the onset and end of transition. Hence, for example, the film heating coefficient is given by

$$h = \frac{Re - Re_{tr}}{Re_E - Re_{tr}} h_T + \left[ 1 - \frac{Re - Re_{tr}}{Re_E - Re_{tr}} \right] h_L \quad (2-38)$$

$$= f_T h_T + f_L h_L$$

The values usually used are  $Re_{tr} = 10^6$  and  $Re_E = 2 \times 10^6$  such that

$$f_{tr} = \frac{Re_E}{Re_{tr}} = 2 \quad (2-39)$$

These values are reasonable (Figures 2-10 and 2-11) according to Masaki and Yakura (Reference 16).

**2.2.3 SPHERE AND CYLINDER AERODYNAMIC HEATING.** At high angle of attack, swept cylinder theories are used to predict the aerodynamic heating. For laminar flow, heating is computed by method of Kemp and Riddell, while the method of Beckwith and Gallagher is used to compute the turbulent heating.

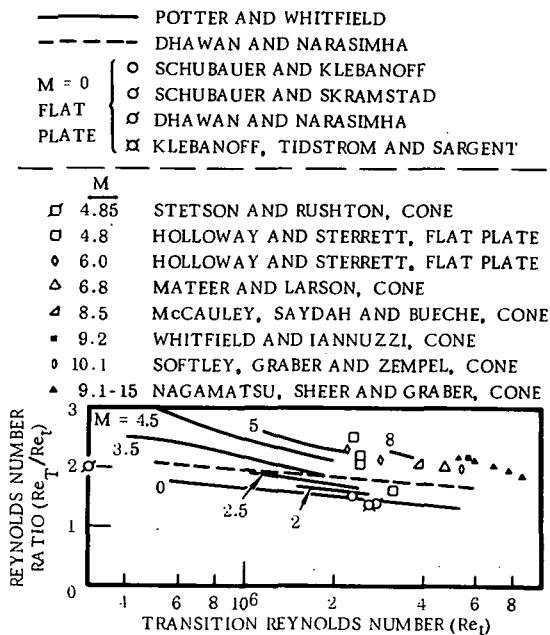


Figure 2-10. Correlation Between  $Re_{tr}$  and Ratio  $Re_E/Re_{tr}$

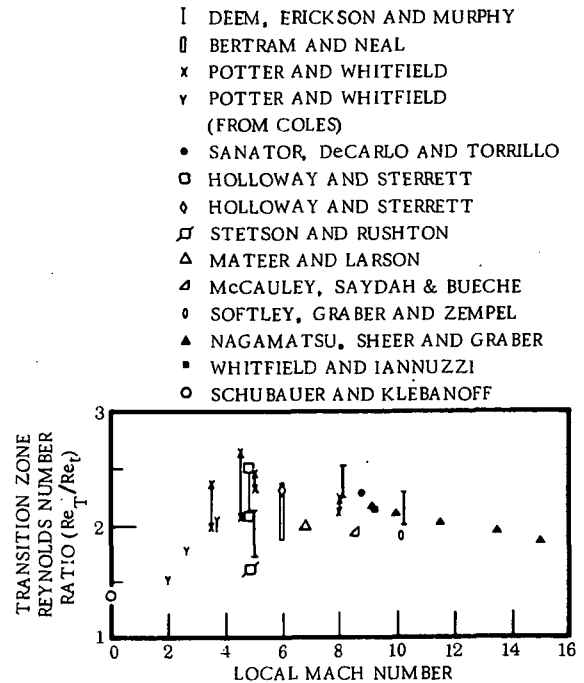


Figure 2-11. Effect of Mach Number on the Transition Zone Reynolds Number

2.2.3.1 Laminar Swept Cylinder. Laminar heat transfer to a swept cylinder is computed through a transformation of spherical heating rates. Heat transfer to a sphere is calculated by the Kemp-Riddell (Reference 17) expression

$$q_{sph} = \frac{2.49 (10)^4}{\sqrt{D}} \sqrt{\frac{\rho_\infty}{2.38 (10)^{-3}}} \left( \frac{V_\infty}{26,000} \right)^{3.15} \left[ \frac{i_s - i_w}{i_s - i_\infty} \right] \quad (2-40)$$

Cylindrical heating rates are then obtained by adjusting for sweep by

$$q_{cyl} = 0.75 q_{sph} (\cos \Lambda)^{1.2} \quad (2-41)$$

where the sweep angle

$$\Lambda = 90^\circ - \tau$$

2.2.3.2 Turbulent Swept Cylinder. Turbulent heat transfer to a cylinder is computed by the method of Beckwick and Gallagher (Reference 18). Equation for heat transfer to the stagnation line of a swept cylinder is



$$\frac{h_s D}{k_\infty} = \left[ \frac{U_{R, \infty} D}{\nu_\infty} \right]^{\frac{n}{n+1}} Pr^{1/3} \left[ a \frac{p_s}{p_\infty} \frac{\mu_r}{\mu_o} \frac{T_\infty}{T_r} \right]^{\frac{n}{1+n}} \cdot$$

$$(\sin \Lambda)^{\frac{n-1}{n+1}} \left[ \frac{49}{376} \frac{\mu_o}{\mu_\infty} \cos \Lambda \left( \frac{D}{u_\infty} \frac{du}{dx} \right)_s \right]^{\frac{1}{1+n}} \quad (2-43)$$

where  $a$  and  $n$  are constant in the Blasius skin friction law and were taken as  $a = 0.0228$  and  $n = 4$ .  $U_{R, \infty}$  is the free stream velocity vector and  $u_\infty$  is the component of  $U_{R, \infty}$  normal to the cylinder stagnation line; thus

$$u_\infty = U_{R, \infty} (\cos \Lambda) \quad (2-44)$$

Using this relationship and the definition of Stanton number gives

$$St = \frac{0.03231}{(Pr)^{2/3}} \left[ \frac{\mu_\infty}{D u_\infty \rho_\infty} \right]^{1/5} (\cos \Lambda)^{1/5} (\sin \Lambda)^{3/5} \left[ \frac{\mu_r}{\mu_o} \frac{T_\infty}{T_r} \frac{p_s}{p_\infty} \right]^{4/5} \cdot$$

$$\left[ \frac{\mu_o}{\mu_\infty} \right]^{1/5} \left[ \left( \frac{D}{u_\infty} \frac{du}{dx} \right)_s \right]^{1/5} \quad (2-45)$$

Sutherland's equation for the viscosity of air is used. Static pressure at the wall,  $p_s$ , is that which would be sensed by a pitot tube placed normal to the bow shock when  $u_\infty$  is supersonic. This pressure is

$$p_s = p_\infty \left\{ \left[ \frac{\gamma + 1}{2} M_{N, \infty}^2 \right]^{\frac{\gamma}{\gamma-1}} \left[ \frac{\gamma + 1}{2 \gamma M_{N, \infty}^2 - (\gamma - 1)} \right]^{\frac{\gamma}{\gamma-1}} \right\} \quad (2-46)$$

where

$$M_{N, \infty} = M_\infty \cos \Lambda.$$

The stagnation line velocity gradient can be expressed as

$$\left[ \frac{D}{u_\infty} \frac{du}{dx} \right]_s = \frac{2}{M_{N, \infty}} \left[ \frac{2}{\gamma} \frac{T_s}{T_\infty} \left( 1 - \frac{p_\infty}{p_s} \right) \right]^{1/2} \quad (2-47)$$

where

$$T_s = \frac{a_{N,0}^2}{\gamma R} \quad (2-48)$$

and  $a_{N,0}$  is the normal component of the free stream stagnation sonic velocity (Reference 18); therefore

$$T_s = T_\infty \left[ 1 + \frac{\gamma - 1}{2} M_{N,\infty}^2 \right] \quad (2-49)$$

Reference conditions  $T_r$  and  $\mu_r$  were evaluated at  $T_s$  in Equation 2-45.

The final expression for heat transfer to the stagnation line was given as

$$q_{cyl, T} = St \rho_\infty V_\infty g (i_r - i_w) \quad (2-50)$$

where values of recovery factor used in evaluating  $i_r$  were obtained by curve fit of the data in Beckwith and Gallagher (Figure 2-12).

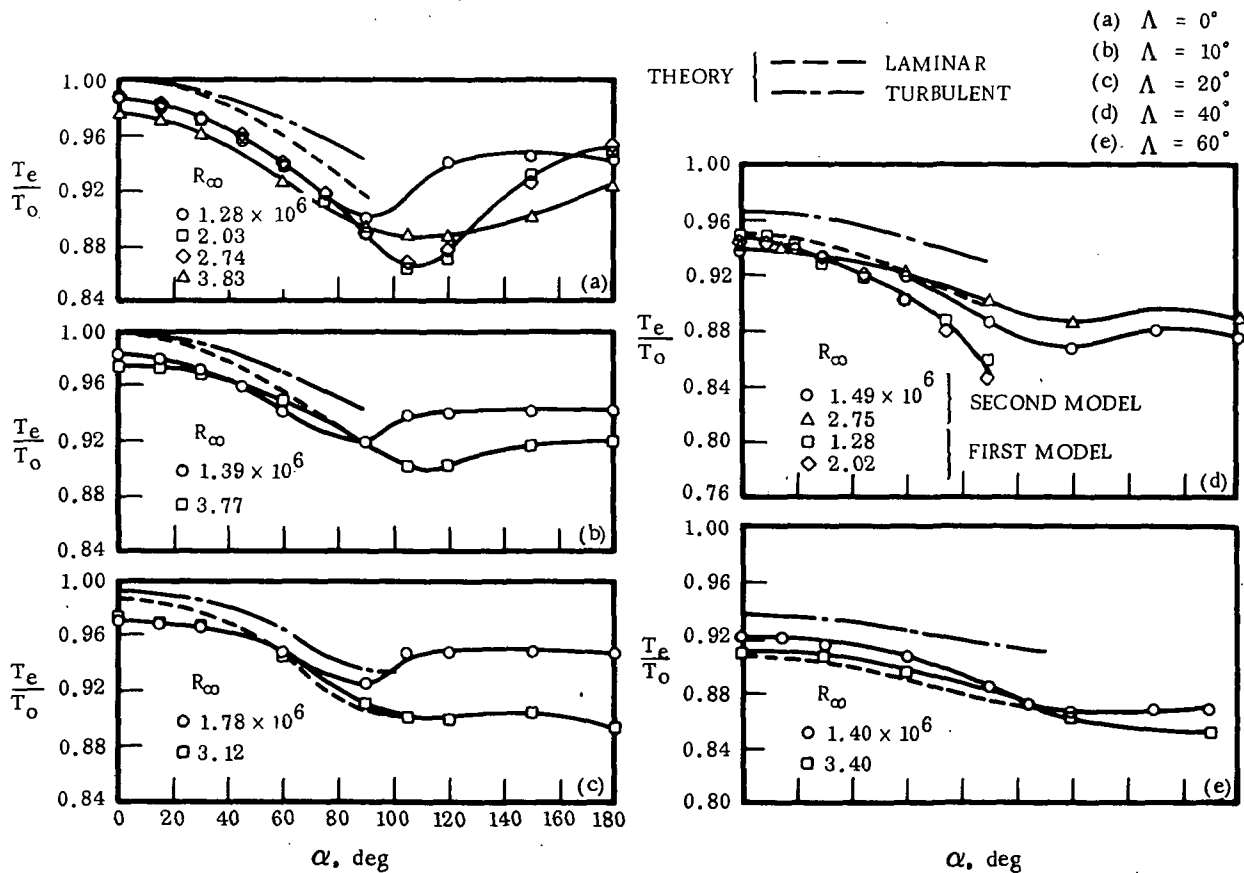
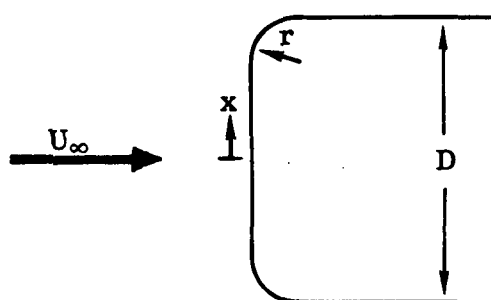


Figure 2-12. Variation of Recovery Temperature Around Circumference of Cylinder at Station 2

2.2.3.3 Correction for Flat Face Velocity Gradients. The methods of Bertram and Henderson (Reference 19) are used to correct the flat face velocity gradients. Since stagnation heating is proportional to the square root of free stream velocity gradient, it was postulated that

$$\frac{q_{\text{flat}}}{q_{\text{cyl}}} = \sqrt{\frac{\left(\frac{d U_e}{dx}\right)_{x=0} \bigg|_{\text{flat}}}{\left(\frac{d U_e}{dx}\right)_{x=0} \bigg|_{\text{cyl}}}} \quad (2-51)$$



For laminar boundary layer of a flat disc  
(Figure 2-13)

$$\left(\frac{d U_e}{dx}\right)_{x=0} = 0.745 + 3.14 \left(\frac{r}{D}\right) \quad (2-52)$$

the laminar centerline heating rates are with the form

Figure 2-13. Geometry of Flat Face  
Velocity Gradient  
Correction

$$q_{\text{flat}} = q_{\text{cyl}} \sqrt{\frac{0.745 + 3.14 \left(\frac{r}{D}\right)}{2.315}} \quad (2-53)$$

For turbulent boundary layer a 1/5 power correction was used.

$$q_{\text{flat}} = q_{\text{cyl}} \left[ \frac{0.745 + 3.14 (r/D)}{2.315} \right]^{1/5} \quad (2-54)$$

2.2.3.4 Transport Properties. The transport properties given by Hansen (Reference 8) are shown in Figures 2-14 and 2-15. From these, curve fit equations were obtained for  $\rho$  and  $\mu$  as functions of enthalpy and pressure:

$$i < 1300, \quad \rho = 0.576 \times 10^{-4} P_s i^{-0.849} \quad (2-53)$$

$$\mu = 0.42642 \times 10^{-7} i^{0.493} \quad (2-54)$$

$$i \geq 1300, \quad \rho = 0.865 \times 10^{-5} P_s i^{-0.584} \quad (2-55)$$

$$\mu = 0.28428 \times 10^{-6} i^{0.228} \quad (2-56)$$

where base values of  $\rho_b$  and  $\mu_b$  evaluated at  $T_b = 400R$  were used as reference values in the  $\mu/\mu_b$  and  $\rho/\rho_b$  ratios shown on the figures. The base value of density  $\rho_b$  is adjusted as a function of the local static pressure.

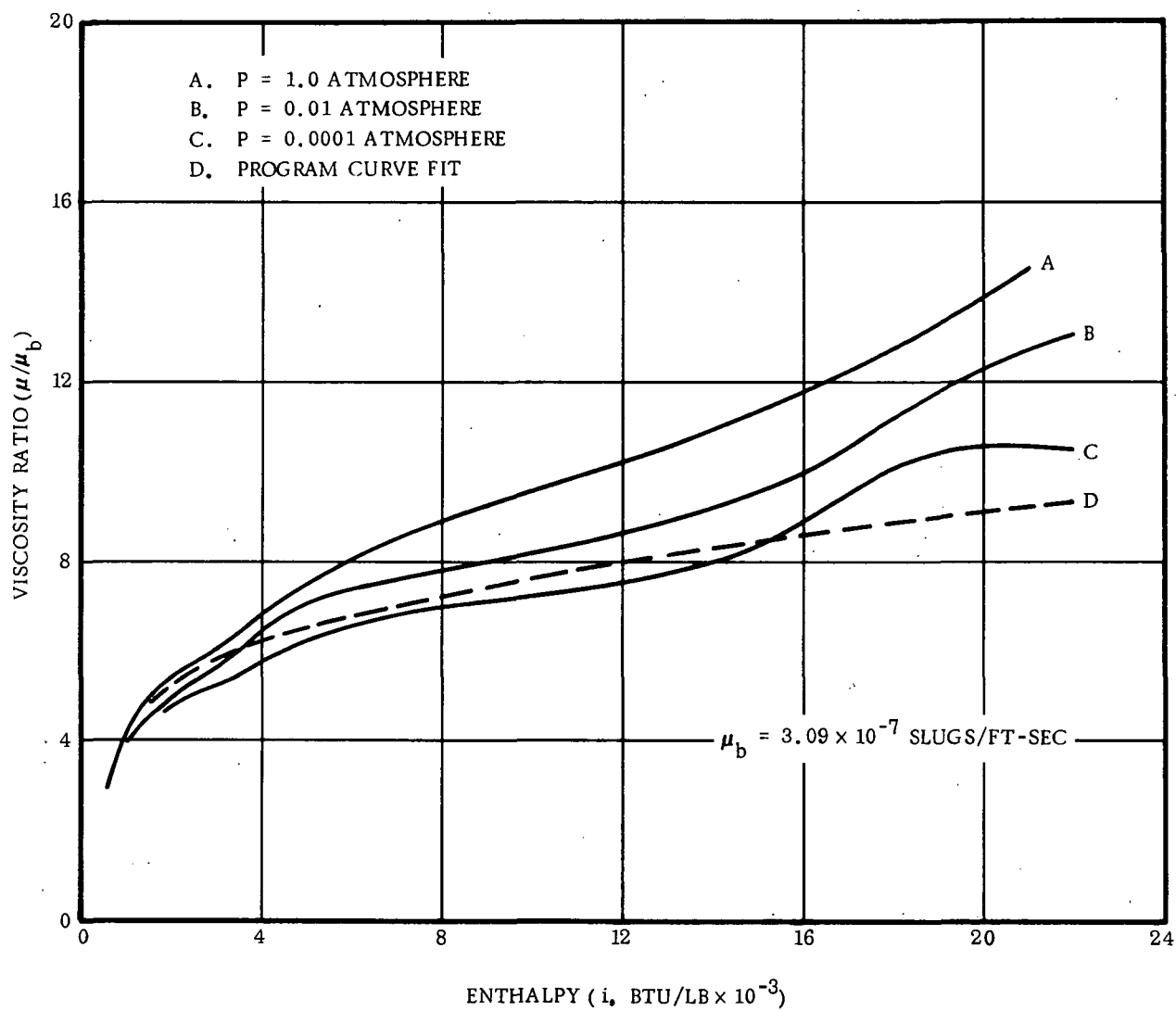


Figure 2-14. Viscosity Ratio Vs. Enthalpy

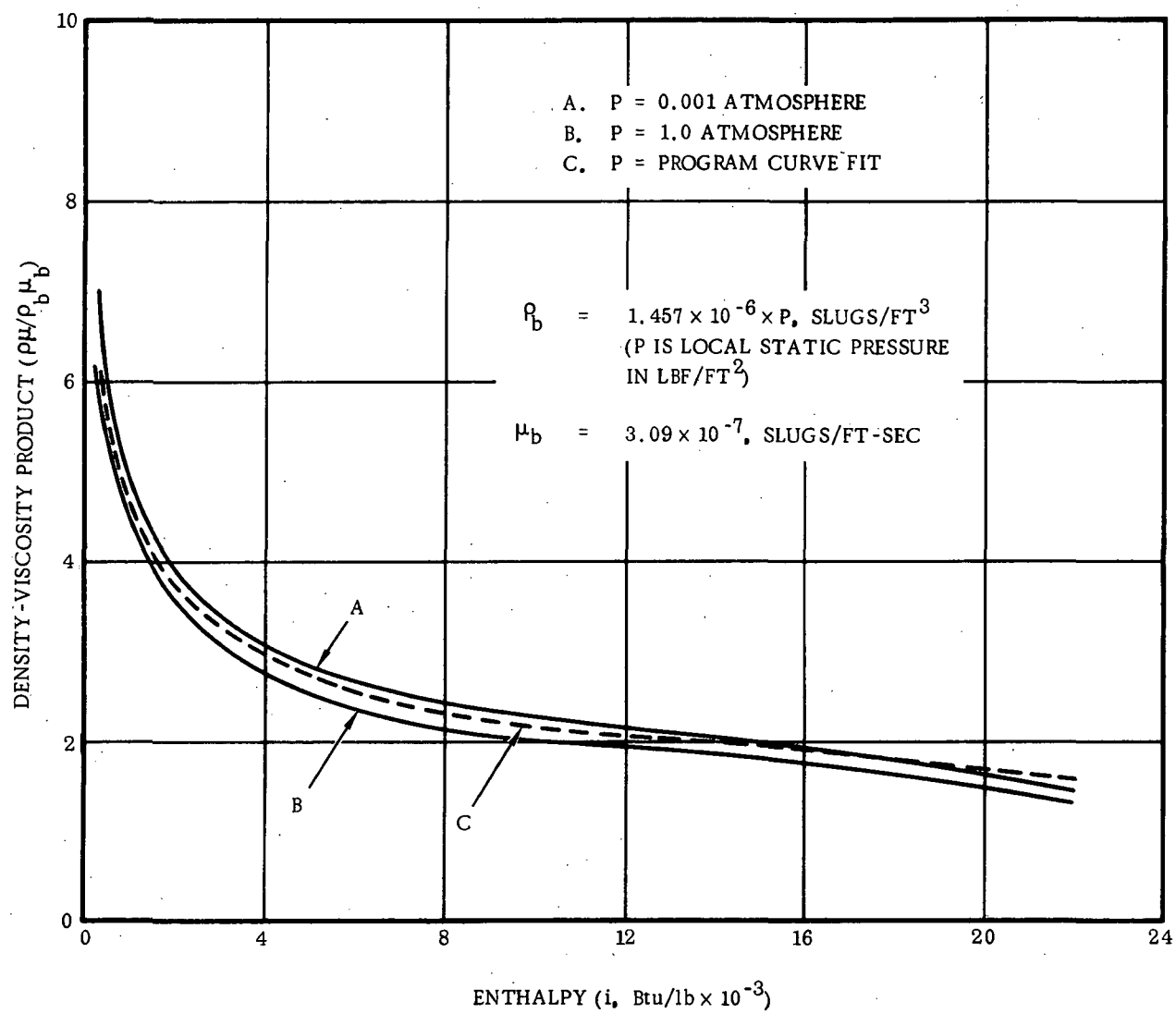


Figure 2-15. Density-Viscosity Product Vs. Enthalpy

Sutherland's formula is used to compute the viscosity at free stream conditions.

$$\mu = 2.27 \times 10^{-8} \frac{T^{3/2}}{T + 198.6} \quad (2-57)$$

### 2.3 STRUCTURAL TEMPERATURE DETERMINATION

The temperature at any point in the structure is a function of external and internal convection and radiation rates and the conductivity and thermal inertia properties of the structure itself. In this program, structural temperature distributions are evaluated through use of the lumped parameter method of finite differences.

The surface and/or structure is divided into an arbitrary number of small segments. The segments are arranged in rows parallel and columns perpendicular to the surface as shown in Figure 2-16.

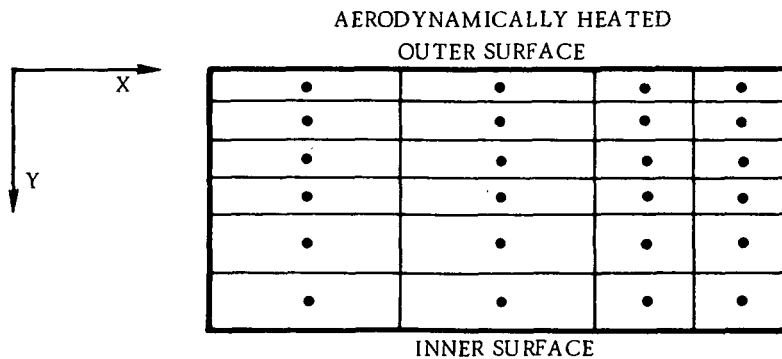


Figure 2-16. Surface/Structure Segmentation

Then, for some small time increment ( $\Delta t$ ), the net heat flux to each surface segment is determined. For a segment  $i$ , then, the temperature change from time to time,  $t + \Delta t$ , is

$$T_i(t + \Delta t) - T_i(t) = \left[ q_{\text{net}} A_{\text{BL}} - (qA)_{\text{INSD}} - \sum (kA \frac{\Delta T}{X})_N - \sum (q_{\text{rad}} A)_N \right] \frac{\Delta t}{(WC_p)_i} \quad (2-58)$$

where

$A_N$  = area perpendicular to direction  $N$

$k_N$  = effective thermal conductivity in direction  $N$

$X_N$  = length of conduction path in direction N

$\Delta T_N$  = temperature difference between adjacent elements in direction N at time t

$q_{\text{rad}}$  = heat transfer by radiation between nodes

$W$  = weight of element i

$C_p$  = specific heat of element i

It is assumed that all the mass is concentrated in a point at the centroid of the segment,  $A_N$  is equal to the segment interface area, and  $X_N$  is equal to the distance between centroids in direction N.

The net heat transfer is given by

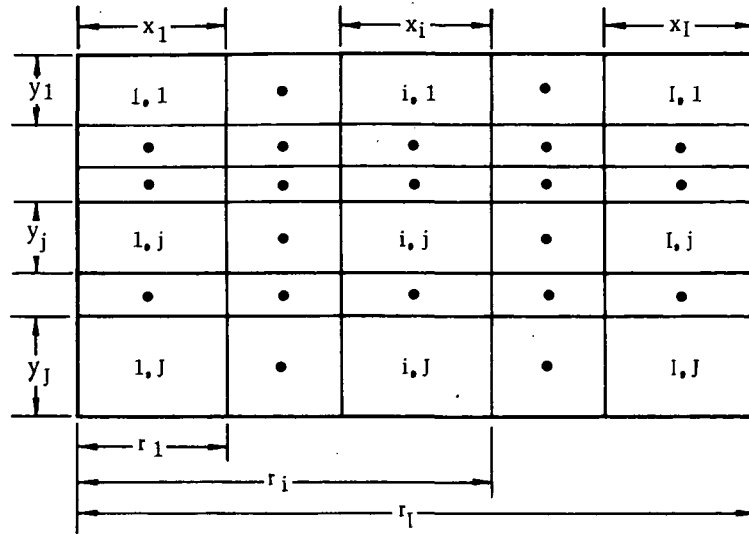
$$q_{\text{net}} = q_{\text{cons}} q_i - q_{\text{rad}} \quad (2-59)$$

where  $q_i$  is the boundary layer convective heat transfer rate,  $q_{\text{rad}}$  represents the energy loss due to surface radiation, and  $q_{\text{cons}}$  is an optional multiplying factor. This factor may be used to approximately allow for the effects of shock wave interactions, flow divergence, etc.

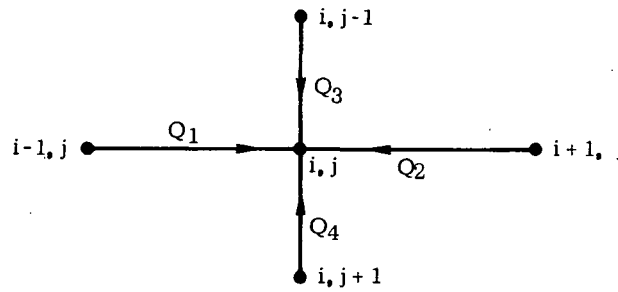
The term  $(qA)_{\text{INSD}}$  provides an optional capability to include internal convective cooling of the structure. The cooling occurs on the backface of the last segment.

Terms in Equation 2-58 which do not apply to a given element are dropped out for that element. Thus, the  $q_{\text{net}}$  term applies only to elements of the first row, i.e., those representing the surface, and the  $(qA)_{\text{INSD}}$  term applies only to elements of the last row, i.e. those representing the backface. Internal radiation heat transfer is also taken into account in this program. The accuracy of Equation 2-58 is dependent upon the size of the segments and the computation interval and improves as these parameters are decreased. The program may be used for either one-dimensional or two-dimensional arrays of segments.

In the following, the two-dimensional case is discussed; the one-dimensional problem is treated as a special case of a single column. The structure is set up in a matrix shown in Figure 2-17. In addition to the rectangular coordinate system, the cylindrical coordinate is also included as an option. The material may not be homogeneous in either the x-direction or the y-direction. The maximum number of rows and columns is nine each. Configurations are given in Figure 2-18, and nodal breakdowns for the thermodynamic and stress analyses are given in Figure 2-19.



(a) STRUCTURE ARRAY



(b) TYPICAL NODES

Figure 2-17. Structure Heat Transfer Matrix

The temperature at any segment at time  $t + \Delta t$  is dependent upon the summation of direction heat transfer rates at time  $t$ . The general equation is given by Equation 2-58. From Figure 2-17, for a typical node, the temperature,  $\tau$ , changes from time  $t$  to  $t + \Delta t$  by

$$T_{ij}(t + \Delta t) = T_{ij}(t) + \frac{\Delta t}{A_{ij}} \sum_{k=1}^4 Q_K \quad (2-60)$$

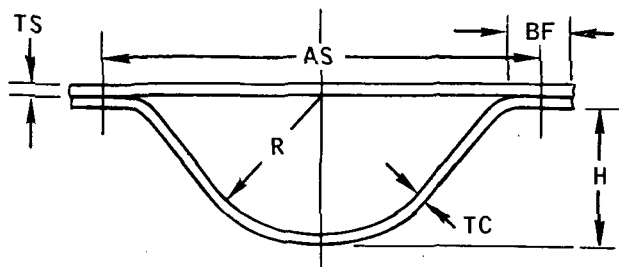
$A_{ij}$  is the thermal mass of the node as defined in Table 2-1, together with other parameters. The equations for computing  $Q_K$ 's are listed in the following:

a. Conduction heat transfer

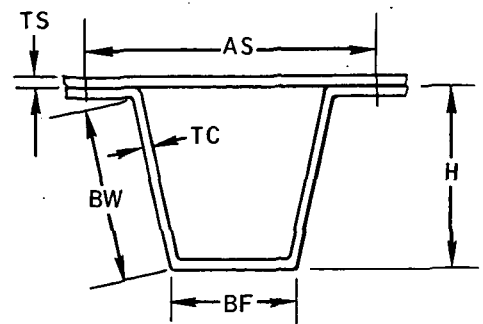
$$Q_1 = (T_{i-1, j} - T_{i, j}) / E_{i-1, j} \quad (2-61)$$

$$Q_2 = (T_{i+1, j} - T_{i, j}) / E_{i, j} \quad (2-62)$$

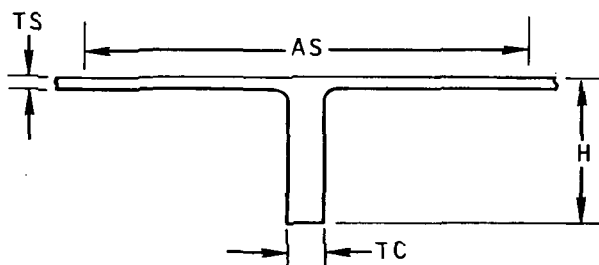




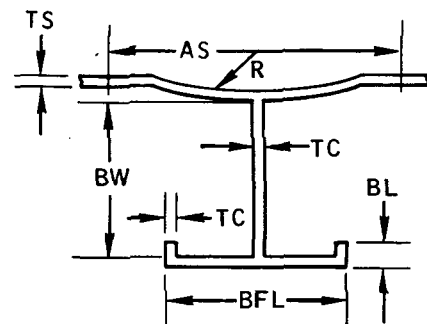
1. CONVAIR TRAPEZOIDAL



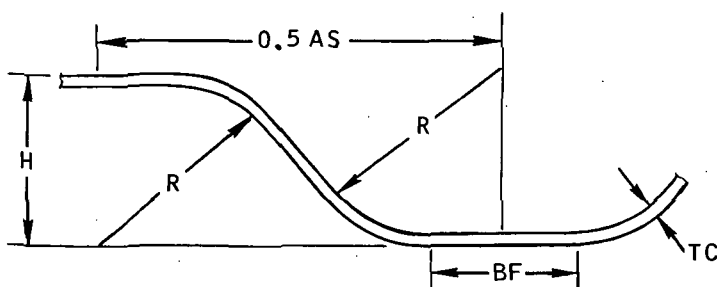
2. FLAT CORRUGATION WITH SKIN



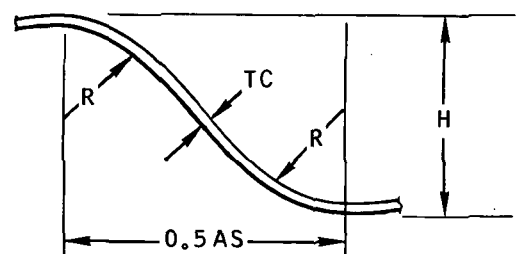
3. RIB-STIFFENED PANEL



4. SKIN-STRINGER



5. OPEN CORRUGATION



6. OPEN CORRUGATION  
(CIRCULAR ARC CORRUGATION)

Figure 2-18. Panel Geometries

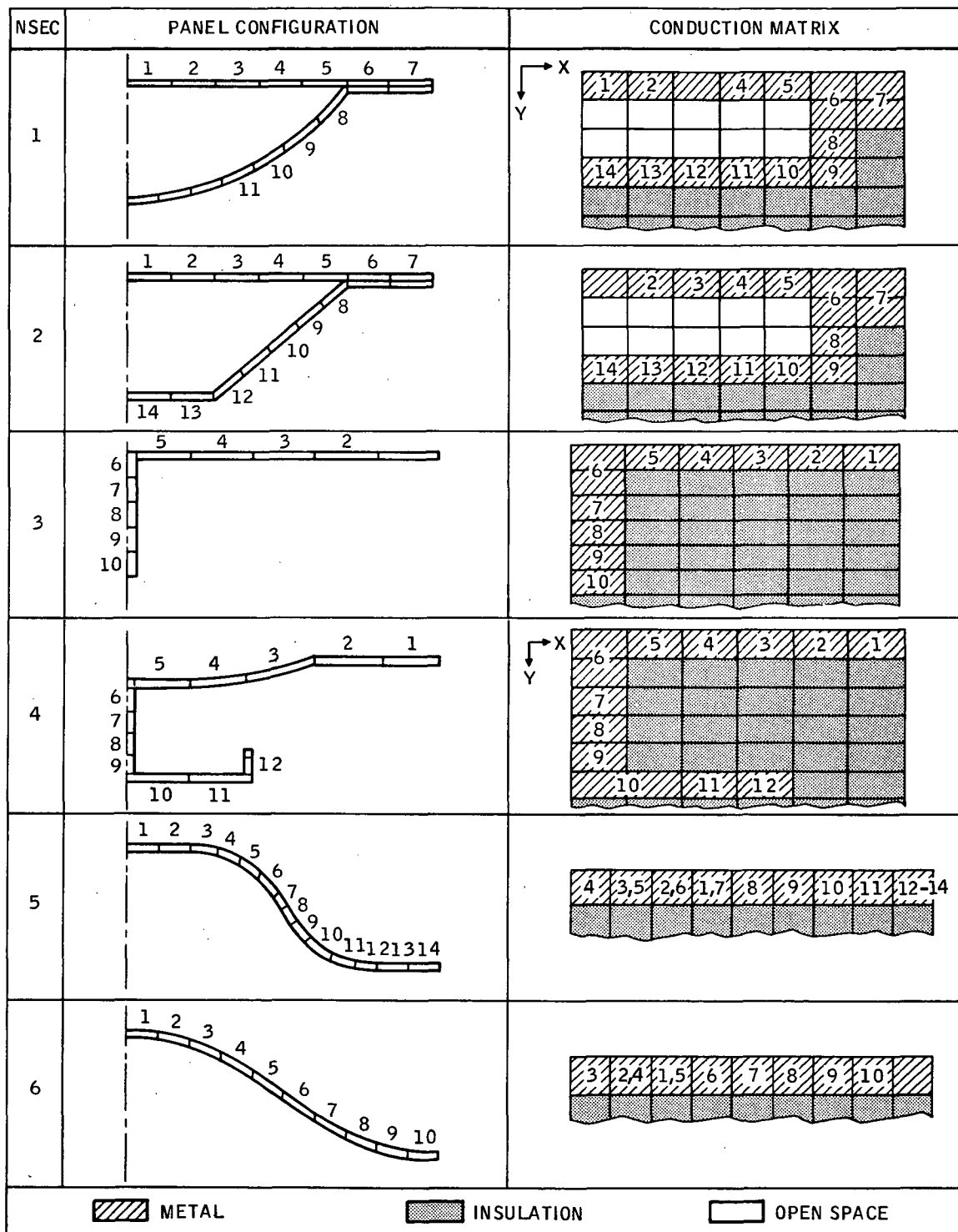


Figure 2-19. Configurations for Thermodynamic and Stress Analysis  
2-29

Table 2-1. Notations for Two Coordinate Systems

Symbol	Coordinate System	
	Rectangular	Cylindrical
$x'_i$	$x_i$	$\pi (r_i^2 - r_{i-1}^2)$
$y'_{i,j}$	$y_j$	$2\pi r_i y_j$
$A_{i,j}$	$(\rho c_p)_{ij} x'_i y_j$	
$B_{i,j}$	$\frac{x'_i}{2 K_{ij} y_j}$	$\frac{\ln [r_i / (r_i - 0.5 \times i)]}{2\pi K_{ij} y_j}$
$C_{i,j}$	$\frac{y_j}{2 K_{ij} x_i}$	
$D_{i,j}$	—	$\frac{\ln [(r_i - 0.5 \times i) / r_{i-1}]}{2\pi K_{ij} y_j}$
$E_{i,j}$	$B_{ij} + B_{i+1,j}$	$B_{i,j} + D_{i+1,j}$
$F_{i,j}$	$C_{i,j} + C_{i,j+1}$	

$$Q_3 = (T_{i,j-1} - T_{ij}) / F_{i,j-1} \quad (2-63)$$

$$Q_4 = (T_{i,j+1} - T_{i,j}) / F_{i,j} \quad (2-64)$$

b. Radiation heat transfer

$$Q_K = \sigma \Sigma L \epsilon_{a,b} (T_{m,n}^4 - T_{i,j}^4) \quad (2-65)$$

where

$$L = x'_i \text{ (for } k = 3, 4)$$

$$= y'_{ij} \text{ (for } k = 1, 2)$$

c. Nodes on the first column

$$Q_1 = 0 \quad (2-66)$$

d. Nodes on the last column

$$Q_2 = 0 \quad (2-67)$$

e. Nodes on the first row

$$Q_3 = x'_i q_{net_i} \quad (2-68)$$

f. Nodes on the last row

$$Q_4 = h_{ins} x'_i (T_{ins} - T_{ij}) \quad (2-69)$$

## 2.4 STRUCTURAL ANALYSIS

This discussion covers the short-time static strength and creep analysis of TPS panels and support members. The analysis is restricted to simply-supported panels with expansion joints which permit free thermal expansion. The loadings considered are bending due to aerodynamic pressure, and the internal forces induced by temperature gradients within the panel cross section.

Given the instantaneous normal pressure and temperature distribution on the TPS panel at each of a series of times throughout a flight trajectory, the internal stresses are determined by stress analysis and hence the instantaneous creep rate for each element comprising the cross section is obtained from Larson-Miller curves. To determine the critical trajectory point or time for each mode of failure considered in the static strength analysis, a number of structural indices relating the applied and allowable stresses throughout the cross section are computed. The critical time for each mode of failure is determined upon completion of the trajectory by selecting the maximum value of this appropriate index.

The failure modes considered are yielding, ultimate tension, ultimate compression and/or crippling of the various elements comprising each panel cross section. Margins of safety are computed at the critical trajectory points for each of these modes.

The total creep strain accumulated in each element of the panel cross section during the trajectory is obtained by the summation of the product of the average creep rate in each time interval and the time increment.

The final step in the analysis is a redesign procedure which increments the panel thickness in the event that the minimum margin of safety is negative and/or the maximum creep strain exceeds the permissible value. Each step in the analysis procedure is further discussed in the following paragraphs.

**2.4.1 LOADS ANALYSIS AND NODAL BREAKDOWN OF PANEL.** The TPS panels considered in this investigation are of sheet stringer or corrugated construction (both exposed and covered corrugations) with simply-supported edges and joints which permit free thermal expansion. All configurations are illustrated in Figure 2-18. Each stiffening element or corrugation in the panel is assumed to behave as a simply-supported beam subjected to normal pressure loading and to a self-equilibrating system of internal loads due to temperature gradients across the section. Figure 2-20 illustrates a corrugated section attached to support configuration number one in which the panel rests

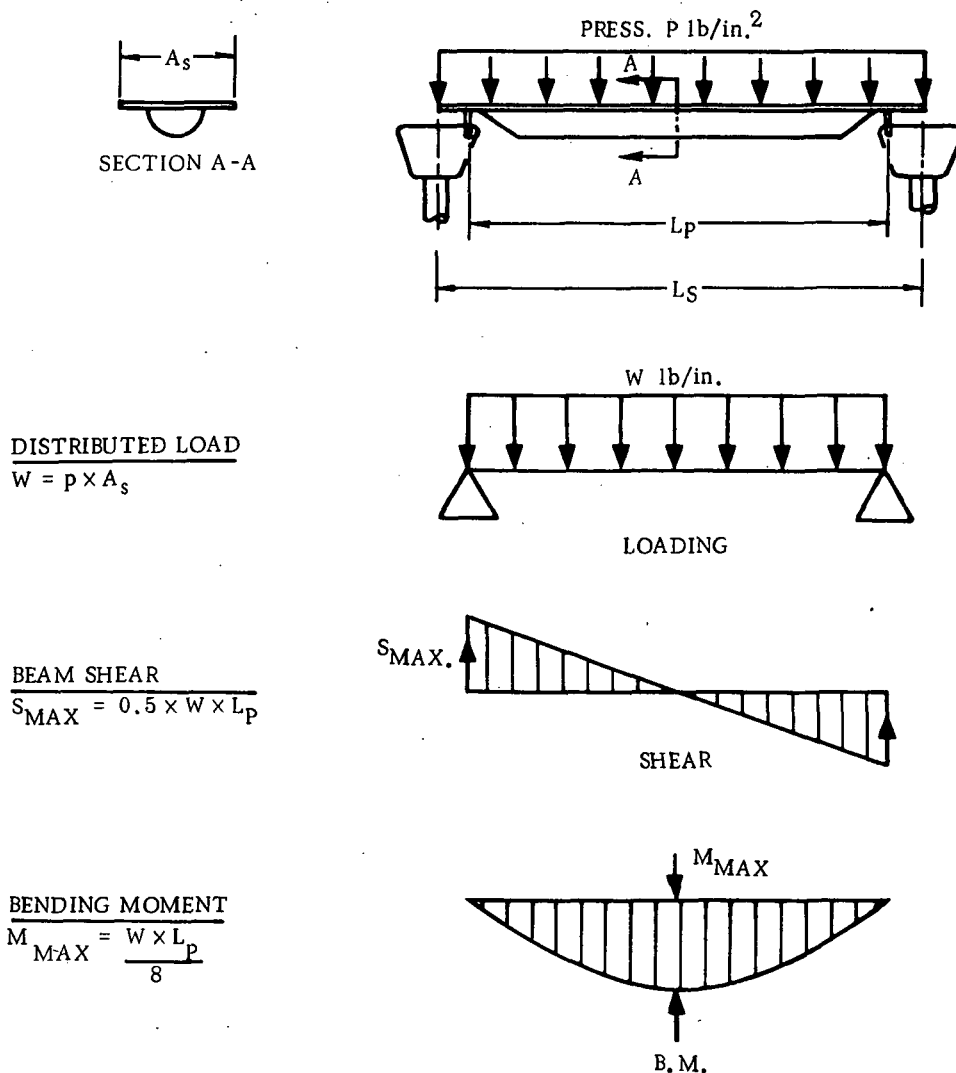


Figure 2-20. Panel Loads Analysis

on rails which in turn are supported by heat posts. Shear stresses and bending moments resulting from the loading are also shown. Section properties and the nodal breakdown are computed first. As an illustration, panel configuration number one is shown in Figure 2-21. Since the section is symmetrical about its centerline, only half of it need be considered. For n-segments of the area under consideration, the section area, centroid, and moments of inertia are given respectively by the general expressions

$$A = \sum_{i=1}^n \Delta s_i t_i$$

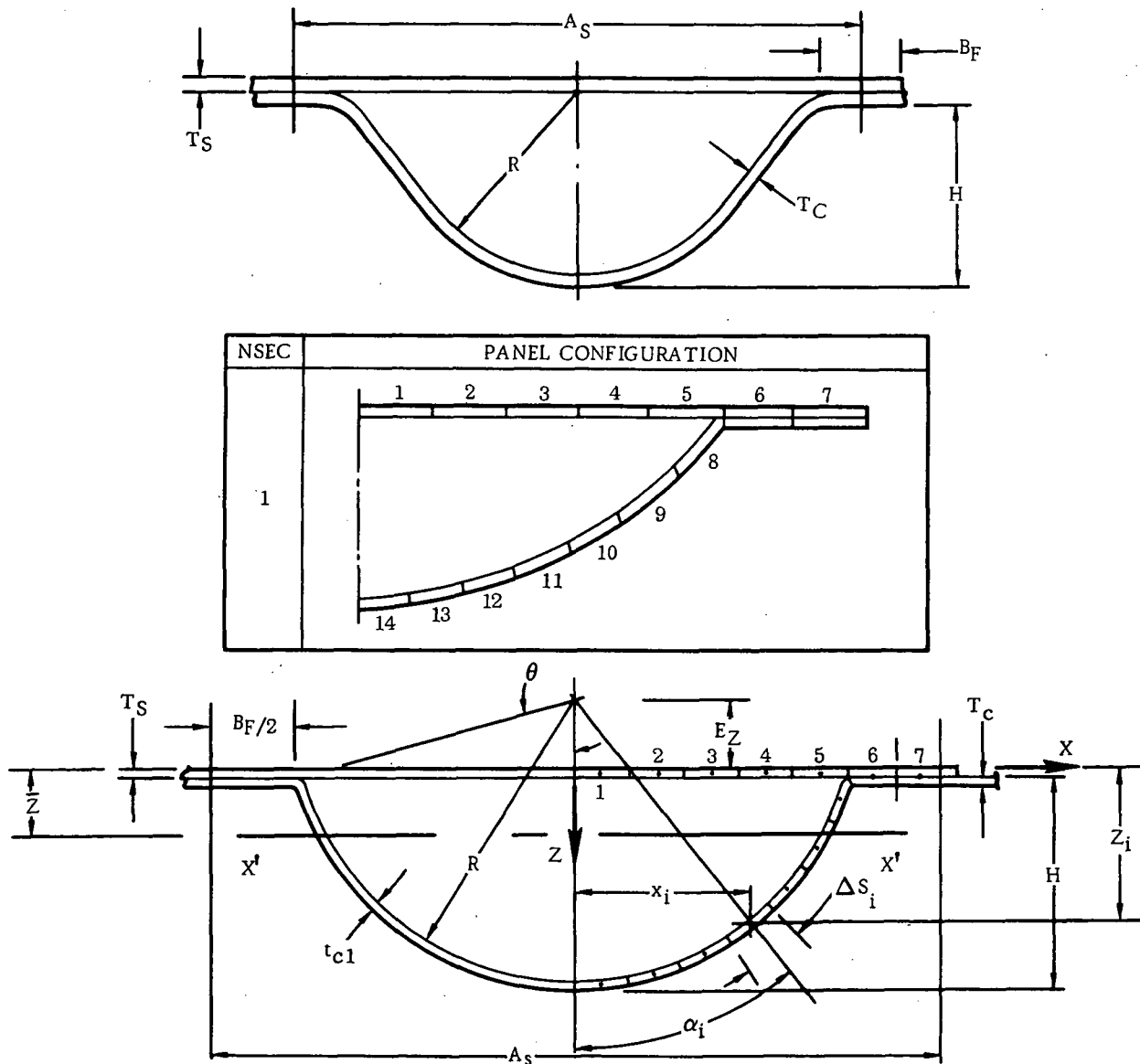


Figure 2-21. Geometry of Configuration No. 1

$$\bar{z} = \frac{\sum_{i=1}^n \Delta s_i t_i z_i}{\sum_{i=1}^n \Delta s_i t_i}$$

$$I_{xx} = 2 \sum_{i=1}^n \Delta s_i t_i (\bar{z} - z_i)^2$$

$$I_{zz} = 2 \sum_{i=1}^n \Delta s_i t_i x_i^2$$

$$I_{xz} = \sum_{i=1}^n \Delta s_i t_i x_i z_i = 0$$

Geometry is computed for this particular configuration more specifically in the following manner. First the angle  $\theta$  is computed as

$$\theta = \cos^{-1} \left( \frac{R-H}{R} \right)$$

Next, the areas of the first five segments of half the cross section are determined as

$$A_i = \frac{1}{10} (A_s - B_F) t_s \quad i = 1, \dots, 5$$

and their orientation in terms of the lateral and vertical coordinates  $x$  and  $z$  is given respectively by the distances to the centroid

$$\left. \begin{aligned} X_i &= X_{i-1} + 2 X_1 \\ Z_i &= Z_1 \end{aligned} \right\} \quad i = 2, \dots, 5$$

where

$$X_1 = 0.05 (A_s - B_F)$$

$$Z_1 = 1/2 t_s$$

$A_s$  and  $B_F$  are the width of the full corrugation and flange, not just half widths. The sixth and seventh nodes consider the combined thicknesses of the skin such that

$$A_i = 1/4 B_F (t_s + t_c)$$

Note that the portion of the panel being analyzed extends from centerline of the corrugation to the centerline of the flange areas. The lateral distances are then determined as

$$X_6 = \frac{1}{2} (A_s - B_F) + \frac{1}{8} B_F = \frac{1}{2} A_s - \frac{3}{8} B_F$$

$$Z_6 = \frac{1}{2} (t_s + t_c)$$

and

$$X_7 = X_6 + \frac{1}{4} B_F$$

$$Z_7 = Z_6$$

The next calculations in the nodal breakdown concern areas and orientation of the curved portion of corrugation. This area is separated into seven segments of equal length and area. Hence

$$A_i = 1/7 (R \theta t_{c1}) \quad i = 8, 9, \dots, 14$$

where the parameter

$$t_{c1} = \frac{2 R \sin \theta}{2 R \theta} t_c$$

considers the fact that the corrugation is formed by stretching a flat plate of width  $2 R \sin \theta$  to a circular arc of length  $2 R \theta$ , a constant volume process. The angle theta is now broken into seven equal segments and centers of the segment are located by the angular increment  $\theta/14$ . Hence

$$\Delta_\alpha = \theta/14$$

and

$$X_8 = R \sin \alpha$$

$$Z_8 = R \cos \alpha - (R - H + t_s)$$

as seen from the geometry of Figure 2-19.



The last values are incremented

$$\alpha_i = \alpha_{i=1} - 2 \Delta \alpha$$

$$X_i = R \sin \alpha_i \quad i = 9, 10, \dots, 14$$

$$Z_i = R \cos \alpha_i - (R - W - t_s)$$

The other configurations of Figure 2-19 are broken up into finite elements by similar computational procedures.

Stresses on the section are given by two loadings: (1) the applied bending moment due to normal pressure, and (2) a self-equilibrating system of internal loads due to temperature gradients across the section. The stress of any of the discrete elements of Figure 2-21 is given by

$$f_i = \frac{M_{\max} (Z_i - \bar{Z})}{I_{xx}} + f_{T_i}$$

where  $f_{T_i}$  is the thermal stress. The critical buckling stress (an allowable stress) for the flat plate section of the corrugation (discrete elements 1 through 5 of Figure 2-21) is given by

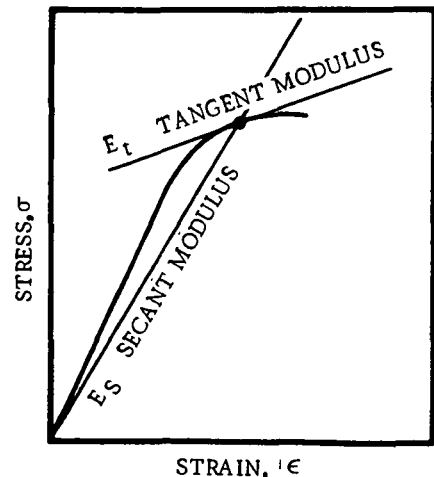
$$F_{CR} = K \eta E \left( \frac{t_s}{b} \right)^2$$

where  $b$  is the width of the flat section (i.e.,  $b = A_S - B_F$ ). The constant  $K$  is the buckling stress coefficient which depends on the edge conditions. For simply-supported edges with no restraints against lateral expansion, a value of  $K = 3.62$  is used. The term  $\eta$  is the plasticity correction factor (see the accompanying sketch) which is given by

$$\eta = \frac{E_s}{E} \left( \frac{1}{2} - \frac{1}{2} \sqrt{\frac{1}{4} + \frac{3}{4} \frac{E_t}{E_s}} \right)$$

The tangent and secant moduli,  $E_t$  and  $E_s$  respectively, are given by

$$E_s = \frac{E}{1 + \frac{3}{7} \left( \frac{F_{CR}}{F \cdot 7} \right)^{n-1}}$$



and

$$E_t = \frac{E}{1 + \frac{3}{7} n \left( \frac{F_{CR}}{F_{.7}} \right)^{n-1}}$$

where  $E$ ,  $n$ , and  $F_{.7}$  are material properties dependent upon temperature. The expressions for the critical stress  $F_{CR}$  and the plasticity correction factor  $\eta$  are solved iteratively in terms of the shear and tangent moduli. If the critical stress exceeds an upper limit of either 100 percent of the critical yield stress or the ultimate tensile stress, whichever is greater, the flat skin of the corrugation has buckled. This portion of the panel cross section is considered ineffective in bending, and the stress analysis is performed as if these elements of the cross section were not involved. Note that the buckling of the panel skin is applicable only to panel configurations 1 and 2, the corrugation stiffened panels.

**2.4.2 TEMPERATURE INTERPOLATION.** Temperatures through the panel cross-section members are calculated throughout the trajectory in the thermodynamic analysis. External heating rates are either computed or input, and the temperature response of finite elemental volumes are predicted by numerical solution of the energy equation. In the stress analysis, the temperatures of each of the nodes set up for the discrete element analysis for stress determination are predicted by linear interpolation of the thermodynamic and stress models are shown in Figure 2-19 where the stress nodal indices are superposed on the two-dimensional conduction matrix.

**2.4.3 COMPUTATION OF STRESSES.** (Thermoelastic Analysis of Statically Determinant Beams.) The stress analysis procedure is based on the finite sum method of Reference 20. This sub-section presents the method for determining the deformation and stresses of an unrestrained beam subjected to temperature variations through the beam cross section. The section properties for the general case of variable modulus (due to temperature and construction) are given in integral form for the purpose of determining the response of the cross section to both temperature and load. The general solution is then presented in integral form and is evaluated by the methods of finite sum.

**2.4.3.1 General Solution.** The following paragraphs present the general thermoelastic solution for an unrestrained beam in integral form, as derived in Reference 20. Evaluation of these integrals, which causes most of the difficulty in obtaining numerical solutions to specific problems, is discussed in a subsequent section.

The following assumptions and limitations apply to the thermoelastic solution of the unrestrained beam:

- a. Plane cross sections before bending remain plane after bending.
- b. Material is linear elastic at any temperature. Thus, a single relationship of stress to strain ( $\sigma = E \epsilon$ ) can be utilized to connect the equations of deformation and equilibrium and the principle of superposition can be employed.

- c. The variation of the cross section and temperature along the length of the beam is both continuous and smooth and does not produce any significant shear forces.

The unrestrained beam with temperature variation in the cross section is analyzed by subjecting the beam to a set of force systems which satisfy equilibrium and produce deformations which are compatible with the requirement of plane cross sections remaining plane after bending.

Consider a unit length of beam. Initially, each fiber of the beam is liberated from the influence of its neighbors. The temperature distribution is then applied to the beam which causes each fiber to expand by an amount  $\alpha T$ . In general, the thermal expansion of the fibers will cause the cross-sectional plane formed by the ends of the fibers to warp. To satisfy the requirement of plane cross sections remaining plane, a pressure loading of  $-E\alpha T$  is applied to eliminate the thermal expansion and return the cross section to its original position and condition (plane). This pressure loading upsets the equilibrium of the cross section. An axial load ( $F' = \int E\alpha T da$ ), equal in magnitude but opposite in direction to the force on the cross section due to the pressure, is applied at the elastic centroid of the cross section. This balancing axial force causes pure translation without rotation of the cross section plane so that the requirement of plane cross sections remaining plane is not violated. Rotational equilibrium still remains to be satisfied since the location of the resultant restoring force  $\bar{y}$ , in general, will not coincide with the centroid of elastic area  $\bar{y}$ . Equilibrium is achieved by applying a balancing moment to the cross section of sufficient magnitude ( $M' = [\bar{y} - \bar{y}] F'$ ) to cause pure rotation of the cross-sectional plane.

The superposed force systems now satisfy equilibrium and produce deformations which are compatible with the requirement of plane cross sections remaining plane. Thus, the procedure outlined above must result in a stress-deformation distribution for an unrestrained beam which is consistent and unique under the assumptions.

Elastic Section Properties of Cross Section. The structural response to both mechanical loads and thermal stimulæ is governed by the effective bending ( $\overline{EI}$ ) and axial ( $\overline{EA}$ ) stiffness of the cross section. The equations for these properties, which are stated below, are identical to those for cross sections having constant  $E$  except that  $E$  is retained within the integral sign since it is permitted to vary over the cross section.

$$\overline{EA} = \int E da \quad (2-70)$$

$$\left. \begin{aligned} \bar{y} &= \int E y da / \int E da \\ \bar{z} &= \int E z da / \int E da \end{aligned} \right\} \quad (2-71)$$

$$\left. \begin{aligned} \overline{EI}_{yy} &= \int E z^2 dA - \bar{z}^2 \int E dA \\ \overline{EI}_{zz} &= \int E y^2 dA - \bar{y}^2 \int E dA \\ \overline{EI}_{yz} &= \int E yz dA - \bar{y} \bar{z} \int E dA \end{aligned} \right\} \quad (2-72)$$

$$(\overline{EI}_{uu}, \overline{EI}_{vv}) = \frac{\overline{EI}_{yy} + \overline{EI}_{zz}}{2} \pm \sqrt{\left(\frac{\overline{EI}_{yy} - \overline{EI}_{zz}}{2}\right)^2 + (\overline{EI}_{yz})^2} \quad (2-73)$$

The distances  $\bar{y}$  and  $\bar{z}$  to the elastic centroid are given by Equation 2-71. Thus, the elastic centroid, Equation 2-70, is the centroid of the effective elastic area  $EA$ , not of the geometric area. Similarly, the geometric moments of inertia are of no significance when  $E$  varies over the cross section. The effective bending stiffnesses, Equation 2-72, must be employed.

Equation 2-73 expresses the bending stiffnesses about the elastic centroid principal axes in terms of the bending stiffnesses about arbitrary centroidal axes. The elastic principal axes are defined as those orthogonal axes for which

$$\overline{EI}_{uv} = \int Euv dA = 0$$

**2.4.3.2 Stresses and Deformations of the Cross Section Due to Temperature.** No thermal stresses are caused in an unrestrained isotropic, homogeneous, linearly elastic body by an  $\alpha T$  distribution which varies linearly in a rectangular coordinate system. Clearly, in the particular case of an unrestrained beam, a linear  $\alpha T$  distribution over the cross section produces free thermal expansions which cause cross sections to remain plane after deformation. No stresses are required to maintain the plane cross section.

In general, a non-linear temperature distribution over the cross section would cause free thermal expansions of the beam fibers which would warp a plane cross section out of plane. Thermal stresses are produced which restore the plane cross section. In this respect, a temperature distribution can be considered as a "thermal load" which, when applied in the absence of mechanical load, still produces stresses and deformations.

Following are the equations for the stresses and deformations in an unrestrained beam due to thermal load.

$$\bar{\epsilon}' = \frac{F'}{EA}$$

$$\begin{aligned}
w'_z &= \frac{\left( \bar{EI}_{yy} M'_{zz} \right) + \left( \bar{EI}_{yz} M'_{yy} \right)}{\left( \bar{EI}_{yy} \bar{EI}_{zz} \right) - \left( \bar{EI}_{yz} \right)^2} \\
w'_y &= \frac{\left( -\bar{EI}_{zz} M'_{yy} \right) + \left( \bar{EI}_{yz} M'_{zz} \right)}{\left( \bar{EI}_{yy} \bar{EI}_{zz} \right) - \left( \bar{EI}_{yz} \right)^2} \\
\sigma &= E \left[ -\alpha T + \bar{\epsilon}' + w'_z (y - \bar{y}) + w'_y (z - \bar{z}) \right]
\end{aligned}$$

where

$$\begin{aligned}
F' &= \int E \alpha T \, dA \\
\bar{y} &= \int E \alpha T y \, dA / \int E \alpha T \, dA \\
\bar{z} &= \int E \alpha T z \, dA / \int E \alpha T \, dA \\
M'_{zz} &= (\bar{y} - \tilde{y}) F' \\
M'_{yy} &= (\bar{z} - \tilde{z}) F'
\end{aligned}$$

**2.4.3.3 Stresses and Deformations of the Cross Section Due to Combined Mechanical and Thermal Loading.** For a linearly elastic beam, mechanical loads can be combined with thermal loads simply by superposition. Thus

$$\begin{aligned}
\bar{\epsilon}_t &= \frac{(F' + F)}{EA} \\
(w_z)_t &= \frac{\left[ -\bar{EI}_{yy} (M'_{zz} + M_{zz}) \right] + \left[ \bar{EI}_{yz} (M'_{yy} + M_{yy}) \right]}{\left( \bar{EI}_{yy} \bar{EI}_{zz} \right) - \left( \bar{EI}_{yz} \right)^2} \\
(w_y)_t &= \frac{\left[ -\bar{EI}_{zz} (M'_{yy} + M_{yy}) \right] + \left[ \bar{EI}_{yz} (M'_{zz} + M_{zz}) \right]}{\left( \bar{EI}_{yy} \bar{EI}_{zz} \right) - \left( \bar{EI}_{yz} \right)^2} \\
\sigma &= E \left[ -\alpha T + \bar{\epsilon}_t + (w_z)_t (y - \bar{y}) + (w_y)_t (z - \bar{z}) \right]
\end{aligned}$$

Moments about  $\bar{y}\bar{y}$  and  $\bar{z}\bar{z}$  centroidal axes are positive when their sense is such that they tend to cause compressive stresses in the positive quadrant (quadrant where both  $y - \bar{y}$  and  $z - \bar{z}$  have positive values). "F" is positive when tensile, and "T" is positive when above a datum value.

2.4.3.4 Evaluation of Integrals. The solution of the thermoelastic beam problem requires the evaluation of the integrals discussed in the previous sections. The cross section is broken up into a finite number of elemental areas, selected so that the variation of  $\alpha T$  and  $E$  in each element is small. The procedure is adaptable to all cross sections and the degree of accuracy increases with the number of elements.

The finite sum solution for the deformations of the cross section is based on an approximating geometry consisting of a finite number of points of concentrated elastic area located at the centroids of elements. Once the deformations ( $\bar{\epsilon}$ ,  $w_y$ ,  $w_z$ ) have been calculated from the tabular solution, stresses can be obtained at any points on the cross section.

2.4.4 CALCULATION OF DESIGN FACTORS. Applied stresses vary throughout the trajectory depending on the gradients across the panel induced by aerodynamic pressure and heating, whereas the allowable stresses and elastic module vary with temperature. Each mode of failure of the static strength analysis is considered by determining the stress ratios (the ratio of applied to allowable stress) for each element in the cross section at each point in the trajectory at which the stress analysis is performed. Presently, the stress analysis is undertaken at each print-out interval of the computer program. The most critical time for each mode of failure is determined as the maximum value of the particular stress ratio. The computed ratios and the corresponding failure models are given in the following table.

<u>Failure Mode</u>	<u>Stress Ratio</u>	<u>Fortran Name</u>
1. Ultimate Tension	$f/F_{TU}$	R1
2. Ultimate Compression	$f/F_{CY}$	R2C
3. Yielding	$f/F_{CY}$	R2
4. Crippling	$f/(F_{CY}^D)^{1/2}$	R3
5. Elastic Stability	$f/E$	R4

where  $f$  is the local stress of the incremental structural model node, and  $F_{TU}$ ,  $F_{CY}$ , and  $E$  are ultimate tensile stress, ultimate compressive stress in yield, and modulus of elasticity.

These maximum values, and the times at which they occur, determine the design point for the particular configuration. All elements comprising the cross section are considered for failure modes 1, 2 and 3. The expressions for the corresponding margins of safety are given as follows:

1. Ultimate Tension:

$$M.S. = (F_{TU_i} / (UF) \cdot f_i) - 1 \quad (2-74)$$

2. Ultimate Compression:

$$M.S. = (1.1 F_{CY_i} / (UF) \cdot f_i) - 1 \quad (2-75)$$

If  $1.1 F_{CY} > F_{TU}$  then the above expression is replaced by:

$$M.S. = (F_{TU_i} / (UF) f_i) - 1 \quad (2-76)$$

3. Yielding (tension and/or compression):

$$M.S. = (F_{TY_i} / f_i) - 1 \quad (2-77)$$

Note that

- a. The compression yield stress  $F_{CY}$  is assumed equal to the tension yield stress ( $F_{TY}$ ) since for most materials of interest,  $F_{CY}$  is not available.
- b.  $(UF)$  = ultimate factor, a factor of safety applied to the limit loads to determine the ultimate loads.

The remaining failure modes (4 and 5) are applicable only to selected elements and configurations. For example, consider the analysis of configuration 1, Figure 2-20.

2.4.4.1 Crippling of Flange (Width - BF). The analysis is made for the trajectory point which gives a maximum value of the stress ratio

$$f_i / \left( E_i F_{CY_i} \right)^{1/2} \quad i = 6, 7 \quad (2-78)$$

The crippling stress is given by

$$F'_{cc} = 1.385 F_{CY} / [(F_{CY} / E)^{1/2} \cdot BF/t]^{.808} \quad (2-79)$$

When this value of the allowable crippling stress exceeds 1.1 times the crippling yield stress, then the latter value is used as the allowable crippling stress. When, in turn,  $1.1 F_{CY}$  exceeds the ultimate allowable tensile stress, then the ultimate allowable tensile stress is used for the allowable crippling stress. Hence, mathematically

$$\left. \begin{aligned}
 F_{cc} &= F'_{cc} & F'_{cc} &\leq 1.1 F_{CY} \\
 F_{cc} &= 1.1 F_{CY} & 1.1 F_{CY} &< F'_{cc} \\
 F_{cc} &= F_{TU} & F_{TU} &\leq 1.1 F_{CY} \leq F'_{cc}
 \end{aligned} \right\} \quad (2-80)$$

The panel thickness  $t$  in Equation 2-79 is given by

$$t = t_s + t_c$$

and the margin of safety in crippling is

$$M.S. = \frac{F_{cc}}{f_i (UF)} - 1$$

**2.4.4.2 Buckling of the Semicircular Arc Corrugation (Elastic Stability).** This analysis is performed for the trajectory point which gives a maximum value of the stress ratio  $f_i/E_i$  for nodes  $i = 8, 9 \dots, 14$  of configuration No. 1. The buckling stress is given by

$$F'_{CR} = \frac{k E_s t}{R} \quad (2-81)$$

where

$E_s$  is material secant modulus

$k$  is buckling stress coefficient

$t$  is the corrugation thickness.

This value of the allowable crippling stress is determined by the same procedure as in the previous section. When the value of the allowable crippling stress given by Equation 2-81 exceeds 110 percent of the crippling yield stress, then the latter value is used as the allowable crippling stress. When, in turn,  $1.1 F_{CY}$  exceeds the ultimate allowable tensile stress, then this value is used for  $F'_{CR}$ . Hence,

$$\begin{aligned}
 F_{cc} &= F'_{cc} \text{ for } F'_{cc} \leq 1.1 F_{CY} \\
 F_{cc} &= 1.1 F_{CY} \text{ for } 1.1 F_{CY} < F'_{cc}
 \end{aligned}$$



$$F_{cc} = F_{TU} \text{ for } F_{TU} \leq 1.1 F_{CY} \leq F'_{cc}$$

The margin of safety (MS) is given by

$$MS = \frac{F_{CR}}{f_i (UF)} - 1$$

In the computer program, if all the elements in a flange or corrugation only experience tensile loading, the compression crippling or buckling analyses are not applicable; in this event the corresponding MS is equated to 100. If the analysis is not applicable to a given configuration the MS is equated to 1000.

**2.4.5 CALCULATION OF CREEP STRAIN.** The total creep strain accumulated in each elemental area of the panel cross section is evaluated throughout the trajectory under the following simplifying assumptions:

- a. The creep strain accumulated in each flight is identical.
- b. The stress distributions are identical in every flight (i.e., stress redistribution due to accumulated plastic strains is not considered).

During the stress analysis, instantaneous creep rates for each element are determined from relevant Larson-Miller data for the particular material under consideration. The computational procedure is outlined below. Strain data is presented as a function of stress and the Larson-Miller parameter (LMP) where

$$LMP = (460 + T) (20 + \log t)$$

and

$T$  = temperature in °F

$t$  = time in seconds

The problem is to find the creep rate,  $\dot{\epsilon} = d\epsilon/dt$ , at the stress and temperature levels being experienced by the particular element of interest. The derivative is approximated by

$$\frac{d\epsilon}{dt} = \frac{\Delta\epsilon}{\Delta t}$$

where  $\Delta\epsilon$  denotes the strain difference between the two curves of Figure 2-22, co-ordinates of which are input to the program. The difference in time,  $\Delta t$ , is determined from the two values of time corresponding to the two values of the Larson-Miller parameter at the specified temperature and stress level.

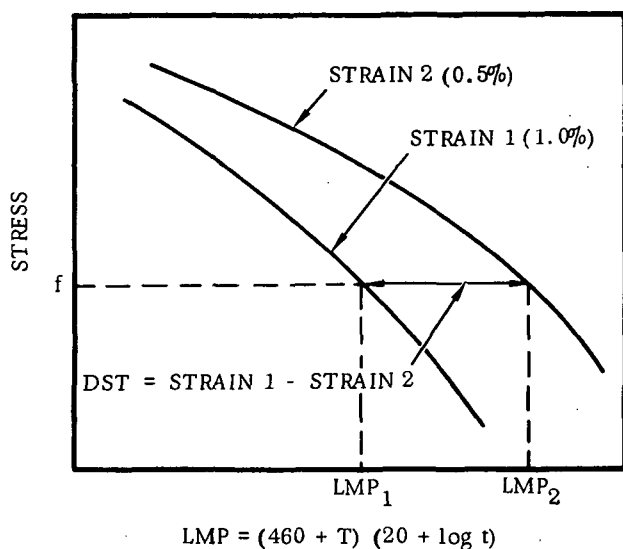


Figure 2-22. Larson-Miller Plot of Creep Data

Hence, since

$$t = 10^{\left( \frac{\text{LMP}}{460 + T} - 20 \right)}$$

then

$$t_1 = 10^{\left( \frac{\text{LMP}}{460 + T_1} - 20 \right)}$$

$$t_2 = 10^{\left( \frac{\text{LMP}}{460 + T_2} - 20 \right)}$$

where the subscripts 1 and 2 correspond to the two strain curves, 1 and 2, shown in Figure 2-22. Upon completion of the trajectory, the total creep is derived by

integrating the creep rates over the trajectory by the trapezoidal rule. Then

$$\dot{\epsilon} = \frac{\text{DST}}{T} = \frac{\text{DST}}{t_2 - t_1} \quad \epsilon = \text{NF} \sum_i \dot{\epsilon}_i$$

where NF is number of flights.

## 2.5 FATIGUE ANALYSIS

**2.5.1 PREDICTION OF FATIGUE LIFE.** Fatigue, which results from an accumulation of alternating stress levels greater than the endurance limit of a material or structure, can always be induced if the applied loads are sufficiently large. (Endurance limit is defined as the highest stress under which repeated application can be endured indefinitely.) In acoustic fatigue, however, the applied loads are small. Therefore, the high stresses required to produce fatigue must be generated by other means. The prime contributor to the problem is the phenomenon of resonance. It is axiomatic that nearly all aircraft structural fatigue failures resulting from steady-state inputs such as noise or vibration are due to resonance. A structure will resonate when there is coincidence between one or more of its natural frequencies and frequencies of applied alternating forces. From the fatigue standpoint, the significant attribute of structural resonance is that of dynamic stress amplitude magnification,  $Q$ .

For a linear oscillator with small damping being driven sinusoidally at resonance,  $Q = 1/2 \frac{c}{c_c}$ , where  $\frac{c}{c_c}$  is the ratio of equivalent viscous damping to critical damping. This shows that the dynamic magnification is directly related to the damping.

When the oscillator (structure) is driven by a broad band random forcing function, only the energy near the resonant frequency of the structure performs significant work. This effective bandwidth, which is defined by the "half-power" points, is approximately equal to twice the damping coefficient,  $2 \frac{c}{c_c}$ . For example, if the resonant frequency ( $f_n$ ) is 100 Hz and the damping is 2 percent of critical, the effective bandwidth is 4 Hz, i.e., 98 to 102 Hz. Thus, increasing the damping of a structure decreases its dynamic stress amplification, but increases the effective driving force level because of the increase in effective bandwidth. If the damping of the above structure were increased to 4 percent of critical, the Q would be reduced by a factor of 2 while the effective force would increase by the factor  $\sqrt{2}$  (assuming a flat input spectral density). Hence, increasing the damping of a structure is advantageous, as shown in Figure 2-23.

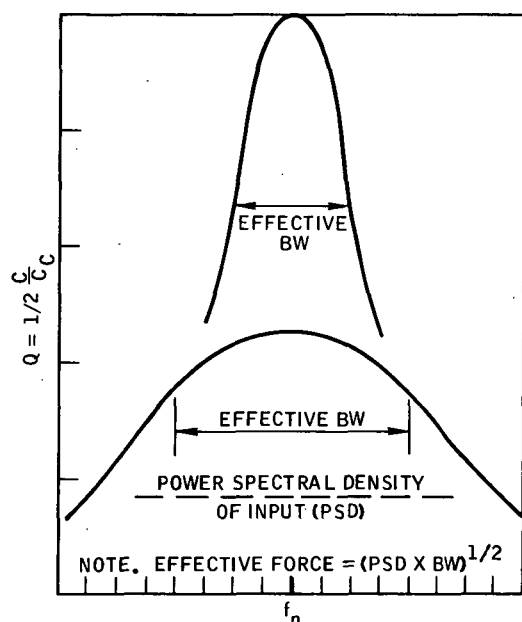


Figure 2-23. Relationship Between Q and Effective Bandwidth ( $f_n/Q$ )

Another factor which must not be neglected in any fatigue problem is that of stress raisers. Experience at Convair Aerospace has shown, and has been confirmed by independent tests under NASA contract, that stress raisers in conventional aircraft structure correspond closely to  $K_T = 4.0$  for acoustic fatigue problems. Experience at Convair Aerospace has also shown that for conventional aircraft structures, reduction of a stress raiser in itself (by changing methods of fastening, for example) may provide the difference between a structure with an adequate or inadequate fatigue life. This arises from the fact that for a structure adequately designed for other service loads, acoustic fatigue failures almost always are initiated at fastener lines (because of the stress raisers) and then propagate into the skin and secondary structure (see Figure 2-24).

In estimating the acoustic fatigue life of a TPS panel, there is a logical, straightforward procedure which is carried out. Up to a point this procedure is independent of any cumulative damage estimation theory.

The first step is to calculate the flexural natural frequencies of the panel. A rapid, approximate method has been found with errors in the lower modes of less than 10 percent. This method assumes that, in flexural vibration with small amplitudes, the natural frequencies are primarily a function of the flexural bending wavelengths in the panel. In the case of an isotropic, rectangular, simply-supported panel, the general expression for the frequencies of the natural modes of vibration is:

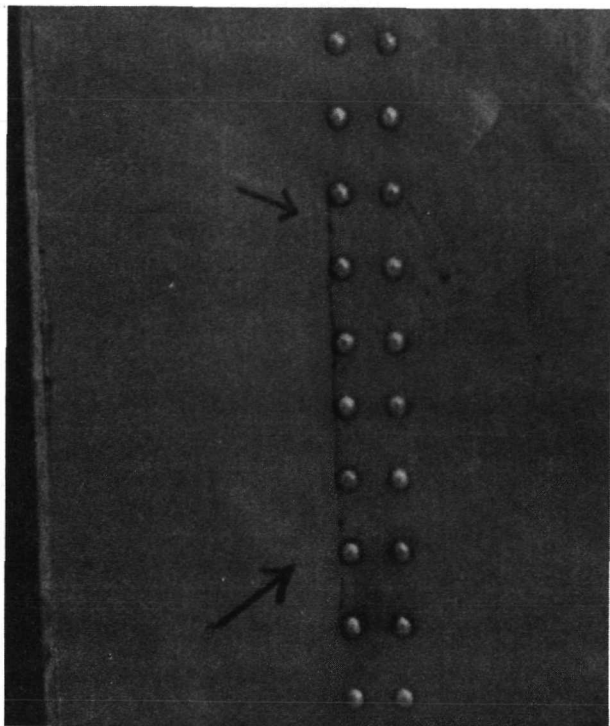


Figure 2-24. Acoustic Fatigue Failure Showing Crack Propagation Along Rivet Line

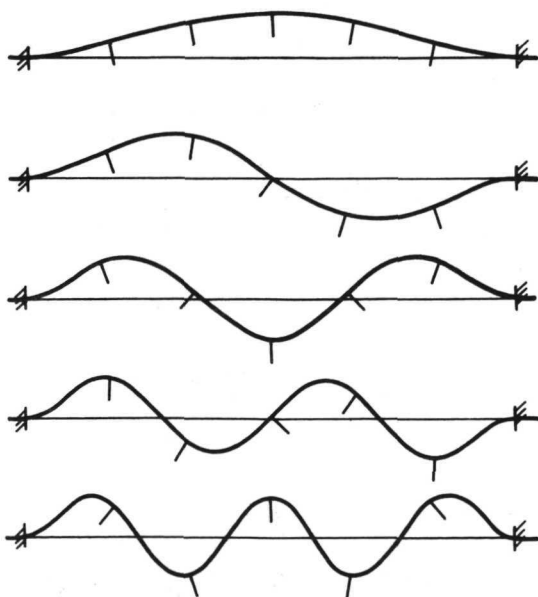


Figure 2-25. Mode Shapes of First Five Modes of an Integrally Stiffened Panel

$$\omega_n = \left( \frac{D}{M} \right)^{1/2} \left( k_m^2 + k_n^2 \right)$$

where

$D$  is the flexural stiffness per unit area of the panel

$M$  is the mass per unit area of the panel

$k_m, k_n$  are panel wave numbers in orthogonal coordinate directions

For a clamped panel, wavelength equivalence factors can be used with the above expression. For two-dimensionally-stiffened panels, the basic flat panel stiffness is used and to it is added the averaged stiffness of the reinforcing beams or corrugations, as may be applicable. In general, this procedure can be employed for any structure that can be said to have a well defined mode shape which can be expressed in terms of simple mode shape functions (Figure 2-25). The number of frequencies and modes which must be calculated is directly related to the type of acoustic excitation involved. For the analysis of this program, only the fundamental mode of each panel is considered as the panel's resonant frequency.

It is next necessary to estimate the energy available to drive the panel at its resonant frequency(s). This is a function of the spectral density of the acoustic pressures and the damping of the panel (Figure 2-23). Assuming that the effective rms acoustic pressure is a static pressure, the equivalent rms static stress of the panel is calculated by standard procedures. This equivalent static stress is then multiplied by the  $Q$  of the panel and again by the appropriate local stress raiser. This, then, yields the dynamic rms stress at the resonant

frequency. Test data has shown that the statistical distribution of the instantaneous acoustic pressures due to rocket noise, for example, is approximately normal. Thus, for rocket noise, the peak pressure distribution which is of significance in the fatigue problem and which is the same as the peak stress distribution for a linear structural system can be represented by an integrated Rayleigh distribution:

$$[p > s_p] = e^{-\frac{1}{2} \left( \frac{s_p}{s_o} \right)^2}$$

where  $[p > s_p]$  is the probability of exceeding  $s_p$  in percent, and  $s_p/s_o$  is the ratio of peak stress/rms stress. Knowing the temporal life requirement for the panel and the stress distributions at the important resonant frequencies, the fatigue life can now be expressed in terms of numbers of significant stress reversals.

At this point, assuming that the required S-N data is available, it is ready to be combined with a cumulative damage estimation procedure, as shown in Figure 2-26.

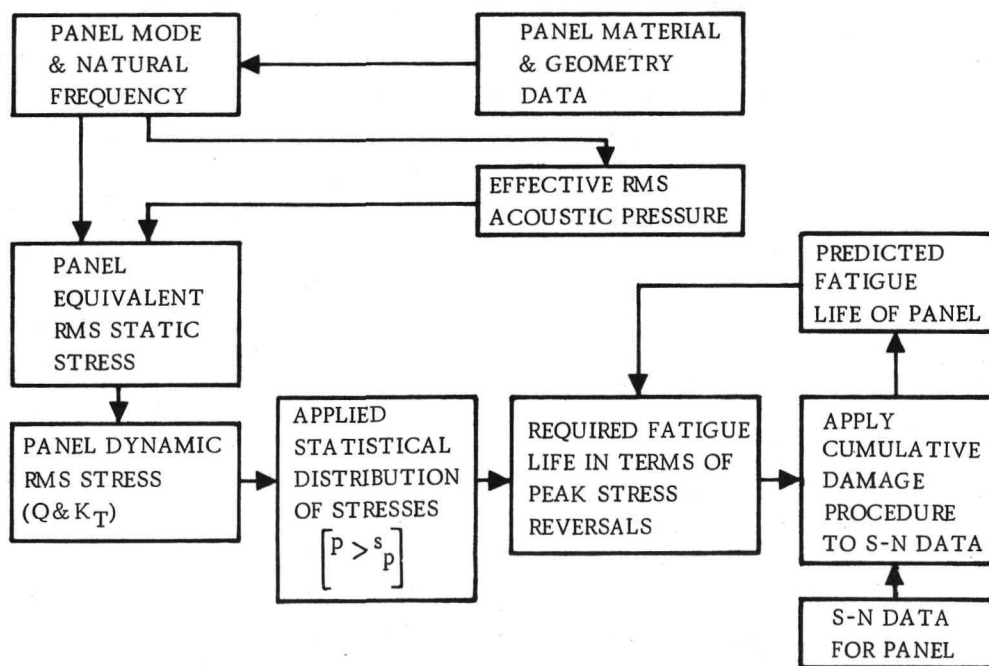


Figure 2-26. Acoustic Fatigue Estimation Procedure

**2.5.2 LIFE PREDICTION METHODS.** All theories relating to fatigue damage under random loading have in them, either explicitly or implicitly, a concept of cumulative damage concept or cumulative partial damage. The simplest and hence the most attractive theory is the linear cumulative damage concept, or Palmgren-Miner theory.

This states that the sum of the partial damage is equal to unity,  $\sum \frac{n_i}{N_i} = 1$ , where  $n_i$  is

the actual number of stress reversals at stress level  $S_i$ , and  $N_i$  is the number of stress reversals required to cause fatigue failure at this level. This is shown in Figure 2-27.

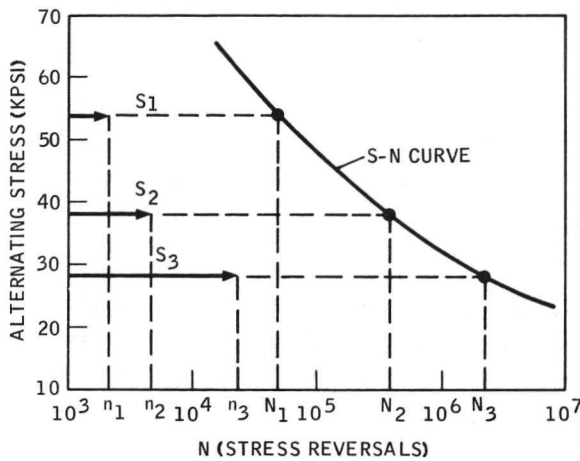


Figure 2-27. Linear Damage Rule Diagram

To salvage the basic idea with its simplistic approach, Freudenthal has proposed a quasilinear rule which employs stress interaction factors as functions of the stress spectrum. Thus, for the linear rule

$$V_R = 1/\sum (p_i/V_{si})$$

and for the quasilinear rule

$$V'_R = 1/\sum (p_i \omega_i/V_{si})$$

where

$V_R$  = fatigue life estimated on basis of linear damage rule

$V'_R$  = fatigue life estimated on basis of quasilinear damage rule

$p_i$  = relative frequency ratio of cycles of stress amplitude  $S_i$  in spectrum

$\omega_i$  = stress interaction factors

$V_{si}$  = "characteristic" values of extreme value distributions of fatigue lives  $N_{si}$

The overall trend of test results indicates (particularly for reversed bending) that the linear rule generally overestimates fatigue lives according to Freudenthal (References 21 and 22). The actual values in any given circumstances will depend on the maximum and minimum stress levels involved in the random loading distribution.

According to Freudenthal, the unconservatism of the linear rule results from neglect of consideration of the interaction between the infrequent high-stress amplitudes and the frequent low-stress amplitudes which produces a disproportionately high degree of damage at the low-stress amplitudes.

Other workers have attempted to handle the stress interaction problem in a similar manner with varying degrees of success (References 23, 24, 25, 26, 27, 28, and 29). At Convair Aerospace, another approach which has proved successful has been taken with respect to acoustic fatigue life prediction.

Since the phenomenon of fatigue deals with applied oscillating loads and structural vibratory responses, it may be considered as one of energy absorption and/or dissipation. Above its endurance limit (if one exists) a material (or structure) has only a finite or limited capacity for absorbing energy or having work done on it before failure will occur. Where the applied loads (and structural responses) vary sinusoidally, the standard S-N curve defines the amount of work which can be accomplished without failure. With this basic concept in mind, one can consider its extension with the idea that if there is a limit to the energy which a structure can absorb without failure, then, within certain restrictions which will be discussed later, the limiting energy for work should be independent of the rate, sequence, or level of application.

If a continuous, randomly variable schedule of oscillating peak stresses is considered (such as an integrated Rayleigh distribution) and plotted on S-N coordinates, then it is apparent that the curve envelope at any given time represents the cumulative partial damage, as shown in Figure 2-28. However, since total damage information is generally available in the form of S-N curves for sinusoidally varying stresses, the partial damage must be interpreted in terms of an equivalent sinusoidal stress level.

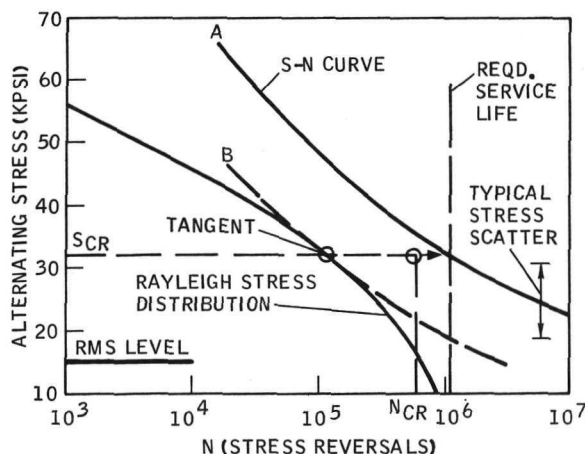


Figure 2-28. Equivalent Fatigue Damage Diagram, Random Loading

If the random stress distribution envelope is plotted for the required number of stress reversals (Figure 2-28) and a curve B parallel to the applicable S-N curve A is plotted so as to be tangent to it, it is seen that the stress level at the point of tangency will, at any given time, have contributed the greatest partial damage. This stress level is referred to as the "critical" stress level,  $S_{cr}$ , and if the point of tangency were with the actual S-N curve, failure obviously would already have occurred. However, if the critical stress level,  $S_{cr}$ , is extended to  $N_{cr}$  stress reversals so that the area  $S_{cr}N_{cr}$  is equal to that under the random stress envelope, the work accomplished at  $N_{cr}$  reversals by stress  $S_{cr}$  is equal to that accomplished at the required number of stress reversals by the randomly varying stresses. If  $N_{cr}$  is less than the required service life, no failure would be predicted. Life expectancy would be prorated on the basis of the ratio between  $N_{cr}$  and the required service life.

Any simplistic view of cumulative fatigue damage ignores many parameters which could modify the analytical results. For example, the improvement in endurance limit of some materials by exposure to very low stress levels is an obvious point. Or again, the sequence in which a structure is exposed to a wide range of stress levels may be important. One point that cannot be ignored, however, is that if stress maxima approach yield values, no simple theory will hold. Another important consideration is that if the range of stress levels is such as to cause redistribution of the structural stress pattern, as the stresses vary from minimum to maximum, again no simple theory will hold.

Convair Aerospace has successfully used its equivalent work acoustic fatigue analysis procedure on its own 880 and 990 commercial jet aircraft, on the North American A3J engine inlets, and on the C-141 and C-5A empennages. The procedure is presently being used on NASA Contract NAS1-9793 (LRC), "Coated Columbium Alloy Heat Shields for Space Shuttle Application." It is also being applied to the acoustic fatigue evaluation of the Convair Aerospace SSV booster.

For the Convair Aerospace technique, the digital computer program computes sound pressure levels from basic engine and aerodynamic data, computes the dynamic response characteristics of the TPS panels as a function of their material properties, geometry, damping and restraint, computes equivalent static and dynamic stresses and computes fatigue life. All input data, except S-N data, is programmed. S-N data is included by a curve-fitting process for the individual materials under consideration. Details of the computational procedure are given in the following paragraphs.

**2.5.3 PROGRAM ORGANIZATION.** The sonic fatigue analysis subroutines are organized into a number of basic functional tasks which include input, determination of panel fundamental frequencies, noise source computations, and the calculation of (1) dynamic stresses, (2) the number of stress reversals, and (3) the critical stress levels. Each of these computations is explained in the following subsections.

**2.5.3.1 Input.** Input parameters are read into the computer in records which allow description of each of the four noise sources as well as panel geometry and the allowable S-N data of the material in question. The latter are coefficients to a cubic least-squares curve fit of stress (in thousands of pounds per square inch) as a function of the number of stress reversals to failure. The moments of inertia which are input to the acoustic fatigue analysis are for the panel cross section under investigation and lie in the plane of the panel. The parameter is used to compute dynamic bending stresses in the classical manner. At the moment, the panel moments of inertia must be computed external to the program since the computation itself is rather lengthy and a function of complex geometry, the size and number of corrugations, and the like. The moment of inertia for the cross section of the panel can be determined by superposition of the moments of inertia of the simpler areas of components comprising the total structure. The technique can be found in any handbook or fundamental text of stress analysis. The list of input parameters is given in Table 2-2 along with the appropriate units of each parameter.



Table 2-2. Input Parameters for Sonic Fatigue Analysis

DT(1)	Period of turbulent boundary layer noise excitation, sec
XL	Run length of turbulent boundary layer, ft
REY	Local Reynolds number
VU	Local velocity, ft/sec
QL	Local dynamic pressure, psf
AMACH	Local Mach number
DT(2)	Period of rocket engine noise excitation
TT	Rocket engine thrust, lb
WER	Rocket engine weight flow, lb/sec
D	Rocket nozzle exit diameter, ft
VS	Local speed of sound, ft/sec
XI	Distance between point of interest and rocket engine exit
DVEH	Vehicle diameter, ft
YCL	Y-distance from vehicle centerline to point of interest, ft
DREF	Distance from rocket exhaust plane to reflecting surface on pad, ft
IPAD	= 0, vehicle not on pad ≠ 0, vehicle on pad
DT(3)	Period of jet (flyback) engine noise excitation, sec
AE	Nozzle exit area, ft <sup>2</sup>
UJ	Jet velocity, ft/sec
WEJ	Jet engine weight flow, lb/sec
VV	Vehicle velocity at flyback cruise, ft/sec
TJ	Jet engine thrust, lb
XJ	Axial distance from point of interest to jet engine exit nozzle, ft
YP	Radial distance from point of interest to jet engine exit nozzle (less than 200 ft but greater than the nozzle exit diameter), ft

Table 2-2. Input Parameters for Sonic Fatigue Analysis, Contd

DT(4)	Period of jet (flyback) engine scrubbing noise excitation, sec
HPAN	Panel thickness, in.
HC	Core thickness, in. (for honeycomb sandwich)
AI	Panel moment of inertia, in. <sup>4</sup>
AIY	Panel moment of inertia, in. <sup>4</sup> (for normal direction of corrugated panel)
AW	Panel length, ft
BW	Panel width, ft
EP	Modulus of elasticity for panel, psi
KFLEX	Flexural rigidity index = 0, if structure symmetrical, rigid = 1, if structure unsymmetrical and/or flexible
NPAN	Panel configuration index = 1, flat plate = 2, honeycomb sandwich = 3, integrally stiffened = 4, corrugated
C(1)	First coefficient of a least-squares, third-order curve fit of allowable S-N data
C(2)	Second coefficient of a least squares, third order curve fit of allowable S-N data
C(3)	Third coefficient of a least-squares, third-order curve fit of allowable S-N data
	NOTE: The curve must be fitted to the allowable S-N data with the ordinate, S, in thousands of pounds per in. <sup>2</sup> and the abscissa as the logarithm of the number of cycles, N.
RHOP	Panel density, lb/ft <sup>3</sup>

**2.5.3.2 Calculation of Fundamental Frequencies.** For the present analysis, it is assumed that the panel resonates (and suffers its fatigue damage) at its fundamental frequency. Four different types of rectangular panels are currently considered: (1) isotropic, (2) honeycomb, (3) integrally-stiffened, and (4) corrugated. The program itself determines which configuration to utilize. The technique for calculating the fundamental mode of each of these configurations is essentially the same.

**Rectangular Isotropic Panel.** The fundamental frequency is computed as a function of the panel unit mass, its flexural rigidity, and the length of its shorter side. Hence

$$f = \frac{K}{2\pi a^2 \sqrt{M/D}} \quad \text{Hertz} \quad (2-82)$$

M, the mass per unit area of the panel, is given by

$$M = \frac{\rho h}{g_o} \quad (2-83)$$

where

$\rho$  = panel density in lb/ft<sup>3</sup>

$h$  = panel thickness in inches

$g_o$  = gravitational constant = 32.2 ft/sec<sup>2</sup>

and the flexural rigidity D is given by

$$D = \frac{E h^3}{12 (1 - \nu^2)} \quad (2-84)$$

with

$E$  = modulus of elasticity

$\nu$  = Poisson's ratio (for materials of interest, this is approximately 0.3)

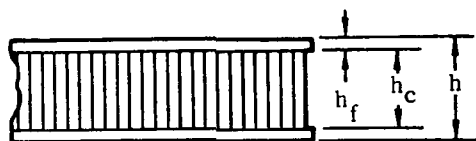
It is assumed, based on actual airplane experience, that the plate vibrates as an average between a clamped edge and a simply supported edge along all four edges. For the rectangular isotropic panel, this coefficient is given by the following table. In addition, if the plate supporting the structure is symmetrical and rigid compared to the plate, the frequency is as calculated from Equation 2-82. If, however, the supporting structure is unsymmetrical and/or flexible compared to the plate, then the fundamental frequency is reduced by a factor of 4, i.e.,  $f_1 = f/4$ .

$b/a$	$K$ avg
1.0	27.89
1.5	20.63
2.0	18.45
2.5	17.61
3.0	17.08
$\infty$	16.12

Rectangular Honeycomb Panel. The fundamental frequency is computed by Equation 2-82, the same as the rectangular isotropic plate, except now the flexural rigidity is given by

$$D = \frac{E_{f_1} E_{f_2} t_{f_1} t_{f_2} (t_t t_c)^2}{4 (1 - \nu^2) (E_{f_1} t_{f_1} + E_{f_2} t_{f_2})}$$

where the subscripts  $f_1$  and  $f_2$  denote the outer and inner face sheets respectively (Reference 31). The geometry is given in Figure 2-29. Under the assumption that the face sheets are the same thickness and Poisson's ratio is approximately 0.3 for materials of interest, this expression reduces to



$$D = \frac{E t_f t_c t}{1.82} \quad (2-85)$$

Figure 2-29. Rectangular Honeycomb Panel Geometry

It is assumed that the sandwich panel vibrates as simply-supported on all four edges. Thus, the coefficient  $K$  of equation (2-82) is given by the following table for the honeycomb panel. The panel frequency is then given by combining Equations 2-82 and 2-85.

$b/a$	$K$
1.0	19.74
1.5	14.26
2.0	12.34
2.5	11.45
3.0	10.97
$\infty$	9.87

Integrally Stiffened Panel. This configuration is often referred to as a machined plank. The geometry is given by Figure 2-30. If pure flexure is considered and all torsion neglected, the overall flexural stiffness of the panel can be taken as the effects of the panel and stringer stiffness in parallel (Reference 32). The total flexural stiffness is the sum of that of a homogeneous panel plus that of a number of beams averaged over the panel width. The assumption is valid for evenly dis-

tributed stiffeners and is applicable only to the fundamental mode where all stringers can be assumed in flexure. The flexural rigidity for a uniform panel is given by

$$D = \frac{Eh^3}{12 (1 - \nu^2)}$$

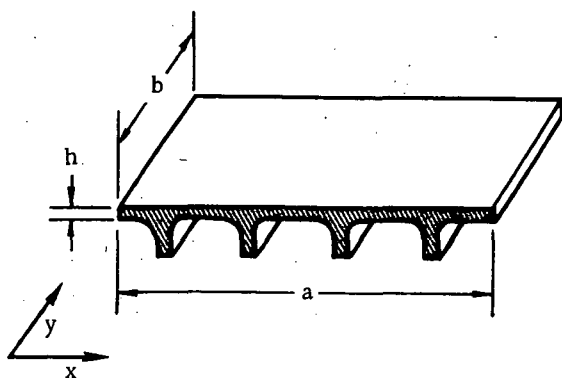


Figure 2-30. Integrally-Stiffened Panel Geometry

which, for metallics of interest where  $\nu = 0.3$ , simplifies to

$$D = \frac{Eh^3}{10.9}$$

The panel wave numbers in the x- and y-coordinate directions respectively are given by  $k_m = m\pi/a$  and  $k_n = n\pi/b$  where  $m$  and  $n$  are the mode numbers or the number of half wave lengths.

For the simply-supported panel in the fundamental mode,  $m = n = 1$ . For

a homogeneous panel, the flexural stiffness is given by

$$D' = D (k_m^2 + k_n^2)^2$$

and if the stiffnesses in the two coordinate directions are uniform but not the same, the flexural stiffness is given by

$$D' = D_x k_m^4 + 2 D_{xy} k_m^2 k_n^2 + D_y k_n^4$$

where  $D_x$  and  $D_y$  are flexural rigidities in the coordinate directions, and  $D_{xy}$  is a cross flexural rigidity. If, in addition, stiffness is added in one direction by stiffeners or stringers, then the rigidity in that direction and the cross-flexural rigidity will be altered. Assuming that the stiffness is added in the y-direction, then the stiffness in the x-direction,  $D_x$ , remains constant. Assuming thin stringers, the stiffness in the y-direction becomes the sum of flexural stiffnesses of the homogeneous panel,  $D$ , and of the stiffeners per unit panel width if they are spread evenly across the panel surface. (One is assuming that the stringers do not affect the panel mode shape.) Thus

$$D_x = D + \frac{EI}{b}$$

$$D_y = D = \frac{Eh^3}{12(1-\nu)^2} = \frac{Eh^3}{10.9}$$

With the cross flexural rigidity given by

$$D_{xy} = (D_x D_y)^{1/2}$$

the total flexural stiffness of the structure is given by

$$K_T = \left[ (D_x)^{1/2} k_m^2 + (D_y)^{1/2} k_n^2 \right]^2$$

For the mass per unit area of the configuration  $M_T$  being the sum of the masses per unit area of the unstiffened panel and the uniformly distributed stringers, then the circular frequency of the integrally stiffened panel in purely flexural modes is simply

$$\omega = \left( \frac{K_T}{M_T} \right)^{1/2} = \left( \frac{1}{M_T} \right)^{1/2} \left[ (D_x)^{1/2} k_m^2 + (D_y)^{1/2} k_n^2 \right] \quad (2-86)$$

and the natural frequency is given by

$$f = \frac{\omega}{2\pi} \quad \text{Hertz}$$

Corrugated Panel. The computation of the natural frequency of the corrugated panel (Figure 2-31) is similar to that of the integrally stiffened panel. It is assumed that

- Flexural properties are uniform but not necessarily equal along the x and y axes.
- The flexural rigidities along the x and y axes are given respectively by  $D_x$  and  $D_y$ .

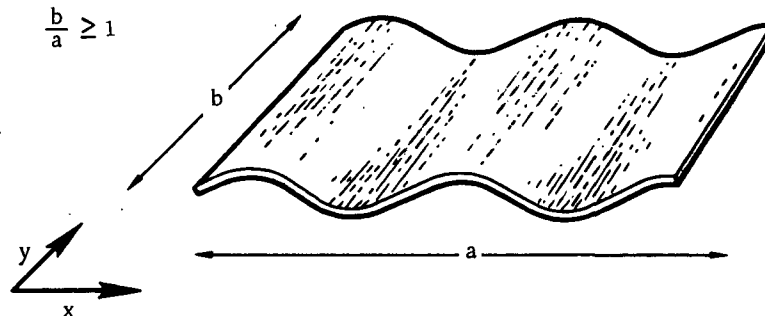


Figure 2-31. Corrugated Panel Geometry

- The panel is vibrating in its fundamental mode such that the wave numbers are given respectively by  $k_m = \pi/a$  and  $k_n = \pi/b$ .
- The cross-rigidity is given by  $D_{xy} = (D_x D_y)^{1/2}$

Then the flexural stiffness is given by

$$K_T = \left[ (D_x)^{1/2} \left( \frac{\pi}{a} \right)^2 + (D_y)^{1/2} \left( \frac{\pi}{b} \right)^2 \right]^2 \quad (2-87)$$

where  $D_y = EI_x/a$  and  $D_x = EI_y/b$  are the flexural stiffnesses per unit panel width. For a mass per unit area  $M_T$  given approximately by

$$M_T = \frac{\rho h}{g_o}$$

the circular frequency of the panel is then

$$\omega = \left( \frac{K_T}{M_T} \right)^{1/2} = \pi^2 \left( \frac{E}{M_T} \right)^{1/2} \left[ \frac{1}{b^2} \left( \frac{I_x}{a} \right)^{1/2} + \frac{1}{a^2} \left( \frac{I_y}{b} \right)^{1/2} \right] \quad (2-88)$$

and the natural frequency is

$$f = \frac{\omega}{2\pi} \quad \text{Hertz}$$

**2.5.3.3 Calculation of Noise.** The following paragraphs describe the computation of noise produced by four different sources: the turbulent boundary layer, the boost rocket engines, and the flyback (jet) engines (including noise on the vehicle and scrubbing of the jet exhaust on the panel or location of interest).

**Turbulent Boundary Layer.** The theory developed for these computations relates to the attached turbulent boundary layer of a large aircraft structure. It is based on wind tunnel and aircraft data (Reference 32) and has been modified to fit analytical expressions (Reference 33).

The overall intensity is given by

$$\frac{\bar{p}}{q} = \frac{0.012}{1 + 0.14 M^2}$$

where  $\bar{p}$  and  $q$  are the overall and dynamic pressures respectively in psf, and  $M$  is the local Mach number.

The sound pressure level is given by

$$FPL_f = 20 \log_{10} \left( \frac{p(f)}{41.8 \times 10^{-8}} \right) \text{ db} \quad (2-89)$$

where

$$p(f) = q \left\{ \left( \frac{0.012}{1 + 0.14 M^2} \right) \frac{1}{f_o \left( 1 + \frac{f^2}{f_o^2} \right)^{3/2}} \right\}^{1/2} \quad (2-90)$$

The parameter  $f$  is the fundamental frequency of the panel, whereas the characteristic frequency of the boundary layer  $f_o$  is given by

$$f_o = \frac{\left( \frac{u}{x} \right)}{\left( \frac{\delta}{x} \right)}$$

with  $u$  being the local velocity in feet per second,  $x$  the local run length in feet, and the ratio of boundary layer thickness to local run length being given in terms of Reynolds number as

$$\frac{\delta}{x} = 0.37 \text{ Rey}^{-1/5} \left\{ 1 + \left( \frac{\text{Rey}}{2.9 \times 10^7} \right)^2 \right\}^{0.1}$$

Rocket Noise on Vehicle at Lift-off. The sound pressure level measured in db in octave bands over the surface of a rocket-powered vehicle on the launch pad is given by

$$\text{OBSPL} = 10 \log_{10} (0.676 mV^2) + SPL_o - 20 \log_{10} R - \Delta B' \quad (2-91)$$

where

- (1)  $0.676 mV^2 = 0.676 t^2 g_o/w$  is the mechanical stream power of the rocket exhaust in watts when  $t$  is the total thrust in pounds,  $w$  is the total weight flow in pounds per second,  $g_o$  is the gravitational constant in  $\text{ft/sec}^2$ , and  $V = tg_o/w$  is the gas velocity at the nozzle exit in  $\text{ft/sec}$ .
- (2)  $SPL_o$  is a reference octave band sound pressure level at a distance  $R$  of one foot.



- (3) R is the distance from the point of interest on the vehicle surface to the noise source location in the jet stream.
- (4)  $\Delta B'$  is a correction for ambient conditions to obtain levels actually existing at the vehicle surface.

Calculation of the mechanical stream power of the rocket exhaust is straight-forward and simple. However, determination of the reference sound pressure level  $SPL_o$  is a more complicated matter. This is dependent on the geometry of the booster-orbiter configuration and characteristics of the rocket exhaust as represented in the Strouhal number  $fD/V$  where  $f$  is the fundamental frequency of the panel,  $V$  is the rocket exhaust velocity, and  $D$  is the nozzle diameter. The reference octave band sound pressure level is then given by

$$\left. \begin{aligned} SPL_o &= 70 + 16.6 \log \left( \frac{\left( \frac{fD}{V} \right)}{0.003} \right) && \text{for } \frac{fD}{V} \leq 0.016 \\ \\ SPL_o &= 82 && \text{for } 0.016 < \frac{fD}{V} < 0.152 \\ \\ SPL_o &= 70 - 16.6 \log \left( \frac{\left( \frac{fD}{V} \right)}{0.8} \right) && \text{for } 0.152 \leq \frac{fD}{V} \end{aligned} \right\} \quad (2-92)$$

The term involving  $R$ , the average distance from the point of interest on the TPS panel to the noise source in the rocket exhaust stream, is best explained by referring to Figure 2-32. The average distance from the noise source of frequency  $f$  to the rocket nozzle exit plane is the distance  $X_o$ . Again, in terms of the Strouhal number  $fD/V$ , this is given by the expressions:

$$\log_{10} \left( \frac{X_o}{D} \right) = - \left[ 0.222 + 1.315 \log_{10} \left( \frac{fD}{V} \right) \right]$$

for  $\frac{fD}{V} > 0.175$

and

$$\log_{10} \left( \frac{X_o}{D} \right) = 0.625 - 0.202 \log_{10} \left( \frac{fD}{V} \right)$$

for  $\frac{fD}{V} \leq 0.175$



Table 2-3. Bandwidth Frequencies

f (Hz)	BW (Hz)
2	1.37
4	2.75
8	5.5
16	11.0
31.5	22.5
63	45
125	90
250	180
500	355
1000	700
2000	1400
4000	2800
8000	5600

data (References 35 and 36). Values of the near-field sound pressure levels obtained by this procedure will generally apply at a distance aft of the jet nozzle corresponding to termination of the jet core (i.e.,  $X/D \cong 5$ ) (Figure 2-33). Values will be typical ( $\pm 5$  db)

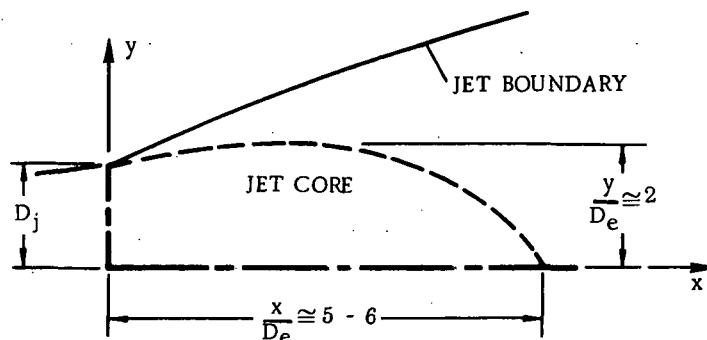


Figure 2-33. Schematic of Jet Flow Field

to about twice the distance of the jet core termination (i.e.,  $X/D \cong 10$ ). At distances greater than  $X/D \cong 10$ , and at side distances of  $y \cong 2$ , the jet boundary will wipe the airframe and pressures in this region will be controlled by the actual jet pressure at the particular location of interest. These calculations will be outlined in the following section entitled "Flyback (Jet) Exhaust Scrubbing." The procedure outlined herein is valid for jet velocities between 1000 and 2500 feet per second.

The overall sound pressure level at a distance of  $y = 200$  feet and at an angle of maximum radiation is given by the expression

$$\text{OASPL}_{200} = 10 \log_{10} (f(V_R)) + 10 \log_{10} (\rho_e^2 A_e) \quad (2-94)$$

where

$V_R$  = relative jet velocity (i.e., jet velocity minus aircraft forward velocity) ft/sec

$A_e$  = nozzle exit area in  $\text{ft}^2$

$\rho = \frac{w}{A_e V_j}$  = engine exhaust density where  $w$  is the engine weight flow in lb/sec,  $A_e$  is the nozzle exit area in  $\text{ft}^2$ , and  $V_j$  is the jet velocity in ft/sec.

The function  $10 \log f(V_R)$  is given by

$$10 \log_{10} f(V_e) = 145 + 100 \log_{10} \left( \frac{V_R}{1600} \right)$$

which has been normalized for unit density and unit exit area.

The overall sound pressure level in the near field must now be computed by correcting the far-field value (i.e.,  $y = 200$  ft). This is done in terms of the dimensionless parameter  $y/D$  where  $D$  is the nozzle exit plane diameter. The correction takes the form

$$\Delta \text{ db} = B \log_{10} \left( \frac{\frac{y'_2}{D}}{\frac{y'_1}{D}} \right)$$

where

$$B = 20 \text{ db/decade for } 30.0 \leq y/D$$

$$B = 16 \text{ db/decade for } 2.5 \leq y/D < 30.5$$

$$B = 14 \text{ db/decade for } 1.0 \leq y/D < 2.5$$

The terms  $y'_1$  and  $y'_2$  are dummy parameters to cover the distance from  $y_2 = 200$  feet to the point of interest; i.e.,  $y$ .

A sample calculation of this correction is given below for the case of the radial distance from the engine centerline to the point of interest of 6 feet (i.e.,  $y_1 = 6$  ft) and a jet engine nozzle exit plane diameter of 4 feet (i.e.,  $D = 4$  ft). Thus, the total correction is given by

$$\Delta \text{ db} = 20 \log_{10} \left( \frac{\frac{200}{4}}{\frac{30}{4}} \right) + 16 \log_{10} \frac{30}{2.5} + 14 \log_{10} \left( \frac{2.5}{\frac{6}{4}} \right)$$

An additional correction of 6 db is made to account for the sound pressure level actually experienced by the structure. Hence, the near-field overall sound pressure level is given by

$$\text{OASPL}_{\text{nf}} = \text{OASPL}_{200} + \Delta \text{ db} + 6 \text{ db}$$

Finally, for the case of the jet flyback engine, the octave band sound pressure level is computed by correcting the overall sound pressure level for the bandwidth of the center

frequency. The octave band sound pressure level (OBSPL) will have a maximum value when the Strouhal number is 0.8, i.e., a characteristic frequency is given by the expression  $f'D/V = 0.8$  where D and V are nozzle plane diameter and velocity. Next the center frequency of the bandwidth in which this characteristic frequency  $f'$  falls is computed from Table 2-3, and the level of the maximum octave band sound pressure level is calculated as

$$\text{OBSPL}_{\text{max}} = \text{OASPL}_{\text{nf}} - 5 \text{ db}$$

Below this maximum value, the OBSPLs decrease at the rate of 4 db/octave, and above it at 3.5 db/octave. This decrease from the maximum is computed by determining how many octaves the fundamental panel frequency is above or below the center frequency of the octave band in which  $f'$  falls.

Next, the spectrum pressure level  $\text{SPL}_f$  is computed as

$$\text{SPL}_f = \text{OBSPL} - 10 \log_{10} (\text{BW})$$

where the bandwidth BW is given in Table 2-3 for the band in which the panel fundamental mode, f, falls. Finally, the spectrum pressure is computed as

$$p(f) = 10^{(\text{SPL}_f - 2.09 \times 10^{-8})} \text{ psf (rms)}$$

Flyback (Jet) Engine Exhaust Scrubbing. For the case in which the jet exhaust stream actually impinges on the panel of interest (i.e., the panel falls within a seven-degree half angle), the component of actual jet pressure is computed as follows. First, the normal pressure in the exit plane is given by

$$P_e = \frac{T}{A_e} = \frac{1.275 T}{D_e^2}$$

where T is engine thrust in pounds and  $D_e$  is the exhaust nozzle exit diameter. The grazing jet pressure  $\bar{P}_x$  is given by

$$\bar{P}_x = \frac{0.155 T}{D_x^2}$$

where  $D_x$  is the jet diameter at a station x feet from the exhaust plane, i.e.,

$$D_x = D_e \left( 1 + 0.244 \frac{x}{D_e} \right)$$

The overall sound pressure level can now be computed from the grazing pressure as

$$\text{OASPL}_x = 20 \log_{10} \left( \frac{\bar{p}_x}{2.09 \times 10^{-8}} \right) \text{ db}$$

Next, as was the case for noise due to the jet engine alone, the maximum octave band sound pressure level is computed at the characteristic frequency  $f'$  which occurs for the value of the Strouhal number,

$$\frac{f' D_e}{V_j} \cong 0.4$$

Using the center frequency for the octave band in which  $f'$  falls (Table 2-3), the maximum octave band sound pressure level is computed

$$\text{OBSPL}_{\max} = \text{OASPL}_x - 5 \text{ db}$$

and the deviation from this maximum (either 4 db/octave below or 3.5 db/octave above) is computed by comparing the panel's fundamental frequency to the center frequency computed above. Finally, the spectrum pressure level and the spectrum pressure are computed respectively from

$$\text{SPL}_f = \text{OBSPL} - 10 \log_{10} (\text{BW}) \text{ db}$$

and

$$p(f) = 10^{(2.09 \times 10^{-8} \text{ SPL}_f)} \text{ psf (rms)}$$

where the bandwidth BW (given by Table 2-3) psf (rms) corresponds to the panel's fundamental frequency.

**2.5.3.4 Calculation of Dynamic Stresses in a Resonating Panel.** The fundamental frequencies for each of the panel configurations of this study have been calculated as outlined in the previous sections, and all noise sources have been investigated to determine sound pressure levels and rms acoustic pressures for each source. Next, the dynamic stresses for each type of panel are to be calculated for each noise source. It is assumed that the acoustic pressures will be phase correlated over the entire surface of the plate.

**Rectangular Isotropic Panel.** For the case in which the panel is symmetrical and the supporting structure is rigid, the deflections and stresses are calculated for a clamped

panel. The maximum bending stresses occur at the center, and the stress and deflection are given respectively by

$$S_{\max} = \frac{0.5 \bar{P} a^2}{h^2} \text{ lb/in}^2 \text{ rms}$$

$$Y_{\max} = \frac{0.0284 \bar{P} a^4}{E h^3} \text{ in. rms}$$

where  $\bar{p}$  is the rms acoustic pressure in psi

$$\bar{p} = p(f) \sqrt{BW}$$

The acoustic pressures  $p(f)$  have already been computed as shown in previous sections, and the bandwidth  $BW$  is given by

$$BW = 2 \left( \frac{c}{c_c} \right) f$$

where  $f$  is the panel fundamental frequency and the term  $(c_c/c)$  is the critical damping coefficient. However, the stress  $S_{\max}$  is an equivalent static stress, and since the plate is resonating, it must be multiplied by the dynamic magnification factor,

$$Q = \frac{1}{2 \left( \frac{c}{c_c} \right)}$$

For mechanically fastened plate (i.e., rivets, screws, etc.), a typical value is  $c/c_c \cong 0.02$  and  $Q = 25$ . The dynamic stress is then given by,

$$S_d = 25 S_{\max}$$

A local stress raiser of four is next included at the fastener (Reference 37). Thus the local dynamic stress is given by the equation

$$S_{ld} = 100 S_{\max} \text{ lb/in}^2 \text{ rms}$$

The stresses are considered to be distributed according to an integrated Rayleigh distribution with a maximum peak to rms ratio of four based on experience. Thus, the maximum peak stress will be given by

$$S_{P_{\max}} = 400 S_{\max}$$

For the case in which the rectangular isotropic panel is unsymmetrical and/or has a flexible supporting structure, it is assumed that alternate frames will twist such that the panel wave length is  $2a$  instead of just  $a$  (the case for the symmetrical panel and/or rigid supporting structure).

The length of the panel that will now have phase correlated pressures is  $1.25a$ , and this will be treated as a clamped panel. Thus, the maximum stress and deflection are given by

$$S_{\max} = \frac{0.5 \bar{p} (1.25a)^2}{h^2}$$

$$Y_{\max} = \frac{0.0284 \bar{p} (1.25a)^4}{E h^3}$$

The dynamic stress  $S_d$ , the local dynamic stress  $S_{ld}$ , and the maximum peak stress  $S_{p\max}$  are all computed from the maximum static stress  $S_{\max}$  just as outlined in the previous paragraphs for the symmetrical panel (Reference 30).

Stresses in a Resonating Honeycomb Sandwich Panel. As in the case for the rectangular isotropic panel, it is assumed that the acoustic pressures will be phase correlated over the entire surface of the panel. For the simply-supported panel, the maximum bending stresses and deflection occur at the panel center. Hence,

$$S_{\max} = \frac{0.75 \bar{p} a^2}{h_{\text{eff}}^2} \text{ psi (rms)}$$

$$Y_{\max} = \frac{0.01421 \bar{p} a^4}{E h_{\text{eff}}^3} \text{ in. (rms)}$$

where the effective thickness  $h_{\text{eff}}$  is given by

$$h_{\text{eff}} = 1.817 (h_c h_f h)^{1/3}$$

The dynamic stress  $S_d$ , the local dynamic stress  $S_{ld}$ , and the maximum peak stress  $S_{p\max}$  are computed as in the case of the rectangular isotropic panel.

Stresses in a Resonating Integrally Stiffened Panel. For a simply-supported panel for which the acoustic pressures are phase correlated over the surface of the panel, the maximum stress and deflection are



$$S_{\max} = \frac{0.75 \bar{p} a^2}{h_{\text{eff}}^2} \text{ psi (rms)}$$

$$Y_{\max} = \frac{0.0142 \bar{p} a^4}{E h_{\text{eff}}^3} \text{ in. (rms)}$$

where here the effective panel thickness is given by a somewhat more elaborate calculation than was necessary in the two previous cases. The task is to find an effective thickness of an isotropic panel whose stiffness equals that of an integrally stiffened one. For the isotropic panel, stiffness is given by

$$k_i = D_x (k_m^2 + k_n^2)^2$$

whereas, for the stiffened panel

$$k_s = \left[ (D_x)^{1/2} k_m^2 + (D_y)^{1/2} k_n^2 \right]^2$$

where

$$D_y = D_x + \frac{EI}{b}$$

The stiffness ratio is defined as

$$r_s = \frac{k_s}{k_i}$$

$D'$ , the flexural rigidity of the integrally stiffened panel, can be expressed as

$$D' = D_x r_s$$

where  $D_x$  is the flexural rigidity of the panel without stiffeners, then

$$D_x = \frac{E h^3}{12 (1 - \nu^2)} \quad D' = \frac{E h_{\text{eff}}^3}{12 (1 - \nu^2)} r_s$$

which combine to give

$$h_{\text{eff}} = \sqrt[3]{r_s} h$$

Stresses in a Resonating Corrugated Panel. Once again, for the simply-supported panel, the maximum stress and deflection are given by

$$S_{\max} = \frac{0.75 \bar{p} a^2}{h_{\text{eff}}^2}$$

$$Y_{\max} = \frac{0.0142 \bar{p} a^4}{E h_{\text{eff}}^3}$$

where, as in the case of the integrally stiffened panel, the effective thickness is determined by equating stiffnesses of a rectangular isotropic and a corrugated panel. The stiffnesses for the corrugated panel and the equivalent isotropic one are given respectively by

$$k_c = \left[ (D_x)^{1/2} k_m^2 + (D_y)^{1/2} k_n^2 \right]^2$$

and

$$k_i = D \left( k_m^2 + k_n^2 \right)$$

Equating these expressions (assuming equal stiffness) and solving for D such that

$$D = \frac{E h_{\text{eff}}^3}{12 (1 - \nu^2)}$$

gives, after suitable substitution for  $D_x$ ,  $D_y$ ,  $k_m$ , and  $k_n$ ,

$$h_{\text{eff}} = \left\{ 10.9 \left[ \frac{\left( \frac{I_x}{b} \right)^{1/2} \left( \frac{1}{a^2} \right) + \left( \frac{I_y}{a} \right)^{1/2} \left( \frac{1}{b^2} \right)}{\left( \frac{1}{a^2} + \frac{1}{b^2} \right)} \right]^2 \right\}^{1/3}$$

#### 2.5.3.5 Computation of Critical Stress Levels and Number of Stress Reversals.

In applying the Convaire Aerospace particle damage theory outlined in the opening paragraphs of this section, the next task is to determine the critical stress levels and number of stress reversals corresponding to each local dynamic stress on the panel of interest. It is assumed that the applied stresses obey a random Rayleigh distribution; that is, the distribution has the form

$$\left[ p > s_p \right] = e^{-\frac{1}{2} \left( \frac{s_p}{s_{ld}} \right)^2}$$

where  $[p > S_p]$  denotes the probability of exceeding the stress  $S_p$  and  $(S_p/S_{ld})$  is the ratio of peak stress to rms stress. Thus, the distribution of the number of times a stress reversal corresponding to a stress of a given magnitude will occur is given by

$$\frac{N}{N_{\text{Life}}} = 1 - \int_0^{\frac{S}{S_{ld}}} \frac{\left(\frac{S}{S_{ld}}\right)}{e^{1/2 \left(\frac{S}{S_{ld}}\right)^2}} d \left(\frac{S}{S_{ld}}\right) \quad (2-95)$$

The ratio of probable stress to the local dynamic stress as a function of the number of times this stress will occur over the lifetime number of stress reversals is given by the inverse of Equation 2-95. Such a curve is shown in dimensionless form in Figure 2-34.

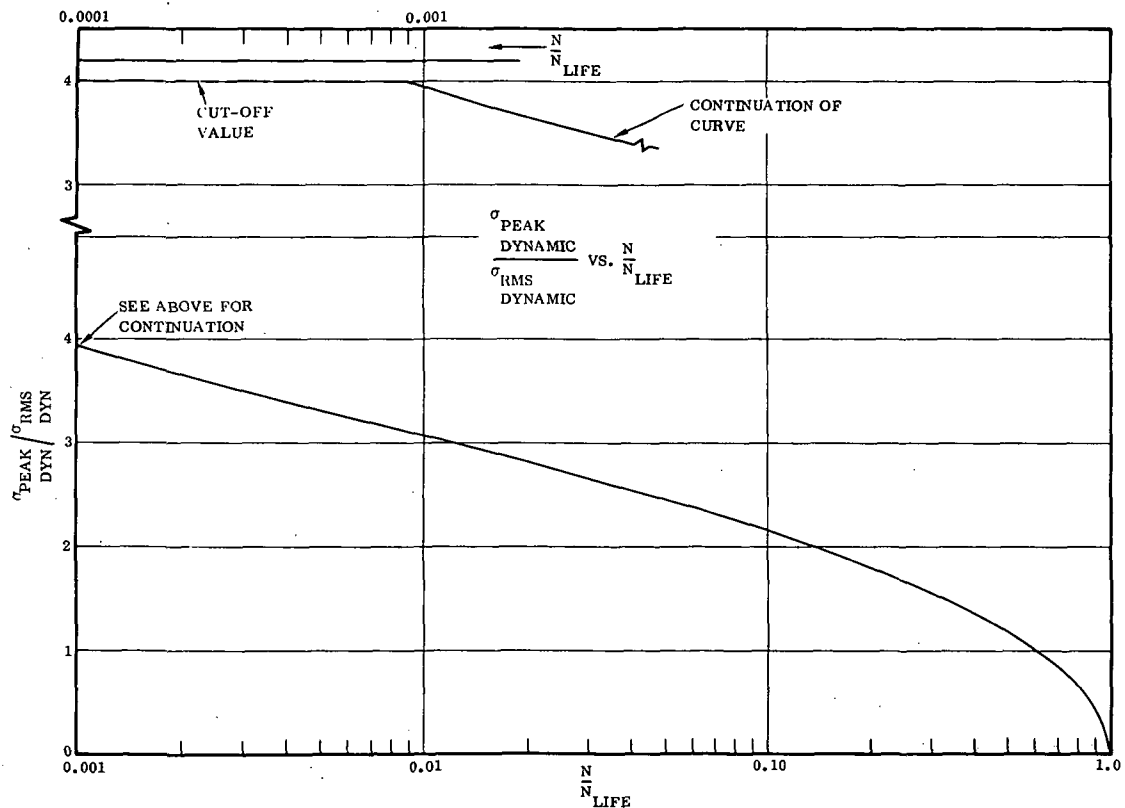


**Figure 2-34. Rayleigh Stress Distribution**

As a part of the present effort to predict the effects of acoustic fatigue, both the Rayleigh distribution and its inverse have been curve fitted for automatic computations which will be explained in later paragraphs.

The Rayleigh distribution for the applied random stress is given by the curve fits

$$\frac{S}{S_{ld}} = f_1 \left( \frac{N}{N_L} \right) \quad \text{and} \quad \frac{N}{N_L} = g_1 \left( \frac{S}{S_{ld}} \right)$$

where

$$\frac{S}{S_{ld}} = \frac{2}{\pi} \cos^{-1} \left[ 1 + \frac{\pi}{1.212} \left( 1 - \frac{N}{N_L} \right) \right] \quad \text{for} \quad 0.455 < \frac{N}{N_L} < 1.0$$

$$\frac{S}{S_{ld}} = \frac{-C_2 - \sqrt{C_2^2 - 4C_3 \left[ C_1 - \log_{10} \left( \frac{N}{N_L} \right) \right]}}{2C_3} \quad \text{for} \quad \frac{N}{N_L} < 0.455$$

and the inverses are

$$\frac{N}{N_L} = 1 - \frac{1.212}{\pi} \left[ 1 - \cos \left( \frac{\pi}{2} \frac{S}{S_{ld}} \right) \right] \quad \text{for} \quad 0 < \frac{S}{S_{ld}} < 1.25$$

$$\frac{N}{N_L} = \exp \left[ C_1 + C_2 \left( \frac{S}{S_{ld}} \right) + C_3 \left( \frac{S}{S_{ld}} \right)^2 \right] \quad \text{for} \quad \frac{S}{S_{ld}} > 1.25$$

where

$$C_1 = 2.631102 \times 10^{-2} \quad C_2 = -2.635 \times 10^{-2} \quad C_3 = -4.939331 \times 10^{-1}$$

Since the stresses are distributed as described, the purpose of the next calculations is to determine the stress which is contributing the greatest partial damage to the TPS panel (Figure 2-35). This clearly occurs at that critical stress ( $S_{cr}$ ) on the Rayleigh distribution which is closest to the allowable S-N curve (i.e., the locus of actual material failures). This is found mathematically to be the point at which the applied S-N curve (the Rayleigh stress distribution) is tangent to the allowable S-N curve (established by experiment). A critical stress is found in this manner for each of the local dynamic stresses (corresponding to each noise source), and a composite critical stress is next determined as

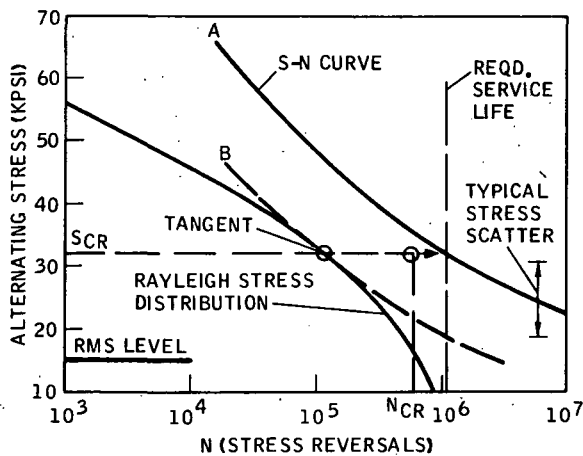


Figure 2-35. Equivalent Fatigue Damage Diagram for Random Loading

$$\bar{S} = \left\{ \sum_{j=1}^n S_{crj} \right\}^{1/2}$$

where  $n$  is the total number of local dynamic stresses being considered for the particular case at hand. Finally, the equivalent number of stress reversals for the sinusoidally applied effective stress ( $N_{cr}$ ) is determined by equating the work applied by the critical stress  $\bar{S}$  to the work done by the random stresses (i.e., the area under the stress envelope). Hence,

$$\bar{N} = \frac{1.261}{\bar{S}} \sum_{j=1}^n \left\{ N_{Lj} S_{ldj} \right\}$$

where the constant 1.261 has been evaluated by numerically integrating the Rayleigh stress curve.

The point  $(\bar{S}, \bar{N})$  is compared to the allowable S-N curve. If the point falls above the allowable S-N curve, then failure has occurred - the number of stress reversals at the composite critical stress level  $\bar{S}$  has exceeded those at which the material failed during testing. If the point falls below the allowable S-N curve, failure due to sonic fatigue is predicted not to occur.

## 2.6 TPS SECTION REDESIGN

The TPS redesign is performed on two separate components of the system - the metallic re-radiative panel and the underlying insulation. The thickness of the metallic cover panel is varied to provide just enough strength to transfer the mechanical loads of air pressure to the supporting structure and balance the thermal stresses of the panel itself. The thickness of the underlying insulation is varied to allow enough resistance to heat transfer to maintain a specified allowable temperature in the underlying structure. Only the thicknesses of the cover panel and the insulation are variable; all other dimensions and properties are constant.

**2.6.1 STRESS REDESIGN OF THE PANEL.** A particular configuration is input to the computer program by specifying the configuration number (e.g., circular corrugation with skin, flat corrugation with skin, rib-stiffened panel, skin stringer, open corrugation, or circular corrugation) and other geometric quantities such as panel length, width, number and depth corrugations, radius of corrugations, and the like.

Throughout the trajectory, indices measuring the margins of safety for various modes of panel failure, as described in Section 2.3, are stored for evaluation at the end of the trajectory. At that time, the redesign procedure of the stress analysis is activated by the program. The margins are scanned and the one with the largest negative value identified. This, then, becomes the design point. The thickness of the panel is increased by ten thousandths (0.010) inch, and the stress analysis using the loads and temperatures stored for each node of the stress model for that time in the trajectory is performed again. It has been ascertained during program development that temperature gradients (the physical parameters which govern structural design of the panel) do not change significantly (many times not at all) with panel thickness. The margin or design factor from the new stress analysis is then investigated to see if the increased thickness is sufficient to handle the load. If so, the design is complete and program control passes to the weights/cost analysis. If not, a new panel thickness is chosen by extrapolation of a Newton-Raphson-type iteration. After each stress analysis, the margins are rechecked until the design point shows a positive margin of safety. A design is considered optimum when the minimum design factor is between 0 and 10 percent. Results should be checked carefully since the panel thickness is not decreased during the redesign procedure; an over-design panel may result which can be eliminated by a subsequent computer run.

**2.6.2 THERMODYNAMIC REDESIGN OF PANEL.** Heat transfer to the underlying structure can be reduced in two ways for a given panel configuration: the metallic panel thickness may be increased or the insulation thickness may be increased, both cases thereby increasing the heat capacity of the respective material. Of the two techniques, the latter is the more efficient in terms of system weight. For this reason, only the insulation thickness can be varied to affect the temperature of the structure.

The computational procedure is as follows: For each material of the TPS, an associated allowable maximum temperature is input. For example, an aluminum node will not be allowed to get above 300°F. One particular material is identified as being the insulation. At each new temperature calculation, material temperatures are compared to allowables. If one is exceeded, the insulation thickness is increased, the program is returned to the starting point of the trajectory, and calculations are resumed. When the temperature allowables no longer exceed the actuals, the design is considered finished as far as thermodynamic considerations are concerned. At the present time, the insulation variation is performed by doubling the insulation thickness, but this technique is currently under refinement. A typical sketch of the thermodynamic re-sizing procedure is shown in Figure 2-36.

When an actual temperature exceeds the maximum allowable, the insulation thickness is doubled, the program returns to the starting point of the calculations, and the computations are begun anew. The insulation thickness is continually doubled until either the actual temperature of the critical material is less than the maximum allowable, or

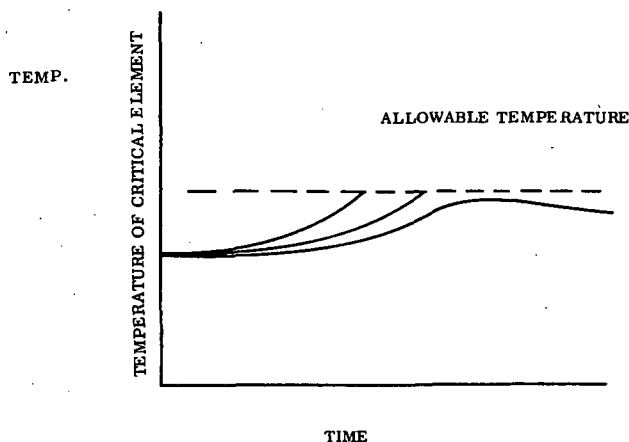


Figure 2-36. Thermodynamic Resizing Procedure

until the insulation thickness reaches one foot. For the latter case, the run is terminated. Here, the program user should again be critical of the printed results. This first generation computer program does not decrease the insulation thickness once a value is found which satisfies the temperature constraints. Hence, the insulation thickness may be over design, and only perusal of the resulting temperature distribution will determine this fact. A subsequent computer run with a different initial insulation thickness may be necessary. Messages describing all changes in insulation thicknesses and/or termination of the case (along with appropriate temperatures) are printed out.

## 2.7 WEIGHTS/COST ANALYSIS

**2.7.1 PARTS LISTING.** The parts listing procedure requires that a library be maintained to call out an associated list of detailed parts when a given panel or structure configuration is specified. Each part has associated with it a list of manufacturing processes and amounts of material required to produce the part. In this way, a method of deriving the manufacturing costs and material costs of the complete TPS system has been developed with its basis at the detail parts level. The parts listing process occurs as a function of the panel concept (specified by KINDP = 1, 2, 3 as shown in Figure 2-37). A detail parts listing for the specified configuration is included in the manufacturing cost summary, Figure 2-38.

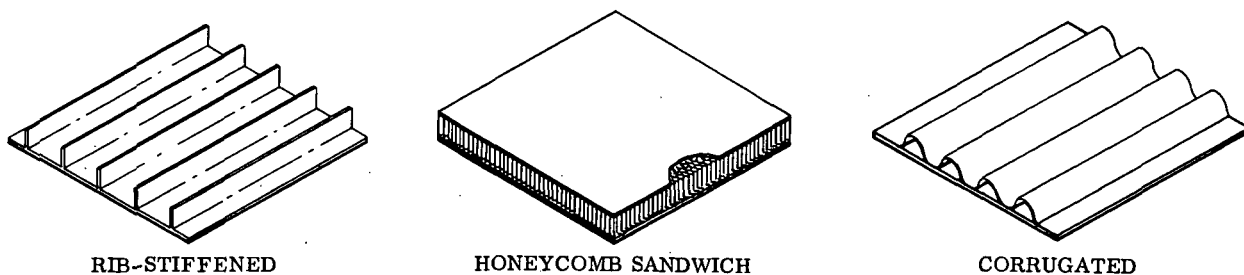


Figure 2-37. Panel Concepts

THEMAL PROTECTION SYSTEM, SPACE SHUTTLE STA XXXX

CONFIGURATION PANEL TYPE 1, CORRUGATED STRUCTURE TYPE A														
NOMINAL PANEL SIZE 3.0 X 2.0 FT NOMINAL STANDOFF LENGTH .5 IN														
DESCRPT	CT	THEORETICAL WEIGHT	ACTUAL WEIGHT	MATL WEIGHT	STD HOURS	LABOR HOURS	LABOR RATE	OV-HR RATE	MATL \$ PER LB	LABOR COST	OVERHD COST	FACTORY COST	MATERIAL COST	FABRICAT COST
PANEL CORRUGMS	1	0.000	14.772	17.719	0.0000	0.00	0.00	0.00	0.00	0.00	0.00	0.00	0.00	0.00
	1	0.000	14.772	17.714	9.8908	24.73	4.75	8.31	14.50	117.45	205.54	323.00	271.38	594.37
STRUCTURE	1	0.000	1.140	1.701	0.0000	0.00	0.00	0.00	0.00	0.00	0.00	0.00	0.00	0.00
PEAK LN A	1	0.000	.346	.425	.3381	.05	4.75	8.31	14.00	4.01	7.03	11.04	6.55	17.59
PEAK SW A	1	0.000	.217	.280	.2103	.53	4.75	8.31	14.00	2.50	4.37	6.87	4.32	11.19
CORNERS	1	0.000	.058	.088	.0622	.16	4.75	8.31	17.50	.75	1.30	2.05	1.30	3.35
POST PCRM	2	0.000	.067	.102	.3111	.59	4.75	8.31	12.00	7.78	4.87	7.65	5.05	12.70
SEAL	1	0.000	.073	.112	.0505	.13	4.75	8.31	14.50	.69	1.05	1.65	1.79	3.44
FASTENERS	40	0.000	.775	.412	0.0000	0.00	0.00	0.00	172.71	0.00	0.00	0.00	60.22	60.22
TOTAL THEORETICAL WEIGHT				0.01 LB										
TOTAL ACTUAL WEIGHT				15.41 LB										
TOTAL MATERIAL WEIGHT				17.72 LB										
TOTAL STANDARD HOURS				10.86 HR										
TOTAL LABOR HOURS				26.67 HR										
TOTAL LABOR COST				122.05 \$										
TOTAL OVER COST				224.16 \$										
TOTAL FACTORY COST				352.25 \$										
TOTAL MATERIAL COST				352.61 \$										
TOTAL FABRICATION COST				700.86 \$										
TOTAL ASSEMBLY COST				21.05 \$										
TOTAL MANUFACTURING COST				722.91 \$										
TFS COST				120.65 \$/SQ FT										
TFS WEIGHT				2.67 LB/SQ FT										
AVERAGE MATERIAL				14.73 \$/LB										
AVERAGE LABOR RATE				4.75 \$/HR										
AVERAGE OVERHEAD RATE				8.31 \$/HR										
AVERAGE FACTORY RATE				12.06 \$/HR										
AVERAGE MFG. RATE				26.06 \$/HR										
AVERAGE MFG. RATE				65.60 \$/LB										
AVERAGE REALIZATION FACTOR				.40										
ASSEMBLY REALIZATION FACTOR				.40										
COMPONENT ACK-CRYTHUM				0.00										
					SUB-ASSEMBLY COST									
					TASK	STD HOURS	TOTAL HOURS	LABOR RATE	OV-HR RATE	LABOR COST	OVERHD COST	ASSEMBLY COST		
					LOCATE	.0456	.11	5.20	1.75	.59	1.04	1.63		
					CLAMP	.2800	.70	5.20	1.75	3.64	6.37	10.01		
					DRILL	.3412	.10	5.20	1.75	.54	.95	1.49		
					SECURE	.0570	.14	5.20	1.75	.74	1.30	2.04		
					INSPECT	.0304	.08	5.20	1.75	.40	.69	1.09		
					DISASSY	.0960	.24	5.20	1.75	1.25	2.18	3.43		
					CLAMP	.0780	.09	5.20	1.75	.49	.86	1.36		

Figure 2-38. Manufacturing Cost Summary

**2.7.2 WEIGHTS.** Actual and purchase weights are computed for each detail specified in the parts listing process; the results are listed in the output under the headings ACTUAL WEIGHT and MATL WEIGHT. Actual weight is just what the name implies. It is computed based on the actual geometry of the finished detail part, taking into consideration all the necessary manufacturing and design requirements that normally go into producing a real part. Purchase weight is the weight of the raw material that must be purchased to produce each detail part. It is always larger than the actual weight. Calculation of the actual and purchase weights for a TPS detail part of the thermal protection system uses an equation of the form demonstrated below.

$$\text{Actual weight} = \text{density} * \text{length} * \text{width} * \text{thickness}$$

$$\text{Purchase weight} = \text{density} * (\text{length} + C_1) * (\text{width} + C_2) * (\text{thickness} + C_3)$$

where  $C_1$ ,  $C_2$ , and  $C_3$  are incremental distances added to the part geometry to account for the material removed during the cutting to size manufacturing operations. The actual equations can be found in the subroutine WTPPS in the program listing.

**2.7.3 MANUFACTURING PROCESSES.** To predict the manufacturing processes required for each detail part, a library of shop orders and shop planning records was established. These processes, along with the San Diego operation standard hour data,



were studied and used to identify basic standard shop operations and to correlate each detail part in the parts list with a set of these standard shop operations. At present, this information is stored in the subroutine BLOCK DATA in tables. The data are used to compute the standard hours necessary for each shop process required in the production sequence of each detail part. Standard hours and their actual method of computation are explained in later sections of this report. Seven standard shop operations were identified for this study:

<u>Manufacturing Operation Index</u>	<u>Manufacturing Operation</u>
1	Cutoff
2	Milling
3	Forming
4	Drilling, Routing, Deburring
5	Surface Treatments
6	Heat Treatments
7	Painting, Identification

Cutoff includes issue of the stock material to the shop and all cutting or sawing operations required during production. Milling includes milling, boring, and turning operations; forming includes all forming, stretch forming, and bending operations. Drilling, routing, and deburring operations are considered as a related group. Surface treatments include chemical milling, etching, anodizing, and peening. Heat treatments, painting, and part identification are also considered. An example of a callout for the manufacturing operations required to produce a corner post is:

Corner Post (Titanium) Manufacturing Operations

KR and KS = 1 . 2 . 4 . 6 . 7

Thus, the operations include cutoff, milling, drilling, heat treating, and identification.

The set of operation indexes KR and KS are then used by the program along with a material form index KK to call out values from the arrays KSETUP (KK, KS) and KRUN (KK, KR) located in the K-TABLES with BLOCK DATA. These values (in hours per pound actual weight) are then used to estimate a setup time and a run time required to manufacture each detail part. It is assumed that one basic machine setup is required per detail part, and that the setup for each additional like part is included with the run time. The equations take the following form:

Setup Time (SETUP): ACWT \* KSETUP (KK, KS)

Run Time (RUNTM): ACWT \* KRUNTIM (KK, KR)

where ACWT is the actual weight of the detail part. The setup and run times calculated are in standard hours as discussed in the following section.

To predict the operations required to assemble the detail parts into the basic subcomponents and then to develop a complete final assembly, a library of shop assembly planning records was established. Basic processes were identified and correlated with each subassembly and with the final assembly. This information is stored BLOCK DATA as constants which are called out for use with equations to compute the standard hours for subassembly and final assembly.

Seven standard assembly operations were identified for this study. They are given in the table below along with their appropriate assembly operation.

<u>Assembly Operation Index</u>	<u>Assembly Operation</u>
1	Setup
2	Clamping
3	Drilling
4	Securing
5	Inspection
6	Disassembly
7	Cleaning

Setup includes the mounting of parts to assembly fixtures, and clamping involves the clamping together of the parts to be assembled. Drilling considers the location, center punching, and the drilling of all required holes. Securing consists of the actual attachment of required fasteners, and inspection is self explanatory. Cleaning involves the final cleaning of the finished assembly and any cleanup required during the assembly process, such as deburring of the holes after drilling. In some cases after drilling, it is necessary to disassemble the assembled parts for inspection and cleanup purposes. The disassembly process is essentially the reverse of the setup and clamping processes, and includes reassembly before the final securing is done. The program calculates a value in hours for each required subassembly and for the final assembly of the finished part. Currently, these calculations are based on constants stored with the BLOCK DATA. The actual equations take the following form.

Setup Time:	HOLES * TIME6
Clamping Time:	CLAMP * TIME1
Drilling Time:	HOLES * VALUE

Securing Time:	HOLES * VALUE
Inspection Time:	HOLES * TIME2
Disassembly Time:	CLAMP * TIME5
Cleaning Time:	HOLES * TIME3

Where: HOLES equals the number of fasteners (fastener holes)

CLAMP equals the number of clamps

VALUE equals the volume of material removed from all the holes  
x a material complexity factor based on the material type  
x TIME7

The material complexity factor is assumed to be 3.0 for titanium. The constants TIMEX where X = 1 through 7 are stored in the BLOCK DATA as:

TIME1	=	0.035 hour/clamp
TIME2	=	0.0008 hour/hole
TIME3	=	0.01 hour/hole
TIME4	=	0.0015 hour/hole
TIME5	=	0.012 hour/clamp
TIME6	=	0.0012 hour/hole
TIME7	=	0.52 hour/cubic inch

Provision has been built into the program so that the constants TIMEX can be replaced with equations. Values replacing the constants will be computed using these equations, which will be based on data collected and curve fit during the course of further study. An example of the type of data available is shown in Figure 2-39 where the hours required for drilling in titanium are shown as a function of the volume of material removed.

**2.7.4 STANDARD HOURS.** For each detail called out in the parts listing process, there is a corresponding list of required manufacturing operations in the cost subroutine. For each manufacturing operation a calculation of required standard hours is made. Standard hours are defined as a standard time, measured in hours, representing an optimum required to perform a task. Standard hours for each production process are established by the industrial engineering department by analysis of time and motion studies of typical tasks. They are used as a means of measuring performance by determination of realization factors (or efficiencies) when compared with actual labor hours acquired through labor accounting processes.

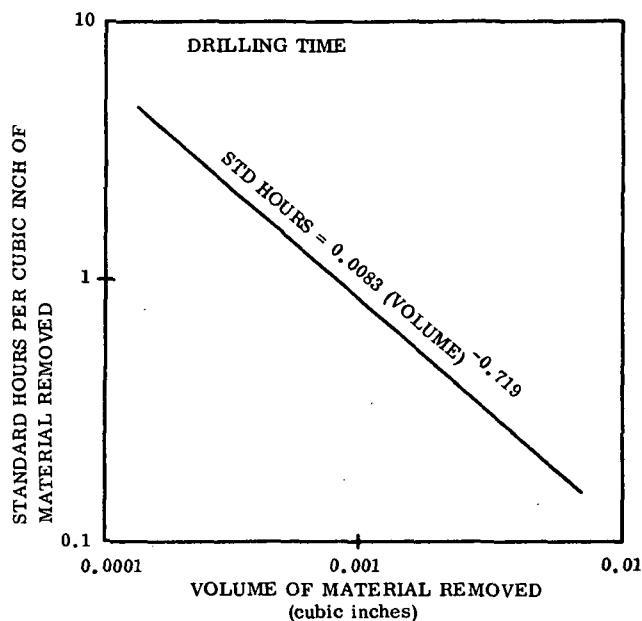


Figure 2-39. Drilling Time in Titanium

required for each of the production processes, and then to estimate the actual labor costs. Figure 2-40 presents an example of a (San Diego operation) shop planning order. Listed are the various manufacturing processes required to produce a brace and the corresponding number of standard hours required for setup and running each shop process. The object of the standard-hour calculation technique in the program is, in effect, to be able to predict the planning order.

Calculation of the standard hours for each of the manufacturing processes is performed in two parts: setup time and actual run time. Setup time is derived based on the size of the part, the complexity of the required setup, and the type of machine to be used. Run time is dependent on the machine operation rate, amount of material to be removed, depth of cut, and the surface area to be covered. The manufacturing standard hour equation is:

$$\text{STDHR} = \text{SETUP} + \text{RUNTM} * \text{KT} * \text{SHIPSET}$$

where

SETUP is the setup time in standard hours

RUNTM is the run time in standard hours

KT is the number of parts required of a given detail to produce a complete component

SHIPSET is the number of shipsets of that component produced

Within the program, standard hours are calculated for two separate cost areas: factory production and final assembly. Factory production includes the manufacturing and assembly of detailed parts into the basic subcomponents such as posts and beams. Final assembly involves the final assembly of the subcomponents into a finished TPS system. A listing of standard hours is output as part of the cost data under the heading STD HOURS (see Figure 2-38).

Standard-hour data have been collected for each of the seven manufacturing processes and assembly operations discussed; they have been adapted for use with this program. Standard-hour values are used to estimate the actual labor hours re-

GENERAL DYNAMICS CONVAIR  
SHOP ORDER PLANNING

H-DAY AREA PART NUMBER  
471 2 4T11015-133A

LT-N  
A

PLANNER GRP CHG CD D/C P/L QCA-NO PT-CL LT-NO AREA PART NUMBER  
EHUGHES 11 B 592 2 A 2 4T11015-133A

TITLE MATERIAL PERCENT GRP NUMBER A/Z  
BRACE 4.000 12 120471 D

MATL DESCRIPTION GAU/DIA WID/WALL LENGTH SPECIFICATION COND PTS OP/HND  
NOTE A 40.000 QQ-A-200/12 NOTE 01

DATE STK RM QTY BY SPARE CUST SHOP INSP

-----OPERATIONS-----

INSP	STMP	DEPT	CC	OPER NO	OPER SCHD	OPERATION DESCRIPTION	TOOL	TOOL SEQ NO	MACH	SET	RUN
							SYMB		CODE	UP	TIME
				A		H/F LS39157-1 7079 T6511					
				B		DS30004					
	836	07	010			SAW TO LENGTH 4T11015-129A			5880	0.12	0.0031
							SP				
	836	07	020			SAW ANGLE CUTS SP			6880	0.19	0.0032
				025		INSPECT					
	045	00	030			ROUT .50R (1) END			0000		
				035		INSPECT					
	001	06	040			SAW 3.50R CNT (2) 129A SP 4T11012-109A			6881	0.19	0.0042
							SF				
	001	12	050			BURR			2905		0.0106
	001	12	060			IDENTIFY TAG			2910	0.07	0.0003
				065		RW					
				075		INSP					
	002	05	080			ALK. ETCH STP57-301			5845		0.0104
	002	11	090			SULPH. ANOD STP58-208			5807		0.0073
				095		INSPECT					
	002	03	100			(1) ZC PRIMER STP59-201			4815	0.10	0.0063
	002	03	110			IDENTIFY R/S STP63-001			2910	0.07	0.0032
				115		INSPECT					
						TOTAL				0.74	0.0507

Figure 2-40. Example of a Shop Planning Order for a Brace

The setup and run time standard hours are calculated from stored data. These values are constants in terms of hours per pound of material, which were determined for each manufacturing process required to produce each detail part. Data in the tables at present are valid only for titanium, but provision has been made for any number of new materials.

Calculation of the standard hours for each subassembly operation and for the final assembly is performed using the equations discussed in the previous section. The value of standard hours determined for subassembly processes are summed and added to the manufacturing process standard hours and listed for each detail part. The standard hours determined for the final assembly of the completed component are listed separately after each assembly process.

**2.7.5 REALIZATION.** Realization factors are the ratio of standard hours assigned for a given process to the actual hours required. Realization for a process is used as a means of measuring actual performance against a standard time that is typically an ideal number of hours. It is a measure of shop efficiency and, as such, varies from department to department and from day to day within a department. Realization data for the various departments involved in production tasks at the San Diego operation have been collected, studied, and adapted for use with the program. Since these data take into account the effects of the learning curve for a specific task, realizations can be specified either as an average value or as a time-dependent variable. Some of the factors affecting realization are:

- a. Inaccurate planning of the required work, setup times, or run times.
- b. Machine breakdown.
- c. Change in machine, tools, or procedure which are not reflected by corresponding change in standard hour estimates.
- d. Tool breakage and part spoilage.
- e. Availability of previous setups.
- f. Use of special supervision.
- g. Ability and level of effort of individuals assigned to the task.

Some of these factors are subject to control by managers and foremen, but they can also vary based on the current shop work load. Realization factors are useful in determining the overall effect of deviations from standard hour estimates. Realization for a particular task is defined as standard hours divided by actual labor hours.

In the program, values for realization are stored for each manufacturing and assembly process, and since standard hours can be estimated, the actual labor hours can be calculated:

$$\text{Actual labor hours} = \text{standard hours} / \text{realization.}$$

Realization factors, along with labor rates and overhead ratios, are stored within the program. Provision has been made in the program for a different realization factor for each of the manufacturing processes, for subassembly, and for final assembly operations. However, at present, a constant realization factor of 0.40 is used for all operations, but data is readily available to establish an individual realization for each operation (although these factors would be strictly valid only within the San Diego operation shops).

Average realization factors, along with the computed labor hours, are listed for each part in the cost output data under the headings REAL FACT, LABOR HOURS, and TOTAL HOURS. Figure 2-41 illustrates some typical realization factors and manufacturing standard hours plotted as a function of the number of ship sets.

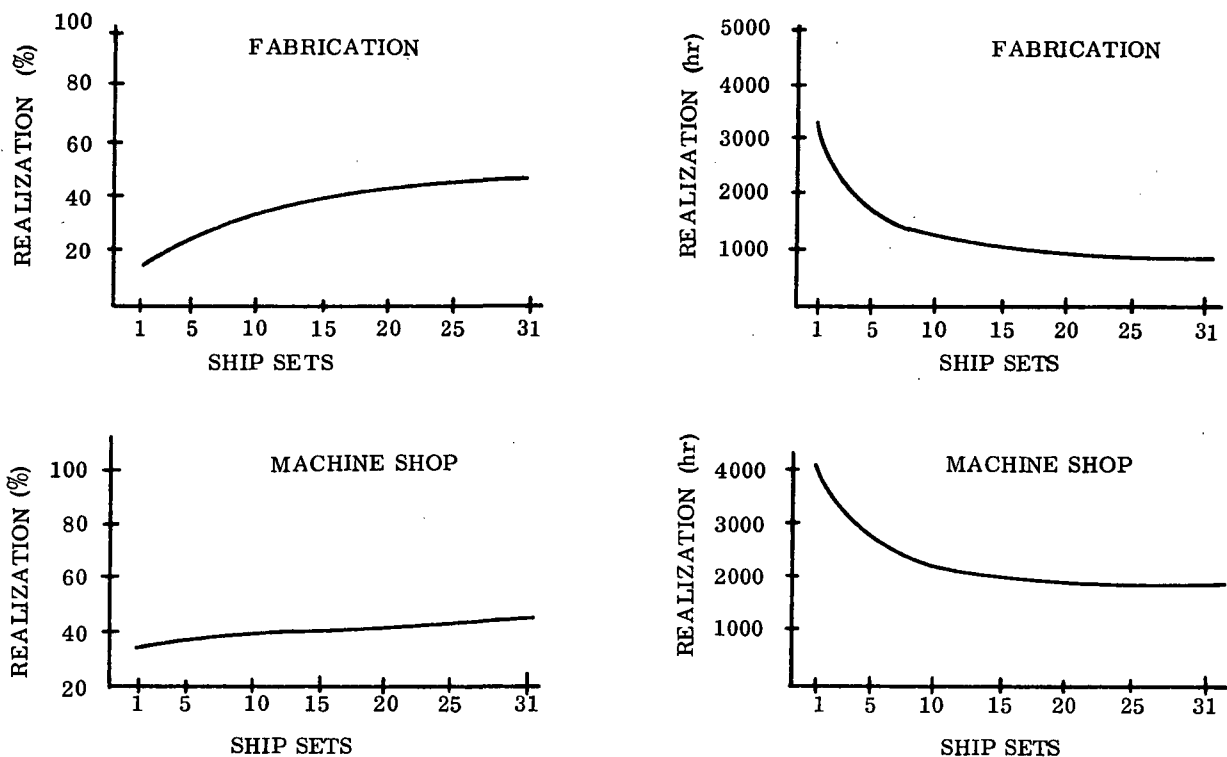


Figure 2-41. Typical Realization Factors and Standard Hours

**2.7.6 LABOR AND OVERHEAD RATES.** Labor and overhead rates are used within the program to calculate appropriate costs, based on the number of actual labor hours required for each manufacturing and assembly process.

Labor rates reflect the wages paid directly to the individual employees for each hour of clock time. The rates do not include fringe benefits or company contributions to retirement, Social Security, and state unemployment; these are considered part of the overhead cost. Also included as part of overhead are indirect labor costs, maintenance, supplies, taxes, insurance, and depreciation.

Labor rates are largely uncontrollable by management, being a function instead of union/management agreements and reflecting current labor supply and demand, general economic conditions, and inflation. Labor rates are a function of time and are readily predictable over the short term, although the incorporation of time-dependent equations has been left for future work. At present, the program can store a labor rate corresponding to each manufacturing process and the assembly operations. However, a constant manufacturing labor rate of \$4.75 per hour is used, and for the assembly operations a constant rate of \$5.20 per hour is used.

The overhead ratio is the ratio of overhead costs to labor costs and can, therefore, be used to determine an effective overhead rate:

$$\text{Overhead rate} = \text{Overhead Ratio} * \text{Labor Rate}$$

The overhead ratio is a useful tool for estimating purposes, and is readily available based on past labor cost and overhead cost data. The program can store an overhead ratio corresponding to each manufacturing process and the assembly operations. A constant ratio of 1.75 is used at present. Representative values of labor rates and overhead ratios as a function of time are presented in Figure 2-42. Values for the realization factor, labor rate, and overhead ratio are stored in the program.

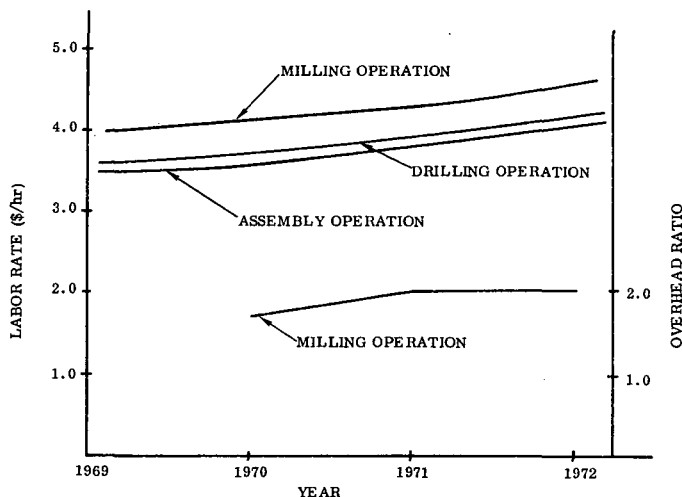


Figure 2-42. Typical Factory Direct Labor Rates and Overhead Ratios

The average labor rate for each part is output with the cost data, along with the corresponding average overhead rate (overhead ratio for final assembly costs). Labor cost and overhead costs are calculated for each part as the product of the labor hours and labor rate, and the labor hours and overhead rate, respectively. Factory costs and assembly costs, then, are the sum of the corresponding labor and overhead costs.

**2.7.7 MATERIAL.** Material costs are computed based on the raw material purchase weight of the given material type and form considered. Calculation of material costs required the derivation of a unit material cost (in dollars

per pound purchased), which is then multiplied by the purchase weight and by the manufacturing usage variance factor:

$$\text{Material Cost} = \text{COSWT} * \text{MAWT} * \text{MUV}$$



Total material cost is the sum of the material costs computed for material type and form required to produce each detail part. Material costs are listed in the output for each detail part and are summed for the complete structure. The sum of material cost and factory cost is the fabrication cost, which is also listed in the output for each detail part and each component of the complete structure. The total manufacturing cost is the sum of the total fabrication cost and the total assembly cost.

Material purchase weight is discussed in the section labeled WEIGHTS. The unit material cost is a function of several factors including:

Type:	Titanium, steel, etc.
Form:	Bar, sheet, plate, casting, extrusion, forging, fastener, etc.
Size, shape, complexity:	Standard stock, special lengths or widths, special gages or tolerances, complex cross sections, etc.
Alloy, temper:	Standard stock, special alloying or heat treating, etc.
Availability:	Standard stock or special mill run with corresponding setup changes and die or mold costs.
Quantity, delivery schedule:	Number of shipsets required minimum buy requirements, special large volume rates, need time, changes in unit cost with time, etc.
Packing, shipping:	Standard or special handling.

Material cost as a function of these items has been collected and reduced to a cost per unit weight basis depending on material type and form, and stored in the program along with the corresponding manufacturing usage variance factor. Material cost data are stored in an array; they represent typical values for material unit cost for each of the 16 material forms considered to date by this study (Table 2-4). Material cost (in dollars per pound purchased) is called out by a material form index and a material type index, respectively. At present, values for material cost are stored for titanium only. The capability is present to add any number of additional materials. Current plans call for the addition of a logic sequence that will compute a material unit cost using variables instead of constants for the previously listed items. This capability will also include time. Hence, assuming the labor and overhead rates are also time

Table 2-4. Summary of the Available Material Forms and the Corresponding Material Form Index

Material Form Index KK	Material Form	Part Reference
1	Sheet T1	Edge pieces
2	Sheet T2	Skins, seal strips
3	Sheet T3	Beams
4	Sheet T4	Corners, doublers
5	Sheet T5	Ribs, posts
11	Tubing D1	Posts
12	Tubing D2	Post support rings
13	Tubing D3	Post support tubes
21	Rod R1	Plugs
51	Honeycomb	Honeycomb core
61	Insulators	Insulators
71	Honeycomb inserts	Honeycomb inserts
81	Fasteners	Fasteners
91	Insulation 1	Insulation 1
92	Insulation 2	Insulation 2
93	Insulation 3	Insulation 3

dependent, the complete cost portion of the program will be able to account for changing costs with time. Also included will be a summation of each general type of material form; the corresponding cost will be computed based on a lot buy for the total material requirements of that form, reflecting minimum-buy penalties, quantity-buy discounts, special mill charges, die costs, form complexity factors, and tolerance requirements. This type of data has been accumulated, and it is only necessary to curve-fit them and write in the corresponding equations to adapt this logic to the program. Table 2-5 is an example of available data reflecting mill pricing policies with respect to the quantity of material bought for aluminum.

The manufacturing usage variance is the ratio of the actual material purchased to the original estimated material required. The variance factor is established by accounting practice, and is the result of material and part overbuying, losses, spoilage, duplication, substitution, and changes. Table 2-6 shows some typical values for the manufacturing

Table 2-5. Quantity Buy Price Differentials for Typical Aluminum Extruded Items

Quantity Ordered (Pounds)	Mill Standard Items (Dollars added per pound)
30,000 and over (basic price)*	\$0.0
20,000 thru 29,999	0.004
10,000 thru 19,999	0.008
5,000 thru 9,999	0.030
2,000 thru 4,999	0.055
1,000 thru 1,999	0.080
500 thru 999	0.110
300 thru 499	0.175
100 thru 99	0.375
25 thru 49	0.575
less than 25	0.727

\*The base price applied to 30,000 pounds of any single item, or to 30,000 pounds of grouped items with a minimum of 200 pounds of any one.

substitution and changes. Table 2-6 shows some typical values for the manufacturing usage variance factor for a past commercial transport aircraft program. The subroutine uses a constant value of 1.10 throughout, corresponding to a 10 percent variance between actual and estimated material costs. Values for the manufacturing usage variance factor are stored in an array KMUV (KK, JJ), also located with the BLOCK DATA and called out by the indexes KK and JJ. The K-TABLES KCOSWT and KMUV are discussed under K-TABLES. Table 2-7 summarizes the values stored in the KCOSWT table.

**2.7.8 PROGRAM COST SUMMARY.** An example output of a program cost summary is presented in Figure 2-43. The total program costs are derived on the basis of the TPS gross weight, usually in terms of a Theoretical First Unit Cost or TFU. This is the predicted production cost of the prototype article including manufacturing planning, fabrication, subassembly, sustaining engineering, sustaining tooling, quality control, materials, and subcontracted parts. It is calculated using an equation of the form

$$TFU = C_1 = (WTTPS)^a$$

**Table 2-6. Typical Manufacturing Usage Variance Factors for a Past Commercial Transport Aircraft Program**

Contract Lot No.	Actual Material Costs A (millions of \$)	Original Estimated Material Costs E (millions of \$)	Percent Variance (A - E/A) * 100 (percent)	Manufacturing Usage Variance Factor
1	40.65	34.74	17.0	1.170
2	4.61	4.25	8.5	1.085
3	16.67	14.39	13.8	1.138
4	22.69	21.40	6.1	1.061
5	16.28	15.84	2.8	1.028
6	66.50	62.15	7.0	1.070
7	10.22	9.84	3.9	1.039
8	68.71	61.94	10.9	1.109

**Table 2-7. Summary of the Values Stored in the KCOSWT Table for Titanium**

Material Form Index KK	Material Type Index JJ = 1 (\$/lb purchase wt)	Material Form Index KK	Material Type Index JJ = 1 (\$/lb purchase wt)
1	15.00	21	10.50
2	14.50	51	65.00
3	14.00	61	25.00
4	13.50	71	95.00
5	13.00	81	132.71
11	12.00	91	50.00
12	12.50	92	50.00
13	14.00	93	50.00

# THEMAL PROTECTION SYSTEM - COST SUMMARY

		COST (\$)
THEORETICAL FIRST UNIT COSTS - TFU 9,340		
NON RECURRING COST		
ED AND D		50,919
TOOLING		52,809
GROUND TEST HARDWARE		20,434
FLIGHT TEST ARTICLES		16,681
FLIGHT TEST S AND SP		5,589
TOTAL NONRECURRING TPS COST		146,431
RECURRING PRODUCTION COST		
SUSTAINING ENGINEERING	- INCLUDED IN TFU	
SUSTAINING TOOLING	- INCLUDED IN TFU	
PRODUCTION ARTICLES (1)		8,340
TEST ARTICLE CONVERSION		2,502
TOTAL RECURRING PRODUCTION COST		10,842
RECURRING OPERATIONS COST		
REPLETISHMENT S AND RE		11,109
TOTAL RECURRING OPERATIONS COST		11,109
TOTAL THEMAL PROTECTION SYS PROGRAM COSTS 168,282		

Figure 2-43. Program Cost Summary

where  $C_1$  is a complexity factor for the material and the panel configuration,  $a$ , is a constant, and WTPPS represents the complete TPS system gross weight. At present an area of 22,000 square feet is assumed for the complete TPS system, and this area is, in turn, used to compute the complete TPS system gross weight based on the unitized panel weight.

Included under nonrecurring costs are engineering design and development, tooling, ground test hardware, flight test article, and flight test spares costs. Within these categories, engineering design and development costs include the engineering, design, development, laboratory test, support activities for subsystem development, and the cost of hardware required to support

laboratory development testing and component qualification testing. Tooling costs include initial tooling for subsystem fabrication and general structural tooling. Ground test hardware, flight test articles, and flight test spares reflect the production costs of all the hardware used in subsystem and combined subsystem development testing. Engineering design and development (ED&D) costs are derived using an equation similar in form to that used to calculate the TFU:

$$ED \& D = C_2 * (WTPPS)^{C_1}$$

where  $C_2$  and  $C_1$  are constants. Tooling costs are derived based on an equation of the form;

$$\text{Tooling} = C_3 * WTPPS$$

where  $C_3$  is a complexity factor representing tooling dollars per pound. Ground test hardware, flight test articles, and flight test spares are derived based on an equation of the form:

$$\text{Cost} = C_4 * TFU$$

where  $C_4$  is a complexity factor representing the equivalent ground test hardware, number of flight test articles, or equivalent flight test spares, respectively.

Included under recurring production costs are sustaining engineering and tooling costs (included as part of the TFU cost), production article costs, and test article conversion cost. Production article costs are for general production articles, and test article conversion costs reflect the cost of conversion to operational configurations. Both of these costs are derived based on an equation of the form:

$$\text{Cost} = C_5 * TFU$$

where  $C_5$  is a complexity factor representing the number of production articles and the equivalent test articles, respectively.

Included under recurring operations cost are refurbishment costs which reflect the cost of vehicle servicing and spares, and making it ready for flight validation over a ten year life of operation. Refurbishment costs are derived using an equation of the form:

$$\text{Refurbishment} = C_6 * \text{TFU}$$

where  $C_6$  is a complexity factor representing the equivalent flight articles. The various complexity factors required for the program cost summary were derived based on work done at the San Diego operation by the Economic Analysis Department during the course of study on several advanced technology vehicles including the space shuttle vehicles.

**2.7.9 K-TABLES.** These tables provide storage for values relating to the manufacturing usage variance factor, manufacturing process setup time, manufacturing process run time, material unit cost, and realization, labor rate, and overhead ratios, respectively. Although these tables currently contain constant values, they will later be replaced with equations, located in the COST subroutine, that will calculate the necessary data.

KMUV (KK, JJ) refers to a table of manufacturing usage variance factors, which are called out by the material form index KK and the material type index JJ.

Table 2-5 summarizes the presently available material forms referenced within the K-TABLES and the corresponding material form index KK. The material type index JJ is derived within the program as a function of the material type. At present, the KMUV table stores a constant value of 1.10 for all values of KK and JJ, as discussed previously.

KSETUP (KK, KS) refers to a table of manufacturing process setup time values in hours per pound actual weight (ACWT). These are called out by the material form index KK and the manufacturing operation index KS, which is set equal to JJ where JJ is a function of material type. Values of the index KS for the various manufacturing operations required to produce a given part in titanium have been summarized previously (Section 2.7.3). Once the initial value of KS is established, the corresponding setup time is picked from the KSETUP table and the standard hour calculation for the cutoff operation is made, as discussed previously. Then the value of KS is incremented and a new setup time is taken from the table and the standard hour calculation is made for milling. This procedure is continued until each manufacturing operation is considered. Table 2-8 summarizes the values stored in the KSETUP table for titanium: zero is stored when a given operation is not required for a particular part.

KRUN (KK, KR) refers to a table of manufacturing process run time values in hours per pound actual weight (ACWT), which are called out by the material form index KK and the manufacturing operation index KR, which is analogous to the value of KS.

Table 2-8. Summary of the Values Stored in the KSETUP Table for Titanium

Material Form Index KK	Manufacturing Process Index KS*						
	1	2	3	4	5	6	7
	Standard Hours per Pound Actual Weight						
1	0.0050	0	0.0120	0.0200	0.0100	0.0120	0.0080
2	0.0060	0	0	0.0250	0.0100	0.0140	0.0080
3	0.0070	0	0.0160	0.0300	0.0100	0.0160	0.0090
4	0.0080	0	0.0180	0.0350	0.0100	0.0180	0.0090
5	0.0100	0	0.0200	0.0400	0.0100	0.0200	0.0100
11	0.0160	0.1000	0	0.0500	0	0.0400	0.0140
12	0.0200	0.1100	0	0.0700	0	0.0600	0.0160
13	0.0240	0.1200	0	0.0900	0	0.0800	0.0180
21	0.0160	0.1000	0	0.0500	0	0.0400	0.0140
51	0.0300	0.2000	0	0	0	0	0.0200
61	0.0010	0	0	0	0	0	0
71	0.0010	0	0	0	0	0	0
81	0	0	0	0	0	0	0
91	0.0080	0	0	0	0	0	0
92	0.0010	0	0	0	0	0	0
93	0.0010	0	0	0	0	0	0

\* Refer to Table 2-4.

Section 2.7.3 gives values of KR for the various manufacturing operations, and Table 2-9 summarizes the values stored in the KRUN table for titanium. The index KR is initialized and incremented in the same manner as KS. For each cycle, a run time in standard hours is calculated for a given operation using a value from the KRUN table and the procedure discussed previously.

KCOSWT (KK, JJ) refers to a table of material costs in dollars per pound purchase weight (MAWT), which are called out by the material form index KK and the material type index JJ. Table 2-7 summarizes the values stored in the KCOSWT table for titanium. The calculation of material costs using values of KCOSWT is discussed in the section labeled MATERIAL.

Table 2-9. Summary of the Values Stored in the KRUN Table for Titanium

Material Form Index KK	Manufacturing Process Index KR*						
	1	2	3	4	5	6	7
	Standard Hours per Pound Actual Weight						
1	0.0500	0	0.1200	0.2000	0.1000	0.1200	0.0800
2	0.0600	0	0	0.2500	0.1000	0.1400	0.0800
3	0.0700	0	0.1600	0.3000	0.1000	0.1600	0.0900
4	0.0800	0	0.1800	0.3500	0.1000	0.1800	0.0900
5	0.1000	0	0.2000	0.4000	0.1000	0.2000	0.1000
11	0.1600	1.000	0	0.5000	0	0.4000	0.1400
12	0.2000	1.100	0	0.7000	0	0.6000	0.1600
13	0.2400	1.200	0	0.9000	0	0.8000	0.1800
21	0.1600	1.000	0	0.5000	0	0.4000	0.1400
51	0.3000	2.000	0	0	0	0	0.2000
61	0.0100	0	0	0	0	0	0
71	0.0100	0	0	0	0	0	0
81	0	0	0	0	0	0	0
91	0.0800	0	0	0	0	0	0
92	0.0800	0	0	0	0	0	0
93	0.0800	0	0	0	0	0	0

\* Refer to Table 2-4.

KCC (KC, X) refers to a table of realization factors ( $X = KF$ ), labor rates ( $X = KL$ ), and overhead ratios ( $X = KV$ ), which are called out by the cost center or operation index KC, and the factor index KF, KL, or KV for realization, labor rate, or overhead ratio, respectively. The cost center index KC is effectively a manufacturing process index and has values from one to seven, each corresponding to one of the production operations. Table 2-10 summarizes the values stored in the KCC table.

## 2.8 INPUT, OUTPUT, AND MATERIAL PROPERTIES

The input and output subroutines provide communication between the program user and the computer. Both aspects are discussed in detail in the User's Manual. Input parameters can be described in a number of broad categories:



Table 2-10. Summary of the Values Stored in the KCC Table

Operation Index KC	Factor Index		
	Realization KF	Labor Rate KL (\$)	Overhead Ratio KV
1	0.40	4.75	1.75
2	0.40	4.75	1.75
3	0.40	4.75	1.75
4	0.40	4.75	1.75
5	0.40	4.75	1.75
6	0.40	4.75	1.75
7	0.40	4.75	1.75

- a. Analysis indices which indicate the user's preference for particular options in the analysis such as heating prediction method, panel configuration, the choice of one- or two-dimensional conduction, etc.
- b. Panel configuration, supporting structure, and vehicle geometry to define the parameters necessary to perform thermodynamic, stress, and sonic fatigue analyses as well as to determine the weight and cost of the resulting TPS.
- c. Trajectory data (altitude, velocity, and angles of attack and sideslip as a function of time) or heating rates and panel pressure.
- d. Overall interchange factors for radiation between nodes of the thermodynamic configuration.
- e. Material property data.

Input parameters for the first three categories of data are well explained in the User's Manual; the computation of overall interchange factors can be performed externally by any number of suitable programs available in the industry which take into account direct and indirect radiation exchange between all combinations of components. The remainder of this chapter will be devoted to presenting a summary of material property data which are applicable to the investigation of metallic heat shield panels. The thermodynamic and mechanical properties needed for the TPS design are shown in Table 2-11.

Candidate metallic heat shield materials applicable to this study are given in Table 2-12 along with estimated temperature and heat transfer rate limits for their use.

The material properties for the first six of Table 2-11 are presented in plots 2-44 through 2-49 as functions of temperature. A less extensive collection of material

Table 2-11. Thermomechanical Properties

Item Number	Property
1	Thermal conductivity
2	Heat capacity
3	Modules of elasticity
4	Coefficient of thermal expansion
5	Yield strength
6	Ultimate tensile strength
7	Larson-Miller data for creep deformation
8	S-N curves for fatigue evaluation

Table 2-12. Candidate Heat Shield Materials

	Maximum Use	
	Temperature	Heat Flux
Metallic		
Titanium Alloys 6 Al - 4 V; 8 Al - 1 Mo - 1 V	To 1000°F,	1.6 Btu/ft <sup>2</sup> sec
Nickel Alloys		
Rene 41; Inconel 718; Inconel 625	To 1700°F	9.0 Btu/ft <sup>2</sup> sec
Cobalt Alloys		
L-605; Haynes - 188	To 2000°F,	15.0 Btu/ft <sup>2</sup> sec
Dispersioned Strengthened		
TD Ni; TD Ni Cr	To 2200°F,	20.0 Btu/ft <sup>2</sup> sec
Columbium Alloy		
Cb - 752	To 2500°F,	35.0 Btu/ft <sup>2</sup> sec
Tantalum Alloys		
T-222; Ta-10W	To 2800°F,	60.0 Btu/ft <sup>2</sup> sec

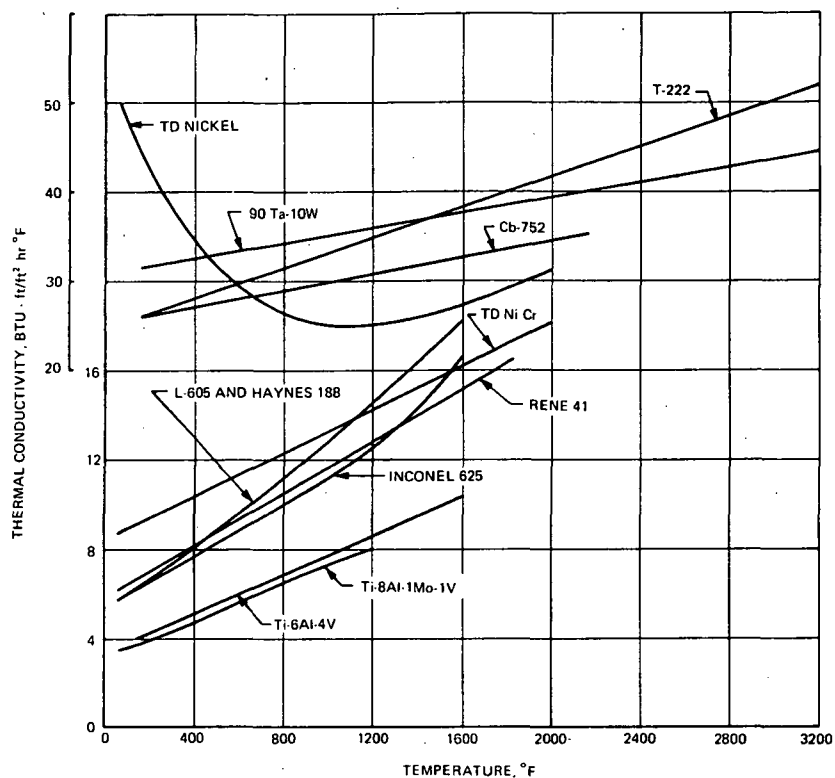


Figure 2-44. Thermal Conductivity for Candidate Metals for Heat Shield Applications

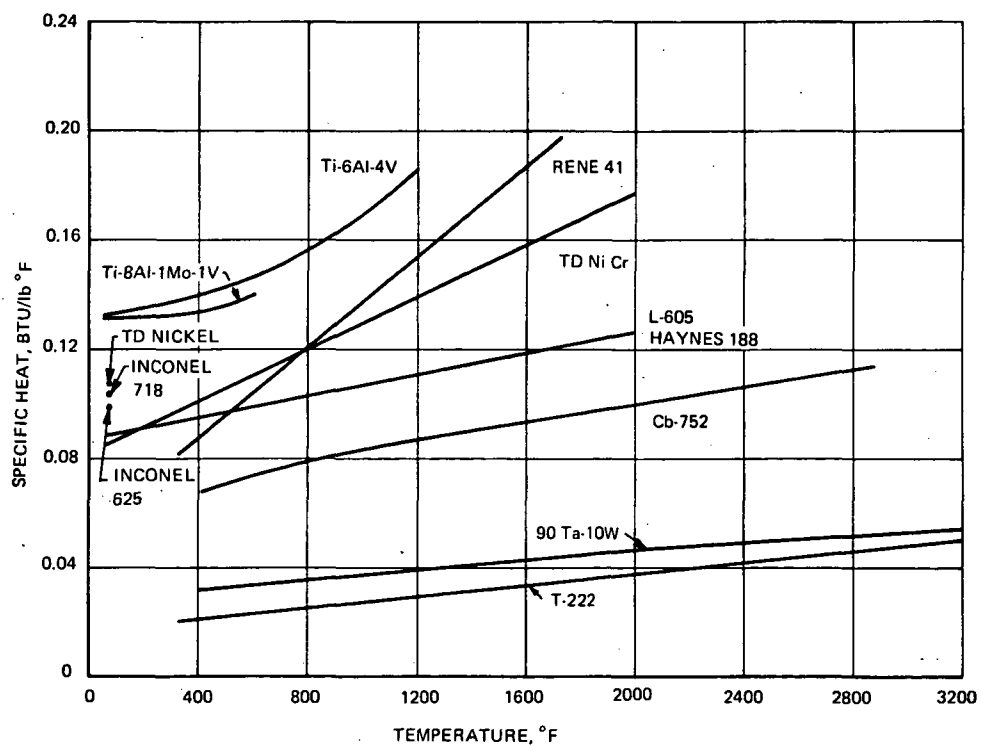


Figure 2-45. Specific Heat for Candidate Metals for Heat Shield Applications

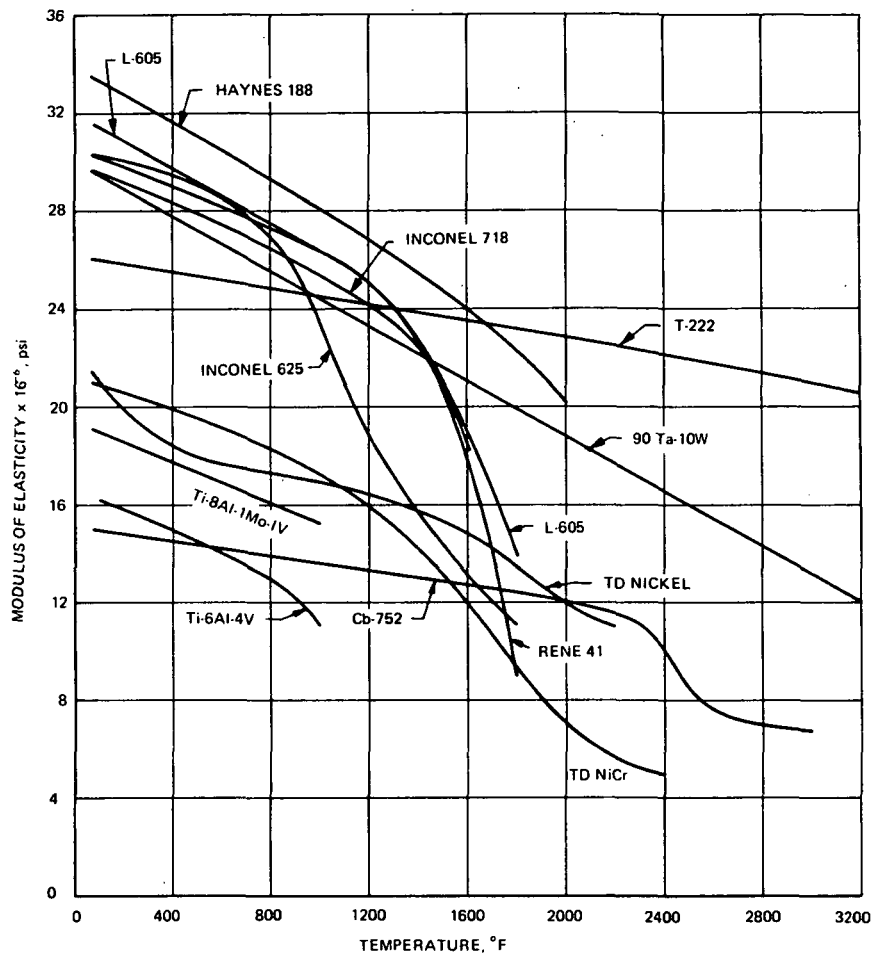


Figure 2-46. Modulus of Elasticity for Candidate Metals for Heat Shield Applications

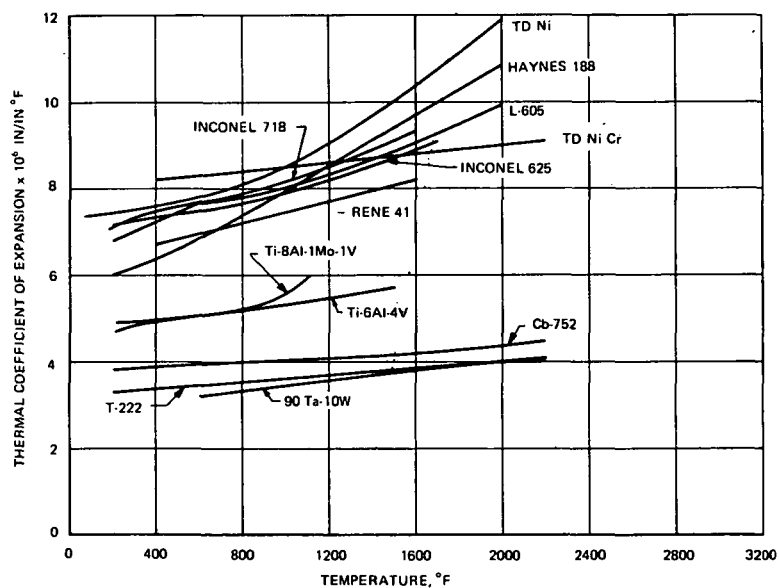


Figure 2-47. Coefficient of Thermal Expansion for Candidate Metals for Heat Shield Applications

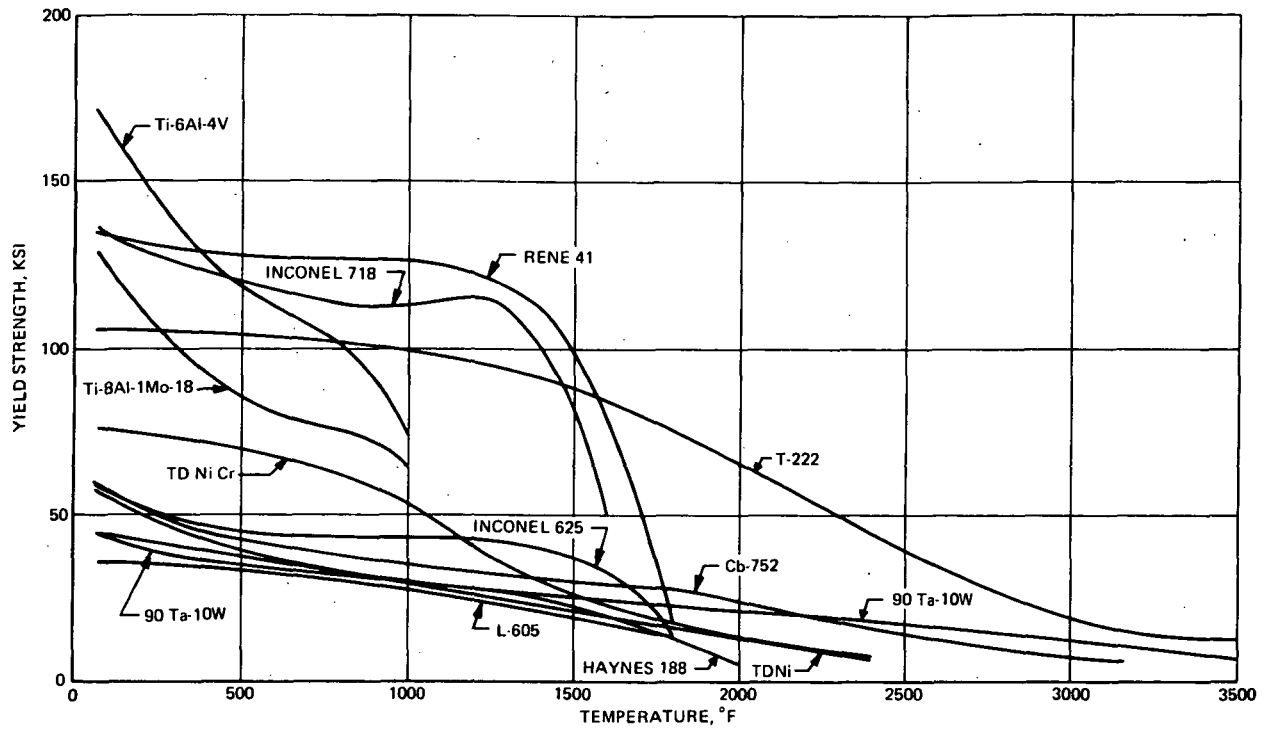


Figure 2-48. Yield Strength for Candidate Metals for Heat Shield Applications

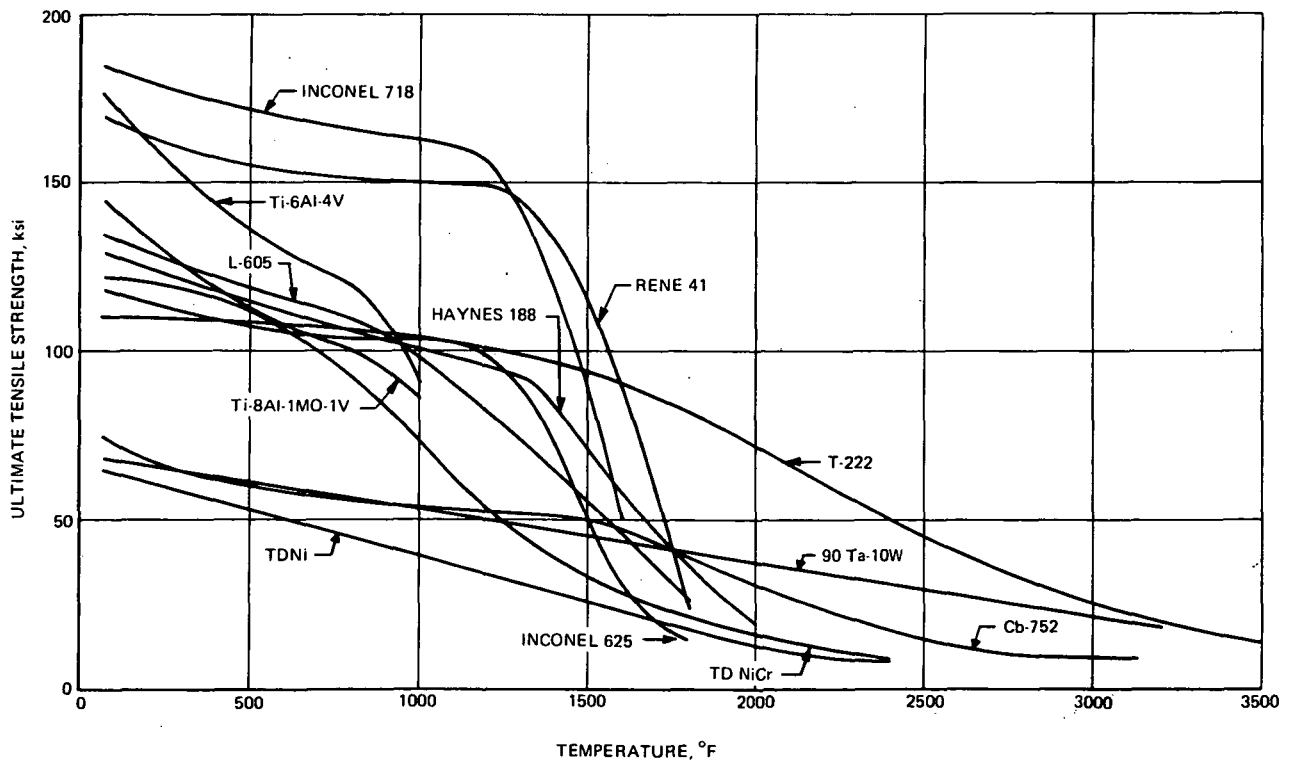


Figure 2-49. Ultimate Tensile Strength for Candidate Metals for Heat Shield Applications

properties for Larson-Miller creep deformation data and S-N fatigue data is currently available in the literature. A partial summary of creep data (Table 2-13) is given in Figures 2-50 through 2-66.

Table 2-13. Larson-Miller Creep Rupture Data

---

2219-T6 Aluminum

(Annealed) Titanium, Ti-3Al-2.5 Sn

Titanium, Ti-8Al-1Mo-1V (Mill Annealed)

718 Nickel, Aged

718 Nickel, 20% CW + Aged

René 41, ST + Aged

L-605 Cobalt, Annealed

Columbium, Cb-5V-5Mo-1Zr (B-66), Stress Relieved, RT to 3000°F, Strength at Temperature

Columbium, Cb-5V-5Mo-1Zr (B-66) Recrystallized, RT to 3000°F Strength at Temperature

Molybdenum, Mo-0.5 Ti-0.8Zr-0.03C (TZM) Stress Relieved Sheet, RT to 3000°F, Strength at Temperature

Molybdenum, Mo-0.5Ti-0.8Zr-0.03C (TZM) Recrystallized Sheet, RT to 3000°F, Strength at Temperature

Molybdenum, Mo-0.5Ti-0.8Zr-0.03C (TZM) Coated Sheet (Si, Cr, B Pack Cementation), RT to 2700°F, Strength at Temperature

Tantalum, Ta-8W-2Hf (T-111), Stress Relieved, RT to 3000°F, Strength at Temperature

Tantalum, Ta-8W-2Hf (T-111) Recrystallized, RT to 3000°F, Strength at Temperature

---

S-N data for fatigue analyses are even more difficult to locate than are creep results. For this report, two standard reports are cited (Reference 38 and 39). Some of these data which are applicable to the present study are presented herein in Figures 2-67 through 2-74. The materials included are René 41 for a number of different heat treatments, and a number of different titanium alloys. Under Contract NAS8-27017 with MSFC in Huntsville, Convair Aerospace is currently conducting a literature survey under a contract to perform fatigue evaluation of thermal protection systems. The result of this survey is a compilation and placement in a compatible format of available S-N information at various temperatures for the following materials:

Columbium (up to 2500°F)

Titanium (up to 650°F)

René 41 (up to 1600°F)

Haynes 25 (up to 1900°F)

Boron composites } Data on whatever matrices and temperatures are available.  
Carbon composites }

The S-N data are to be presented:

- a. Tabular form, showing fatigue strengths at three values (minimum) of stress cycles (N). The N's selected shall be a minimum value, a maximum value, and an average value.
- b. The tabulated data shall also be shown, as may be applicable, in graph form as S-N curves (showing effects of stress raisers), Goodman diagrams, plots of alternating vs. mean stress, etc.

As a further task under the fatigue evaluation contract, the tables and graphs will show explicitly gaps in the data required for the space shuttle vehicle. As these new experimental data are developed and tabulated, they will be made available for the present study of TPS optimization. It is further anticipated that data sources for other TPS materials (both metallic and non-metallic) will be recognized so that available data can be presented although no new data will be developed.

Thermodynamic properties for a number of insulation materials applicable to the TPS sizing program are included in Table 2-14 as a function of temperature. No mechanical properties are necessary since the insulation does not transfer a mechanical load to the structure.

Table 2-14. Insulation Properties

Insulation	Mean Temperature (°F)	Thermal Conductivity, (Btu - in/hr-ft <sup>2</sup> °F)	Specific Heat, (Btu/lb)	$\rho k$ , (lb/ft <sup>3</sup> ) (Btu - in/ft <sup>2</sup> hr°F)
<u>Fibrous</u>				
Microquarts 3.5 pcf	0	0.18	0.170	0.635
	400	0.336	0.229	1.18
	800	0.515	0.261	1.80
	1200	0.765	0.278	2.68
	1600	1.22	0.288	4.28
Dynaflex 4 pcf	200	0.31	0.195	1.24
	400	0.45	0.215	1.80
	800	0.82	0.243	3.28
	1200	1.34	0.258	5.36
	1600	2.08	0.268	8.30
	2000	3.09	0.272	12.40
Dynaflex 6 pcf	200	0.29	0.195	1.74
	400	0.41	0.215	2.46
	800	0.71	0.243	4.25
	1200	1.09	0.258	6.55
	1600	1.61	0.268	9.65
	2000	2.31	0.272	13.82
Dynaflex 12 pcf	200	0.27	0.195	3.24
	400	0.38	0.215	4.55
	800	0.60	0.243	7.20
	1200	0.85	0.258	10.20
	1600	1.16	0.268	13.90
	2000	1.53	0.272	18.33
Zircar 12 pcf	500	0.60	0.132	7.2
	1000	0.75	0.143	9.0
	1500	0.90	0.149	10.8
	2000	1.25	0.154	15.0
	2500	1.65	0.144	19.8
<u>Packaged</u>				
<u>Powder</u>	75	0.234	0.203	2.80
	200	0.238	0.226	2.85
	400	0.254	0.242	3.06
ADL-17 12 pcf	800	0.320	0.258	3.84
	1200	0.435	0.265	5.21
	1600	0.588	0.269	7.04



Table 2-14. Insulation Properties, Contd

Insulation	Mean Temperature (° F)	Thermal Conductivity, (Btu - in/hr-ft <sup>2</sup> ° F)	Specific Heat, (Btu/lb)	$\rho k$ , (lb/ft <sup>3</sup> ) (Btu - in/ft <sup>2</sup> hr° F)
<u>Rigidized</u>				
Silica	200	0.41	0.200	6.35
(LI-1500)	400	0.46	0.228	7.10
15.5 pcf	800	0.57	0.264	8.85
	1200	0.87	0.277	13.40
	1600	1.18	0.289	18.20
Zirconia	500	0.55	0.132	13.80
25 pcf	1200	0.67	0.145	16.65
	1600	0.88	0.150	21.90
	2000	1.18	0.154	29.50
<u>Foam</u>				
Silica	200	0.57	0.176	5.70
10 pcf	500	0.99	0.210	9.90
	800	1.61	0.241	16.10
Alumina	200	3.68	0.220	136.0
37 pcf	400	3.00	0.245	111.0
	800	2.36	0.275	87.3
	1200	2.20	0.295	81.4
	1600	2.24	0.310	82.9
	2000	2.46	0.320	91.0
Zirconia	200	1.05	0.122	42.0
40 pcf	400	1.1	0.132	44.0
	800	1.32	0.147	52.8
	1200	1.7	0.153	68.0
	1600	2.28	0.158	91.2
	2000	2.88	0.160	115.2

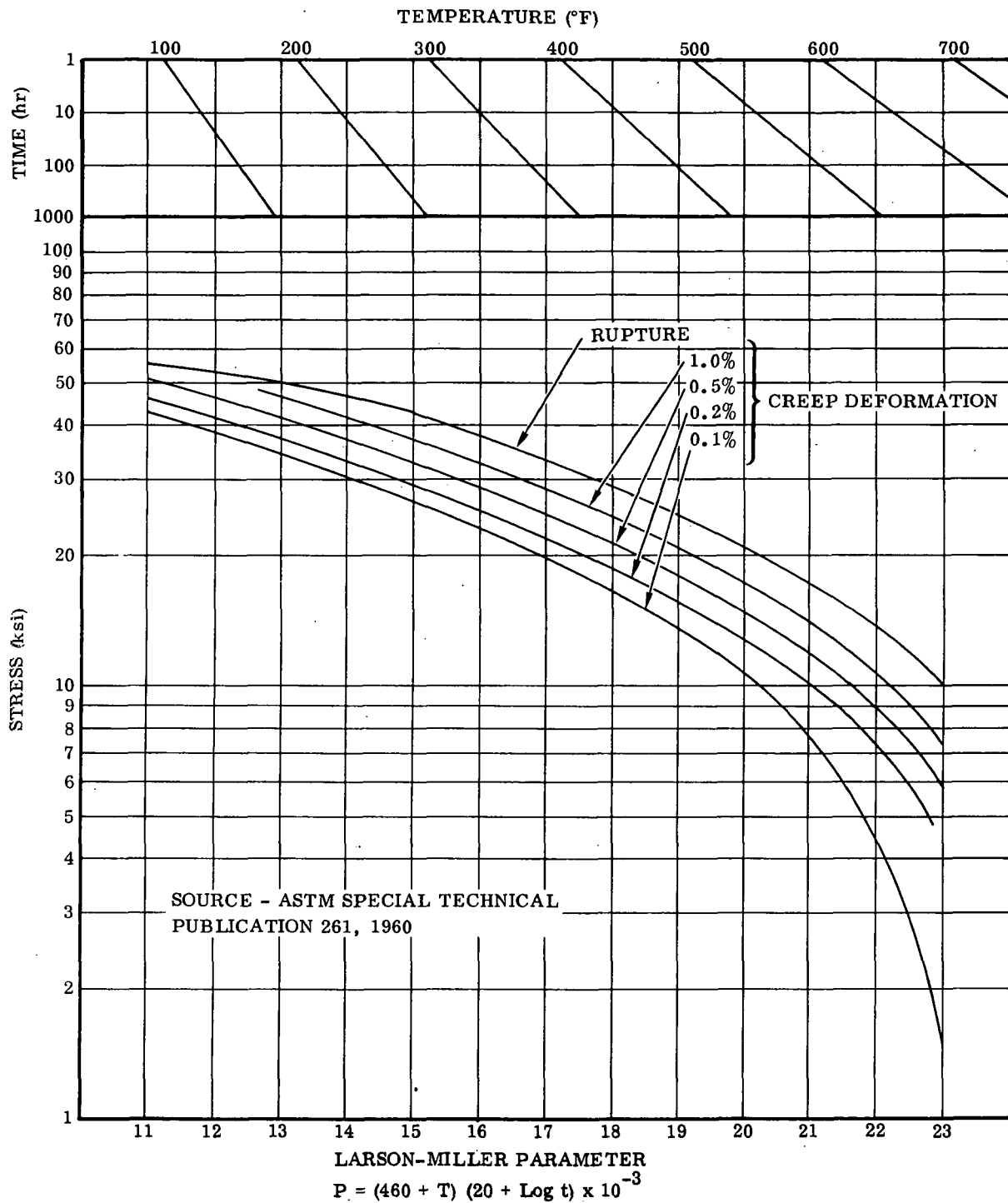


Figure 2-50. Creep Data for 2219-T6 Aluminum

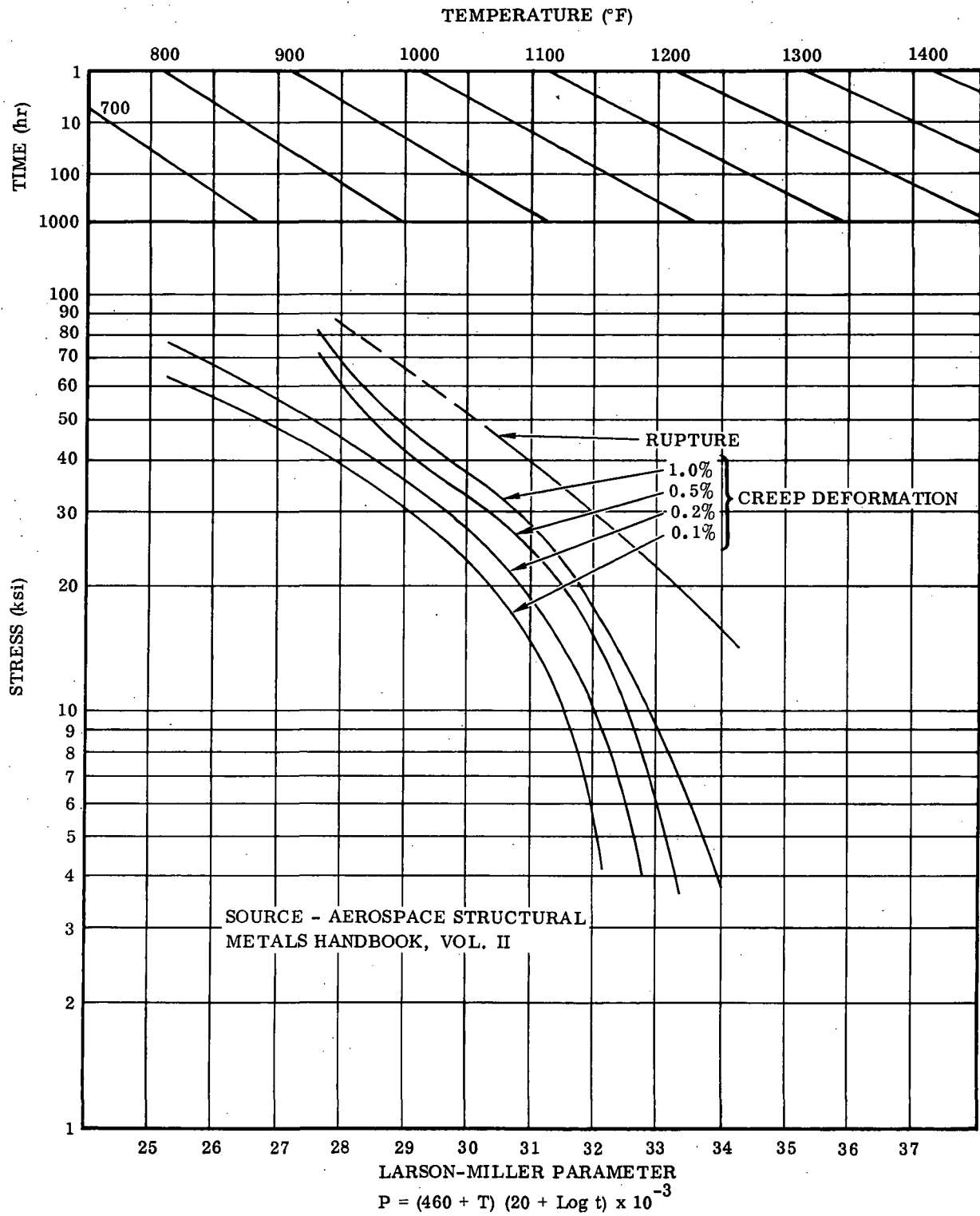


Figure 2-51. Creep Data for (Annealed) Titanium, Ti-5Al-2.5 Sn

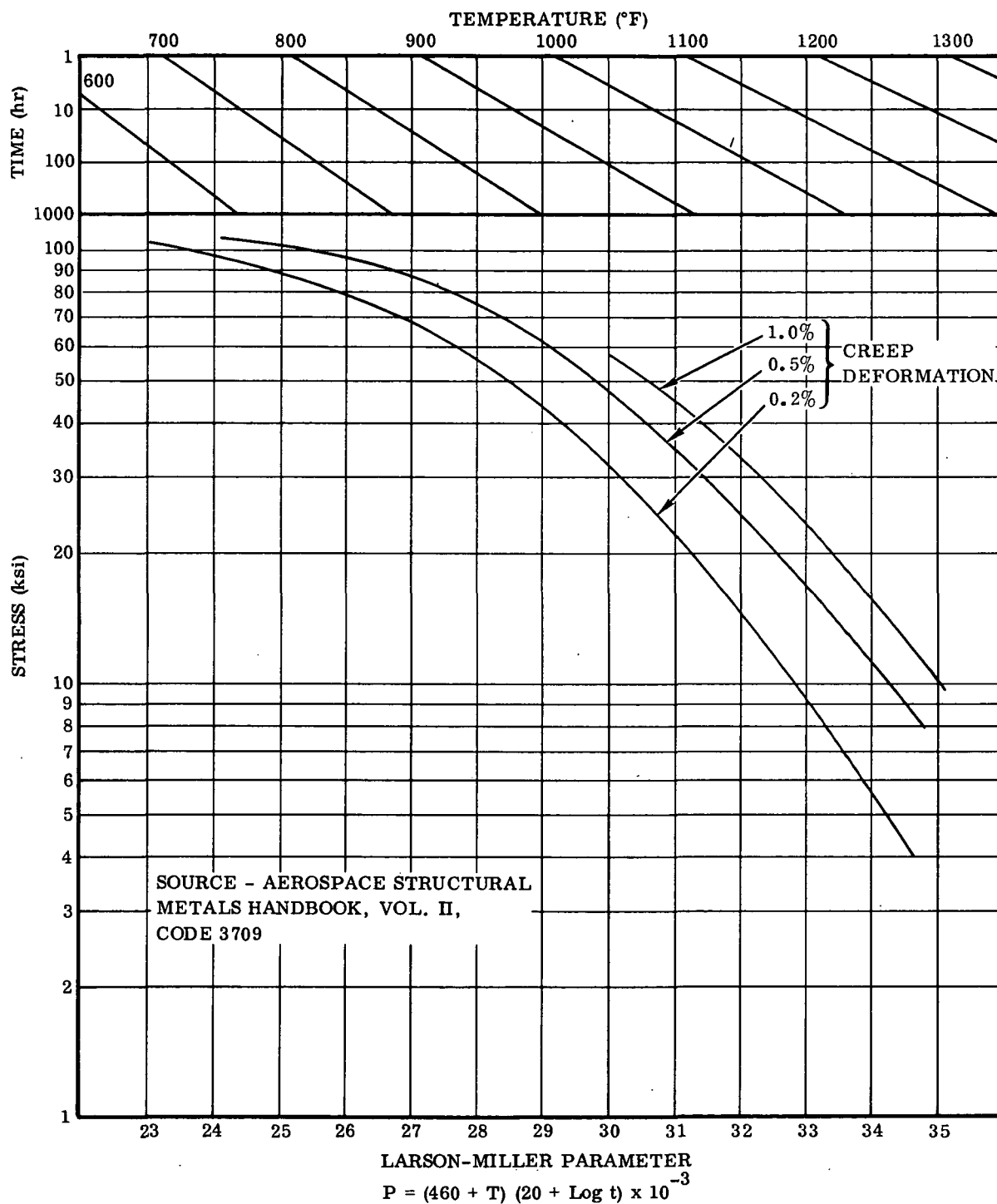


Figure 2-52. Creep Data for Titanium, Ti-8Al-1Mo-1V (Mill Annealed)

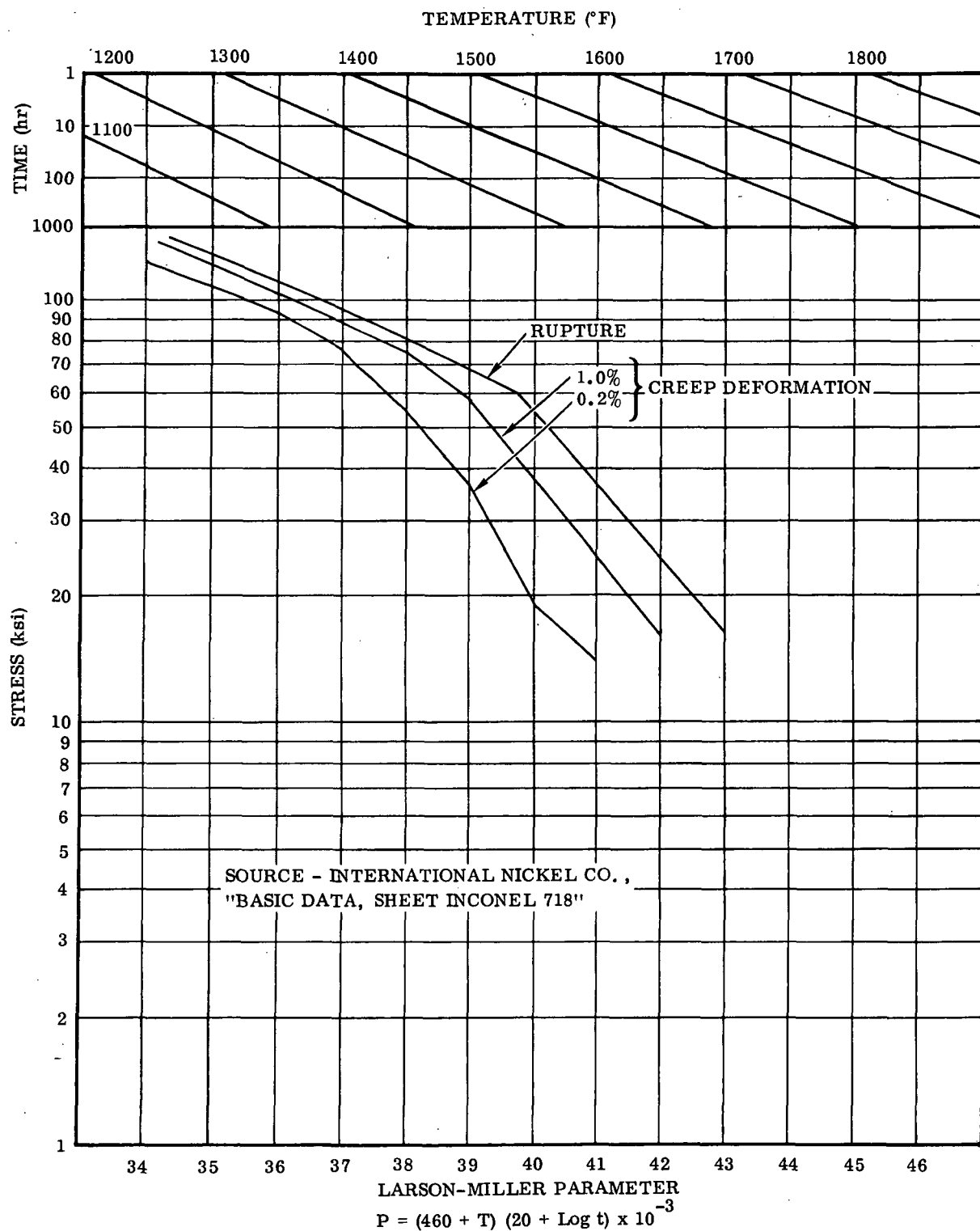


Figure 2-53. Creep Data for 718 Nickel, Aged

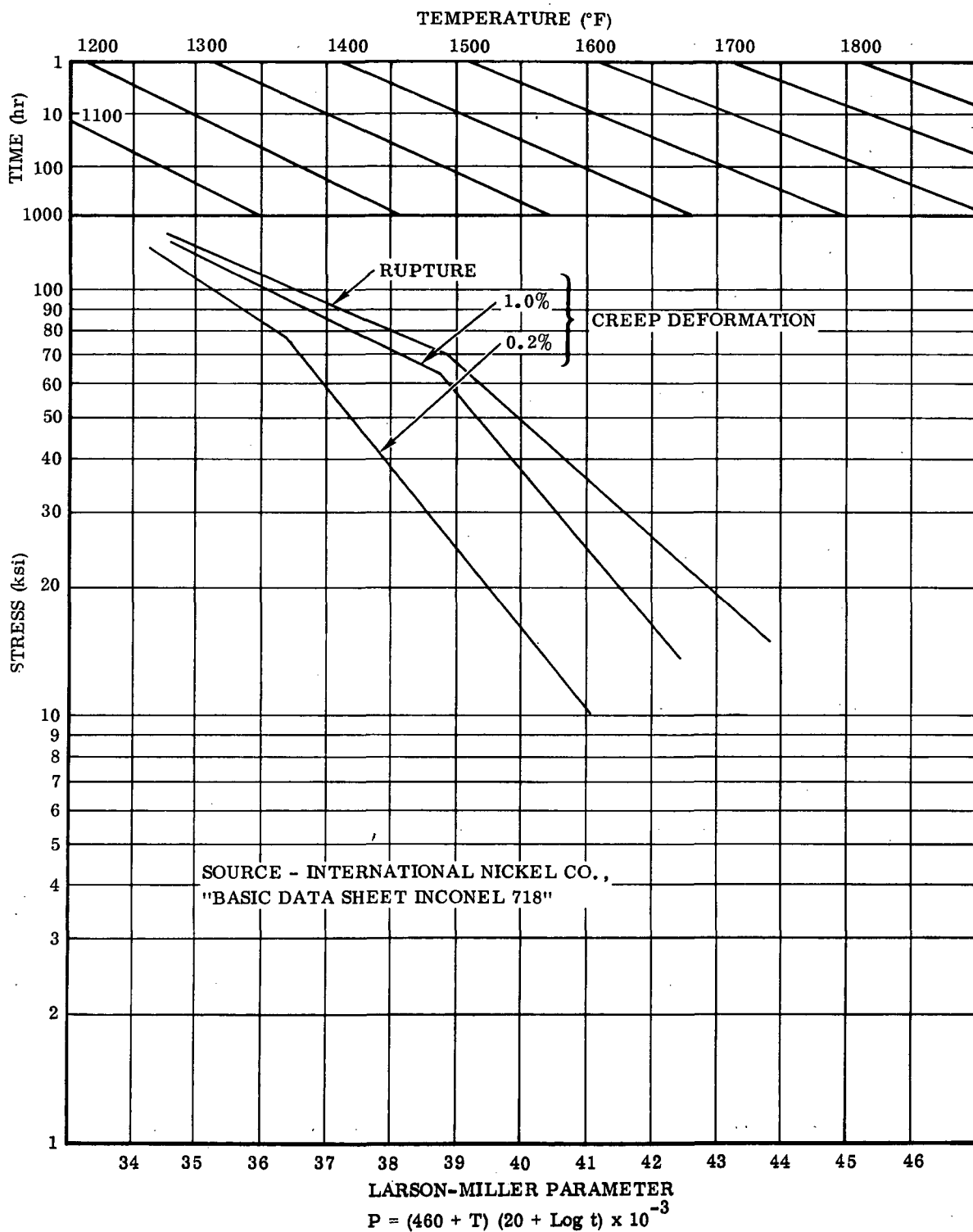


Figure 2-54. Creep Data for 718 Nickel, 20 Percent CW + Aged

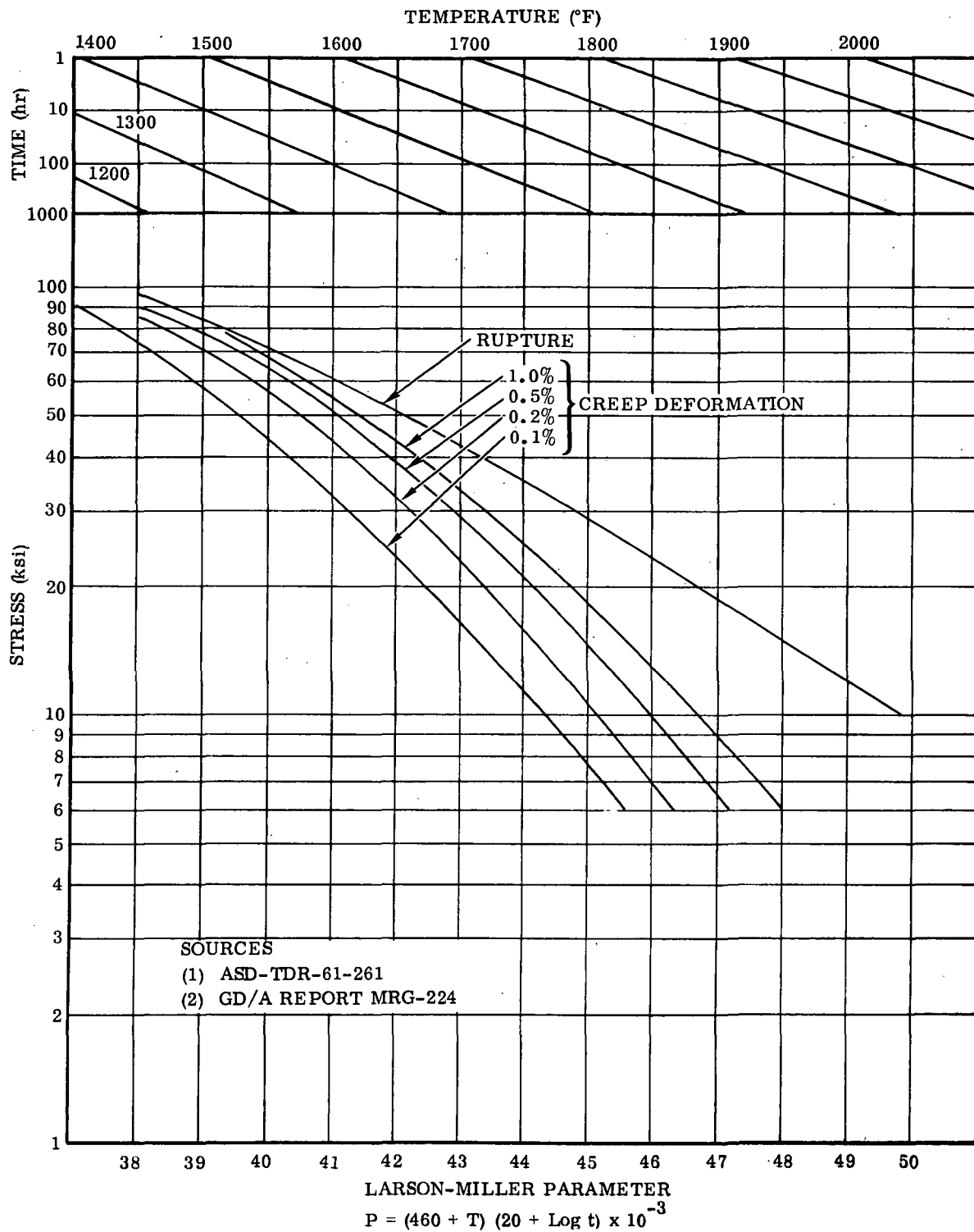


Figure 2-55. Creep Data for René 41, ST + Aged

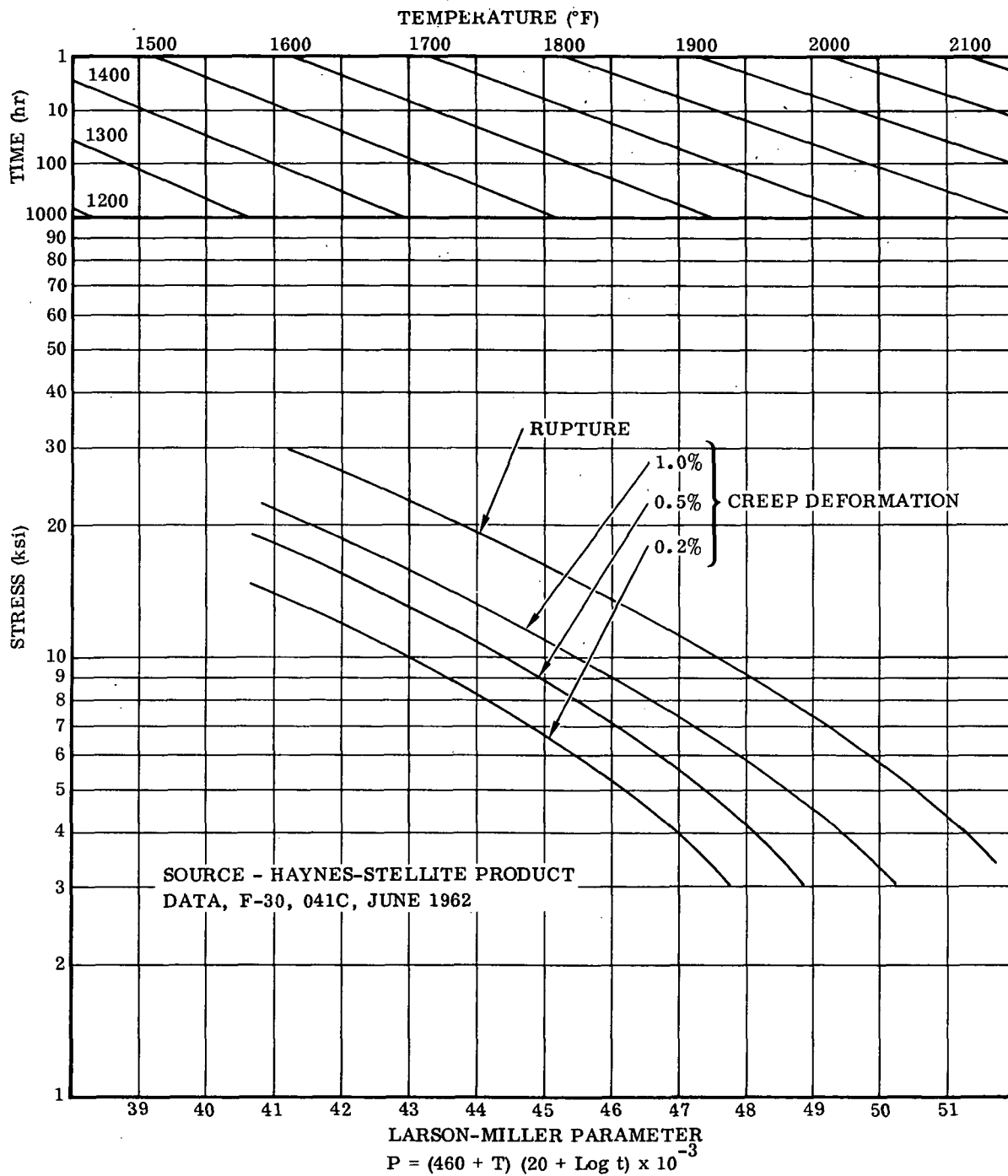


Figure 2-56. Creep Data for L-605 Cobalt, Annealed



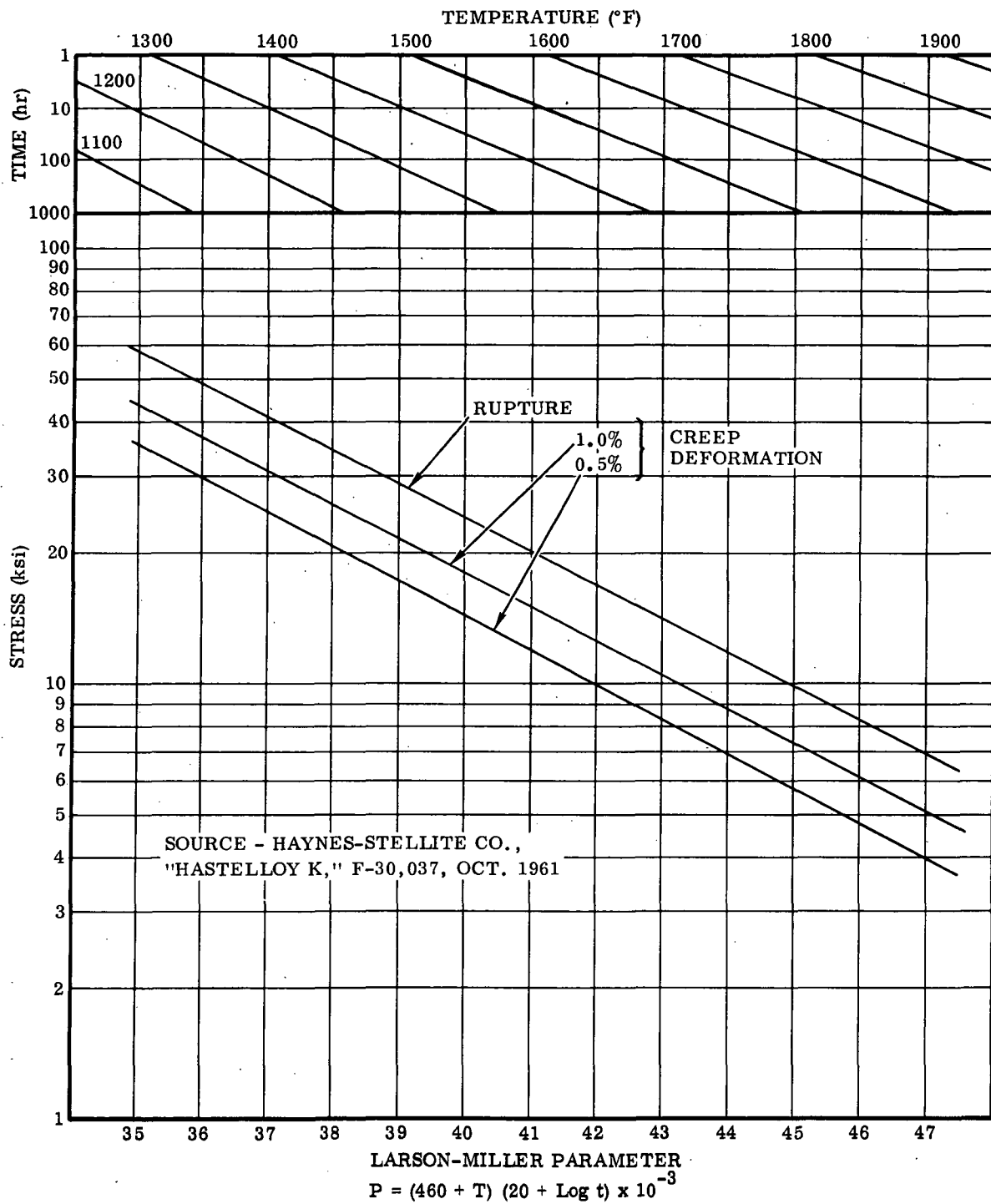


Figure 2-57. Creep Data for Hastelloy X, Annealed

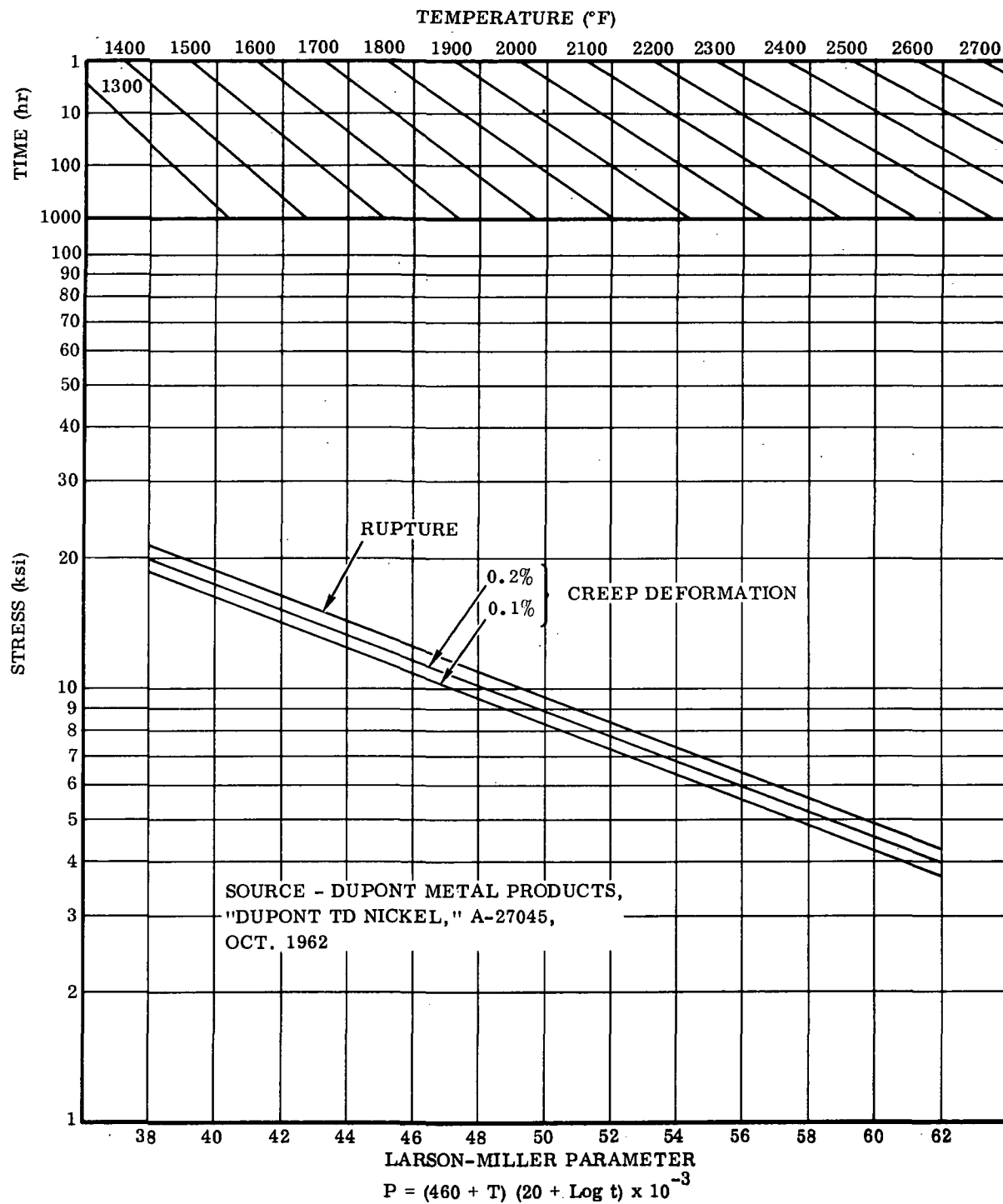


Figure 2-58. Creep Data for TD Nickel, As Rolled

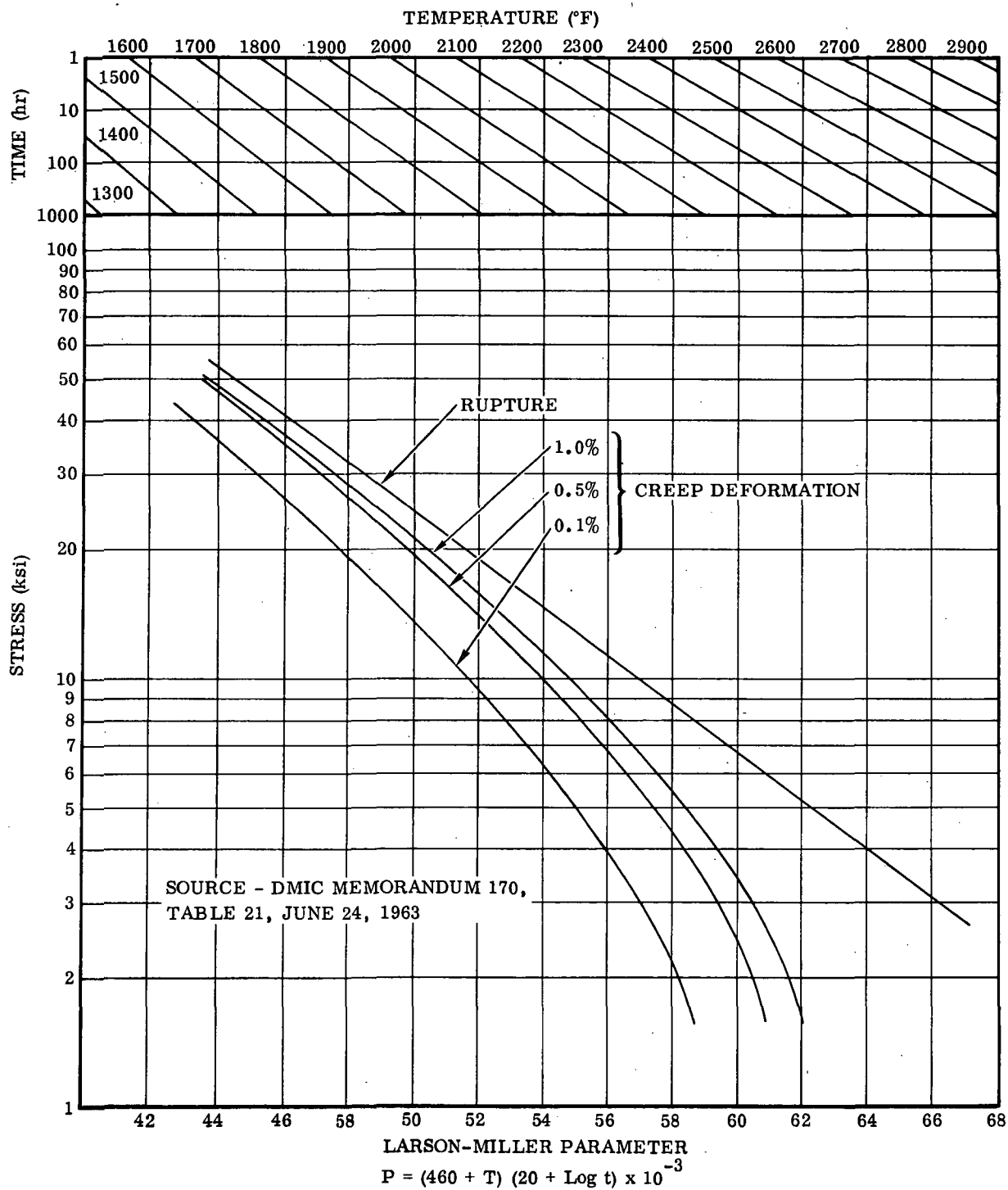


Figure 2-59. Creep Data for B-66 Columbium, Recrystallized, Uncoated

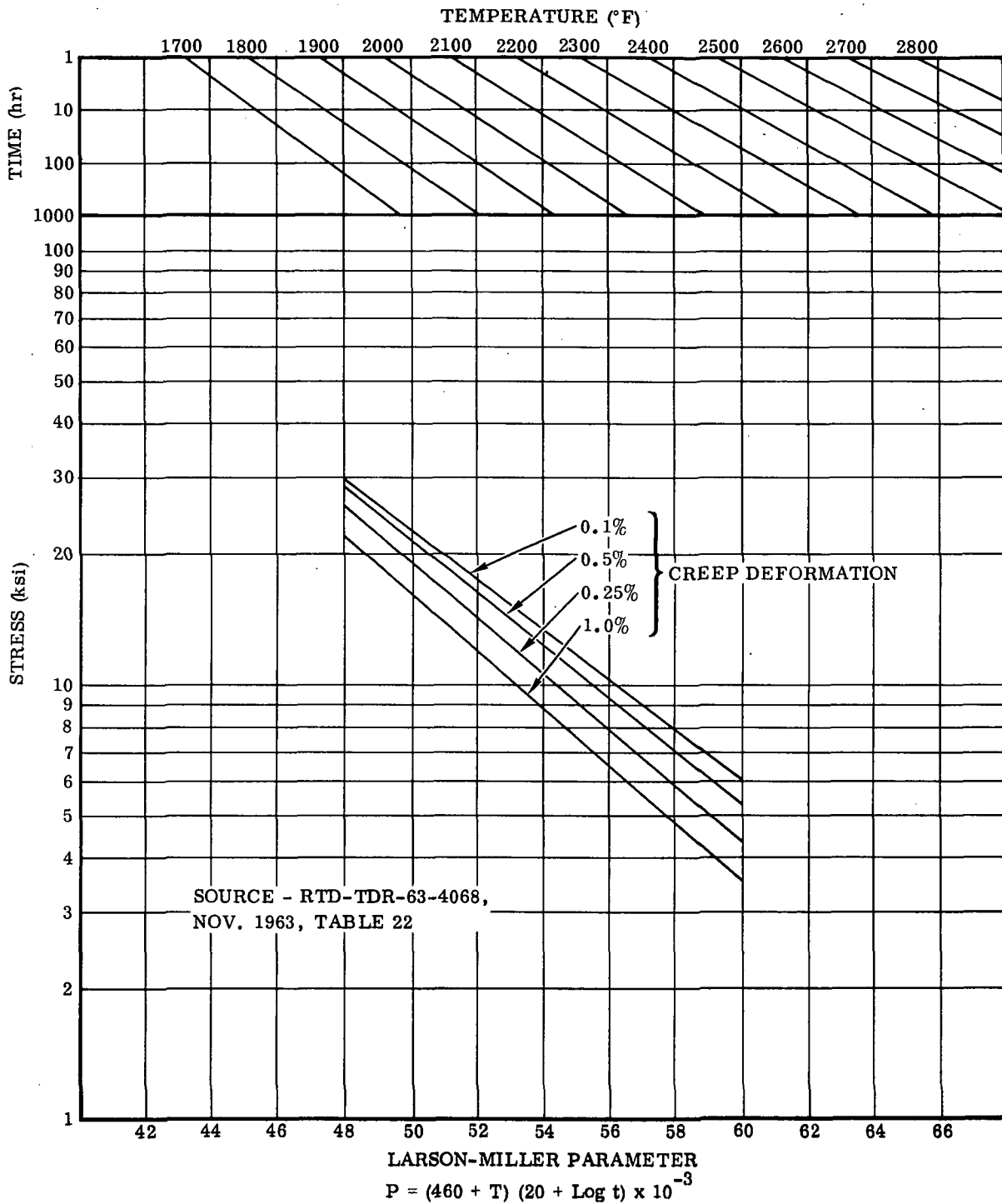


Figure 2-60. Creep Data for B-66 Columbium, Chromizing Corp

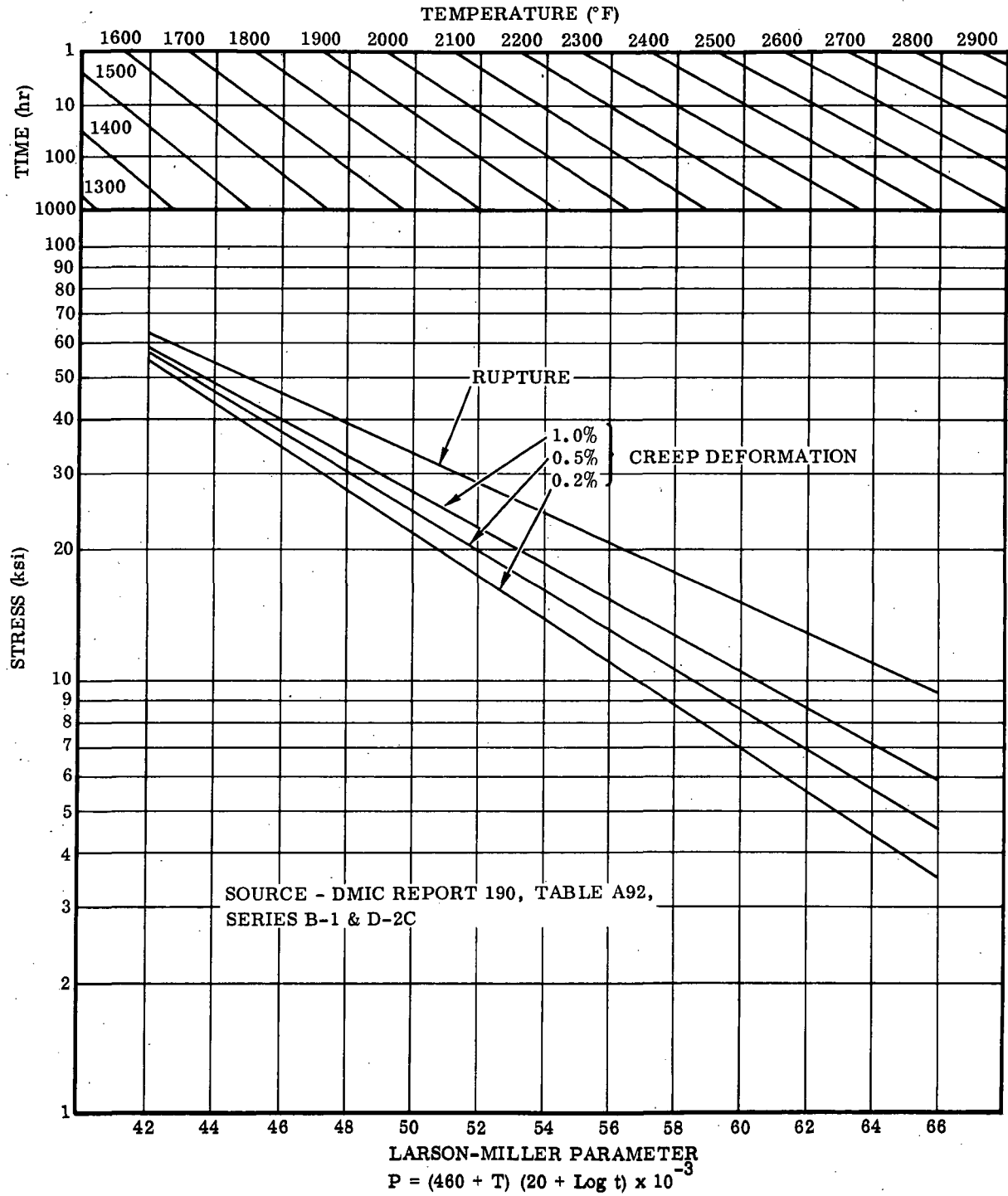


Figure 2-61. Creep Data for TZM Molybdenum, Stream Relieved, Uncoated

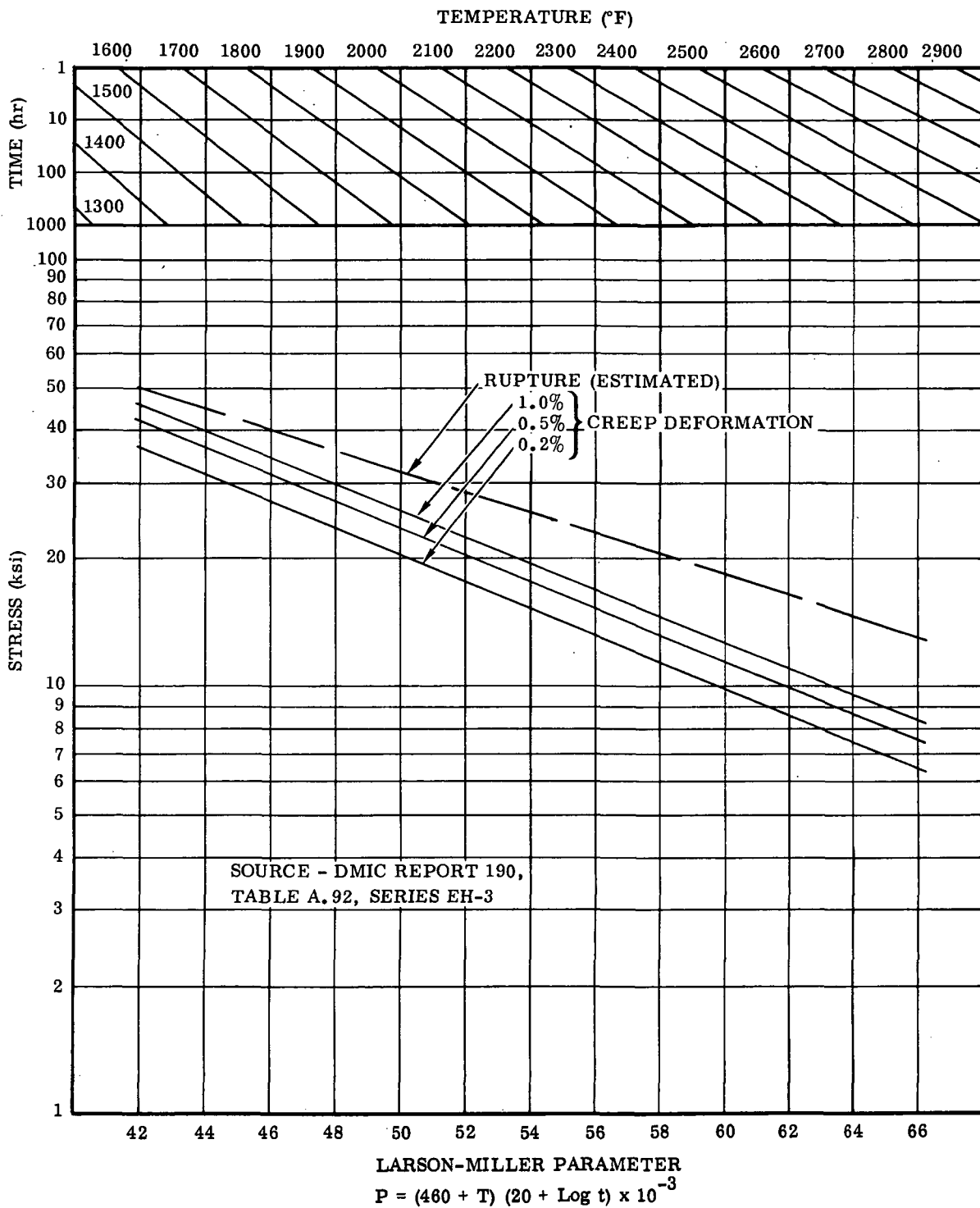


Figure 2-62. Creep Data for TZM Molybdenum, Recrystallized, Uncoated

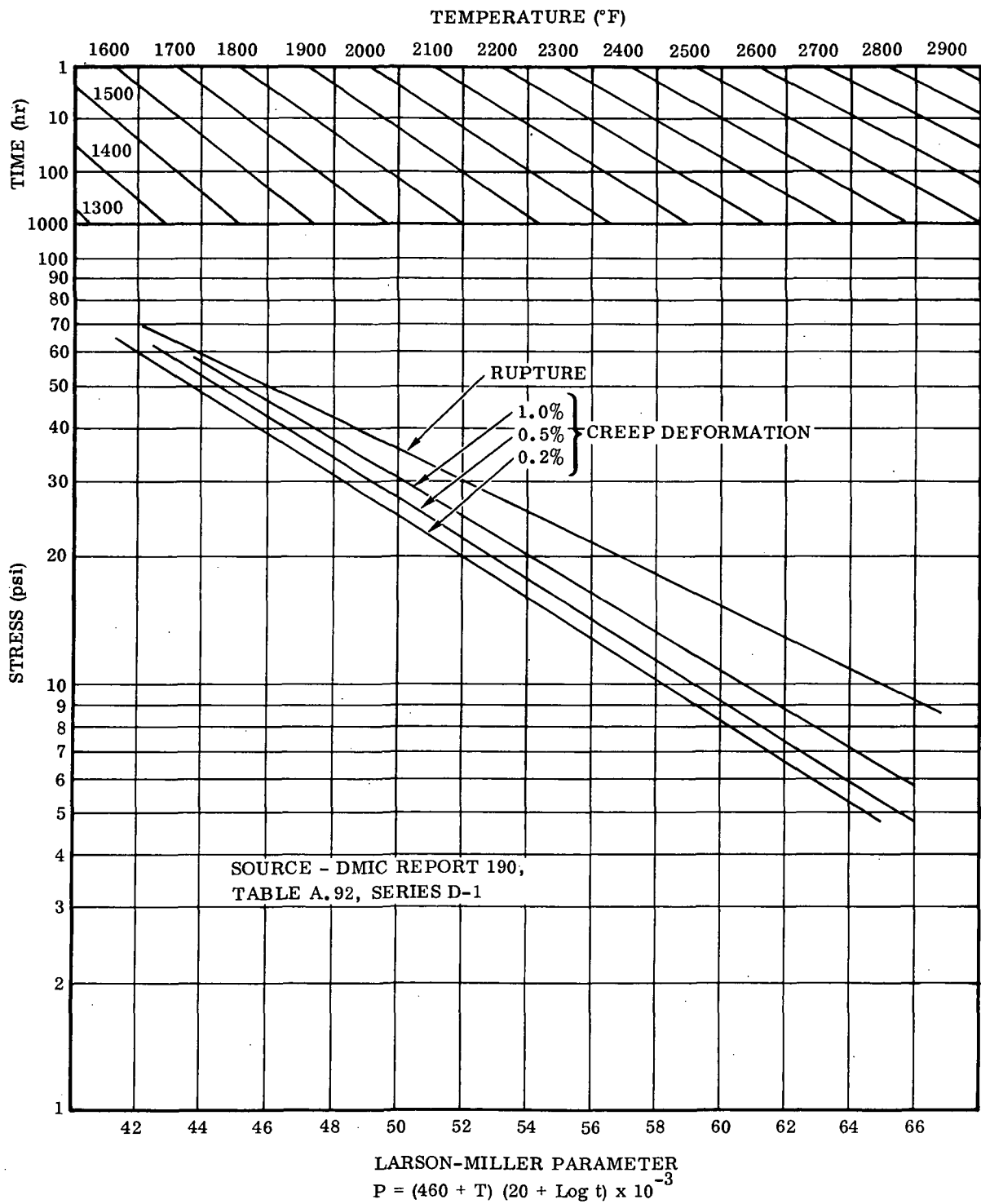


Figure 2-63. Creep Data for TZM Molybdenum, As Rolled, Uncoated

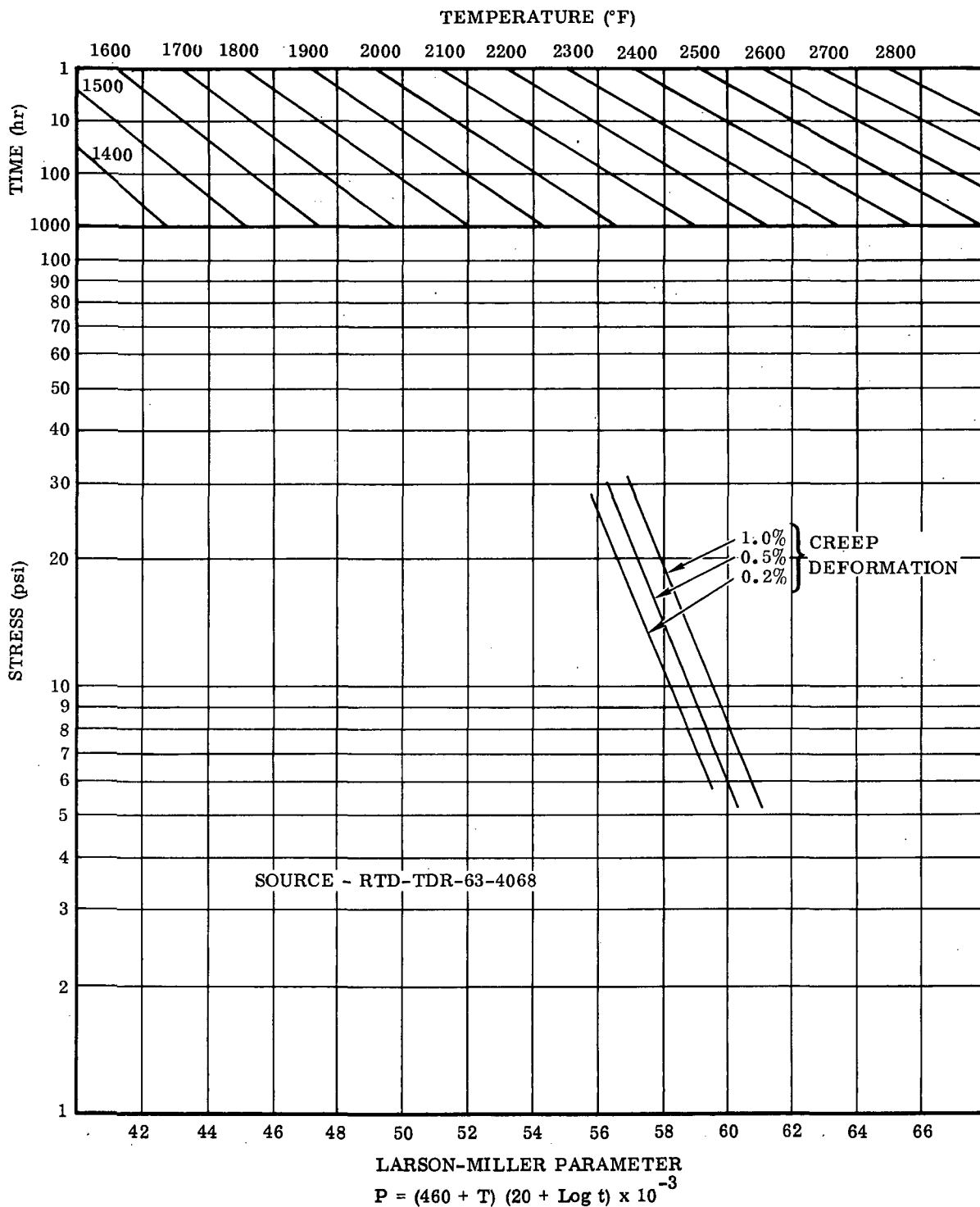


Figure 2-64. Creep Data for TZM Molybdenum, Si, Cr, B Coated  
(Pack Cementation Process)



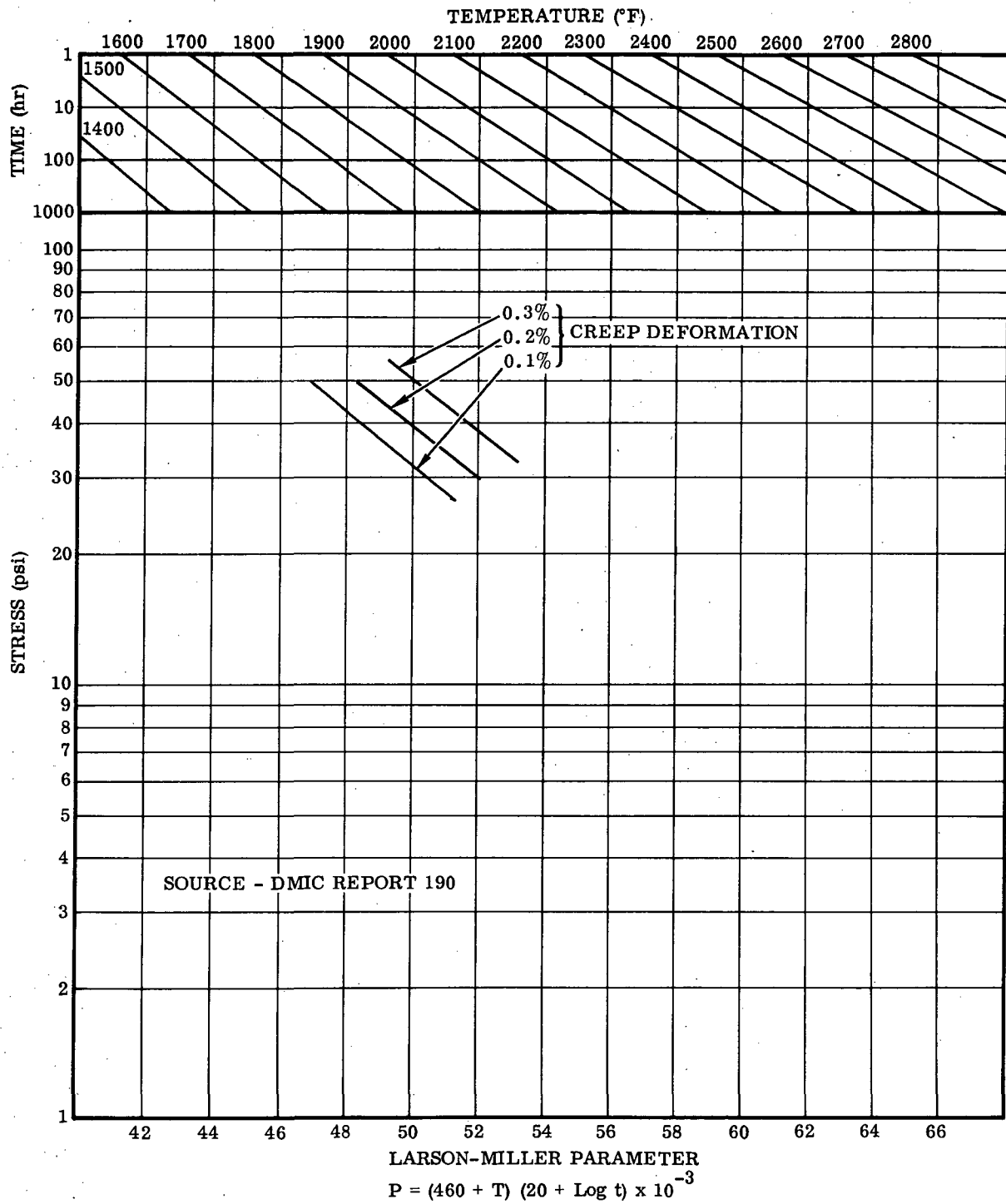


Figure 2-65. Creep Data for TZM Molybdenum, Disilicide Coated

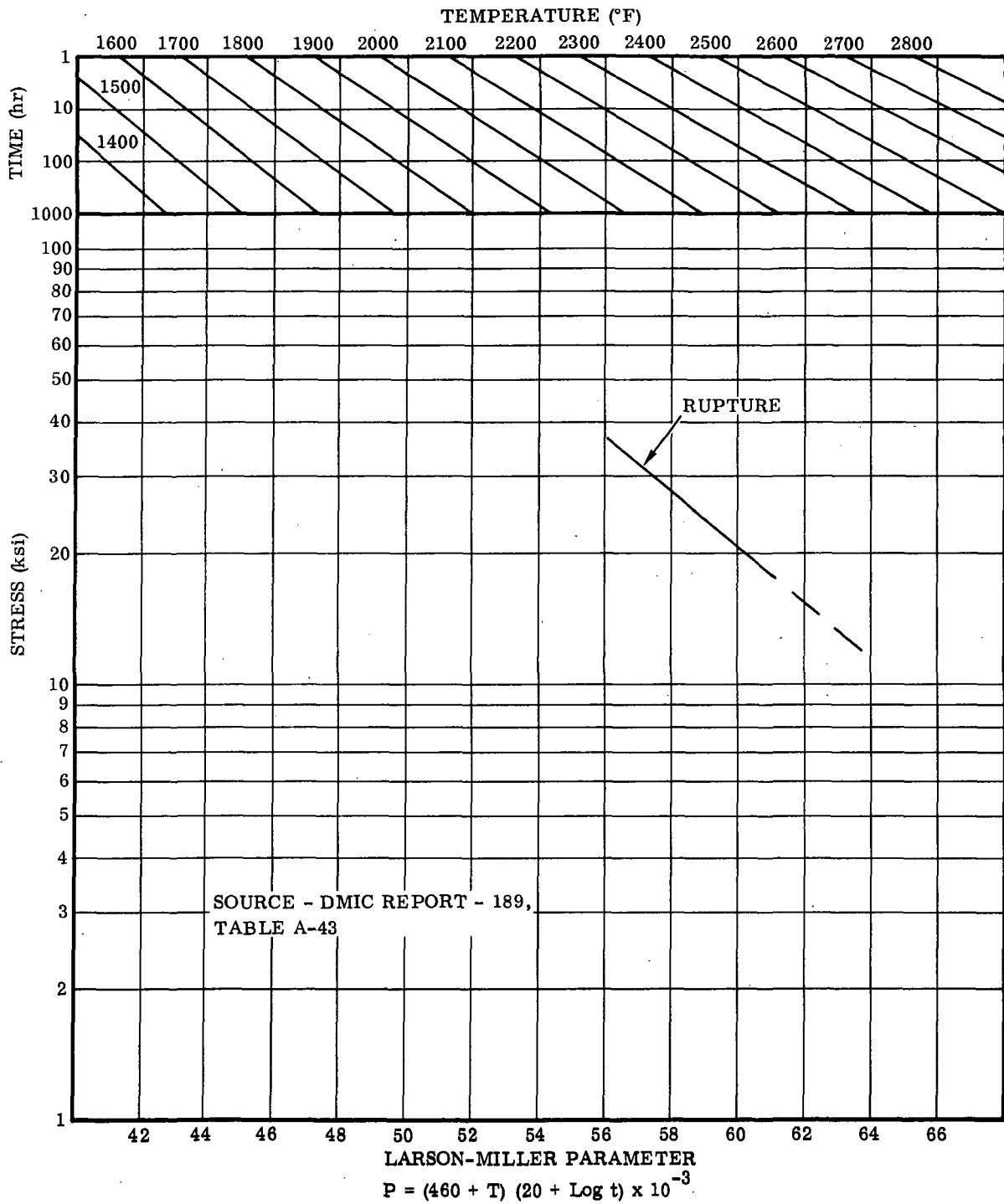


Figure 2-66. Creep Data for T-111 Tantalum, Recrystallized, Uncoated

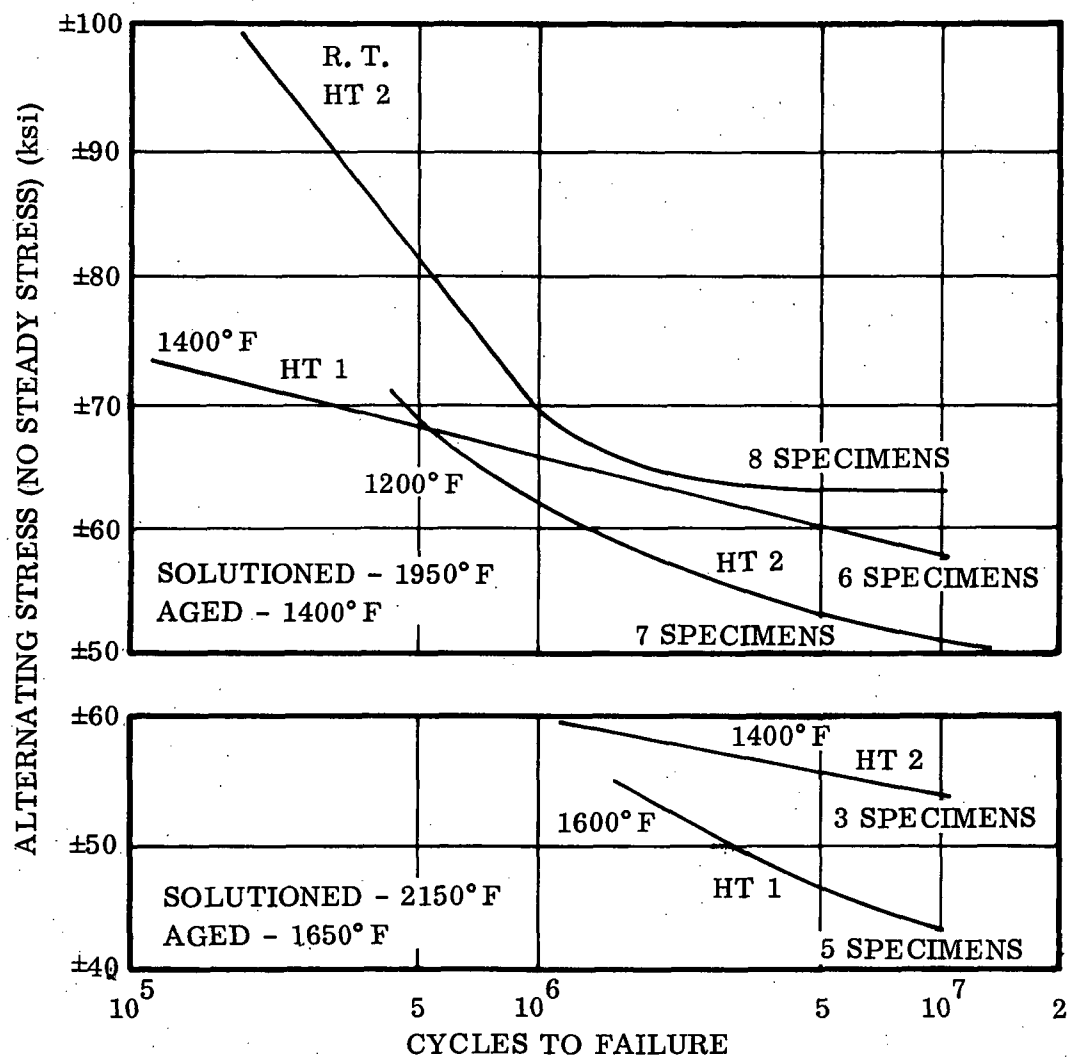


Figure 2-67. S-N Curves for Smooth René 41 Alloy Two Heat Treatments at Room Temperature, 1200°F, 1400°F, and 1600°F with Zero Steady Loads ( $A=\infty$ )

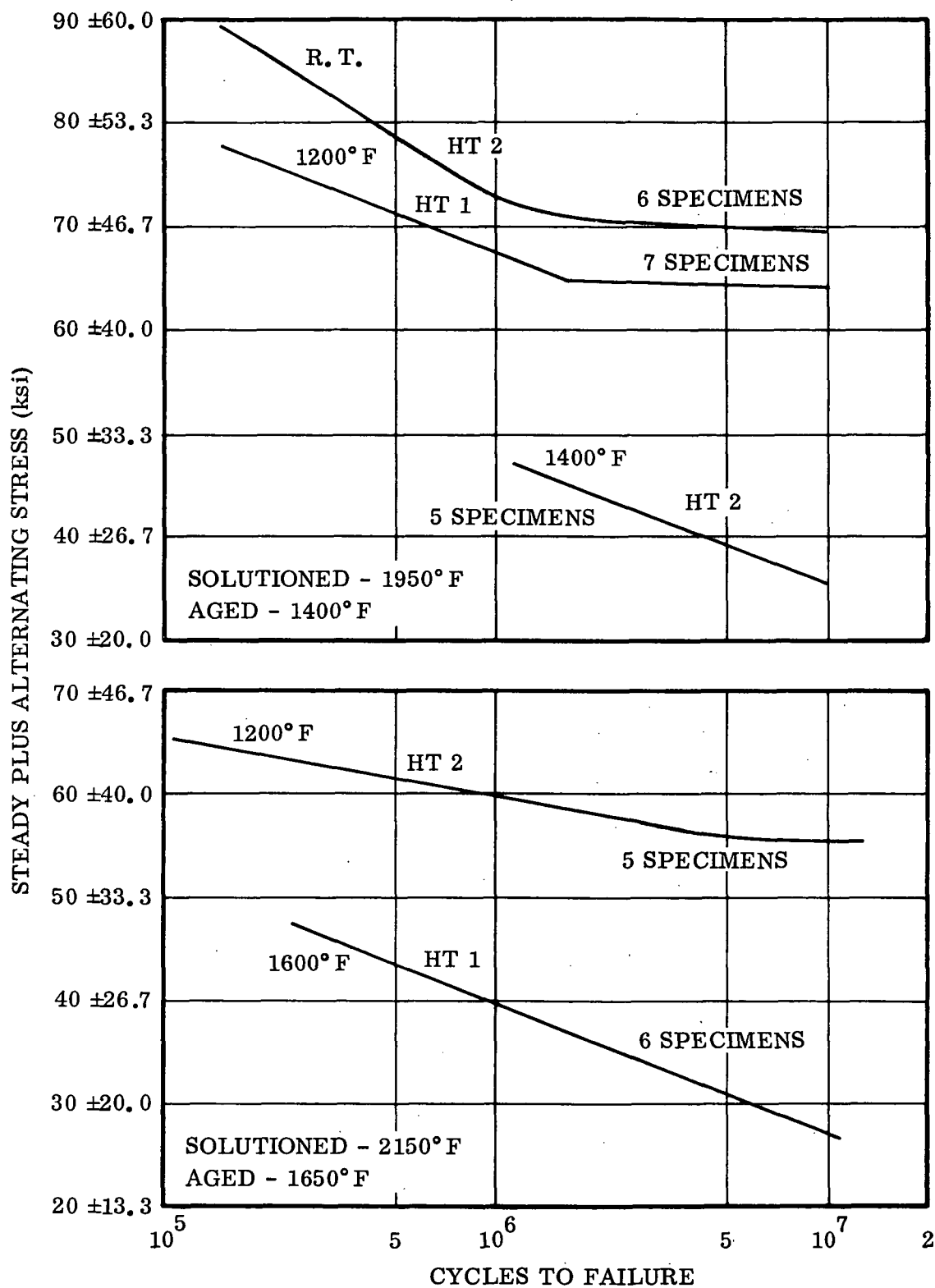


Figure 2-68. S-N Curves for Smooth René 41 Alloy, Two Heat Treatments at Room Temperature, 1200°F, 1400°F, and 1600°F with Steady Loads ( $A=0.67$ )

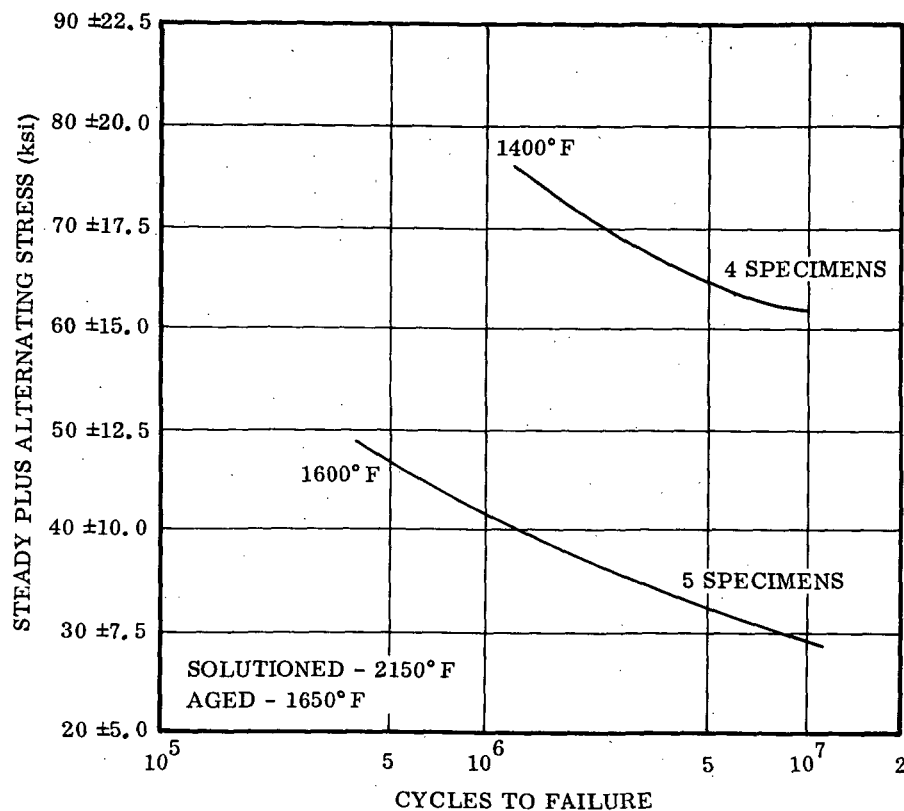


Figure 2-69. S-N Curves for Smooth Rene 41 Alloy, One Heat Treatment, at 1400°F and 1600°F with Steady Loads ( $A = 0.25$ )

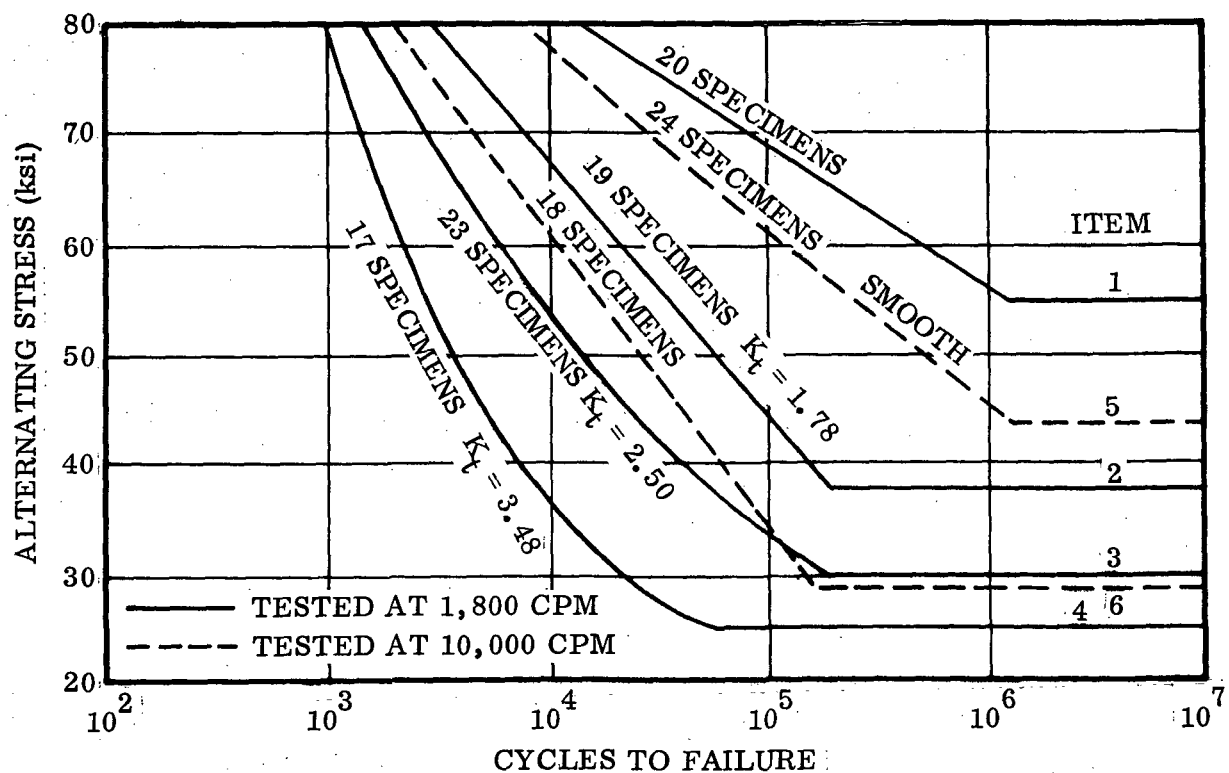


Figure 2-70. S-N Curves for Smooth and Notched Specimens of Titanium Alloy, RC 55 Type

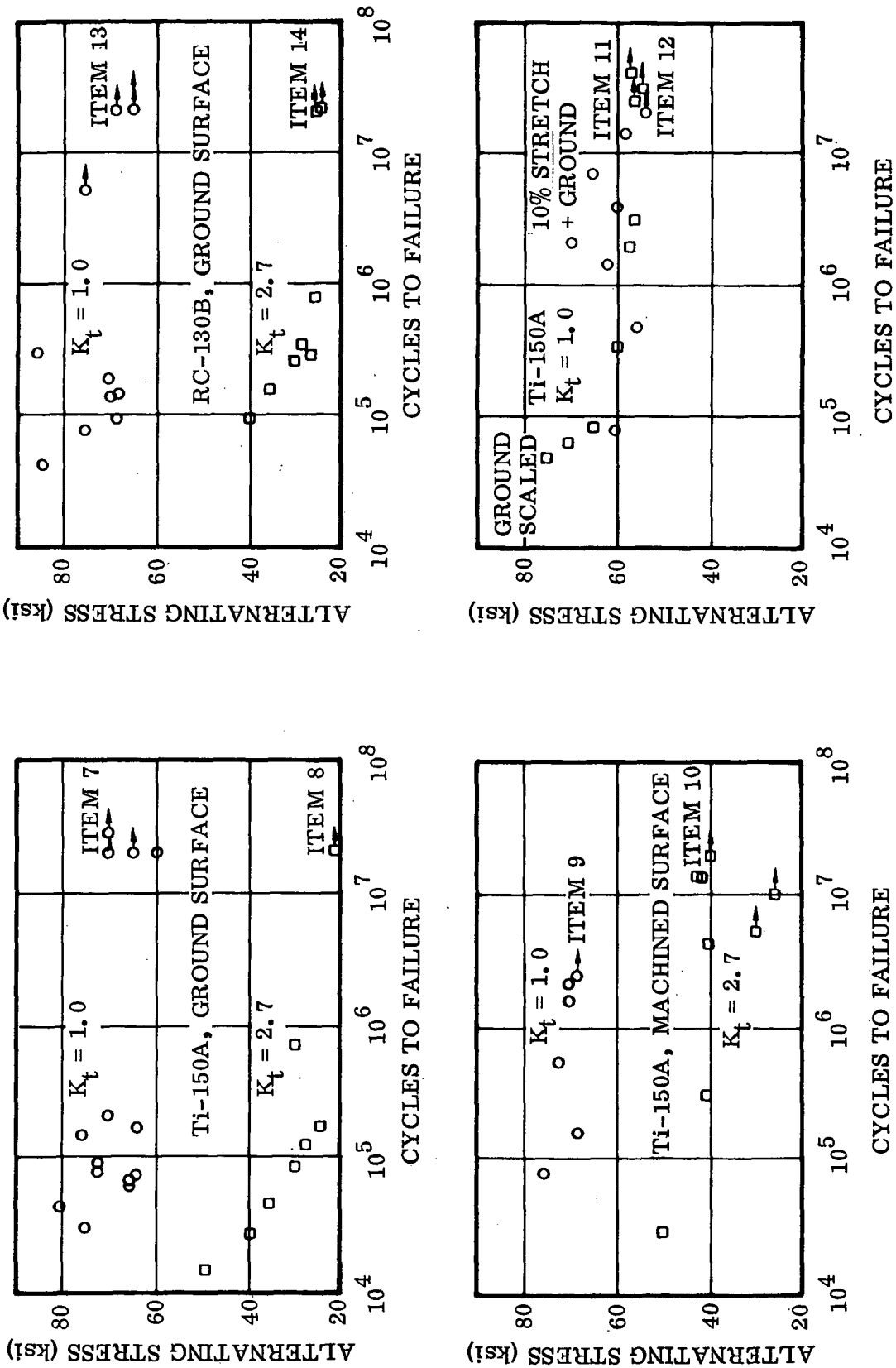


Figure 2-71. S-N Plot of Fatigue Tests of Titanium Alloys Ti-150A and RC-130B

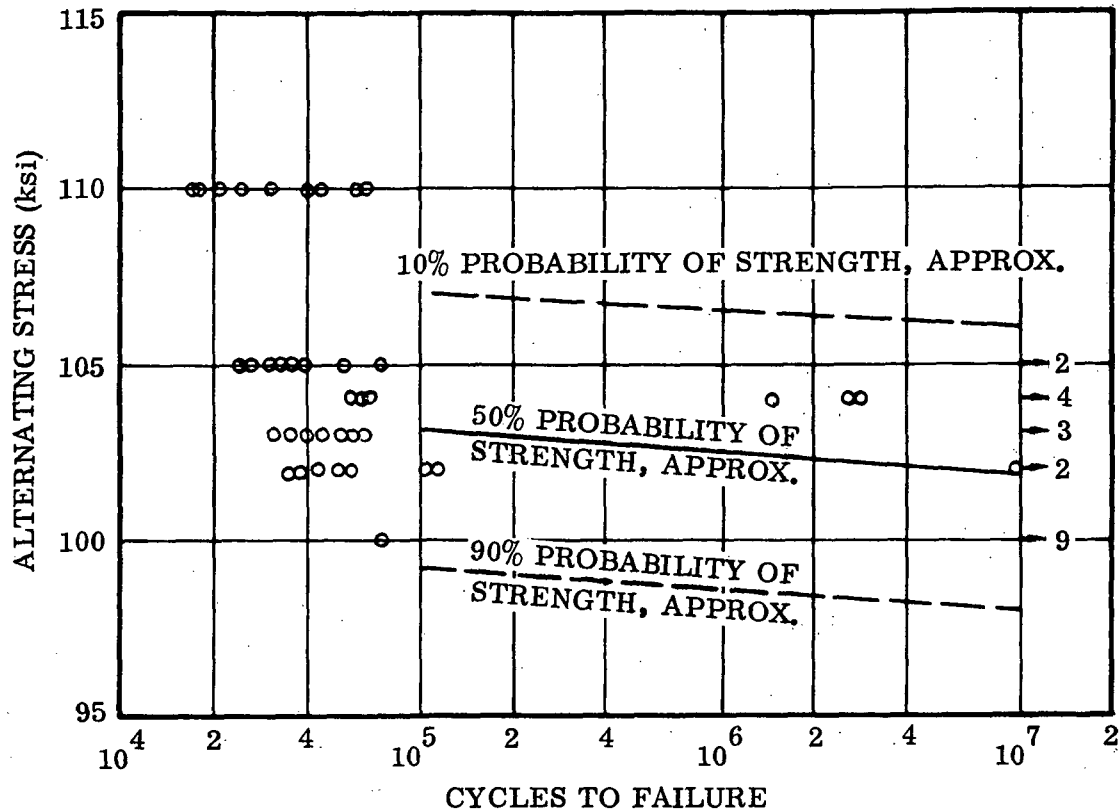


Figure 2-72. S-N Curves for Titanium Alloy RC-130B

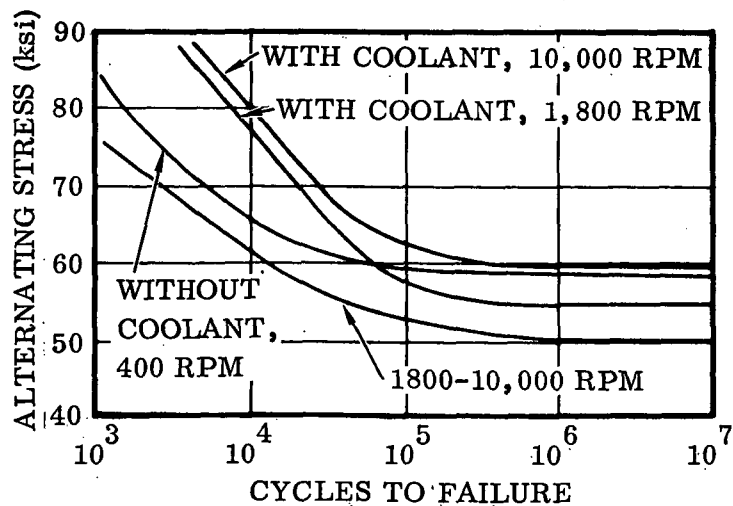


Figure 2-73. S-N Diagram for Ti-75 A Titanium Alloy Tested at Different Speeds With and Without Coolant

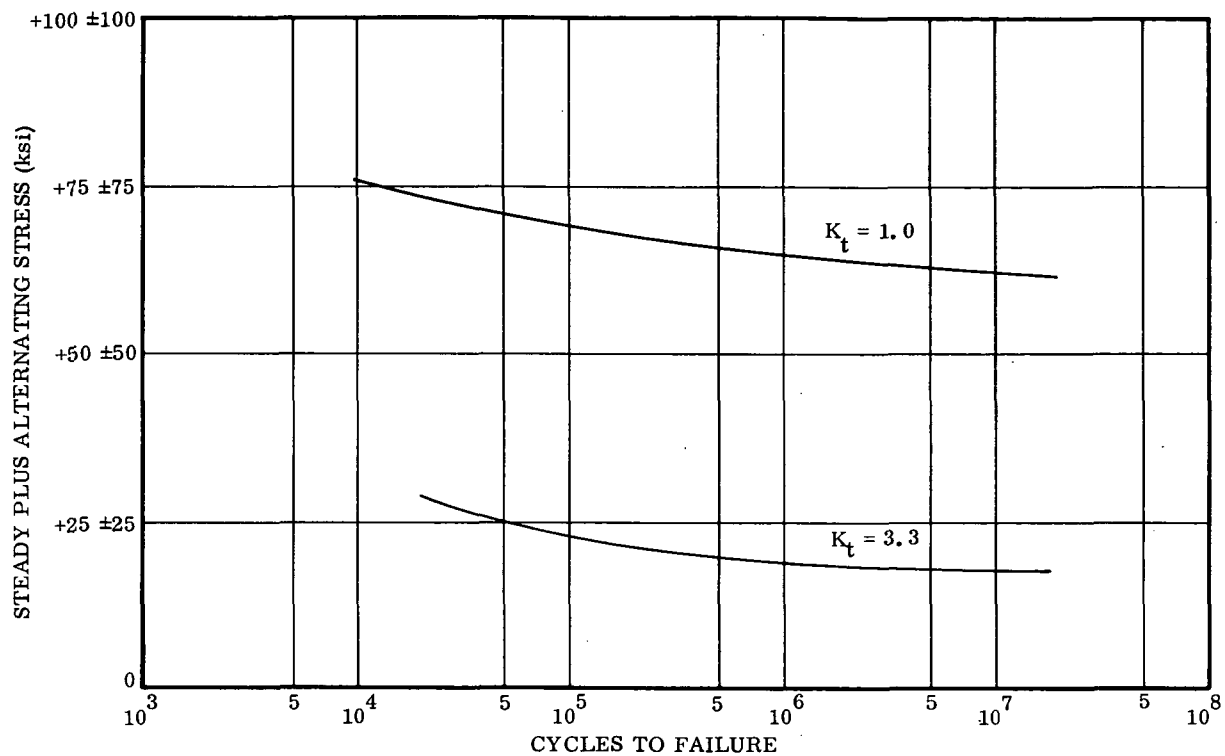


Figure 2-74. S-N Curves for 6Al-4 V Titanium Alloy Bar, Heat Treatment to 160 ksi Minimum UTS



### SECTION 3

#### OPTIMIZATION STUDIES

As part of Task 2 of this contract, a preliminary computer study was undertaken to demonstrate the application of the TPS sizing technique to optimization of the space shuttle TPS. In general, optimization procedures require evaluation of a performance index, which is to be extremized subject to constraints on the system. The constraints are reflected as penalties to the index. For the TPS, two performance indices not necessarily mutually compatible are considered: weight and cost. Under normal circumstances, as system weight decreases, its sophistication and complexity in terms of materials, design, manufacturing, installation, inspection, and refurbishment often drive system cost up. Using either weight or cost as the performance index, a number of control parameters must be considered to evaluate how well the TPS functions. These are the constraints on the system; they determine how well the TPS protects the vehicle from a hostile aerothermodynamic environment. The insulated cover panels provide the aerodynamic surfaces that allow the vehicle to fly by transferring aerodynamic loads from the surface to the load-bearing structure. Aerodynamic heating elevates the temperature of both the cover panels and the underlying structure, a behavior that decreases a materials' capability to handle these loads. In addition to the static loads caused by both mechanical and thermal stresses, the TPS must withstand dynamic loads produced primarily by engine noise and vibration, the turbulent boundary layer, and other sources. Here again performance is measured by how well the system can withstand the adverse effects of this environment.

The variables that determine or "drive" the performance of the TPS are the environments themselves, heating rates, static mechanical loads due to aerodynamic pressure and thermal stresses, and the vibrational environment of acoustic excitation. The environments are affected primarily by the trajectory; i. e., rates and integrated heat loads, pressure, and strength and duration of dynamic loads as influenced by engine thrust, duration of firing or running, and period of oscillation in the turbulent boundary. Other forcing functions such as panel flutter exist (an analysis has already been implemented in the next generation TPS sizing procedure), but they are not considered in the present methodology.

Once a given mission or trajectory has been selected and a certain area of the vehicle considered, the environments are essentially specified. To evaluate how well the system performs requires prediction of the response of the TPS to the environments. For the thermodynamic considerations alone, such an analysis is formidable since it requires solution of a finite difference statement of the energy equation over a period that may last 2500 seconds in real time for the orbiter. One of the simplest constraints on this analysis is to specify that some portion of the system, such as the primary structure, must not experience a temperature greater than some specified value.

If the system has only one component, the trajectory analysis is repeated for different thicknesses of this material until the variation of the primary structure temperature with thickness can be established. Then the TPS thickness that maintains the assigned temperature constraint can be established. For a one-dimensional heat transfer model, the problem is solved. However, problems of the shuttle TPS are more difficult and the solution is more complex. Flat plate panels, although good subjects for a one-dimensional heat transfer analysis, are inefficient in transferring aerodynamic loads. Therefore more complex configurations such as both open and closed corrugated panels are required. These in turn necessitate at least a two-dimensional heat transfer model to adequately predict the conduction and radiation between various elements of the panel. For the extremely high heating rates of the orbiter trajectory, the heat capacity of the metallic panel itself is an inefficient method of reducing heat transfer to the underlying primary structure. In the process of reducing heat transfer through the system, panel temperature is increased at a sacrifice in mechanical strength. Another extremely important factor in establishing metallic panel thickness is panel size, or more to the point, the distance between supporting elements of the structure. For the configurations considered in this contract, in which isolated elements are analyzed by state-of-the-art technique as simply support beams under uniform loading, panel thickness is determined by the distance between supports. The distance between support dictates panel width; hence the problem grows more involved. In an attempt to minimize TPS weight locally per unit area, panel size, thickness, and insulation size must be varied throughout the trajectory and the performance index, weight, must be evaluated.

The next consideration to be made concerning a true TPS optimization procedure is the configuration of the panel. Should it be an open corrugation similar to a sine wave, or should the waves have flat areas? Should one consider a sheet stringer configuration with a flat surface but stiffened by some sort of corrugated back plate? Or should the panel be an integrally stiffened one machined from a single piece of material? The variations are endless. Next, consider the insulation material itself. What is its configuration? What is the value of the insulation emissivity? Finally comes the problem of material selection. Which of the many metallics should be considered? It quickly becomes clear that the number of variations in panel geometry, configuration, and material as well as those of the underlying insulation becomes overwhelmingly large. The number of variables must be drastically reduced to realistically consider a computer program that must be performed in the short run times required. The amount of material property data that can be reasonably stored in a computer of large but finite core size quickly established the limitation of using only one panel material instead of letting the computer select from a number of possibilities. Next, the complexity of the discrete element stress analysis and the necessity of transforming general panel characteristics such as panel length, width, number, and shape of corrugations and the like into the finite elemental volumes of the model dictate the choice of one configuration per run. The resulting variations in parameters were obvious: panel and insulation thicknesses. Since varying the metallic panel thickness to change its heat capacity and thus either increase or decrease the temperature of the underlying primary structure (the usual thermodynamic constraint) is a rather

inefficient technique as opposed to changing insulation thickness, it was decided that the latter would be done to satisfy the thermodynamic analysis. The only variations that reasonably affect strength characteristics and the ability to transfer static loads are either panel thickness or size (length and width). It was determined that of these two, thickness is more desirable. Thus, for a particular trajectory and its associated heat and aerodynamic loadings, the panel size (length and width), its configuration, and its materials are fixed; only the thicknesses are varied. Changing the panel thickness will admittedly change temperature distribution in the panel cross-section. However, for small changes in thickness, the resulting small variations in temperature should have little effect on material property degradation. Also, thermal stresses are a function of temperature gradients, not temperatures, and experience has shown again that for reasonable changes in panel thickness, such as would result from the intelligent choice of initial values made by an experienced TPS designer, gradients and the resulting thermal stresses do not vary drastically.

The optimization procedure, then, is performed by the program user who varies all parameters of interest. For a given panel material and configuration, the usual procedure is to first vary panel size. The user must realize that of the two dimensions, only panel length is significant in the stress analysis. This is the dimension normal to the panel cross-sections defined in Figure 2-18. Panel length determines the forces, hence the internal loads, on the isolated beam used in the stress analysis. For the actual case of sizing the TPS panel, its width will be determined by sizing the supporting structure that handles the load on the panel edges parallel to the cross-section. However, independent analyses conducted at Convair Aerospace indicate that for the high damping ratios generated by the slip joints between panels, minimum gauges are the design point for both support rails and posts. Thus, to determine minimum weight per unit area for a specified configuration and material type, panel length will be varied for a number of panel widths, and the optimum panel dimensions will be those that give minimum weight. The best of a number of different materials for the same panel configuration is determined first by establishing optimum panel dimensions for each material, then comparing weights for each optimum size. For example, the minimum weight of 2 pounds per square foot of a 12 x 24-inch panel of material A will be compared to the minimum weight of 1.9 pounds per square foot of an 18 x 36-inch panel of material B. In turn, the dimensions of the panels of materials A and B have been determined as minimum weights per unit area for variations in length and width of both panels. Each panel configuration can then be compared for a variety of materials. The optimization procedure may also be performed using cost as the performance index.

In this first generation computer program, the determination of panel and insulation thicknesses is performed by an elementary iterative technique which will be improved and whose speed will be increased as experience with the techniques are gained. It is possible that a mathematically rigorous optimization procedure can be adapted to the calculation of thicknesses. However, such an inclusion will require some rather

sophisticated logic at the expense of computer storage space. Improved iterations leading to this investigation will be confined to Newton-Raphson techniques.

The location of the panel on the bottom centerline of the Convair Aerospace booster is shown in Figure 3-1 with an indication of the typical dimensions. Although the booster TPS is really a shell construction as indicated in Figure 3-2, the area was analyzed as a panel under the same assumptions as the orbiter TPS; i. e., each panel is allowed free thermal expansion so that an isolated section can be properly considered as a simply supported beam. The configuration of the panel itself is the so-called "semi-smooth" corrugation of Figure 3-3. The wave length of each corrugation is 6 inches and the depth is 0.4 inch. For the purposes of this analysis, the corrugations were assumed cross-wise to the flow. Two panel widths were considered, one and two feet, and panel lengths were varied from one inch to two feet (Figure 3-4). Since the booster TPS is uninsulated, the mathematical model showing the nodal geometries of the panel and the underlying aluminum cryogenic tank is given in Figure 3-5. For simplicity, the radiation view factors between nodes of the panel and the underlying tank wall were taken as unity; hence, each node of the corrugation sees only the node of the aluminum tank lying immediately below it. (As part of a future study, the radiation interchange factors of this configuration will be more rigorously defined, and the differences effected by this assumption will be assessed.) The panel is René 41, and the thermophysical properties used are shown in Figures 3-6 and 3-7. Parameters were input as tabulated values as required by the computer program. The trajectory flown is given in Figure 3-8. The aerodynamic heating was computed for each run, using the plate-cylinder option for a non-uniform wall temperature distribution (i. e., the flow field is computed as that of a wedge until the shock wave detaches at high angle of attack; thereafter, heating is computed to a swept cylinder). In addition, heating rates to the TPS surface were modified to account for boundary layer separation and reattachment (in a conservative fashion) based on the data of Bertram (Reference 40). This distribution, used for both laminar and turbulent flow, is given in Figure 3-9. Input data required to perform the sonic fatigue analysis are summarized in Table 3-1, and input data for the weights/cost analysis are given in Table 3-2.

The results of this investigation in terms of weight and cost per unit area are shown in Figures 3-10 and 3-11. For this particular minimum gauge supporting structure, with a panel width of two feet, the optimum panel length with respect to weight is six inches; theoretical first unit cost and both recurring and non-recurring production and operations costs (which are primarily weight driven) give the optimum length also at six inches (Figures 3-12 and 3-13). Manufacturing costs show optimum length at six to ten inches. The optimum spacing at such a small panel width (i. e., six inches) for this configuration is not surprising; however, Figure 3-14 shows the results of an earlier study performed by Lockheed for the wing structure of a hypersonic cruise vehicle. For this case also, for a two-foot plate, optimum spacing occurred at twelve

inches (Reference 41). The parameter presented in the Lockheed data is the effective thickness  $\bar{t}$  defined by

$$\text{weight} = (\text{material density}) \times (\text{panel area}) \times (\text{effective thickness})$$

Hence, weight per unit area is proportional to  $\bar{t}$ .

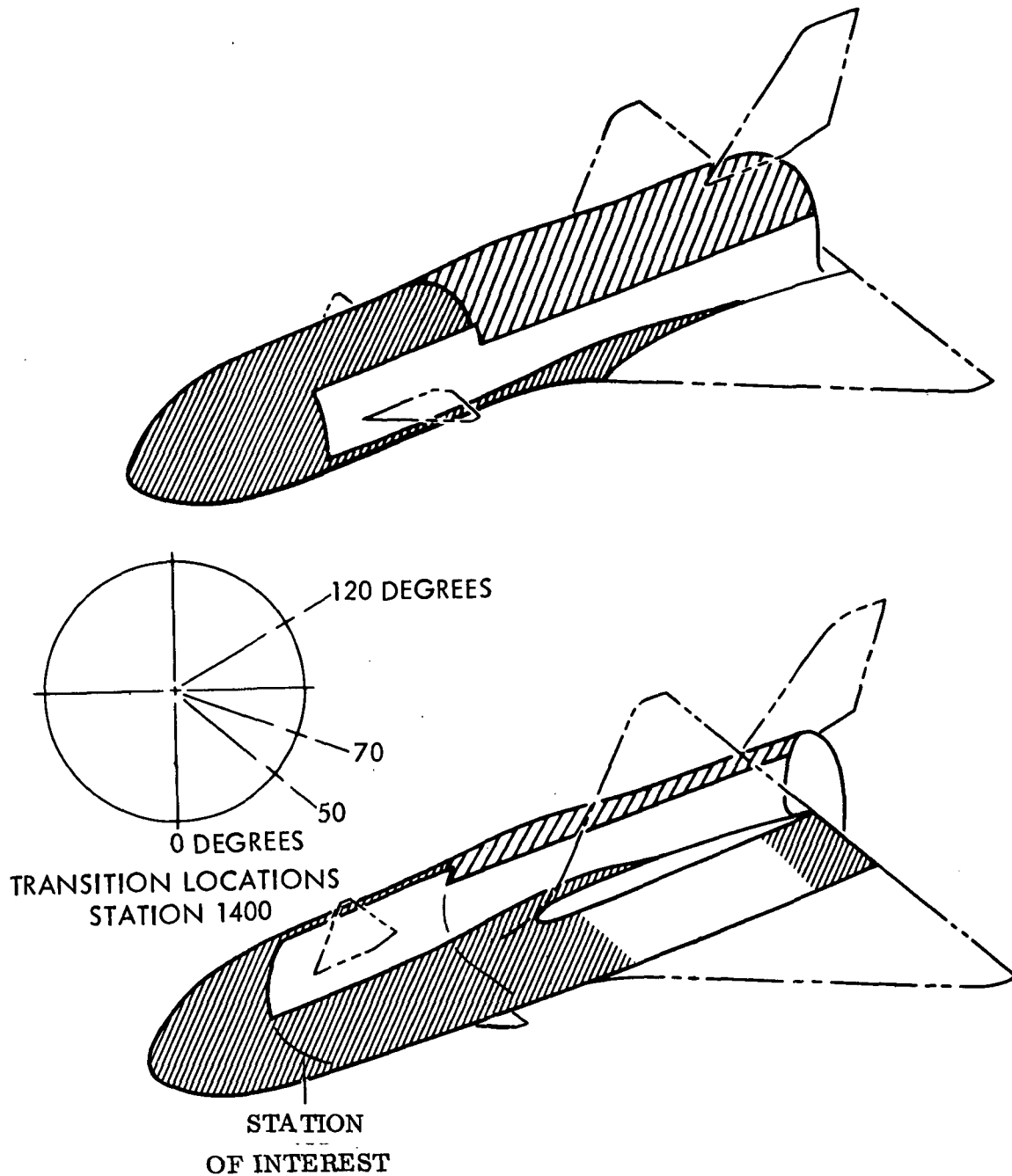


Figure 3-1. Booster Panel Location

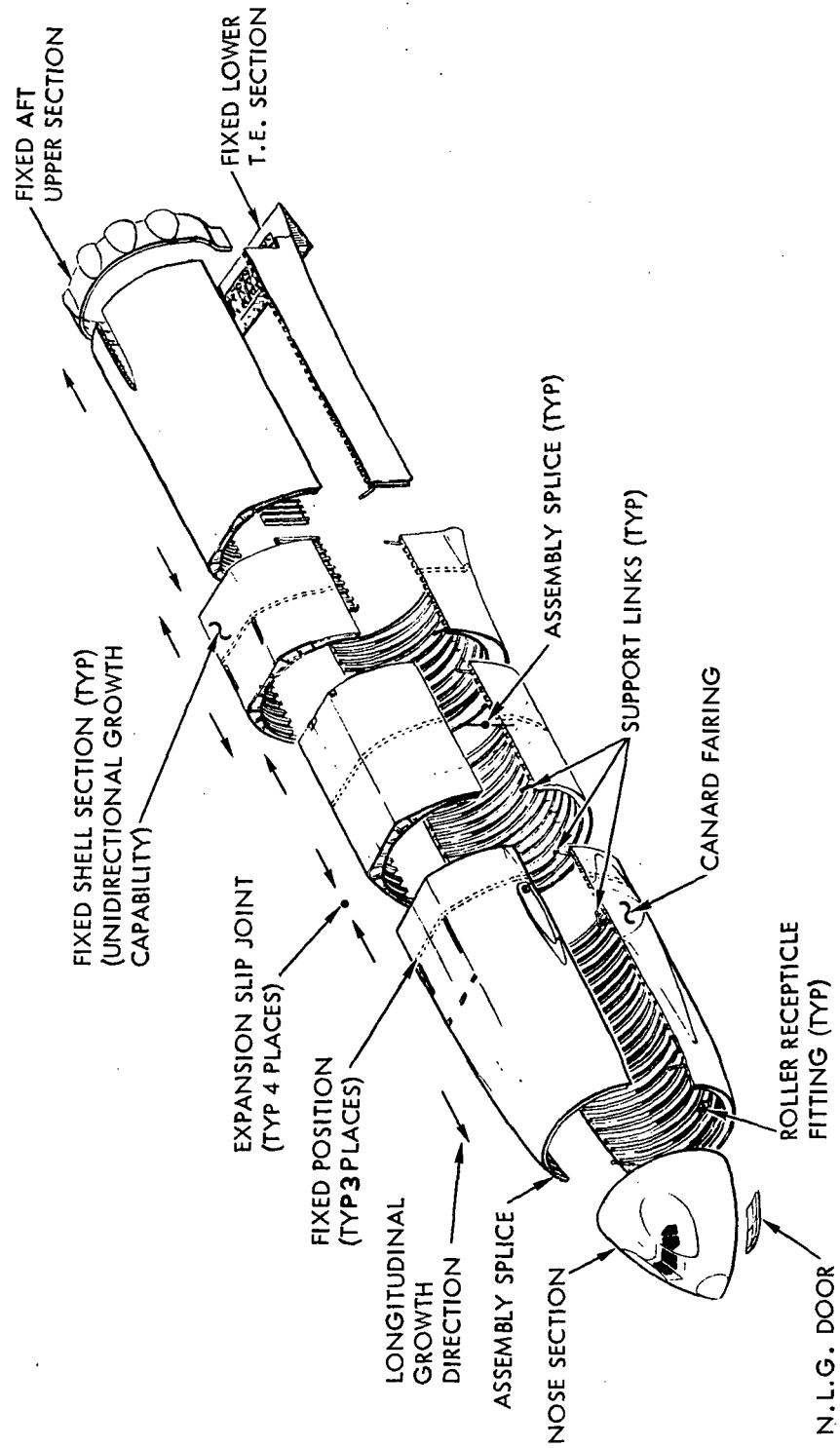
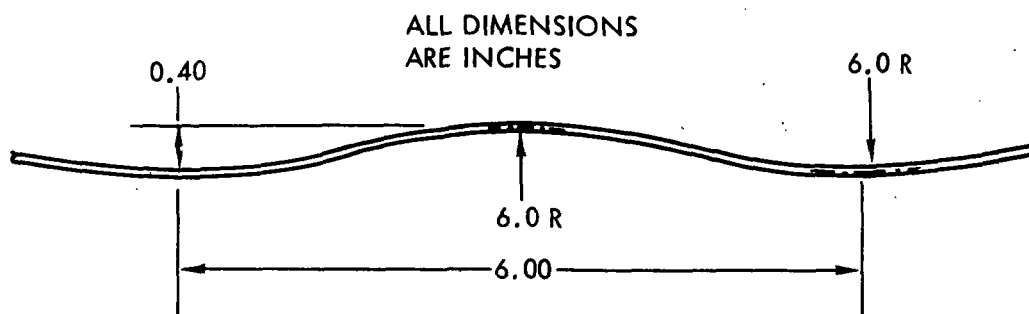
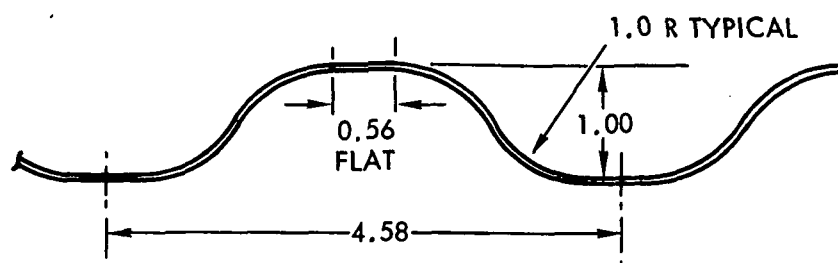


Figure 3-2. Body TPS Shell Structure



SEMI-SMOOTH CORRUGATION



OPEN CORRUGATION

Figure 3-3. Skin Corrugation Geometry

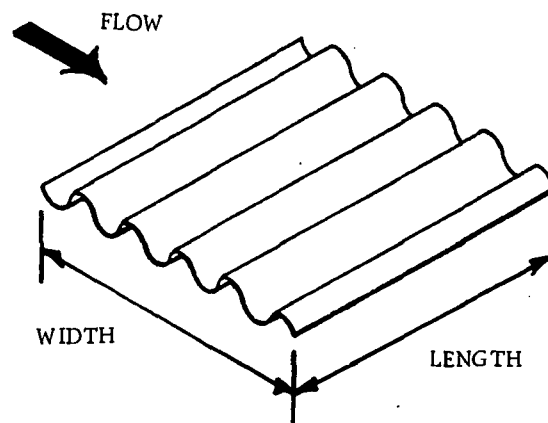


Figure 3-4. Panel Geometry

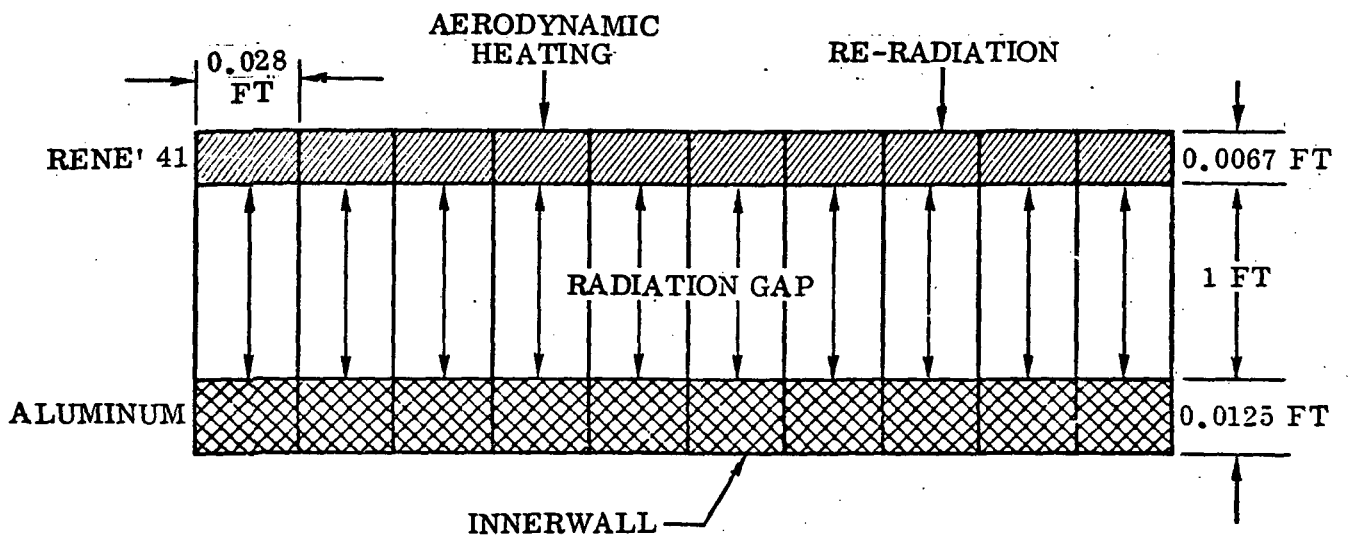


Figure 3-5. Mathematical Model

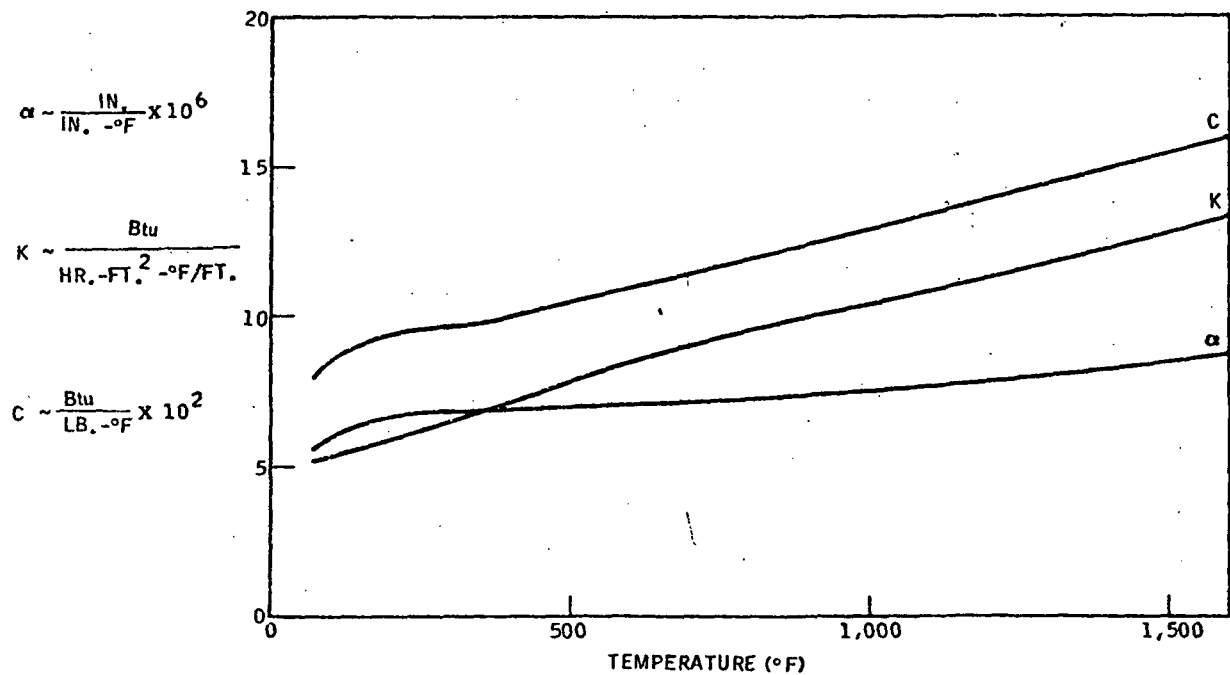


Figure 3-6. Thermodynamic Properties of René 41 Alloy



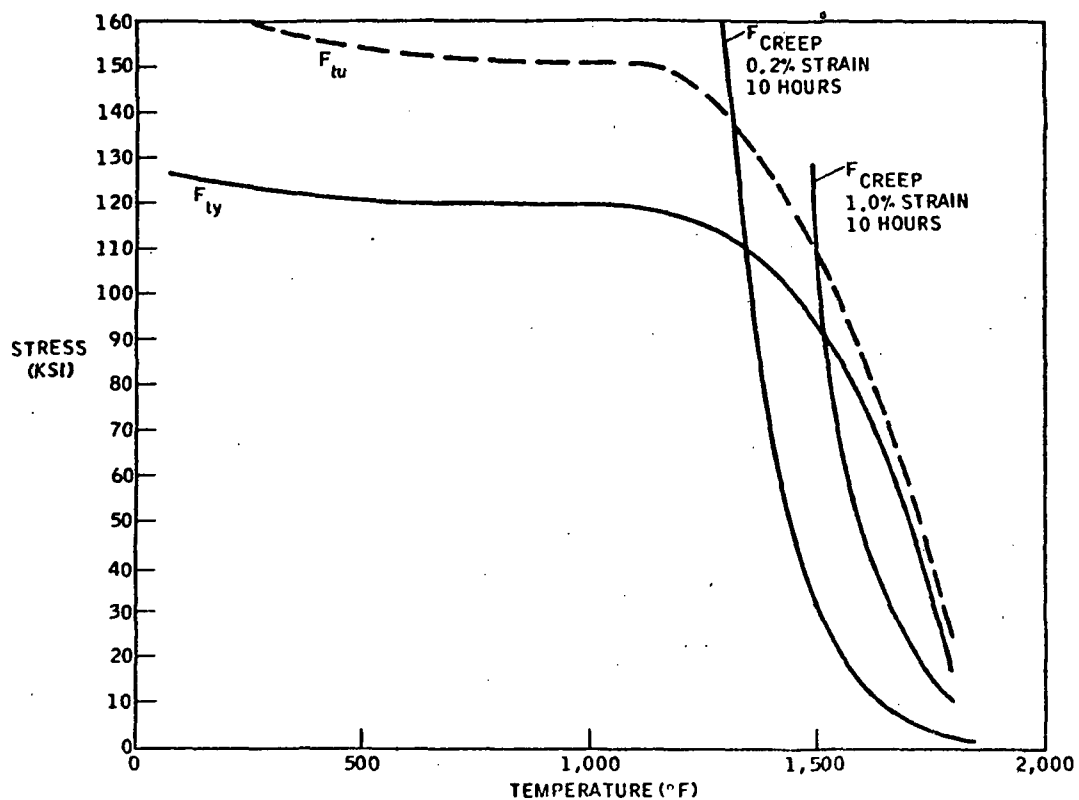


Figure 3-7. Mechanical Properties of René 41

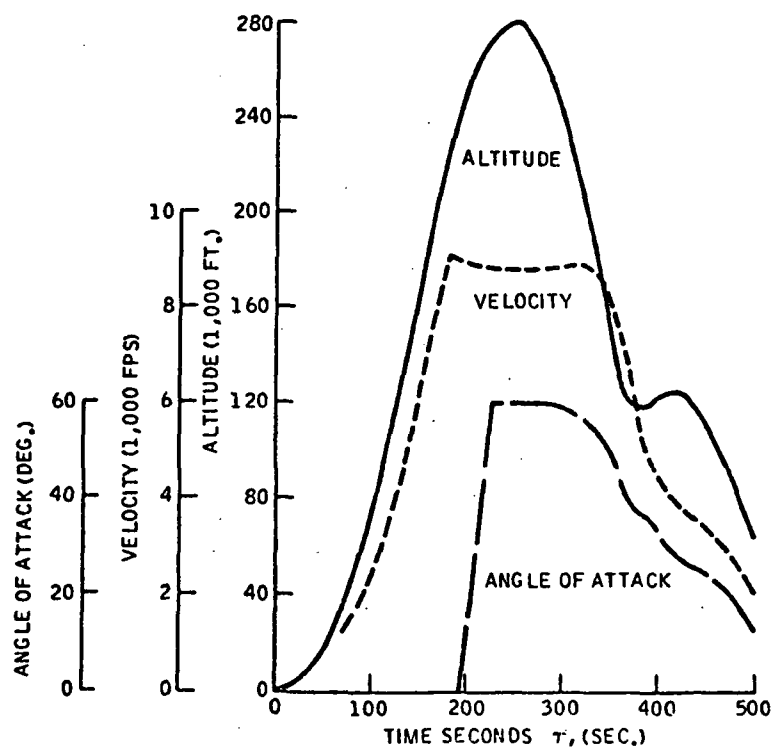


Figure 3-8. Typical Trajectory for Aluminum TPS Study

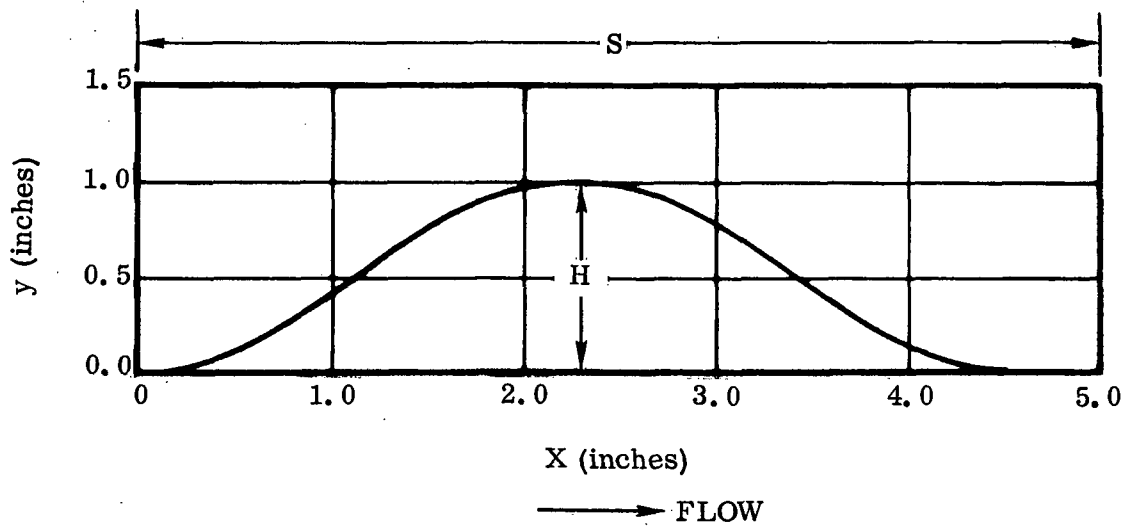
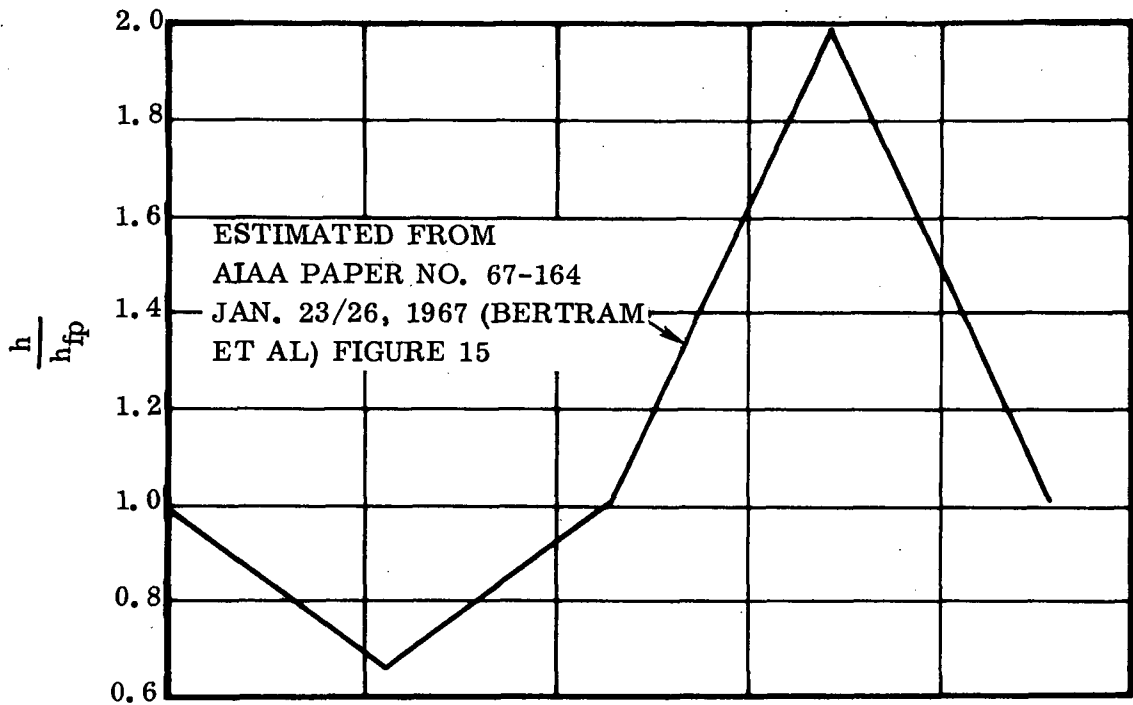


Figure 3-9. Heating Multiplication Factor Distribution

Table 3-1. Fatigue Analysis Input

Period of turbulent boundary layer noise excitation	100 sec
Run length of turbulent boundary layer	100 ft
Local Reynolds number	$10^7$
Local velocity	8000 ft/sec
Local dynamic pressure	$1400 \text{ lb/ft}^2$
Local Mach number	6
Period of rocket engine noise excitation	40 sec
Rocket engine thrust	$10^6 \text{ lb}$
Rocket engine weight flow	1000 lb/sec
Rocket nozzle exit diameter	12 ft
Local sound speed	1000 ft/sec
Distance between point of interest and rocket engine exit	20 ft
Vehicle diameter	40 ft
Period of jet (flyback) engine noise	20 sec
Nozzle exit area	3 ft
Jet velocity	1200 ft/sec
Jet engine weight flow	200 lb/sec
Vehicle velocity at flyback cruise	650 ft/sec
Engine thrust	1000 lb
Axial distance from point of interest to jet exit nozzle	10 ft
Radial distance from point of interest to jet exit nozzle	10 ft
Period of jet (flyback) engine scribbing noise	10 sec
Panel moment of inertia	$10^{-3} \text{ in}^4$
Panel length	0.5 ft
Panel width	2 ft
Panel modulus of elasticity	$10^7 \text{ lb/in}^2$

Table 3-2. Weight/Cost Data Input

Panel type	Corrugated
Panel length	6 in.
Panel width	24 in.
Panel length overlap	1 in.
Panel width overlap	1 in.
Distance between adjacent panels	1/2 in.
Support structure type	1
Insulation thicknesses	0
Insulation densities	0
Number of corrugations across width of panel	5
Corrugation chord length	2 in.
Corrugation radius	6 in.
Skin density	0.300 ft-lb/in <sup>3</sup>
Weight of bolts	0.400 lb/100
Weight of nutplates	0.500 lb/100
Weight of washers	0.100 lb/100
Thickness of corner piece	0.010 in.
Thickness of post	0.020 in.
Density of corner post material	0.300 lb/in <sup>3</sup>
Outside diameter of corner post	1/2 in.
Thickness of corner plates	0.010 in.
Thickness of support tube flange	0.050 in.
Thickness of support tube	0.020 in.
Density of support tube material	0.300 lb/in <sup>3</sup>
Length of support tube	0.600 in.
Thickness of seal strip	0.010 in.

Table 3-2. Weight/Cost Data Input, Contd

Density of seal strip	0.300 lb/in <sup>3</sup>
Thickness of long beam doubler channel	0.010 in.
Thickness of corner doubler plate	0.010 in.
Thickness of long beam	0.010 in.
Thickness of short beam	0.010 in.
Height of long and short beams	0.500 in.
Widths of long and short beam	1.000 in.
Density of beam material	0.300 in.

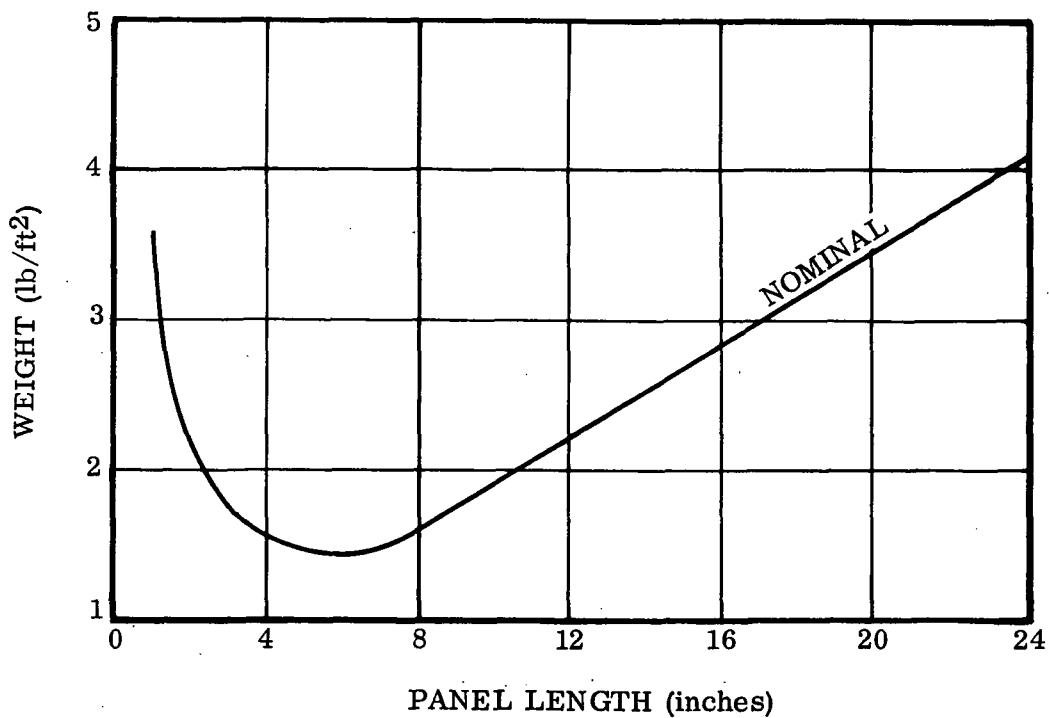


Figure 3-10. TPS Panel Unit Weight

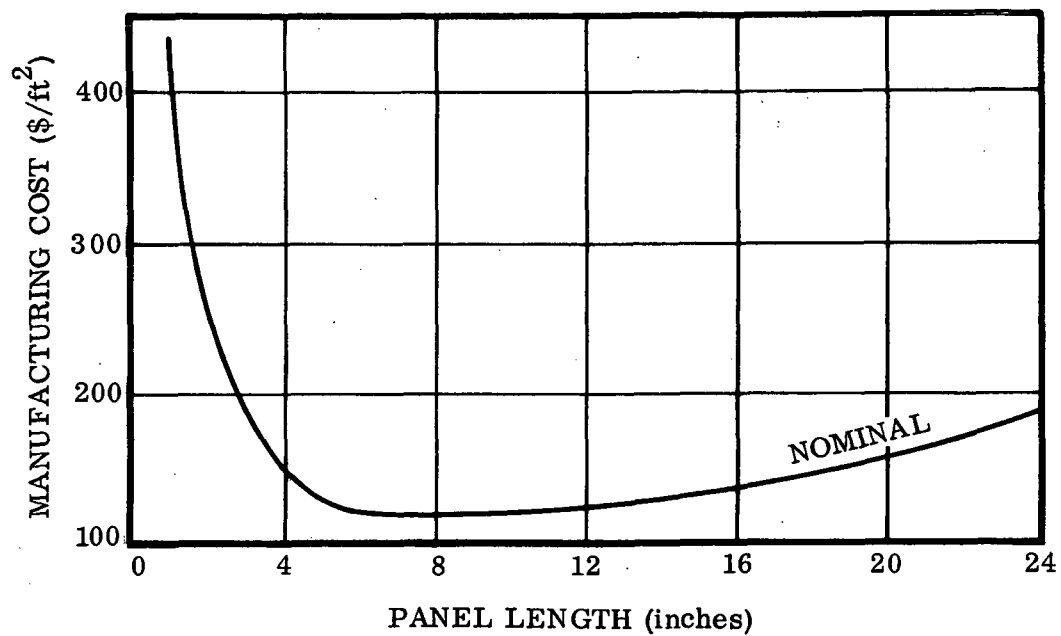


Figure 3-11. TPS Panel Unit Cost

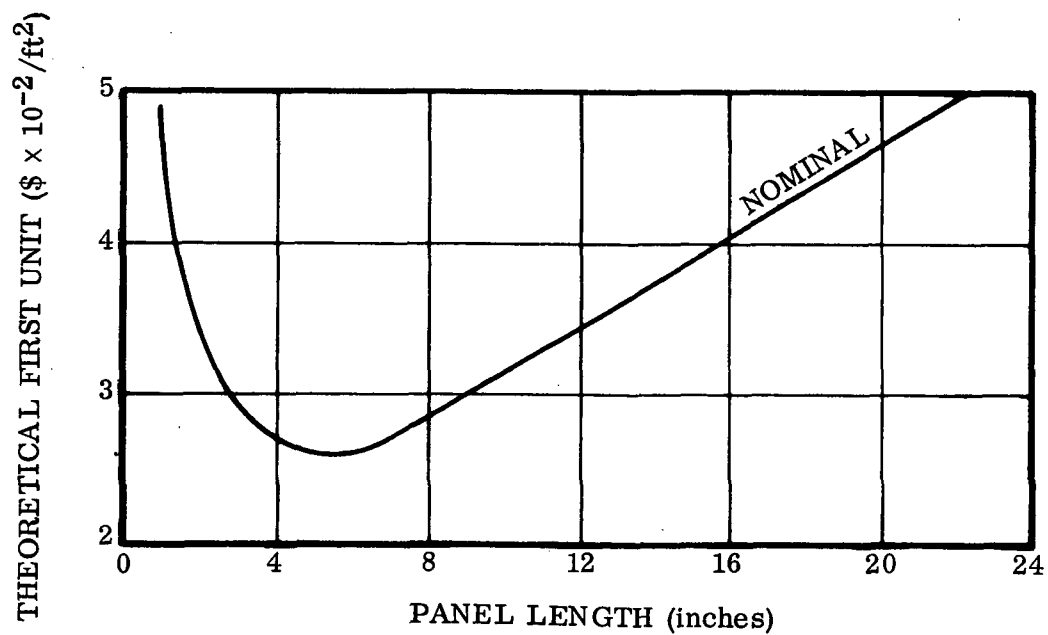


Figure 3-12. TPS Theoretical First Unit Cost

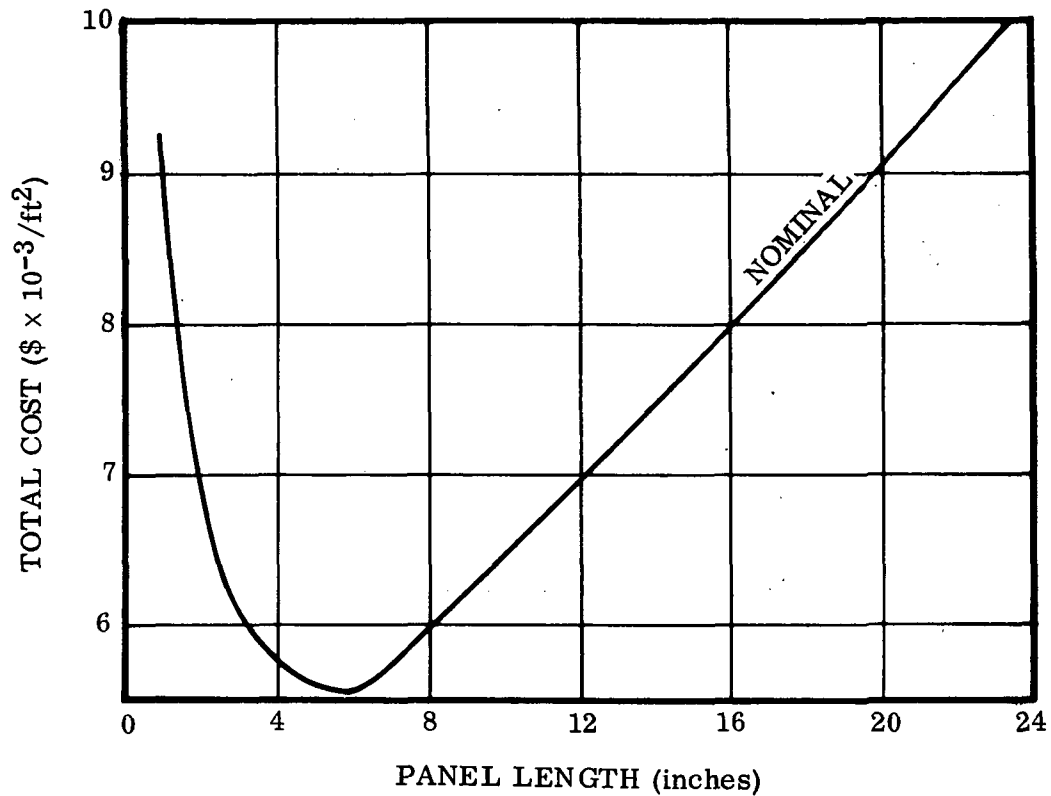


Figure 3-13. TPS Unit Total Cost

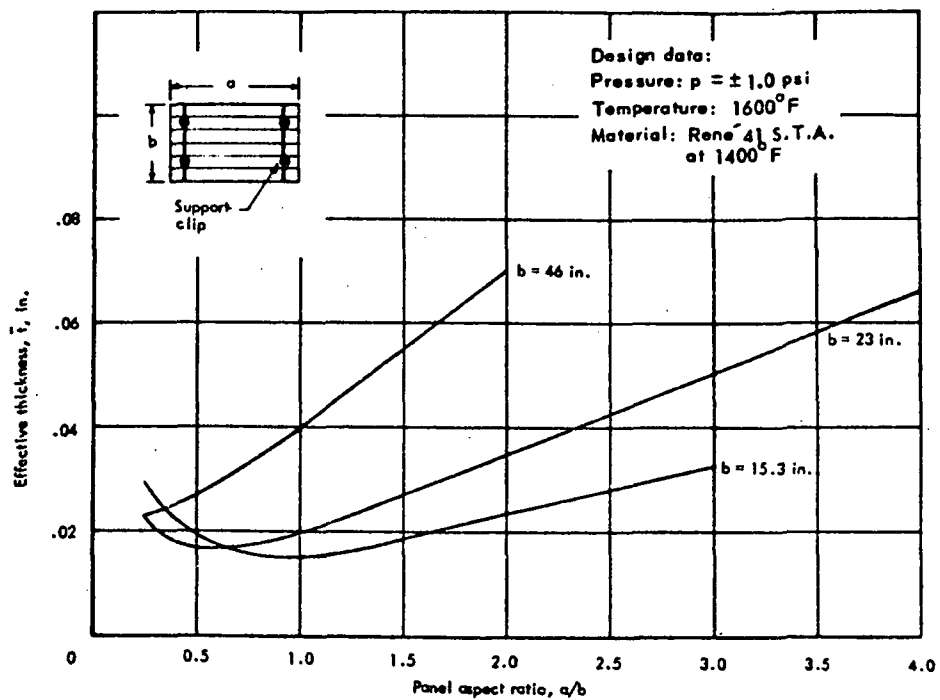


Figure 3-14. Panel Size vs  $\bar{t}$  for Corrugated Heat Shields with Hat Sections and Clip Support

## SECTION 4

### SENSITIVITY STUDIES

The prediction techniques used to design the TPS always have a degree of uncertainty caused by anything from the scatter of data used to correlate heat transfer prediction methods to the experimental error introduced while determining material properties. The system designer must account for these effects by either providing a margin of safety to allow for these contingencies or by limiting or refining mission constraints to avoid catastrophic failure due to the increased loads that may occur. The experience of previous TPS design work indicates that the compounded conservatism introduced by simply adding the margins required to provide system safety can lead to significant weight and performance penalties of the vehicle. To combat these penalties in both the weight and cost of the TPS, two tasks must be performed: (1) the penalties due to the performance prediction uncertainties must be established, and (2) a rational method of combining these penalties must be established since many of the uncertainties and associated penalties are not independent. It is the purpose of a sensitivity study to establish the penalties in system weight and cost due the uncertainties in system design.

Design uncertainties in the TPS itself can be separated into three categories: The environment, physical properties of the system itself, and operational and system characteristics. A partial list of these effects is given in Table 4-1. Parametric data gathered by establishing the weight and cost penalties due to variations in these uncertainties will establish the system sensitivities to these changes.

Consider, for example, the weight of the TPS per unit area as the parameter whose sensitivity is to be established as a function of some uncertainty. First, the weight of the system can be determined for the nominal case. This analysis would include use of nominal aerodynamic heating and pressure prediction methods with a nominal boundary layer transition criterion over a smooth surface. Material and mechanical properties of the TPS would be assigned nominal values as would operations and system characteristics. For this investigation, the nominal case will be based on the optimum panel size for given TPS materials and configuration and a representative trajectory. Next, an off nominal case will be established by a variation in some driving parameter. For example, for the case of turbulent flat plate heating shown by the data of Figure 4-1, a 30% variation in the data amounts to plus or minus 25 percent on the nominal value predicted by the method of Spalding and Chi. The turbulent heating value predicted by this method is then varied by these factors of 1.25 and 0.75 and new unit area weights are determined. The change in weight from the nominal case can then be expressed as



$$\Delta \bar{w} = \left( \frac{\partial \bar{w}}{\partial q_T} \right) \Delta q_T$$

where  $\bar{w}$  denotes system weight and  $q_T$  denote turbulent heating. The change in the heating rate can be established most easily as a percentage increase or decrease in heating rate. The weight penalty and heating increase thus establish the parameter  $\left( \frac{\partial \bar{w}}{\partial q_T} \right)$ , the partial of weight with respect to heating method. For variations in the heating method perturbations, the weight partial can be plotted as a function of these drivers. Parametric analysis of the various uncertainties outlined in Table 4-1 will then establish system sensitivities.

Table 4-1. TPS Uncertainty Factors

---

Environment

- Laminar heating
- Onset of transition to turbulent flow
- Onset of fully developed turbulent flow
- Turbulent heating
- Separated flow heating
- Local flow conditions
- Trajectory dispersions
- Roughness effects
- Vehicle aerodynamic attitude
- Local aerodynamic pressure loading
- Venting pressure

Physical Properties

- Material properties (including conductivity, density, specific heat, surface emissivity, etc.)
- Material temperature limitations
- Mechanical properties

Operations and System Characteristics

- Reentry trajectory corridor
- Attitude control system interactions
- Related systems and structure thermal limits
- Manufacturing, assembly and fabrication limitations
- Reuse constraints
- Inspection requirements
- Initial structural temperatures

---

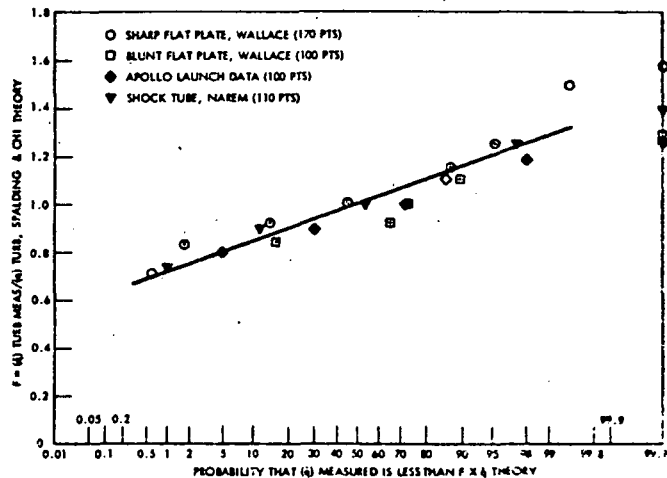
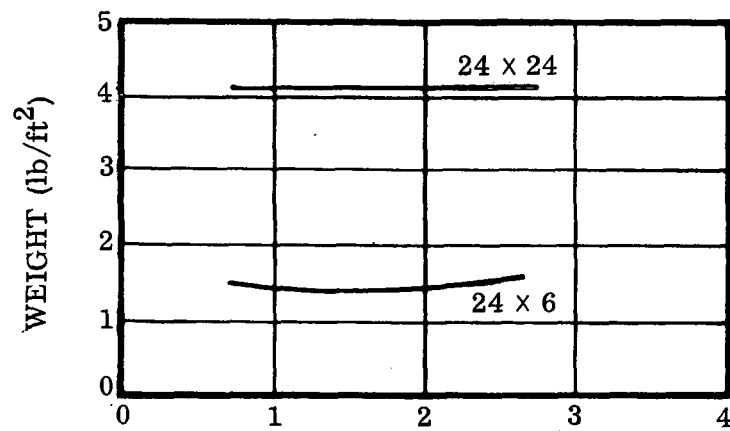


Figure 4-1. Turbulent Flat Plate Heating Data

The establishment of system weight penalties to a number of uncertainties which are mutually compatible is the subject of an extensive study to be undertaken in future work.

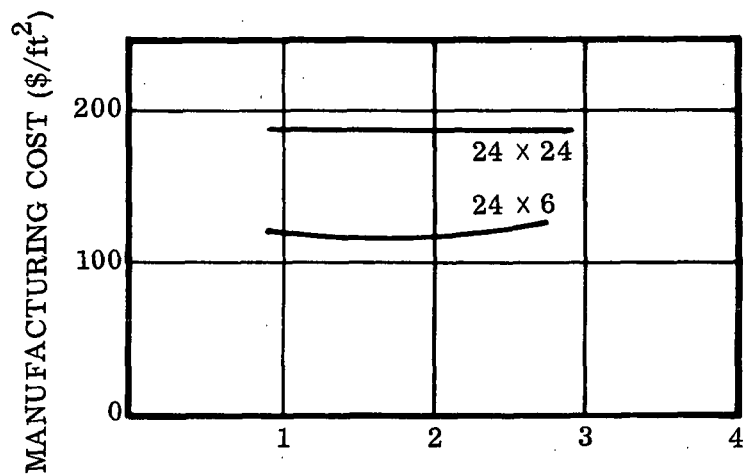
As part of Task 3, some preliminary computer studies were made to illustrate the application of the TPS sizing routines to determine the sensitivities of TPS cost and weight to various perturbations of input parameters. The TPS considered was the same semi-smooth configuration described in the optimization studies. The parameter that was varied was the aerodynamic heating rate computed for the corrugated surface. The nominal case consisted of computing aerodynamic heating for the plate-wedge-cylinder option modified by the heating magnification factors of Figure 3-8. Two perturbations from this case were considered: the first was to assume that heating is unaffected by the corrugated surface. This means that the flow remains attached to the panel, and there is no heating amplification factor due to boundary layer reattachment. The second perturbation considered was a twenty-five percent increase in turbulent heating and a ten percent increase in laminar heating. This distribution is also shown in Figure 3-9. These heating distributions were applied to the case of the 24 x 24-inch panel. In addition, the nominal case and the case for uniform heating (with no magnification) were considered for the optimum panel size of 24 x 6 inches.

For the non-optimum case of the 24 x 24-inch panel, the resulting weights and costs are shown to be relatively insensitive to heating rates (Figures 4-2 and 4-3) whereas the optimum panel design (24 x 6 inches) shows a rather weak sensitivity to variations in heating rates. Temperature distributions are shown in Figures 4-4 and 4-5. Although no temperature constraint was applied to this particular TPS model, a limit of 300°F on the aluminum tank was met for both the nominal and uniform heating cases.



MAXIMUM HEATING AMPLIFICATION FACTOR

Figure 4-2. Weight Sensitivity to Heating Amplification



MAXIMUM HEATING AMPLIFICATION FACTOR

Figure 4-3. Cost Sensitivity to Heating Amplification

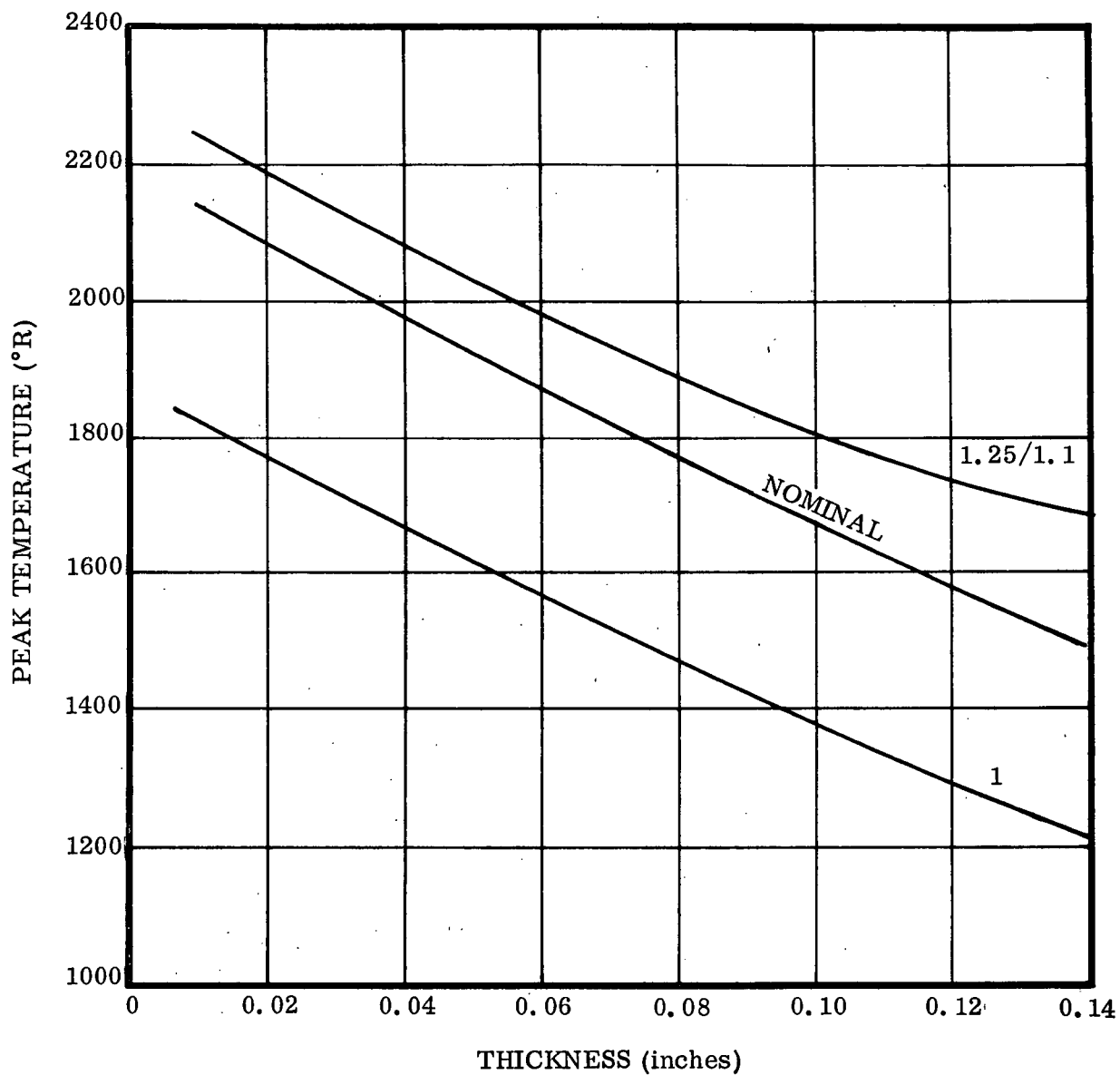


Figure 4-4. Peak Skin Temperature

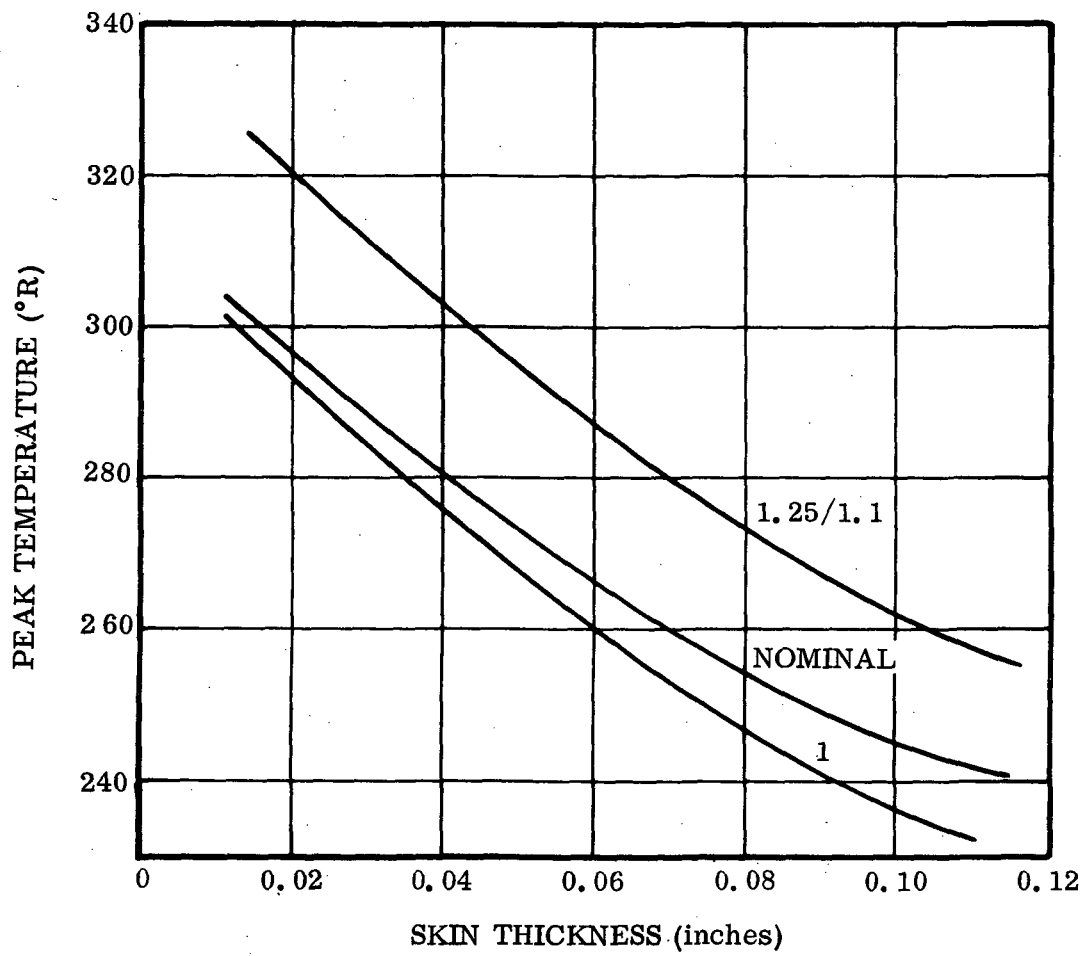


Figure 4-5. Peak Tank Temperature

## SECTION 5

### PROGRAM DEMONSTRATION AND DOCUMENTATION

Running the TPS sizing computer program (a part of Task 4 of this contract) on the Manned Spacecraft Center's Univac 1108 proved to be a straightforward task. The major differences between the programs developed for the CDC 6400 and the Univac 1108 at Convair Aerospace and MSC lay in control cards necessary to set up the runs and a few Fortran statements. Essentially, any Fortran IV program can be run in Fortran V. A list of exceptions is given in Table 5-1. The only other important exceptions concern reading an end of file in the data and the maximum size of a number stored in the memory.

For the case of reading an end of file, the Fortran IV statements for the CDC 6400 operation are

```
READ (Unit, f)
```

```
IF (EOF, Unit)  $l_1$ ,  $l_2$ 
```

The equivalent Fortran V statement is

```
READ (Unit f, ERR =  $l_3$ , END =  $l_1$ )
```

where

Unit      — represents the logical unit involved in the input/output transmissions

f          — represents format references

$l_1, l_2, l_3$  — are statement labels

In the Fortran IV statement, program control passes to statement  $l_1$  if an end of file is experienced; otherwise,  $l_2$ . In the Fortran V statement, control passes to  $l_3$  if an error is detected in execution of the input or to  $l_1$  if an end of file card is encountered.

For the case of the size of a number which can be stored in the MSC 1108, the largest value is E30 ( $10^{30}$ ).

Table 5-1. Fortran V Programming Reminders

- 
1. Do not use parameter names of more than six characters
  2. In computed GO TO statements, the comma after the parentheses is necessary, i.e., GO TO (1, 2, 3, 4), K
  3. Do not use too many parentheses in READ and WRITE statements because the MSC 1108 gets confused. Use

DO 100 J = 1, NSEG

100 READ (5, 8)((MAT (I, J), TAMP (I, J)), I = 1, K)

rather than

READ (5, 8) ((MAT (I, J), TAMP (I, J)), I = 1, K), J = 1, NSEG)

4. The maximum word size on the MSC 1108 is six as opposed to the CDC's ten. Thus, use 10A6 instead of 6A10
5. Use only Hollerith fields and not \*'s in format statements
6. Do not use multiple statements or multiple assignments on one card, i.e.,

A = B \$ C = D \$ F = G      or      A = B = C = D = 0.2

7. Avoid variable names that are the same as MSC library functions, i.e., be a little selective in names. Do not use the word INPUT, STOP, WRITE.
8. Do not use Convair Aerospace special functions or Fortran II library routines, e.g., ATANF(A)
9. Do not use the two branch logical IF, e.g., (X.GE.Y) 13, 14
10. Do not use EXIT but rather call STOP
11. In READ and WRITE statements, use

READ (5, 10) X, Y, Z

and do not use

READ 10, X, Y, Z

---

## SECTION 6

### RECOMMENDATIONS AND PROGRAM REFINEMENTS

The objective of these recommendations, which are a part of Task 5 of this contract, is to improve and update the computational methods used in the optimization of thermal protection systems (TPS) for the space shuttle vehicle and to generate weight and cost data for optimum TPS shuttle designs.

The end product will be an improved TPS optimization computer program for application to the space shuttle. This program will employ refined numerical and mathematical models to decrease computer run time and make application of the computer program for design optimization easier for the program user. User's manuals, in addition to the operational Fortran program, will be delivered to MSC for dissemination to interested users.

The computer program will contain the latest available cost and weight data for shuttle TPS. This data, along with current TPS designs, will be used to perform detailed optimization studies and generate sensitivity coefficients in terms of cost, weight, and performance.

This investigation is divided into four tasks. The first two update the computer program to include new TPS concepts and to improve computational speed. The third, and most important, is the design of optimum TPS at local areas on the shuttle vehicle. The fourth task is documentation of the investigation and the improved computer program.

#### 6.1 COMPUTER PROGRAM IMPROVEMENTS

The primary function of this task is to incorporate refinements in the mathematical and numerical models of the computer code to either increase computational speed and accuracy or allow easier and more valid comparisons of the weight and cost of candidate TPS materials and configurations. In addition, new current TPS concepts on the space shuttle will be included in the sizing program. These include surface insulation, carbon-carbon systems, mass transfer cooling, and ablators. Figure 6-1 illustrates the current arrangement of the TPS sizing routine.

**6.1.1 MATHEMATICAL AND NUMERICAL METHODS.** To speed and simplify computer running times and output results, these methods will be incorporated into the appropriate analysis subroutines which describe thermodynamic (aerodynamic heating, internal heat transfer, and structural temperature response), stress, panel and support fatigue, and weight/cost analyses.



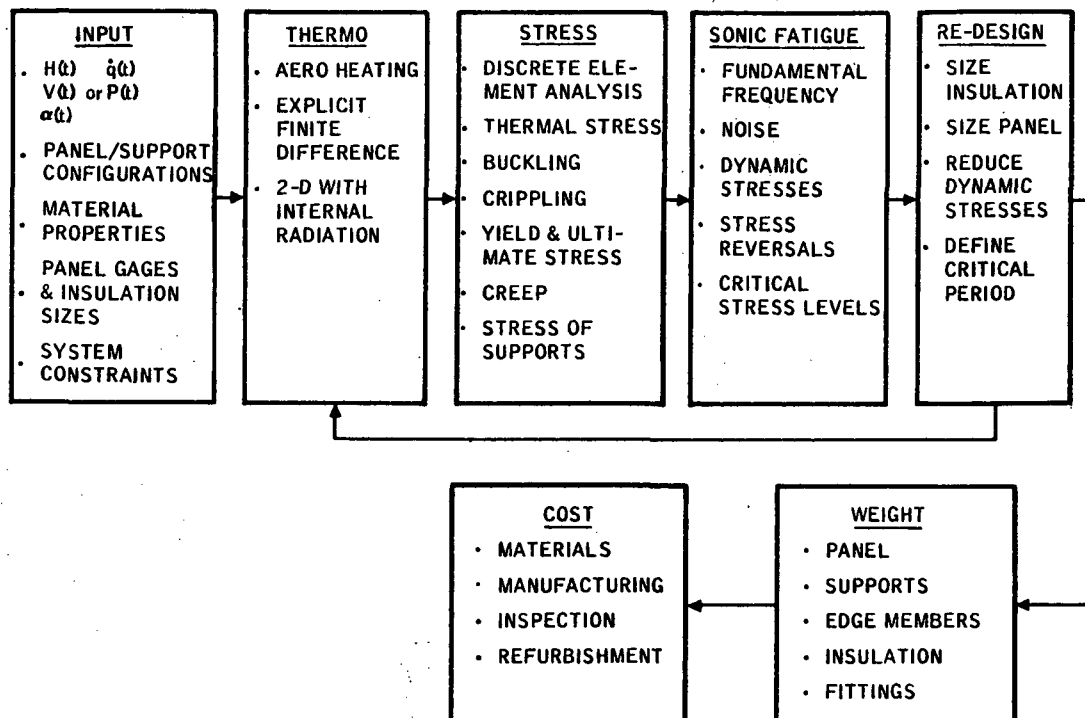


Figure 6-1. TPS Design Computer Program

#### 6.1.1.1 Thermodynamic Analysis.

Aeroheating. Typical improvements will include development of real gas oblique and conical shock theories at high angle of attack which are suitable for quick, easy, and economical computer usage. Also, real air properties will be added to the boundary layer calculations. Suitable curve fits (a Mollier chart for air) are available in computer programs existing at Convair Aerospace. The boundary layer edge properties necessary for any transition rationale are also available. Pressure methods themselves will be the subject of a short, concerted investigation and evaluation effort.

Implicit Heat Transfer. The computation of TPS heat transfer and temperature response in one or two dimensions with internal radiation and in both steady-state and time-dependent analysis will be studied to speed computer time. Several alternative heat transfer routines are available at Convair Aerospace in a number of heat transfer program and thermal analyzers. These consist of Program 2162 using the Crank-Nicholson forward-backward differencing scheme; Program 4560 using a similar technique; and Program 2772 using the Runge-Kutta-Gill method to solve the differential equations.

It is proposed that two or three typical TPS panels (for example a one-dimensional plate, a two-dimensional honeycomb, or a two-dimensional beaded panel) be input to each existing computer program and the computational times over a realistic portion of a trajectory be compared. A representative sampling of typical problems will select the best overall technique. This technique will be adapted to TPSOPT, either as an option to the explicit technique or as a replacement.

6.1.1.2 Structural Analysis. The major changes and additions proposed for the TPS stress analysis routines are:

- a. Improvements and extension of existing analyses of the metallic reradiative TPS.
- b. The inclusion of additional analyses for stress redistribution due to creep and panel deflection.
- c. The addition of mathematical models and routines for additional TPS for external insulation, carbon-carbon, ablators, and mass transfer cooling.

Details of the work to be performed under each of the other headings are discussed in the following paragraphs.

Panel Analysis and Support Structure. To increase the flexibility of the existing stress analysis procedure and to make it readily adaptable to additional configurations, separate subroutines to accomplish each major step in the analysis (e.g., finite element breakdown, thermal stress, creep, deflection, buckling, static strength, and redesign procedure) will be organized. The program will be extended to provide additional routines for the analysis of panel edges or support points and the support structure (i.e., beams, posts, clips). This will consider bending, crippling, column instability, creep, and deflection.

A simplification of the redesign procedure is possible for panels in which creep is found to be noncritical, as determined by an initial trajectory analysis. Subsequent iterations of the redesign procedure need be made only for static strength at the most critical trajectory point.

Stress Redistribution Due to Accumulated Creep Strains. In a beam member subjected to bending and/or thermal stresses, the accumulated creep strains due to exposure at temperature tend to relax the peak stresses and, hence, modify the subsequent creep rates and total creep strain. This effect can readily be included in the program by combining the cumulative creep strains throughout the cross section with the thermal strains ( $\alpha T$ ) in the existing thermal stress analysis. This stress analysis with creep relief will be included as an optional alternative to the existing technique since the additional computer run time required for the method may not be desired for all cases.

Deflection Analysis. A panel creep deflection analysis, combined with the addition of support deflections and the existing analyses for deflections due to pressure loading and temperature gradient, will allow prediction of deflection throughout the life of the TPS.

A design constraint based on deflection will be included in the redesign procedure. The maximum allowable deflection is given by the following expression:

$$\text{ALLOW DEFLECTION} = \pm (c + KL)$$

where  $c$  and  $K$  are input parameters and  $L$  is the panel width.

### 6.1.1.3 Dynamics Analysis

**Panel Flutter and Stability.** Panel flutter is a self-excited instability of elastic panels in supersonic flow, during which the panel oscillates in a direction normal to its plane at a constant amplitude; flutter usually results in fatigue damage to the panel. Considerable theoretical and experimental research has been conducted to understand the phenomenon and to develop design criteria to prevent it (Reference 42). The design approach recommended by Lemley will be incorporated into the TPS sizing routine, TPSOPT. The minimum panel thickness required to preclude panel flutter within the flight envelope will thereby be established as a design constraint. The non-dimensional

flutter parameter  $\phi = \left[ \frac{f(M)E}{q} \right]^{1/3} \left( \frac{t_B}{\ell} \right)$  is the governing function for the flutter criterion and reflects the influence of Mach number (M), dynamic pressure (q), Young's modulus (E), and panel thickness ( $t_B$ ) and length  $\ell$ . The Mach number correlation parameter,  $f(M)$ , shown in Figure 6-2, has replaced the familiar compressibility parameter.

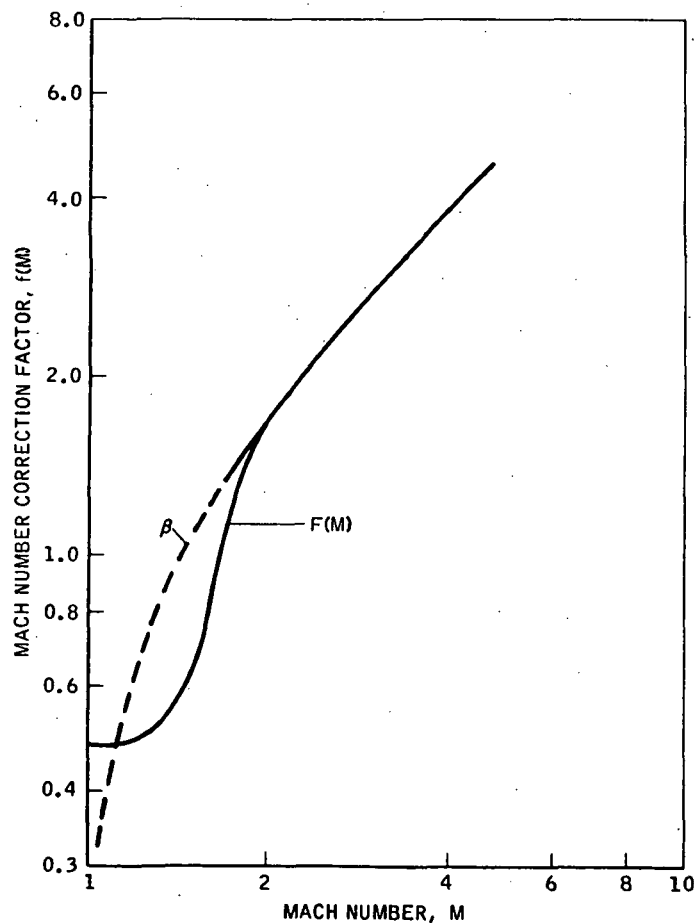


Figure 6-2. Mach Number Correction Factor Versus Mach Number

$\beta = \sqrt{M^2 - 1}$  since theory requires a prohibitively large panel thickness to prevent flutter at low transonic Mach numbers when  $\beta$  approaches zero. Figure 6-3 presents the quotient of the Mach number correlation factor and the local dynamic pressure as a function of trajectory altitude and local Mach number. (A typical shuttle boost trajectory is given for reference.) The critical flight condition generally occurs at  $[q/f(M)]_{\max}$ , although other trajectory points may require investigation, particularly if the panels are hotter at other flight points.

Finally, Figure 6-4 gives the minimum panel thickness,  $t_B$ , for flutter-free flight in terms of dynamic pressure, Mach number correlation parameter, material property  $E$ , and panel geometry. These curves will be programmed for the TPS sizing routine to allow determination of a panel thickness  $t_B$  in terms of vehicle trajectory and panel geometry.

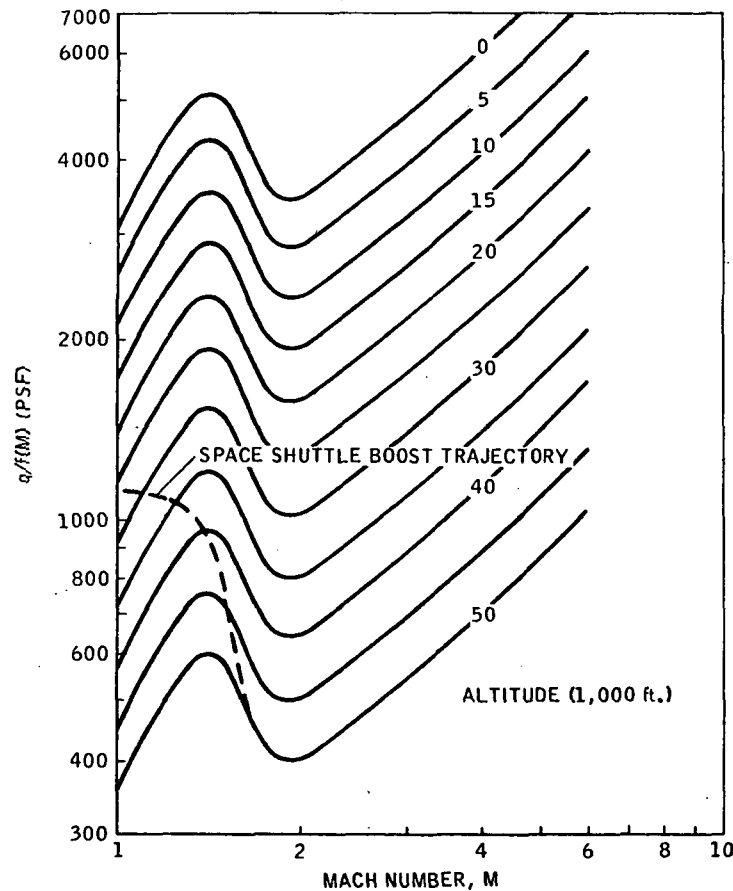


Figure 6-3. Plot of  $q/f(M)$  Versus Mach Number With Parametric Variation in Altitude

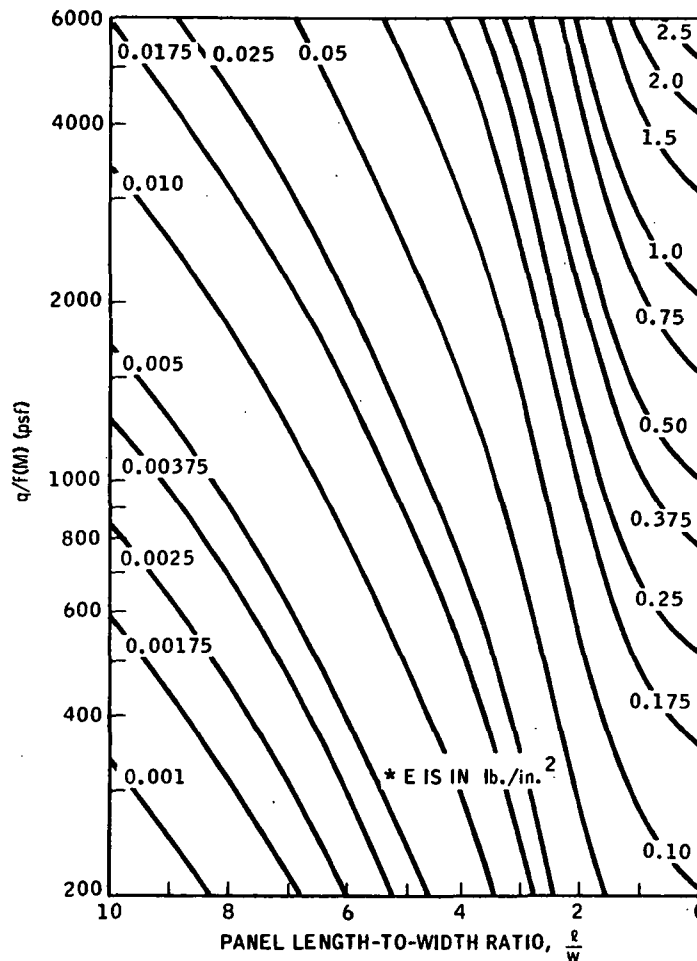


Figure 6-4. Aerodynamic Parameter  $q/f(M)$  Versus  $l/w$   
With Variation in Structural Parameter  $(t_B/l)^3$

**Acoustic Fatigue Analysis.** The acoustic fatigue analysis, now part of the computer program TPSOPT, is considered by Convair Aerospace to be an excellent approach, within the defined scope of effort, to the estimation of the acoustically induced loads and fatigue life of representative TPS panel configurations. Panel configurations include (1) isotropic, (2) beaded, (3) corrugated, (4) honeycomb, and (5) integrally stiffened plates.

Convair Aerospace was recently awarded Contract NAS8-27017, "Fatigue Evaluation of Thermal Protection Systems," by the Marshall Space Flight Center. Among the objectives of the contract are three pertinent to the effort of a continuing TPS optimization study.

- a. Obtain and compile basic fatigue (S-N) data for six candidate materials for space shuttle thermal protection systems.

- b. Evaluate fatigue life prediction methods applicable to space shuttle thermal protection systems.
- c. Investigate the damping provided by thermal insulation.

The new acoustic fatigue refinements for the TPS optimization study are described in the following paragraphs.

**Higher Panel Modes and Associated Stresses.** As in the case for the fundamental mode, the maximum stress in any higher mode will occur at a clamped edge of the panel. Therefore, the maximum stress can be calculated for each higher mode by considering only the clamped edge and the adjacent section of the panel extending to the first mode line. This approach provides an effective panel segment whose elements all move in phase in response to a correlated pressure. By equating bending moments, it can be shown, for example, that a clamped, simply-supported segment can be replaced by an equivalent clamped-clamped segment whose length is increased by 25%, as shown in Figure 6-5.

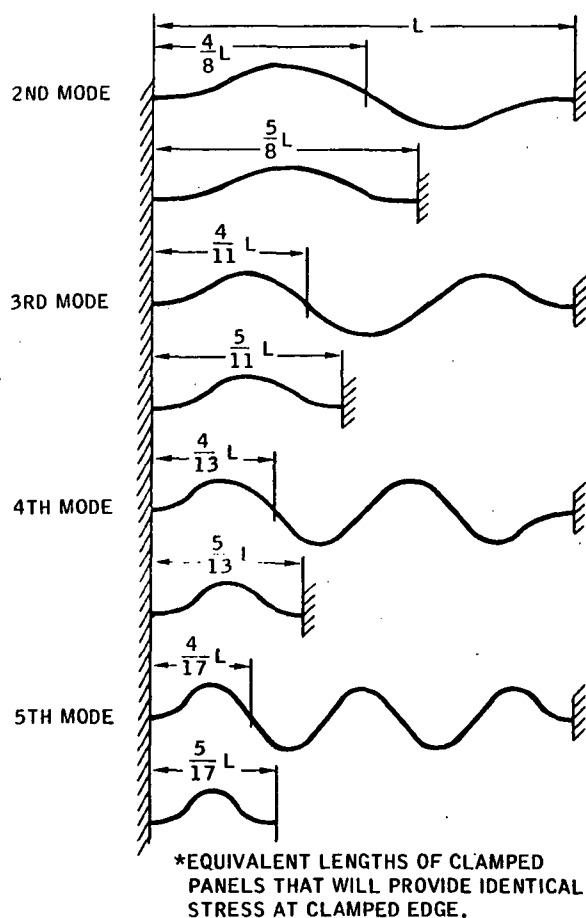


Figure 6-5. Equivalent Panel Segments for Computation of Stress in Higher Panel Modes

**Acoustic Pressure Correlation.** A review will be made of pressure correlation lengths associated with the various noise sources and at representative locations on the space shuttle vehicle. This study will determine the maximum number of modes and the upper frequency limits that will be required in the investigation of higher panel modes.

**Fatigue Characteristics of Panel Supporting Structure.** For normalized loads, comparative stress levels in representative panels and supports will be evaluated to determine whether, from the fatigue standpoint, one is significant with respect to the other. If there is significant correlation, an attempt will be made to arrive at general weighting factors that could be applied to fatigue life computations to ensure that prediction techniques will be nominal.

**Cumulative Damage Theory.** From Contract NAS8-27017, if a significantly improved damage theory is derived it will be incorporated into the TPSOPT program.

Damping Evaluation. A review of representative TPS configurations will be made and their damping properties estimated. If the spread in damping ratios is small, an average value will be assigned to the computer program. If there is a wide variation, it may be necessary to assign a nominal value for each type of configuration.

Fatigue Data Compilation. All applicable S-N data obtained on Contract NAS8-27017 will be included in the program data bank as it becomes available.

6.1.1.4 Weight/Cost Analysis. The weight and cost analysis portion of the program will be expanded in scope, and the existing techniques will be updated and refined to simplify program organization and to speed program flow. The overall weight/cost subroutine will be simplified to facilitate future additions and changes. The input requirements will be generalized to increase the flexibility of the subroutine by making it possible to combine the structural elements of various existing TPS configurations and, thus, be able to synthesize new TPS configurations within the program. (At present, only specific configurations may be called at the user's option.) This additional capability will allow combining the better elements of several different concepts during optimization and sensitivity studies.

Data storage core requirements will be greatly decreased through the elimination of tables. Standard hour data will be curve fit so that standard hours can then be calculated directly and used immediately (along with labor rates, overhead ratios, and realization factors incorporated into the subroutine) to derive labor and indirect overhead costs without any interim storage or retrieval of data. Other tables will be combined to calculate the cost of the actual purchased material based on the total quantity. Consideration will be made based on a lot buy, reflecting minimum-buy penalties, quantity buy discounts, special mill charges, die costs, form complexity, and tolerance requirements. The manufacturing usage variance factor, which is established by accounting practice, takes into consideration material and part overbuying, losses, surplus, spoilage, duplication, substitution, and charges. Material cost data will be updated and incorporated into the subroutine.

One major advantage resulting from the existing weight/cost analysis is derived from the fundamental level of approach, using a unique detail part listing process within the program. A significant improvement can be made by updating the program in terms of detail design and detailed manufacturing and fabrication techniques. Data relative to detail part identification, including the latest clip and fastener concepts, will be developed and incorporated into the program. A study will be made of state-of-the-art manufacturing operations and procedures and assembly operations including diffusion bonding, electron beam welding, and brazing processes as applied to the various TPS concepts and materials. New TPS configurations under consideration will be analyzed and included in the subroutine.

The program cost summary (Figure 6-6) will be expanded to include recently identified cost elements and cost data factors.

# THERMAL PROTECTION SYSTEM — COST SUMMARY

	COST (\$M)
THEORETICAL FIRST UNIT COSTS — TFU 9.628	
NON RECURRING COST	
ENGINEERING, DESIGN, & DEVELOPMENT	53,009
TOOLING	63,545
GROUND TEST HARDWARE	23,588
FLIGHT TEST ARTICLES	19,256
FLIGHT TEST SPACES	6,451
TOTAL NONRECURRING TPS COST	165,849
RECURRING PRODUCTION COST	
SUSTAINING ENGINEERING	— INCLUDED IN TFU
SUSTAINING TOOLING	— INCLUDED IN TFU
PRODUCTION ARTICLES (1)	9,628
TEST ARTICLE CONVERSION	2,888
TOTAL RECURRING PRODUCTION COST	12,516
RECURRING OPERATIONS COST	
REFURBISHMENT	12,824
TOTAL RECURRING OPERATIONS COST	12,824
TOTAL THERMAL PROTECTION SYSTEM PROGRAM COSTS	191,149
NUMBER OF PRODUCTION UNITS	1

Figure 6-6. Example Output of a Program Cost Summary

The theoretical first unit cost which is, in turn, used to estimate the other cost items, is the predicted production cost of the prototype article, including manufacturing planning, fabrication, subassembly, sustaining engineering, sustaining tooling, quality control, materials, and subcontracted parts. The existing program uses a weight-driven functional relationship to calculate the TFU. This procedure lacks the depth of analysis required to study the sensitivities of design tradeoff choices in terms of structural materials and methodology, other than those that change TPS gross weight. It also is deficient in cases where cost is an inverse function of weight. Indeed, advances in technology are producing components with increased specific strengths and greater structural efficiencies; however, such advances require increasingly exotic materials and fabrication complexities — hence, greater cost. The existing manufacturing cost calculation procedure contains many cost elements making up the TFU cost, including planning, fabrication, subassembly, materials, and subcontracted parts. The existing manufacturing cost procedure will be expanded to cover engineering, tooling, and quality control considerations. The TFU cost will then be derived based on the manufacturing cost portion of the subroutine. In this way the remaining TFU-driven cost items will be made sensitive to design tradeoff studies made at the detail level.

Addition of engineering costs requires the development of a method for predicting the necessary engineering manhours necessary and the related cost elements. Consideration will be made for such items as shop liaison, reliability, engineering changes and



fixes, and technical and preliminary design required during the initial concept phases. The total engineering costs are obtained for the complete TPS by applying current labor rates and overhead ratios to the total labor hours required. The estimating procedure will be used based on the engineering tasks to be performed, and the data will be derived from Convair Aerospace labor accounting records.

Refurbishment cost data is presently becoming available as a result of studies made within Convair Aerospace and at Lockheed and McDonnell-Douglas (References 43 and 44). These studies estimate the tasks required and the relative reliability of the various TPS concepts and materials. This data will be used to refine the analysis of refurbishment costs within the program, and better define complete system nonrecurring operations cost (both refurbishment and maintenance). The existing manufacturing cost methodology, based at the detail part level, will be extended to include an analysis of the refurbishment tasks necessary for each TPS concept. These tasks include inspection, removal, reinstallation, and certification of TPS panels. Associated costs include manhours required to perform the tasks, equipment, indirect overhead, and spares hardware. Since detail parts data are now available within the program, it is possible to relate each task requirement to specific operations necessary at the detail part level, and in this manner to derive the manhour and equipment requirements for the refurbishment phase based on the actual work to be done. Overhead and spares requirements can also be derived on this basis. Consideration will be incorporated into the analysis for the latest available data concerning the various material and system reliabilities.

In this task, additional weights and costs data will be gathered from the literature (Reference 45) and prediction techniques will be developed and refined to include a number of both active and passive cooling systems. Prediction techniques will be developed in each system in sufficient depth to allow a meaningful cost and weight comparison among the concepts and with the metallic reradiative system already described by the existing program.

Material Property Data. A great deal of mechanical and thermodynamic data are currently available in the literature concerning nominal values of density, thermal conductivity, thermal coefficient of expansion, modulus of elasticity, ultimate strength, and yield strength primarily as functions of temperature. Some pressure-dependent data are available for insulating materials. It is suggested that a computer routine be developed to interpolate values of physical properties which are functions of two variables (temperature and pressure).

Not only are thermodynamic and mechanical properties necessary, but also needed are the S-N curves of the fatigue analysis, and, no matter how rudimentary, the cost data for raw materials, machining, and fabrication processes.

Weight data will also be developed in a similar manner, especially for either metallics that oxidize (thus changing panel weights) or metallics that must be coated. Next, the typical nonmetallic panel materials should be investigated in the same depth and detail. Again, material, manufacturing, development, refurbishment, and similar cost data must also be cataloged for input to the sizing program.

**6.1.2 ADDITIONAL TPS DESIGNS.** To evaluate TPS concepts that are truly representative of the state of the art in both performance prediction and hardware production, a number of additional configurations of interest and importance to space shuttle applications will be incorporated into the TPS sizing program.

#### 6.1.2.1 Passive Cooling Systems

**Reusable Surface Insulation (RSI).** The typical concept shown in Figure 6-7 is RSI material bonded to a metal substrate. A gap is shown between it and an internal structure such as an aluminum tank wall. A supporting structure may also be included between substrate and primary structure. Other concepts (such as wing surface) can have the RSI directly bonded to an internal structural panel of titanium or other material. The existing thermal heating analysis will be used to predict the temperature histories and maximum temperature of the outer surface, the bond line, and the internal structure. However, wave band dependence of in-depth radiation effects should be considered.

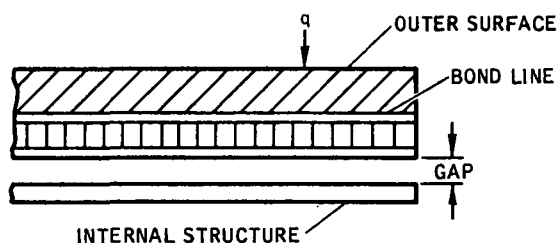


Figure 6-7. RSI Concepts

The primary difficulty in analyzing the RSI system is the stress analysis — in particular, the deformation of the bond line. The approach to the stress analysis of the RSI will be two-pronged: first, finite element methods (for large deflections) will be investigated to see if they can be simplified enough for economic analysis of the RSI; and, second, the contract monitor and program manager will confer early in the program to review the latest analytical techniques and their application to RSI.

Within the scope of this contract, acoustic fatigue behavior of the RSI can be predicted by existing methods of the TPS sizing routine. Weight and cost data will be developed as discussed previously.

**Carbon-Carbon Composites.** Oxidation inhibited carbon-carbon composites are being considered for use as reusable radiative heat shields for space shuttle vehicles. The selection of materials for the leading edge and lower surface areas (Figure 6-8) on

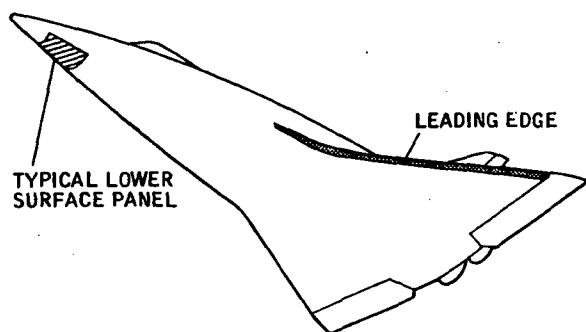


Figure 6-8. Space Shuttle High-Crossrange Orbiter

these vehicles presents a severe design problem based upon the long life and cyclic exposure design criteria established for the multimission space shuttle.

Carbon and graphite composites are unique in that they possess excellent high-temperature stability and retain structural integrity at temperatures above 4000°F. This property alone makes the carbon-graphite class of materials unique to other types being considered as candidate heat shield materials. In addition, they have low thermal expansion and can

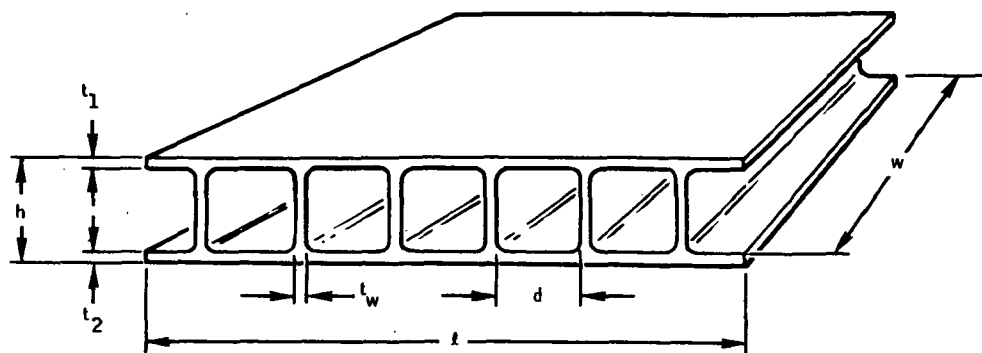
be tailored for mechanical behavior. Laminated carbon materials and unique 3-D reinforced carbon-carbon integrated structures are being developed for heat shield applications.

One concept uses laminated carbon-carbon composite material as an integrally-stiffened shell (Figure 6-9). This idea is based on existing carbon-carbon technology developed over the last six to eight years and is severely limited in design flexibility by problems associated with the complex tooling required, local reinforcements for attachments, and overall reliability. Because of these problems, a 3-D reinforced carbon-carbon fluted core was selected for development (Figure 6-10). This is a lightweight, double-faced, truss core structure that integrates an external heat shield cover panel with a support structure which, in turn, can be attached to a primary load-carrying structure. The concept consists of a 3-D woven truss core fabric rigidized with high-carbon-yield resins, pyrolyzed, and then carbonized up to 4000°F in an inert atmosphere. A typical leading edge design using the carbon-carbon fluted core is also shown in Figure 6-10. For the lower surface area identified in the schematic of the shuttle vehicle (Figure 6-8), candidate heat shields may include several types of fluted core constructions. Carbon-carbon leading edges and panels will be analyzed on the modified version of computer program TPSOPT.

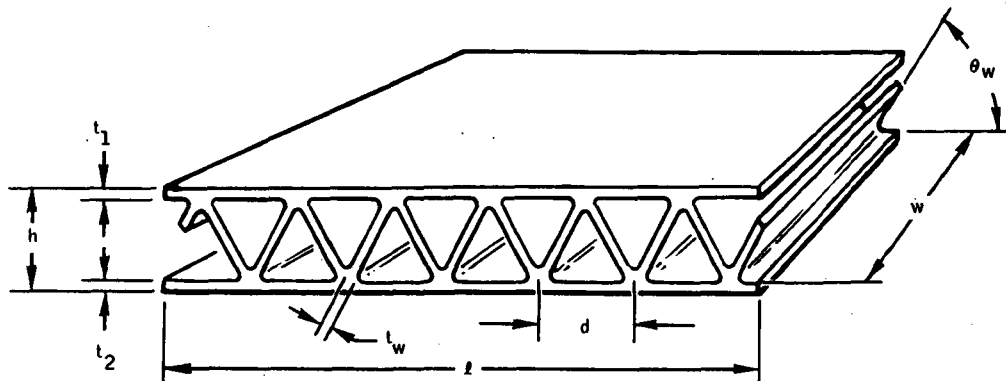
The structural analysis of the carbon-carbon system will be performed using the existing discrete element analysis for the flat panel. The program will be investigated to determine applicability of existing mathematical models to the leading edge.

**Heat Sink Concepts.** The potential benefits of using heat sink thermal control for the space shuttle structure have been shown in a recent study, "Space Shuttle Aluminum Booster Study" conducted by Convair Aerospace.

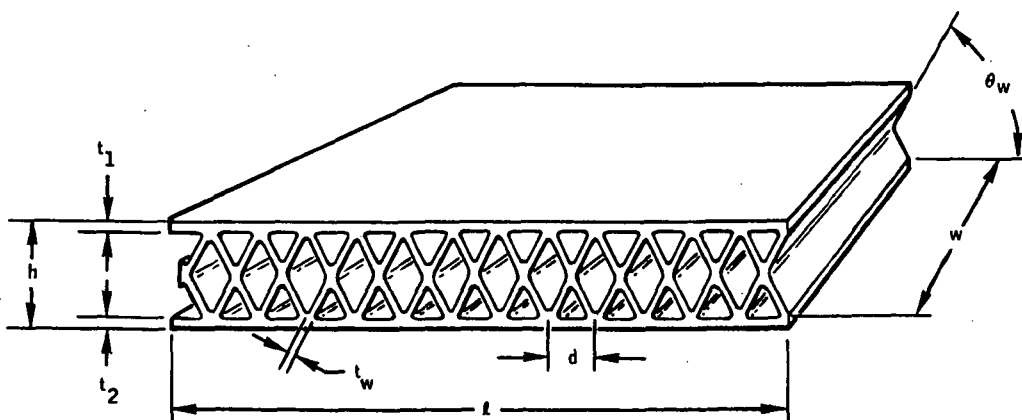
Heat sink thermal protection will be subjected to design conditions and vehicle operating problems that prior studies have shown are the critical criteria in sizing and evaluating different design concepts. The thermal loads will size the amount of heat sink required once materials have been selected and operating temperature limits set.



RECTANGULAR OR SQUARE CORE



TRUSS CORE



"X" CORE

Figure 6-9. Three-Dimensional Reinforced Carbon-Carbon Core Configurations

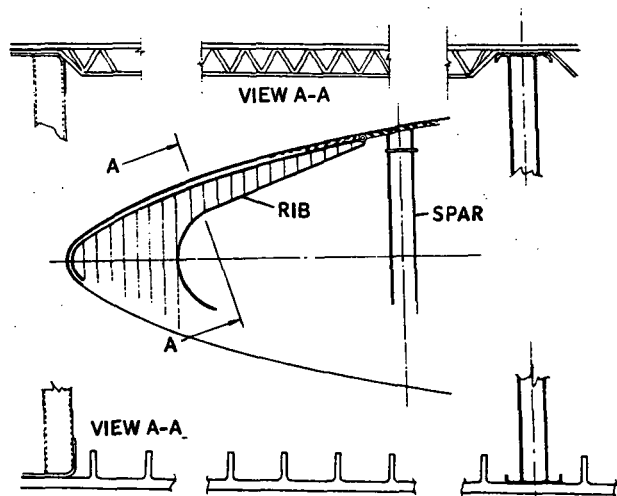


Figure 6-10. Carbon-Carbon Leading Edge Designs

Thermal stresses in the heat sink tank structures using aluminum have been found to be a secondary problem because the maximum allowable temperature used has been 300°F or less and heat sinking has kept the temperature distribution sufficiently uniform that the  $E \propto \Delta T$  product remains less than 4000 psi. Similar results can be expected with other concepts where material stress allowable limits require low operating temperatures.

Potential heat sink designs are included in two basic arrangements: heat sink integral with the airframe structure and heat sink separate from the structure. For the integral concept, the heat sink may be fabricated in the same part as

the structures or it may be a separate panel or shingle bonded or brazed to the structure. The inner surface may be open to ambient conditions, exposed to liquid oxygen, or insulated from exposure to liquid hydrogen with cryogenic insulation such as polyphenylene oxide foam. In case of the separate panel concept, the panel can also consist of jacketed nonstructural or phase-change materials.

Table 6-1 lists candidate heat sink materials and material properties. These materials were selected for their good heat absorption capacities and represent the maximum capacity available in materials relevant to this study.

Along with the geometry of the panel concept and the materials used, operating temperature is an important parameter to consider. Figure 6-11 indicates the influence of operating temperature variation on panel unit weight. The distance between the two curves accounts for variations in the heat absorption and emissivities of the different materials considered. The reduction in the panel weight with increase in outer wall temperature is caused by increased radiation at the higher temperatures.

The thermo-structural, weight, and cost analyses for the various heat sink TPS concepts can be carried out using the existing techniques in the TPSOPT program. Some modifications must be made to accommodate the heat absorption due to phase change. In the transient conduction program, the nodes will be specified to absorb the heat of fusion at constant temperature of melting. Additional changes may be made for stress and some fatigue analysis. Typical results already developed at Convair Aerospace for the aluminum heat sink TPS are shown in Figure 6-12.

Table 6-1. Candidate Heat Sink Materials

MATERIAL	HEAT OF FUSION (Btu/lb.)	T MELT/ T BOIL (°F)	DENSITY (lb./in. 3)	SPECIFIC HEAT (Btu/lb. - °F)	THERMAL CONDUCTIVITY (Btu/lb. ft. - °F)	TOTAL HEAT ABSORPTION (Btu/lb.)				% VOL. CHANGE ON FUSION	CORROSIVE-NESS
						-150° TO 250° F	70° TO 250° F	70° TO 1,000° F	70° TO 2,000° F		
Phase-Change:											
Lithium	286	354/ 2,400	0.019	1.0	22.5	370	180	1,216	2,216	1.5	
Sodium	49.5	208/ 1,638	0.035	0.295	40	159	103	324		2.5	
Water	79.7	32/ 212	0.036	1.0	0.25	320*	130*	—	—	-8.3	
Linear Polymer (PPO)	60	500/-	0.033	0.45	0.19	166	81	478	—		
Non-Phase Change:											
Aluminum	170	1,220/ 3,740	0.099	0.23	120	85	41	214	614**	6.6	
Beryllium	470	2,340/ 5,020	0.066	0.45	87	166	81	418	868	—	
Graphite Composite	—	—	0.061	0.18	100	67	32	167	347	—	
JP-5	—	—	0.027	0.50		185	90	465	965	—	

\* T = 200° F

\*\* Includes heat of fusion

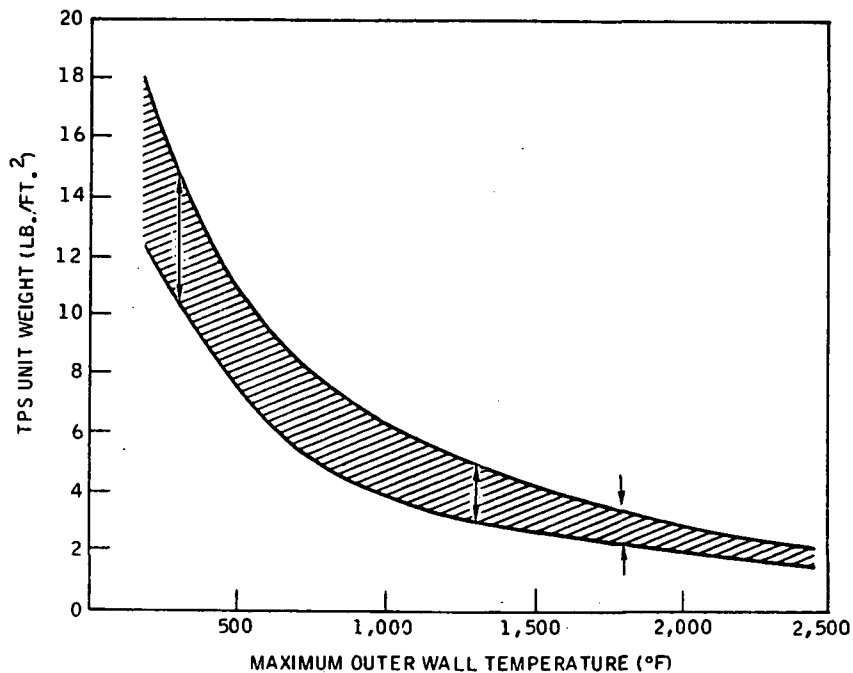


Figure 6-11. Influence of Operating Temperature Variation Upon Panel Unit Weight

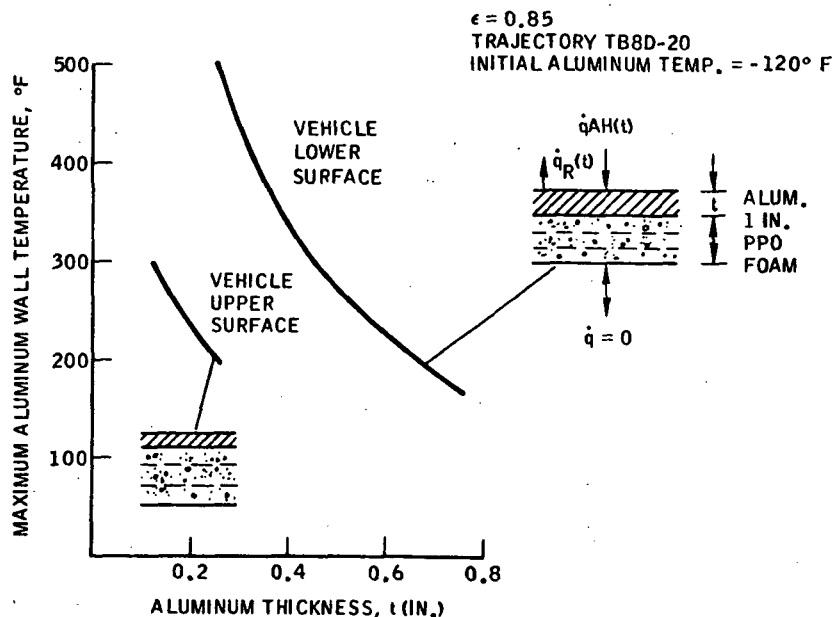


Figure 6-12.  $\text{LH}_2$  Tank Wall Temperature  
Vs. Tank Wall Thickness

#### 6.1.2.2 Active Cooling Systems

Regenerative Systems. A technique has been developed under IRAD funds to predict performance of a space radiator (Reference 46). This method will be investigated for adaptation to the specific applications of convective aeroheating to the shuttle vehicle. It may provide capability to evaluate the performance, weight, and cost of one type of active TPS to be compared with other systems already described by the computer program.

Mass Transfer Cooling. When mass transfer is used as a means of cooling, there are at least two principal heat reducing mechanisms at work. First, heat is absorbed by the cooling fluid as it travels against the direction of heat flow from some reservoir to a surface of higher temperature and, consequently, lowers the wall temperature; second, as the fluid emerges from the surface of the wall, it forms an insulating layer between the surface of the wall and the hot gas.

In one such method of cooling, the wall is manufactured from a porous material and the coolant is blown through the pores. The coolant film on the hot-gas side is, therefore, continuously renewed and the cooling effectiveness can be made to stay constant along the surface. When a liquid is used as a coolant, a liquid film is created on the hot-gas side which is evaporated on its surface, and the heat absorbed by the evaporation process increases the cooling effectiveness. This process is frequently referred

to in the literature as evaporative-transpiration cooling. The ultimate criterion for evaluating coolants is minimization of the system weight required to maintain the wall at the desired temperature. Figure 6-13 gives coolant weights required to maintain the wall at specified temperatures for some coolants.

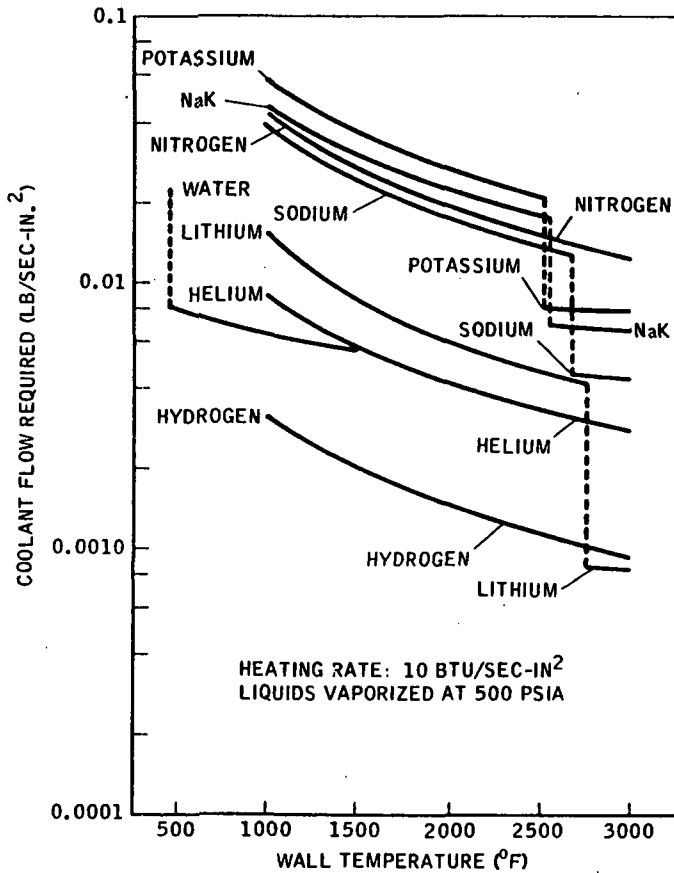


Figure 6-13. Coolant Weight Requirements Versus Wall Temperature

**Single-Phase Mass Transfer.** Most of the analytical investigations on transpiration cooling have been concerned with the laminar boundary layer – primarily a result of the laminar flow problem being more amenable to analytical treatment than the turbulent flow. Unfortunately, transpiration cooling is more likely to be used where turbulent flow and, consequently, higher heating rates are involved. Even if the flow is laminar initially, the disturbance resulting from the injection of the coolant tends to cause transition to turbulent flow.

Transpiration cooling effectiveness will be predicted for this study by considering the single-phase flow of either a liquid or gaseous coolant. The heat transfer analysis is for the one-dimensional case with constant material properties. The temperature of the porous matrix  $T$  through which the coolant flows is described by the equation

$$\rho C_p \frac{\partial T}{\partial \tau} = K \frac{\partial^2 T}{\partial X^2} + \phi$$

where  $\phi$  is a heat source or dissipation function. Under the same assumption, the temperature of the coolant,  $t$ , is given by

$$\rho C_p \frac{\partial t}{\partial \tau} + \rho u C_p \frac{\partial t}{\partial X} = 0$$

where the conduction of the coolant has been neglected and the material properties are those of the coolant. For the case in which either the film heat transfer coefficient between the coolant and matrix is very large or the flow rate of the coolant is moderate, the matrix and coolant are in thermal equilibrium and  $T = t$ . Hence, the energy equations for the two materials may be combined to give



$$C_{pm} \rho_m \frac{\partial T}{\partial \tau} = K_m \frac{\partial^2 T}{\partial X^2} + \rho_c C_{pc} u \frac{\partial T}{\partial X}$$

where the subscript m refers to the matrix of the TPS and c refers to the coolant. This equation is identical to the heat conduction equation already solved in the conduction subroutine of program TPSOPT, with the exception of the heat sink term involving the temperature-dependent properties of the single-phase coolant. The modification to the computer program is a minor one. Sizing the TPS will involve computing the weight and cost per unit area of the TPS as a function of total coolant volume reflected by coolant velocity,  $u$ .

For this preliminary investigation of the transpiration cooling phenomenon, the behavior of the external coolant effectiveness is assumed predicted by the empirical relationship developed by Bartle and Leadon for turbulent flow (Reference 47).

The coolant effectiveness for laminar flow will be handled in a similar manner; e.g., the data correlation of Figure 6-14.

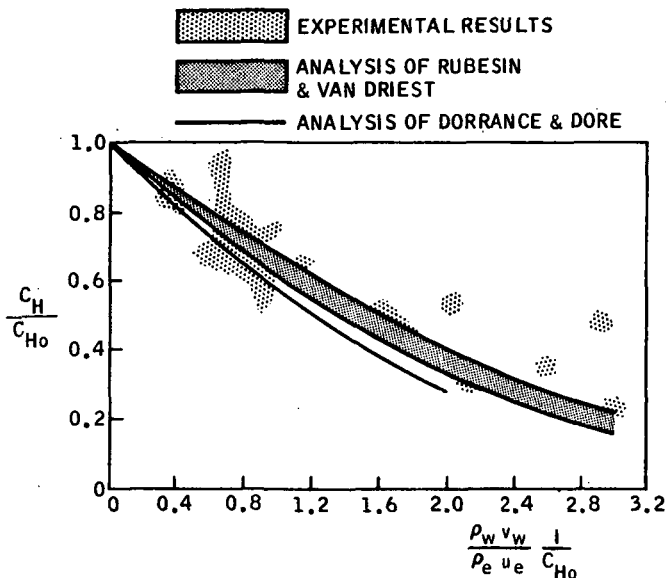


Figure 6-14. Laminar Coolant Effectiveness

**Ablation Analysis.** The computer program will be refined to incorporate at least one type of ablation analysis. The technique selected will be decided after investigation of available methods and by considering the most promising type of ablative materials for space shuttle application.

Methods of analysis of ablative heat shield materials, can be categorized, depending on the material melting point and oxidation chemistry, as:

- Oxidation Controlled. When the melting temperature is greater than the radiation equilibrium temperature.
- Simple Sublimers. When the melting temperature is lower than the radiation equilibrium temperature.
- Pyrolytic Ablators. When the material decomposition into pyrolysis gas and char occurs in depth.

Theoretical methods are available for detailed treatment of these cases. They are based on multicomponent mass injection and mass transfer correlations of the boundary layer coupled with the wall chemical kinetics. For the present study, the treatment for Case 1 is considered too sophisticated to incorporate in the computer program.

It is felt that a less sophisticated method of analysis can be effectively used in the proposed study; the basic problem to be solved is locating the pyrolysis zone as a function of time. Two simplified methods that are candidates for use are discussed in the following paragraphs.

Heat of Pyrolysis Technique. The degradation of an ablative system, and the attendant temperature distribution through the system, can be analyzed in a simplified manner by using a property termed heat of pyrolysis. Heat of pyrolysis is defined as the amount of heat required to degrade one pound of material and has the units of Btu/lb.

The thermal model used with this technique will be composed of three zones. Starting from the heated surface, the first zone is comprised of char (degraded ablator). The second zone is the pyrolysis zone where the degradation of the ablator takes place. For purposes of analysis this zone can be considered to be of zero thickness. The third zone is the virgin ablator material. The thermal model requires a moving coordinate system to account for the increase in thickness of the char zone and the decrease in thickness of the virgin material zone.

At the end of the calculation interval, the amount of heat flowing from the heated boundary to the pyrolysis zone is used in conjunction with the heat of pyrolysis value to compute the amount of material degraded during the calculation interval. This, then, defines the location of the pyrolysis zone for the following calculation interval, and the conduction networks in the char and virgin material zones are redefined accordingly.

Heat of Ablation Technique. A quantity known as heat of ablation can be used to perform a simplified thermal analysis of an ablative TPS. Heat of ablation is a generalized property that accounts for the mass loss from an ablative system as a function of heating rate; the units are Btu/lb.

The thermal model for this technique uses a boundary condition that moves in the ablator coordinate system. This boundary is the pyrolysis zone, which can be treated as a constant-temperature boundary. The constant temperature is the pyrolysis temperature and is material dependent.

For a calculation interval, the surface heating rate is used to determine the heat of ablation. This is then used to calculate the amount of material degraded, and from this is derived the location of the pyrolysis zone for the next calculation interval. A one-dimensional conduction solution is performed from the pyrolysis zone boundary

through the ablator/structural network. At the start of the next calculation interval, the conduction network in the ablator is redefined to account for the movement of the pyrolysis zone.

## 6.2 PROGRAM APPLICATIONS AND OPTIMIZATION TECHNIQUES

This section of the program plan concerns mainly the inclusion of short-term computer coding improvements that will speed and facilitate the actual technique of optimizing the TPS panels and supporting structure at various places or on various areas of the space shuttle vehicle. For the sake of discussion in this program plan, such techniques are divided into two categories: short-term improvements and true optimization procedures.

**6.2.1 SHORT-TERM IMPROVEMENTS.** During the course of checking our computational procedures and performing optimization and sensitivity studies, close attention will be paid to developing automatic methods to speed the overall assimilation of TPS design data and ease the program user's task in generating information that is meaningful and useful to the space effort. The program resulting from Contract NAS9-10956 will size the panel and insulation thicknesses for given values of panel length, width, and materials, for given thermal and structural constraints, and for a given vehicle trajectory (or, alternatively, input heating rates and pressure distribution). For a given panel configuration (e.g., Rene' 41 panel backed by Dynaflex, which is separated by an airgap from a titanium primary structure) and trajectory, the program user will run a series of cases in which support structure spacing and panel width and length are varied. The optimum design for this configuration will be the one that either weighs or costs the least. This can be established quite readily by plotting a curve of cost or weight as a function of the varying parameter (spacing or panel width or length). The design procedure is then repeated for different panel and support configurations, materials, trajectories, vehicle locations, and whatever other variables are of interest. It will help the procedure considerably if subsequent cases of a particular configuration can be stacked and the corresponding weights and costs either plotted out automatically or stored to be curve fitted and the minimum determined analytically later at the end of the runs. The possibility of graphically presenting any and all data will be thoroughly investigated and adopted where it proves feasible.

**6.2.2 FORMAL OPTIMIZATION PROCEDURES.** A great deal of information is currently available at MSC concerning the application of mathematical optimization procedures to the case of a one-dimensional TPS configuration consisting of up to three different materials. The payoff function is usually weight per unit area subject to temperature constraints at the material boundaries or interfaces. Early in this proposed investigation an independent survey will be made of the optimization procedures currently available at Houston (e.g., adoptive creep, pattern search, method of steepest descent, Davidon method, etc.), and the possibility of their application to the complexities of the present problem will be assessed. It is altogether possible

that the application of one optimization procedure that works well for a wide variety of configurations could be implemented to the case in which the TPS weight can be varied by only two parameters: panel thickness and insulation thickness.

### 6.3 OPTIMIZATION AND SENSITIVITY STUDIES

Detailed optimization and sensitivity studies of those TPS concepts already developed in the program TPSOPT will be begun on the first day of the study. For representative trajectories and areas of interest on the vehicle, parametric studies will be undertaken to establish weights and costs of optimum panel sizes and support member spacing for the variety of panel configurations (beaded, corrugated, honeycomb, integrally stiffened) and supporting structures already available in the program.

The most promising candidates will be established initially over their expected range of application. Typical candidates include titanium alloys to 1000°F, nickel alloys to 1700°F, cobalt alloys to 2000°F, dispersion-strengthened such as TD Ni or TD NiCr to 2200°F, columbium to 2500°F, and tantalum alloys to 2800°F. One particular panel configuration and material will be studied in great detail to determine the effects of a variety of insulation materials and orientations.

The results of these studies will be illustrated as carpet plots of weight and cost as a function of heating load, duration, configuration, materials, and vehicle location. Such data will then be in a form convenient for inclusion into a number of available synthesis programs being developed both at Convair Aerospace and NASA.

## SECTION 7

### REFERENCES

1. Scullen, R.S., A Description of the Revised Aerodynamic/Structural Heating and Radiation Equilibrium Temperature Computer Program 3020, Convair Division of General Dynamics Report GDC-ERR-1336, December 1968.
2. Whitehead, K.D., Computer Program 3020 Revision, Convair Aerospace Division of General Dynamics Report GDC-ERR-1416, December 1969.
3. Livett, R.K. and Schadt, G.H., Aerodynamic Heating Using the Real Properties of Air Behind Shock Waves, Convair Aerospace Engineering Department Report No. ZR-658-024, December 1958.
4. Romig, M.F., On the Estimation of Compressible Heat Transfer for High Temperature Air, Convair Aerospace Scientific Research Laboratory Memorandum, June 1958.
5. Rausch, J.R. and Hearn, E.B., Experimental Aerodynamic Characteristics of a Lifting Entry Spacecraft Configuration, Convair Aerospace Report GDC-ERR-1408, March 1970.
6. Love, E.S., Base Pressure at Supersonic Speeds on Two-Dimensional Airfoils and on Bodies of Revolution With and Without Fins Having Turbulent Boundary Layers, NACA TN 3819, January 1957.
7. Eckert, E.R.G., Survey of Heat Transfer at High Speeds, WADC Technical Report 54-70, 1954.
8. Hansen, C.F., Approximations for the Thermodynamic and Transport Properties of High Temperature Air, NASA Technical Report R-50, 1959.
9. Howarth, L., Modern Developments in Fluid Dynamics, High Speed Flow, Vol I, Clarendon Press, Oxford 1953, pp 382-386.
10. Schlichting, H., Boundary Layer Theory, McGraw-Hill, New York, 1960.
11. Roming, M., Conical Flow Parameters for Air in Dissociation Equilibrium, Convair Aerospace Scientific Research Note No. 14.
12. Spalding, D.B. and Chi, S.W., "The Drag of a Compressible Turbulent Boundary Layer on a Smooth Flat Plate With and Without Heat Transfer," Journal of Fluid Mechanics, Vol. 18, Part I, pp 117-143, January 1964.

13. Wallace, J.E., "Hypersonic Turbulent Boundary Layer Studies at Cold Wall Conditions," 1967 Heat Transfer and Fluid Mechanics Institute, La Jolla, Ca., June 1967.
14. Komar, J.J., Improved Turbulent Skin-Friction Coefficient Predictions Utilizing the Spalding-Chi Method, Douglas Aircraft Co. Report DAC-59801, November 1966.
15. Bertram, M.H., and Neal, Luther, Jr., Recent Experiments in Hypersonic Turbulent Boundary Layers, NASA TMX-56335, Presented at the AGARD Specialists' Meeting on Recent Developments in Boundary Layer Research by the Third Dynamics Panel of AGARD, Naples, May 10-14, 1965.
16. Masaki, M., and Yakura, J., "Transitional Boundary Layer Considerations for the Heating Analyses of Lifting Re-entry Vehicles," AIAA Paper No. 68-1155, AIAA Entry Vehicle Systems and Technology Meeting, Williamsburg, Va. December 3-5, 1968.
17. Kemp, N. H. and Riddell, F.R., "Heat Transfer to Satellite Vehicles Reentering the Atmosphere," Jet Propulsion, Vol. 26, No. 12, December 1956.
18. Beckwith, I.E., and Gallagher, J.J., Local Heat Transfer and Recovery Temperatures on a Yawed Cylinder at a Mach Number of 4.15 and High Reynolds Numbers, NASA TR R-104, 1961.
19. Bertram, M.H., and Henderson, A., Jr., "Recent Hypersonic Studies of Wings and Bodies," ARS Journal, pp 1129-1139, August 1961.
20. Thermo-Structural Analysis Manual, Air Force Flight Dynamics Laboratory, Technical Report No. WADD-TR-60-517, Vol. I, August 1962.
21. Freudenthal, A. M., The Expected Time to First Failure, AFML-TR-66-37.
22. Freudenthal, A.M., and Heller, R.A., On Stress Interaction in Fatigue and a Cumulative Damage Rule, WADC TR 58-69.
23. Blatherwick, A., and Viste, N., Fatigue Damage During Two-Level Biaxial-Stress Tests.
24. Swanson, S.R., Random Load Fatigue Testing; A State of the Art Survey, MTS Systems Corp.
25. Jacoby, G.H., Fatigue Life Estimation Processes Under Conditions of Irregularly Varying Loads, AFML-TR-67-215.

26. Torbe, I., A New Framework for the Calculation of Cumulative Damage in Fatigue, USAA Report 111.
27. Smith, C.R., Linear Strain Theory and the Smith Method for Predicting Fatigue Life of Structures for Spectrum Type Loading, ARL 64-55.
28. Schivje, J., "Cumulative Damage Problems in Aircraft Structures and Materials," 11th Conference of the International Committee on Aeronautical Fatigue, May 1969.
29. Birnbaum, E.W., et al, A New Mathematical Model for Fatigue, TR No. 58 (Contract N-ONR-477(38), University of Washington.
30. Development of Analysis for Structural Panel Instabilities, NASA Contract NAS8-11469, GDC-66-035, pp I-12 to I-15.
31. Szechenje, E., An Approximate Method for the Determination of the Natural Frequencies of Single and Stiffened Panel Structures, I.S.V.R. Tech. Report 23, University of Southampton, March 1970.
32. A Review of Flight and Wind Tunnel Measurements of Boundary Layer Pressure Fluctuations and Induced Structural Response, NASA CR-626.
33. Prediction of Boundary Layer Pressure Fluctuations, AFFDL-TR-67-167.
34. Ollerhead, J.B., Prediction of Near Field Noise of Supersonic Jets, NASA CR-857, August 1967.
35. Howes, W.L. and Mull, H.R., Near Noise Field of Jet Engine Exhaust, 1 - Sound Pressures, NACA TN 3763, October 1956.
36. Eldred, K.M., et al., Suppression of Jet Noise With Emphasis on the Near Field, U.S.A.F. ASD - TDR-62-578, February 1963.
37. An Investigation of the Effects of Surrounding Structure on Sonic Fatigue, NASA CR-1536.
38. Cummings, H.N., Some Quantitative Aspects of Fatigue of Materials, Wright Air Development Division, WADD Technical Report 60-42, July 1960.
39. Metallic Materials and Elements for Aerospace Vehicle Structures, MIL-HDBK-5A, Department of Defense, 8 February 1966.

40. Bertram, M.H., Weinstein, L.M., Cary, A.M., Jr., and Arrington, J.P., Effects of Two-Dimensional Multiple-Wave Distortions on the Heat Transfer to a Wall in Hypersonic Flow, AIAA Paper No. 67-164, AIAA 5th Aerospace Sciences Meeting, New York, N.Y., 23-26 January 1967.
41. Plant, P.P. Sakata, I.F., Dvais, G.W., and Richie, C.C., Hypersonic Cruise Vehicle Wing Structure Evaluations, Lockheed Missiles and Space Company, NASA CR-66897-1, February 1970.
42. Lemley, Clark, E., Design Criteria for the Prediction and Prevention of Panel Flutter, Vol. 1, Air Force Flight Dynamics Laboratory (FDDS), Technical Report AFFDL-TR-67-140, August 1968.
43. Peterson, R.J., Final Report for Refurbishment Cost Study of the Thermal Protection System of the Space Shuttle Vehicle, LMSC Contract NAS1-10094, March 1971.
44. Haas, D.W., Final Report - Refurbishment Cost Study of the Thermal Protection System of a Space Shuttle Vehicle, McDonnell Douglas - East, Contract NAS1-10093, 1 March 1971.
45. Gomez, A.V., Radiative, Ablative, and Active Cooling Thermal Protection Studies for the Leading Edge of a Fixed - Straight Wing Space Shuttle, Project Technical Report, Task E&DD-701A, Contract NAS9-B166, TRW Systems Group, Houston, Texas, 31 December 1970.
46. David, D.L., A Method for Evaluating the Performance of Space Radiators, Convair Aerospace Division of General Dynamics Report GDC-ERR-1428, December 1969.
47. Bartle, E.R., and Leadon, B.M., The Effectiveness as a Universal Measure of Mass Transfer Cooling for the Turbulent Boundary Layer, Convair Aerospace Division of General Dynamics Report ERR-AN-147, 2 May 1962.



**GENERAL DYNAMICS**  
*Convair Aerospace Division*